Quality Aware Synthesis of Antenna Systems for Simultaneous Wireless Information and Power Transfer in IoT Applications

A Thesis Submitted

in Partial Fulfilment of the Requirements

for the Degree of

DOCTOR OF PHILOSOPHY

by

Sundeep Kumar

(2019EEZ0004)



DEPARTMENT OF ELECTRICAL ENGINEERING INDIAN INSTITUTE OF TECHNOLOGY ROPAR January, 2025

Sundeep Kumar

Quality Aware Synthesis of Antenna Systems for Simultaneous Wireless Information and Power Transfer in IoT Applications Copyright ©2025, Indian Institute of Technology Ropar

All Rights Reserved

 $Dedicated\ to\ my\ Family.$

Declaration of Originality

I hereby declare that the work which is being presented in the thesis entitled Quality Aware Synthesis of Antenna Systems for Simultaneous Wireless Information and Power Transfer in IoT Applications has been solely authored by me. It presents the result of my own independent investigation/research conducted during the time period from August 2019 to August 2024 under the supervision of Dr. Ashwani Sharma, Assistant Professor, Indian Institute of Technology, Ropar. To the best of my knowledge, it is an original work, both in terms of research content and narrative, and has not been submitted or accepted elsewhere, in part or in full, for the award of any degree, diploma, fellowship, associateship, or similar title of any university or institution. Further, due credit has been attributed to the relevant state-of-the-art and collaborations (if any) with appropriate citations and acknowledgments, in line with established ethical norms and practices. I also declare that any idea/data/fact/source stated in my thesis has not been fabricated/falsified/misrepresented. All the principles of academic honesty and integrity have been followed. I fully understand that if the thesis is found to be unoriginal, fabricated, or plagiarized, the Institute reserves the right to withdraw the thesis from its archive and revoke the associated Degree conferred. Additionally, the Institute also reserves the right to appraise all concerned sections of society of the matter for their information and necessary action (if any). If accepted, I hereby consent for my thesis to be available online in the Institute's Open Access repository, inter-library loan, and the title & abstract to be made available to outside organizations.

Signature

Name: Sundeep Kumar

Entry Number: 2019EEZ0004

Program: Doctor of Philosophy (Ph.D.)
Department: Electrical Engineering
Indian Institute of Technology Ropar

Rupnagar, Punjab 140001

Date: 20/01/2025

Acknowledgement

First and foremost, I express my gratitude to Lord Khatu Shyam Ji for his blessings and unwavering support, which have empowered me to persevere and progress through all facets of my life. I extend heartfelt appreciation to my supervisor, Dr. Ashwani Sharma, for imparting vast knowledge and nurturing my passion for research. invaluable guidance and support during the challenging phases of my research remains etched in my memory, and I am forever beholden to him. Additionally, I also extend my gratitude to the esteemed members of my doctoral committee, Dr. Satyam Aggarwal, Dr. Brijesh Kumbhani, and Dr. Sujata Pal, for their perceptive feedback and suggestions aimed at enhancing the quality of my research endeavors. Furthermore, I appreciate the unwavering support and provision of essential resources from the Director, Deans, Heads of Departments, and faculty at the Indian Institute of Technology Ropar, which facilitated seamless progress in my research pursuits. My journey toward earning a Ph.D. was enriched by meaningful discussions with my esteemed peers Dr. Manoj Kumar, Dr. Ananth Bharadwaj, and Dr. Vivek Kumar Srivastava. I extend my gratitude to my fellow members at the Antenna and Microwave Research lab - Sagar Jain, Suraj Gupta, Parul Rattanpal, Vikas Kumar Malav, and Shivam Bansal for their invaluable assistance and support throughout my Ph.D. journey. I owe a debt of gratitude to my parents, Mr. Jai Bhagwan and Mrs. Kanta Devi, whose unwavering love and guidance have molded me into the person I am today, capable of navigating life's challenges. Special appreciation is extended to my elder brother, Mr. Naveen Kumar, for his steadfast support, which eased my path towards completing my Ph.D. Finally, I offer heartfelt thanks to my beloved wife, Sonam Dahiya, for her boundless love and unwavering encouragement, which has been instrumental in my academic journey.

Certificate

This is to certify that the thesis entitled Quality Aware Synthesis of Antenna Systems for Simultaneous Wireless Information and Power Transfer in IoT Applications, submitted by Sundeep Kumar (2019EEZ0004) for the award of the degree of Doctor of Philosophy of Indian Institute of Technology Ropar, is a record of bonafide research work carried out under my guidance and supervision. To the best of my knowledge and belief, the work presented in this thesis is original and has not been submitted, either in part or full, for the award of any other degree, diploma, fellowship, associateship or similar title of any university or institution.

In my opinion, the thesis has reached the standard fulfilling the requirements of the regulations relating to the Degree.

Bluish

Signature of the Supervisor Dr. Ashwani Sharma Department of Electrical Engineering Indian Institute of Technology Ropar Rupnagar, Punjab 140001

Date: 20/01/2025

Lay Summary

This thesis investigates the quality-aware synthesis of antenna systems tailored for access points, RF energy transmitters, IoT devices, and relay nodes, facilitating the realization of simultaneous wireless information and power transfer (SWIPT) in IoT networks. The primary objective is to enhance communication link quality while promoting the sustainability of IoT applications. The proposed antenna designs specifically tackle key challenges, including interference mitigation, the impact of misalignment between transmitter and receiver antennas on wireless power transfer, and the constrained battery capacity of IoT nodes. By effectively tackling these issues, our approach aims to significantly improve the overall performance and longevity of IoT networks, contributing to more efficient and reliable wireless communication.

Acronyms

2-D Two Dimensional

3-D Three Dimensional

ADS Advanced Design System

AP Access Point

BCE Beam Collection Efficiency

BER Bit Error Rate

CSI Channel State Information

DC Direct Current

ECA Effective Coverage Area

EH Energy Harvesting

EIRP Effective Isotropic Radiated Power

FWR Full Wave Rectification

HB Harmonic Balance

 \mathbf{HFSS} High Frequency Structure Simulator

HPBW Half Power Beamwidth

HWR Half Wave Rectification

iReAS Isotropic coverage Rectenna Array System

LPF Low Pass Filter

LSSP Large Signal S Parameter

MAA Microstrip Antenna Array

MPA Microstrip Patch Array

PAA Patch Antenna Array

PCB Printed Circuit Board

PCE Power Conversion Efficiency

PPA Power Pixel Area

PPV Power Pixel Volume

QCA Quality Coverage Area

QoS Quality of Service

ReAS Rectenna Array System

RF-ET RF Energy Transmitter

Rx Receiver

RF Radio Frequency

RFL Reconfigurable Feed Line

RFN Reconfigurable Feed Network

RN Relay Node

SAA SWIPT Antenna Array

SAE SWIPT Antenna Element

SBA Switched Beam Antenna

SIR Signal-to-Interfrence Ratio

SNR Signal-to-Noise Ratio

STBF Space Time Beamforming

SWIPT Simultaneous Wireless Information and Power Transfer

SMB Switched Multibeam

Tx Transmitter

 \mathbf{VNA} Vector Network Analyzer

WIT Wireless Information Transfer

WPT Wireless Power Transfer

WSN Wireless Sensor Network

Abstract

advancements in wireless communication technologies and electronics manufacturing have enabled the development of low-cost, low-power, miniaturized, and multifunctional Internet of Things (IoT) devices. These devices, part of IoT networks, communicate with each other and relay data to a remote Access Point (AP) via wireless technologies such as Bluetooth Low Energy (BLE), WiFi, and ZigBee. They find applications in diverse fields including environmental monitoring, smart cities, smart agriculture, intelligent healthcare, smart car parking, and tracking systems. The deployment of large-scale wireless sensor networks (WSNs) with high device density generates substantial data traffic between nodes and the AP, necessitating a communication system with wide bandwidth and high capacity at the AP. However, the dense network of WSNs leads to high interference, which limits the achievable capacity and degrades the signal-to-interference ratio (SIR). This reduction in SIR adversely affects effective coverage and link quality, resulting in increased energy consumption due to frequent re-transmissions required to maintain communication reliability. Consequently, energy consumption and the overall lifetime of the IoT devices are significantly impacted. To address the challenges of low SIR and capacity, techniques such as frequency reuse and high-gain antennas are utilized, though they offer limited spatial coverage with adequate SIR. Additionally, the limited battery capacity of miniaturized IoT devices makes battery replacement cumbersome and costly.

To enhance sustainability, wireless power transmission (WPT) techniques, particularly within the IoT framework, offer a promising solution. WPT enables wireless recharging of batteries and, with sufficient power transfer, facilitates battery-less operation of ultra-low-power WPT enabled IoT devices, making power delivery both cost-effective and convenient. Furthermore, the simultaneous wireless information and power transfer (SWIPT) approach can be employed to power IoT devices through base stations and dedicated RF energy sources, promoting a sustainable wireless communication network.

This thesis focuses on the quality-aware synthesis of antenna systems for access points (AP), RF energy transmitters, WPT-enabled IoT devices, and SWIPT-enabled IoT devices and relay nodes, with the aim of enhancing communication link quality and ensuring the sustainability of IoT applications. The proposed antennas aim to address the limitations imposed by interference and limited battery capacity of IoT devices, thereby enhancing the overall performance and longevity of IoT networks.

Keywords: 3–D coverage; access point; beam squint; signal to interference ratio; bit error rate; beamforming; switched beam antenna array; conjugate matching; RF energy transmitter; rectenna; relay node; angular misalignment; wireless information transfer; wireless power transfer; simultaneous wireless information and power transfer.

List of Publications

OUTCOME FROM THIS THESIS

Patent

Patent-1

S. Kumar and A. Sharma, "TITLE: A system and method for designing an improved SWIPT antenna for a relay node." (Patent filed with Indian patent office: Application No. 202411086588)

Transactions/Journal

Article-1

S. Kumar, V. Sharma, and A. Sharma, "SWIPT Module for Battery Less Ultra Low Power Sensor Nodes," in *IEEE Sensors Letters*, vol. 8, no. 12, pp. 1-4, Dec. 2024, Art no. 6015404, doi: 10.1109/LSENS.2024.3482409.

Article-2

S. Kumar, M. Kumar, A. Sharma and I. J. Garcia Zuazola, "Energizing an IoT Sensor Using Regenerative Opposite Fringing Fields From an Embedded Communicating Patch Antenna," in *IEEE Access*, vol. 12, pp. 47951-47960, 2024, doi:10.1109/ACCESS.2024.3382821.

Article-3

S. Kumar, M. Kumar and A. Sharma, "A Compact Stacked Multisector Near-Isotropic Coverage Rectenna Array System for IoT Applications," in *IEEE Microwave and Wireless Technology Letters*, vol. 34, no. 1, pp. 123-126, Jan. 2024, doi: 10.1109/LMWT.2023.3331214.

Article-4

S. Kumar and A. Sharma, "Switched Beam Array Antenna Optimized for Microwave Powering of 3-D Distributed Nodes in Clustered Wireless Sensor Network," in *IEEE Transactions on Antennas and Propagation*, vol. 70, no. 12, pp. 11734-11742, Dec. 2022, doi: 10.1109/TAP.2022.3209744.

Article-5

S. Kumar, S. Jain and A. Sharma, "A BER-Conscious Synthesis of Switched-Beam Antenna to Maximize Reliable Coverage in WSN Applications," in *IEEE Sensors Journal*, vol. 22, no. 4, pp. 3785-3795, 15 Feb.15, 2022, doi: 10.1109/JSEN.2022.3142137.

Article-6

S. Kumar, A. Sharma, S. Kalra and M. Kumar, "Communication Quality-Conscious Synthesis of 3-D Coverage Using Switched Multibeam Multi-Sector Array Antenna for V2I Application," in *IEEE Transactions on Vehicular Technology*, vol. 71, no. 2, pp. 1631-1642, Feb. 2022, doi: 10.1109/TVT.2021.3132304.

Conference Proceeding

Article-1

S. Kumar and A. Sharma, "A Polarization Insensitive Circular Rectenna Array System for Microwave Power Transfer and Energy Harvesting Applications," 2023 17th *European*

Conference on Antennas and Propagation (EuCAP), Florence, Italy, 2023, pp. 1-4, doi: 10.23919/EuCAP57121.2023.10133150.

OTHER COLLABORATIVE WORK

Transactions/Journal

Article-1

S. K. Gupta, M. Kumar, S. Kumar, A. Sharma, "Adaptive Wireless Power Transfer Enabled IoT Sensor Nodes by A Polarization-Insensitive Scalable Planar Rectenna Module," in *IEEE Sensors Journal*, doi: 10.1109/JSEN.2024.3447151.

Article-2

M. Kumar, S. Kumar, A. Sharma, V. K. Malav and P. Rattanpal, "An Orthogonally Polarized Multibeam Rectenna System to Imitate Isotropic DC Pattern for Orientation-Insensitive Microwave Power Delivery," in *IEEE Transactions on Components, Packaging and Manufacturing Technology*, vol. 14, no. 4, pp. 659-668, April 2024, doi: 10.1109/TCPMT.2024.3360304.

Article-3

M. Kumar, S. Kumar, A. S. Bhadauria and A. Sharma, "A Planar Integrated Rectenna Array With 3-D-Spherical DC Coverage for Orientation-Tolerant Wireless-Power-Transfer-Enabled IoT Sensor Nodes," in *IEEE Transactions on Antennas and Propagation*, vol. 71, no. 2, pp. 1285-1294, Feb. 2023, doi: 10.1109/TAP.2022.3228708.

Article-4

S. K. Gupta, **S. Kumar** and A. Sharma, "A Miniaturized Dual-Resonator-Based High-Capacity Chipless Radio Frequency Identification Tag Sensor," in *IEEE Sensors Letters*, vol. 6, no. 11, pp. 1-4, Nov. 2022, Art no. 6003904, doi: 10.1109/LSENS.2022.3218503.

Article-5

M. Kumar, S. Kumar and A. Sharma, "An Analytical Framework of Multisector Rectenna Array Design for Angular Misalignment Tolerant RF Power Transfer Systems," in *IEEE Transactions on Microwave Theory and Techniques*, vol. 71, no. 4, pp. 1835-1847, April 2023, doi: 10.1109/TMTT.2022.3222195.

Article-6

M. Kumar, S. Kumar and A. Sharma, "A Compact 3-D Multisector Orientation Insensitive Wireless Power Transfer System," in *IEEE Microwave and Wireless Technology Letters*, vol. 33, no. 3, pp. 363-366, March 2023, doi: 10.1109/LMWC.2022.3212599.

Article-7

M. Kumar, S. Kumar and A. Sharma, "A Planar Orbicular Rectenna Array System With 3-D Uniform Coverage for Wireless Powering of IoT Nodes," in *IEEE Transactions on Microwave Theory and Techniques*, vol. 71, no. 3, pp. 1366-1373, March 2023, doi: 10.1109/TMTT.2022.3217073.

Article-8

M. Kumar, S. Kumar, S. Jain and A. Sharma, "A Plug-in Type Integrated Rectenna Cell for Scalable RF Battery Using Wireless Energy Harvesting System," in *IEEE Microwave and Wireless Technology Letters*, vol. 33, no. 1, pp. 98-101, Jan. 2023, doi: 10.1109/LMWC.2022.3202711.

Article-9

M. Kumar, **S. Kumar** and A. Sharma, "Dual-Purpose Planar Radial-Array of Rectenna Sensors for Orientation Estimation and RF-Energy Harvesting at IoT Nodes," in *IEEE Microwave and Wireless Components Letters*, vol. 32, no. 3, pp. 245-248, March 2022, doi: 10.1109/LMWC.2022.3145196.

Conference Proceeding

Article-1

V. K. Srivastava, **S. Kumar** and A. Sharma, "3D Polarized Field-Forming for Mitigation of Angular Misalignment Problem in Microwave Power Transfer Systems," 2021 *IEEE 19th International Symposium on Antenna Technology and Applied Electromagnetics (ANTEM)*, Winnipeg, MB, Canada, 2021, pp. 1-2, doi: 10.1109/ANTEM51107.2021.9518942.

Contents

D	eclar	ation	•	vii
A	cknov	wledge	ment	ix
\mathbf{C}	ertific	cate		xi
La	ay Su	mmar	y x	iii
A	crony	vms	3	ΚV
A	bstra	\mathbf{ct}	\mathbf{x}	ix
Li	ist of	Public	eations x	xi
Li	ist of	Figure	es xx	xi
Li	ist of	Tables	S XXXV	⁄ ii
1	Intr	oducti	on	1
	1.1	Simult	aneous Wireless Information and Power Transfer	1
	1.2	Systen	a Architecture of SWIPT Enabled IoT Network	3
	1.3	IoT A	pplications and Challenges	5
	1.4	QoS N	Ietrics of SWIPT Enabled IoT Network	5
	1.5	Anten	na System Requirements and Challenges	7
		1.5.1	Quality of Wireless Information Transfer	7
		1.5.2	Access Point	7
		1.5.3	IoT Devices	7
		1.5.4	Relay Nodes	7
		1.5.5	Quality of Wireless Power Transfer	8
		1.5.6	Dedicated RF Energy Transmitter	9
		1.5.7	IoT Devices	9
		1.5.8	Relay Nodes	10
	1.6	Prior '	Works and Motivation	10
		1.6.1	Access Point Antenna System	10
		1.6.2	Dedicated RF Energy Transmitter	12
		1.6.3	Rectenna Module for IoT Devices	12
		1.6.4	SWIPT Antenna System for IoT Devices	12
		1.6.5	SWIPT Antenna System for Relay Node	14
	1.7	Thesis	Objectives	15
		171	Transmitter Antenna System	15

CONTENTS xxviii

		1.7.2	Receiver Antenna System	16
		1.7.3	Relay Node Antenna System	16
	1.8	Thesis	Outline	16
2	QoS	S Awar	re Transmitter Antenna System	19
	2.1	Syster	n Model of 2-D Coverage Multi-Sector Switched Beam Array Antenna	
		(Desig	gn-O1A)	20
		2.1.1	Analytical Model for Received Power Projection and SIR	21
		2.1.2	BER-Conscious Array Synthesis Process	23
		2.1.3	Analytical Optimization Results and Discussion	25
		2.1.4	The Proposed SBA Antenna Design-O1A Realization and	
			Performance Evaluation	30
	2.2	Syster	n Model of 3-D Coverage Multi-Sector Switched Beam Array Antenna	
		(Desig	gn-O1B)	35
		2.2.1	The Proposed Multibeam Multi-sector Antenna Design Schematic	
			Model	36
		2.2.2	Analytical Model of SIR and Optimization of 360° Azimuth Coverage	37
		2.2.3	Implementation and Radiation Pattern Measurements	47
		2.2.4	Received RF Power Measurements and SIR Evaluations	48
		2.2.5	Performance Comparison with prior work	52
	2.3	RF E	energy Transmitter	53
		2.3.1	Analytical Model for Projected 3-D Power Pixel	54
		2.3.2	Problem Formulation	57
		2.3.3	Analytical Results and Discussion	60
		2.3.4	Design Realization and Verification	64
		2.3.5	Comparison with state-of-the-art	68
	2.4	Summ	ary	69
3	Rec	eiver	Antenna for Ultra Low Power IoT Devices	71
	3.1	Angul	ar Misalignment Tolerant Rectenna Module	71
	3.2	Multi-	Polarized Circular Rectenna Array (Design-O3A)	72
		3.2.1	Single Integrated Rectenna Element	72
		3.2.2	Circular Integrated Rectenna Array	73
		3.2.3	Results and Discussion	73
	3.3	Isotro	pic Rectenna Array System Design (Design-O3B)	76
		3.3.1	Simulation Results and Discussion	77
		3.3.2	Experimental Verification	79
		3.3.3	Performance comparison with state-of-the-art	81
	3.4	SWIP	T Antenna For Ultra Low Power IoT Devices	82
		3.4.1	System Architecture	82
		3.4.2	Description of Proposed SWIPT Antenna (Design-O4A)	83
		3.4.3	Circuit Simulation and Design Evolution	85

CONTENTS xxix

		3.4.4	Simulation Results and Discussion
		3.4.5	Antenna Fabrication and Measurement
		3.4.6	Demonstration of Proposed SWIPT Antenna For Energizing IoT
			Sensors
		3.4.7	Performance Comparison with state of the art
	3.5	SWIP	T Antenna for battery-less IoT Node (Design-O4B) 95
		3.5.1	Results and Discussion
		3.5.2	Performance Comparison
		3.5.3	Relevance to Sustainability
	3.6	Summ	nary
4	\mathbf{SW}	IPT A	Intenna System For Relay Node 105
	4.1	Syster	n Architecture
	4.2	Propo	sed Reconfigurable SWIPT Antenna Array
		4.2.1	WIT Design Configuration
		4.2.2	WPT Design Configuration
	4.3	Result	ts and Discussion
		4.3.1	Circuit and Design Simulation Setup
		4.3.2	WIT Impedance Matching
		4.3.3	WIT Radiation Characteristics
		4.3.4	WPT Matching and Coverage Characteristics
		4.3.5	WPT Power Conversion Efficiency
	4.4	Summ	nary
5	Cor	ıclusio	n and Future Scope 115
	5.1	Concl	usion
		5.1.1	QoS Aware Transmitter Antenna System
		5.1.2	Receiver Antenna for Ultra Low Power IoT Devices
		5.1.3	SWIPT Antenna Systems for Relay Nodes
		5.1.4	Conclusion on Antenna System Design for IoT Network Components 119
	5.2	Future	e Scope
		5.2.1	Access Point
		5.2.2	RF Energy Transmitter
		5.2.3	Rectenna Module
		5.2.4	SWIPT Antenna Design

References

123

CONTENTS xxx

List of Figures

1.1	The schematic diagram of WPT scheme	2
1.2	A general schematic diagram of SWIPT enabled IoT device	2
1.3	A general architecture of SWIPT enabled IoT application scenarios	3
1.4	IoT application scenarios and respective example use cases	4
1.5	Challenges in IoT technology	5
1.6	Basic operations in SWIPT enabled IoT network	6
1.7	QoS metrics of SWIPT enabled IoT network	6
1.8	Design components and loss parameters of a WPT system	8
1.9	Various wireless power transmission schemes for the proposed 3-D clustered wireless sensor network (a) Single antenna, (b) Single beam adaptive array,	11
1 10	(b) Multi beam adaptive array, and (c) Distributed antenna system Various SWIPT techniques described in the literature for receivers	11 13
	Primary functions and corresponding network components of SWIPT	10
	enabled IoT network	15
2.1	Schematic model of the proposed multi-sector SBA antenna as AP and projected communication coverage in one sector	20
2.2	ECA versus θ_t plots for (a) $N=4$ (b) $N=6$ (c) $N=8$ (d) $N=10$ where $SLL_x=15$ dB and $2\times R$ PAA, $R=2,3,4,$ and 5 for BPSK modulation	25
2.3	ECA versus θ_t plots for (a) $N=4$ (b) $N=6$ (c) $N=8$ (d) $N=10$ where $SLL_x=15$ dB and $2\times R$ PAA, $R=2,3,4,$ and 5 for 64-QAM modulation.	26
2.4	ECA versus θ_t for (a) $N=8$ and (b) $N=10$ for $Q\times 3$ elements where	
	$Q = 1, 2, $ and $3 \dots $	26
2.5	ECA versus SLL_x for (a) $N=8$ and (b) $N=10$	27
2.6	γ projection for 2 × 3 PAA at $\theta_t = 20^\circ$, $SLL_x = 15$ dB with (a) $N = 6$ (b) $N = 8$ (c) $N = 10$ using BPSK modulation and (d) $N = 6$ (e) $N = 8$ (f) $N = 10$ employing 64-QAM	27
2.7	γ projection with $\theta_t=25^\circ$, $SLL_x=15$ dB for 2×4 PAA: (a) $N=6$ (b) $N=8$ for BPSK, (d) $N=6$ (e) $N=8$ for 64-QAM, and for 2×5 : (c)	
	BPSK $N = 6$ (f) 64-QAM $N = 6$	28
2.8	γ projection for uniformly excited 2×3 PAA having $\theta_t=0^\circ$ with (a) $N=8,$ BPSK, (b) $N=10,$ BPSK, (c) $N=8,$ 64-QAM and (d) $N=10,$ 64-QAM	29
2.9	γ projection for uniformly excited 2×3 PAA having $\theta_t = 20^\circ$ with (a) $N = 10$, BPSK, (b) $N = 10$, 64-QAM	29
2.10	Layout of the optimized 2×3 PAA and corresponding AP antenna	
	and the state of t	

LIST OF FIGURES xxxii

2.11 (a) Fabricated 2×3 PAA and corresponding AP with $N=10$ sectors (b) Experimental setup inside the anechoic chamber (c) Outdoor experimental	
setup for γ measurement	. 31
2.12 S-Parameter results of 2×3 PAA	
2.13 Analytical, Simulated and Measured Radiation pattern of 2×3 PAA corresponding to 5.8 GHz for (a) $\phi = 0^{\circ}$ and (b) $\phi = 90^{\circ}$ plane	
2.14 Measured P_r from transmitting PAA in sector-1 versus ρ for various ϕ at 5.8 GHz	
2.15 Measured P_I from alternate sector PAA versus ρ for various ϕ at 5.8 GHz.	
2.16 γ versus ρ in sector-1 for various ϕ at 5.8 GHz	
2.17 An access point antenna providing connectivity to crawlers, ground vehicles, and drone vehicles in 3D coverage scenarios (a) smart warehouse (b) smart city applications	
2.18 The schematic model of the proposed antenna Design-O1B	
2.19 Communication coverage in one sector of the multi-sector antenna	
2.20 The QCA versus number of sectors (N) for various $1 \times M$ MAA	
2.21 The SIR distribution and QCA patterns for $1 \times M$ array and (a, b, c) $N = 6$	
(d, e, f) $N = 8$ (g, h, i) $N = 10$. 42
2.22 For elevation coverage (a) L element patch column (b) matching for various	
d_v and $L=3$ (c) upper and lower elevation plane radiation pattern at 5.8	
GHz	. 43
2.23 Elevation plane radiation pattern of the two MAA of a sector for various	
d_v (a),(b) 5.15 GHz and (c),(d) 5.8 GHz	. 43
2.24 The Design-O1B and feed network of the MAA (a) 3×2 MAA (b) 2×3	
MAA (c) 3 × 3 MAA	. 45
2.25 Simulated S-parameter results between MAAs A1, A2, B1, B2 of the SBOA (a) 3×2 MAA (b) 2×3 MAA and (c) 3×3 MAA (d) Gain vs Frequency	4.0
plot	. 46
2.26 Normalized simulated radiation pattern (a, b, c) elevation plane (d, e, f)	40
azimuth plane patterns of 3×2 , 2×3 , and 3×3 MAA respectively	. 48
2.27 Measurement setup of the proposed SBOA antenna (a) Anechoic chamber	40
characterization (b) SIR measurements in open space	. 49
2.28 Measured and simulated S-parameter results of the the proposed SBOA antenna with 3×2 MAA	. 49
2.29 Normalized elevation radiation pattern of A1 of the SBOA with 3×2 MAA	. 49
at (a) 5.15 GHz (b) 5.35 GHz (c) 5.725 GHz (d) 5.825 GHz	. 50
2.30 Normalized azimuth radiation pattern of A1 of the SBOA with 3×2 MAA	. 50
at (a) 5.15 GHz (b) 5.35 GHz (c) 5.725 GHz (d) 5.825 GHz	. 50
2.31 Measured results of (a) P_{Rx} from A2 and (b) γ versus ρ in sector-A at 5.8	. 00
GHz	. 51
2.32 P_{Rx} value in sector-A from upper MAA (A1) at (a) 5.25 GHz (b) 5.8 GHz.	

LIST OF FIGURES xxxiii

2.3	33 γ value in sector-A (signal from A1) with respect to interference from (a)	
	C1 and G1 (b) C2 and G2 at 5.25 GHz	51
2.3	34 γ value in sector-A (signal from A1) with respect to interference from (a) C1 and G1 (b) C2 and G2 at 5.8 GHz	51
2.	35 Application scenario of the cluster based WSN with 3D distributed sensor	
	nodes	54
2.3	36 Switched beam array RF-ET scheme for the proposed 3-D clustered wireless	
	sensor network	55
	37 Analytical Model for proposed SBA RF-ET system	55
2.3	38 (a) Fabricated prototyped of the rectifier circuit (b) Measured and fitted η vs input RF power for rectifier	58
2.	39 Flowchart of the Genetic Algorithm to maximize PPV	59
	40 Subarray and corresponding PPA distribution for analytical analysis	60
	41 % PPA for SA5 at different h_t for 2×2 , 4×4 , and 6×6 MPA	61
	42 % PPA for 4×4 MPA subarray at various h_t for uniform and non-uniform	01
	excitation	61
2.4	43 RF Power Pixel by 4×4 uniformly excited (a) SA1 (b) SA2 (c) SA3 (d)	
	SA4 (e) SA5 (f) SA6 (g) SA7 (h) SA8, and (i) SA9 at $h_t = 7$ m	62
2.4	44 RF Power Pixel generated from GA optimized 4 × 4 non-uniformly excited	
	(a) SA1, (b) SA2, (c) SA3, (d) SA4, (e) SA5, (f) SA6, (g) SA7, (h) SA8,	
	and (i) SA9 at $h_t=7~\mathrm{m.}$	63
2.4	45 Optimal harvested DC Power Pixel for 4×4 non-uniformly excited Tx MPA	
	at (a) $h_t = 2$ m, (b) $h_t = 3$ m, (c) $h_t = 4$ m, (d) $h_t = 5$ m, (e) $h_t = 6$ m, (f)	
	$h_t = 7 \text{ m}$, (g) $h_t = 8 \text{ m}$, (h) $h_t = 8.6 \text{ m}$ and (i) $h_t = 8.7 \text{ m}$ with $P_{th} = -9.5$	
	dBm	63
2.4	46 (a) Cluster head locus for all the power pixel regions generated by 4×4	
	MPA subarray (b) P_n at various h_t for SA1, SA2, and SA5	64
2.4	47 Simulated and Measured S ₁₁ parameter for SA1, SA2, SA4, and SA5	65
2.4	48 Measured S_{21} parameter between SA1, SA2, SA4, and SA5	65
2.4	49 Analytical, measured, and simulated elevation plane radiation pattern of	
	(a) SA1, (b) SA2, (c) SA4, and (d) SA5	65
2.	50 Analytical, measured, and simulated azimuth plane radiation pattern of (a)	
	SA1, (b) SA2, (c) SA4, and (d) SA5	66
2.	51 Measurement setup and subarray (SA1, SA2, SA4, and SA5) designs	66
2.	52 Measured harvested DC Power Pixel patterns on Rx plane at $h_t = 4 \text{ m}$	
	from (a) SA1, (b) SA2, (c) SA4, and (d) SA5	67
2.	53 Measured harvested DC Power Pixel patterns on Rx plane at $h_t = 8 \text{ m}$	
	from (a) SA1, (b) SA2, (c) SA4, and (d) SA5	67
3.	1 Application scenario for the proposed polarization insensitive rectenna system	72
3.	2 Design layout of the proposed single rectenna module	73

LIST OF FIGURES xxxiv

3.3	(a) Layout of the proposed rectenna array, fabricated prototype (b) Bottom layer, and (c) Top layer	73
3.4	Simulated reflection coefficient of the proposed single rectenna module for conjugate impedance matching	74
3.5	Simulated normalized elevation plane RF radiation pattern of the proposed single rectenna module in (a) $\phi = 0^{\circ}$, and (b) $\phi = 90^{\circ}$ elevation plane at	
3.6	5.8 GHz	74 74
3.7	Measured RF-DC conversion efficacy (η) versus load for a single proposed rectenna element.	75
3.8	Measured normalized DC power pattern of the proposed rectenna array for (a) horizontal, and (b) vertical polarized Tx with Rx rotated in elevation	
3.9	plane	75 76
3 10	Proposed isotropic spherical coverage iReAS	77
	(a) Input impedance of a ReE in the proposed ReAS and iReAS, (b)	' '
5.11	Isolation between adjacent ReE in iReAS	78
3.12	(a) Elevation plane ($\phi = 0^{\circ}, 45^{\circ}, 90^{\circ}$) RF patterns of an ReE in ReAS, and Azimuth plane ($\theta = 90^{\circ}$) RF patterns of (b) ReE ₁ and ReE ₂ of single ReAS,	10
	and (c) ReE ₁ , ReE ₂ , and ReE ₅ in the proposed iReAS	78
3.13	(a) $\phi = 0^{\circ}$, (b) $\phi = 45^{\circ}$, and (c) $\phi = 90^{\circ}$ elevation plane RF patterns of	
	rectenna ReE_1 , ReE_2 and ReE_5 in the proposed iReAS	78
3.14	(a) Experimental setup to measure performance of iReAS, (b) wireless sensor node operation utilizing power management unit (PMU) with iReAS.	79
3.15	Normalized V_{dc}^{oc} (in dBV) (a) $\theta = 90^{\circ}$ azimuth plane pattern, (b) $\phi = 0^{\circ}, 15^{\circ}$ and (c) $\phi = 30^{\circ}, 45^{\circ}$ elevation plane patterns at 5.9 GHz	80
3.16	Measured PCE and V_{dc} versus Load for proposed iReAS and ReAS with Tx placed along (a) $\theta = 90^{\circ}$, $\phi = 0^{\circ}$ (b) $\theta = 0^{\circ}$, and (c) $\theta = 180^{\circ}$ direction (d) V_{dc} at various frequencies	
3.17	The proposed SWIPT technique.	
	Application scenario for the proposed SWIPT antenna	
	Exploded view of the proposed SWIPT antenna	
	Equivalent circuit diagram of the proposed SWIPT antenna	
	Current distribution on the proposed SWIPT antenna for (a) forward bias	0.
J.=1	of D1, (b) forward bias of D2, and (c) range	84
3.22	Working Principle of the FWR in the proposed SWIPT antenna	
	Detailed design procedure of the proposed SWIPT antenna	
	Design evolution of the proposed SWIPT antenna	

LIST OF FIGURES XXXV

3.25	(a) Simulated reflection coefficient (S_{33}) of the WIT Port, and (b) Isolation (S_{31}) between the WIT and WPT ports at various design evolution stages	
	of the proposed SWIPT antenna	87
3.26	(a) Real and Imaginary part of the WPT port input impedance and respective (b) S_{11} at various design evolution stages of the proposed SWIPT	
	antenna	87
3.27	Simulated radiation pattern (normalized) of the WIT (with and without FWR) and WPT, for (a) $\phi = 0^{\circ}$, and (b) $\phi = 90^{\circ}$ elevation plane at	
	5.8 GHz and 5.2 GHz, respectively	88
3.28	Fabricated prototype of the proposed SWIPT antenna	89
3.29	Experimental setup in an anechoic chamber for measuring (a) the proposed SWIPT antenna's radiation pattern, and (b) it's DC power pattern and PCE.	90
3.30	Measured reflection coefficient (S_{33}) port and output open dc voltage (V_{dc}^{oc})	
	of the proposed SWIPT antenna	90
3.31	Measured radiation patterns (normalized) of the WIT in (a) $\phi=0^{\circ}$, and (b) $\phi=90^{\circ}$ elevation plane at 5.8 GHz with and without Schottky diode	90
3.32	Simulated and Measured dc power patterns (normalized) of WPT in (a)	
	$\phi = 0^{\circ}$, and (b) $\phi = 90^{\circ}$ elevation plane at 5.2 GHz	91
3.33	(a) Measured and (b) Simulated PCE and harvested DC voltage of the WPT vs the load	92
3.34	(a) Measured and (b) Simulated PCE and harvested DC voltage of the	
	WPT vs input RF power at 5.2 GHz for 610 Ω and 1.5 k Ω , respectively	92
3.35	(a) Experimental setup to measure isolation between WIT and WPT port of the proposed SWIPT antenna, (b) Measured output open dc voltage vs	
	RF power input to WIT feed	93
3.36		94
2 27		
	Design layout of the proposed SWIPT module	96
3.38	(a) Fabricated prototype of the proposed SWIPT module. (b) Equivalent	ne.
2 20	circuit diagram	96
	(a) Experimental setup, and (b) battery-less operation mechanism of the proposed SWIPT Module	97
3.40	(a) S_{11} and V_{dc}^{oc} vs frequency (b) normalized DC power pattern at 5 GHz in $\phi = 0^{\circ}$, $\phi = 90^{\circ}$ elevation plane	98
3.41	(a) PCE and harvested DC voltage variation with load, (b) PCE and V_{dC} variation with input RF power	98
3.42	(a) S parameters of port 1, (b) gain, radiation efficiency (η_{rad}) vs frequency, and (c) BER vs SNR for WIT	99
3 43	WIT radiation pattern at 5 GHz in (a) $\phi = 0^{\circ}$ (b) $\phi = 90^{\circ}$ elevation plane	99
5.10	12 Tadavion particle at 0 of 12 in (a) $\psi = 0$ (b) $\psi = 0$ 0 Giovanion piane	55
4.1	Application scenario for the proposed SWIPT antenna array	106

LIST OF FIGURES xxxvi

4.2	(a) Complete design layout, (b) Top layer, (b) Middle layer, and Bottom
	layer of the proposed SWIPT antenna array
4.3	(a) Equivalent circuit diagram of an SAE in the proposed SAA for WPT
	operation, and (b) Paralle DC combining of SAE_{1-4}
4.4	Fabricated prototype of the proposed reconfigurable SWIPT antenna array. 109
4.5	Reflection coefficient for various WIT modes of the proposed SAA 110
4.6	3-D WIT Radiation patterns in A1, B1, C1, D1 and E1 modes at various
	edge frequencies of 5 GHz WiFi band
4.7	Experimental setup to measure WPT performance
4.8	(a) Simulated reflection coefficient at WPT port, and (b) Open DC voltage
	versus frequency of a single antenna element
4.9	Normalized DC patterns of the proposed SAA in (a) $\phi = 0^{\circ}$, (b) $\phi = 90^{\circ}$,
	and (c) $\phi = 45^{\circ}$ plane
4.10	%PCE and harvested DC voltage of the SAA versus (a) output load, and
	(b) input RF power

List of Tables

2.1	Parameters values initialized in the synthesis process
2.2	The PAA design parameters (dimensions in mm)
2.3	Performance Comparison with State-of-the-Art
2.4	The SBOA antenna design parameters (dimensions in mm) 46
2.5	Simulated Radiation pattern results of the SBOA antennas 47
2.6	Measured radiation performance of the proposed antenna $\dots \dots \dots$
2.7	comparison with state-of-the-art
2.8	Subarray antenna element excitation coefficients 61
2.9	Simulated and Measured Gain values
2.10	PPA range (in m) on a plane at 4 m from Tx
2.11	PPA range (in m) on a plane at 8 m from Tx
2.12	Comparison with State-of-the-Art
3.1	Dimensions of the proposed iReAS
3.2	Performance comparison with state-of-the-art
3.3	Dimensions of the proposed SWIPT antenna
3.4	Link Budget parameters
3.5	Performance comparison with state-of-the-art
3.6	Design parameters of the proposed SWIPT module
3.7	BLE sensor beacon data for WPT at 5 GHz
3.8	Performance comparison with state-of-the-art
4.1	Dimensions of the proposed SWIPT antenna
4.2	Excited SAEs in Various WIT Radiation Modes
4.3	WIT radiation characteristics of the proposed SAA

LIST OF TABLES xxxviii

Chapter 1

Introduction

1.1 Simultaneous Wireless Information and Power Transfer

The Internet of Things (IoT) technology facilitates pervasive device connectivity across diverse sectors, including agriculture, industry, healthcare, and defense [1, 2, 3]. IoT devices typically utilize specialized sensors to monitor environmental parameters, process the acquired data, and transmit it to a remote gateway or access point (AP) [4]. The rapid advancement in wireless information transfer (WIT) systems has led to the proliferation of IoT networks, accommodating a vast number of devices and consequently induced a significant increase in data traffic [5]. This trend necessitates the development of AP antennas with high capacity, spectral efficiency, and extensive coverage [5]. However, realizing wider coverage in far-away and remote locations is difficult to achieve with a single AP due to low signal strength caused by path loss and multi-path fading effects. In such scenarios relay node (RN) plays a crucial role in enhancing signal quality and spectral efficiency through cooperative relaying (CoR) [6].

The RNs are generally battery operated, which inhibits the sustainable operation of the IoT network. Similarly, the IoT devices rely on small batteries with limited lifespans, which necessitates frequent battery replacements for continuous operation. This not only elevates maintenance expenses but also increase battery waste, which constitutes a significant barrier to realizing the goals of energy-efficient and sustainable green communication in future wireless networks [7]. However, to mitigate these issues, integrating energy harvesting (EH) modules with IoT devices offers a potential solution, either by recharging batteries or enabling battery-free operation. The current research has explored various ambient energy sources for EH-enabled IoT devices, including solar, vibrational, piezoelectric, thermoelectric, and radio frequency (RF) energy. These sources, however, are often intermittent and highly dependent on environmental conditions, resulting in unreliable EH performance [8].

In contrast, wireless power transfer (WPT) technique as demonstrated in Fig. 1.1 employs a dedicated RF energy transmitter (RF-ET) [9], providing on-demand RF power, thus ensuring more consistent and sustainable operation of IoT devices. The EH module in a WPT system integrates a rectifier circuit with an antenna, forming a device known as a rectenna (a portmanteau of "rectifier" and "antenna") [10] as shown in Fig. 1.1. In a typical rectenna configuration, a matching network is employed to ensure impedance matching between the antenna and the rectifier [11]. This matching network is crucial for minimizing transmission losses and maximizing the amount of RF power delivered to

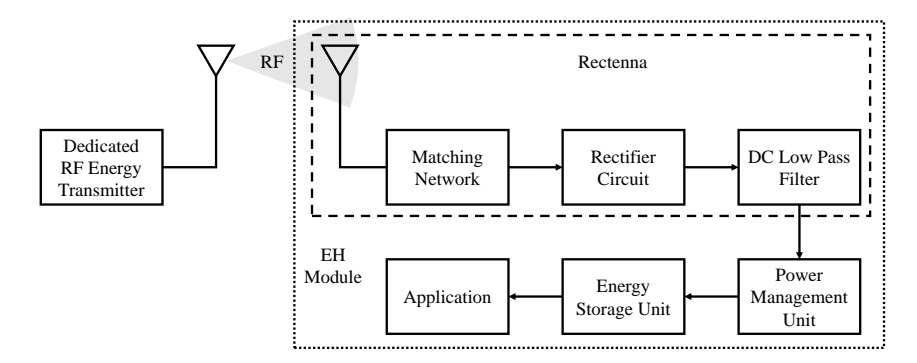


Figure 1.1: The schematic diagram of WPT scheme.

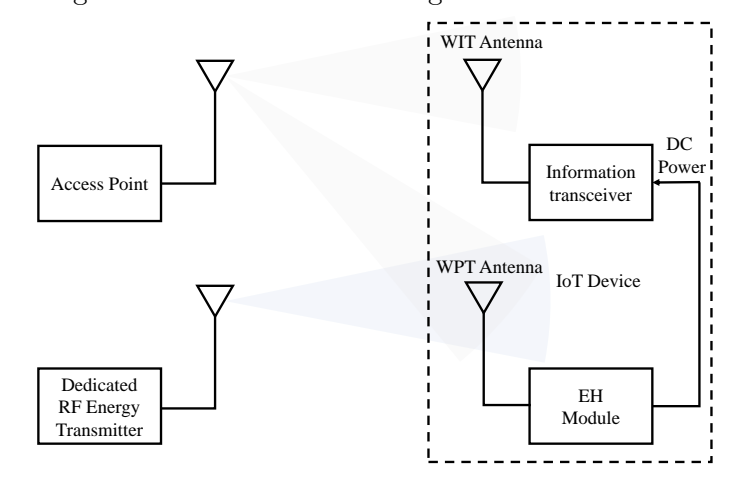


Figure 1.2: A general schematic diagram of SWIPT enabled IoT device.

the rectifier circuit. The rectenna converts incident RF energy into usable direct current (DC) power, which can either recharge the IoT device's battery or facilitate battery-less operation. Unlike other ambient energy sources, which are often bulky and challenging to integrate with communication systems, the compact nature of the rectenna enables straightforward integration [12] and supports simultaneous wireless information and power transfer (SWIPT).

The schematic diagram of a SWIPT enabled IoT device is illustrated in Fig. 1.2, depicting the integration of information receiver and EH module within a single IoT device. While the diagram shows the use of separate antenna elements namely WIT antenna for information and WPT antenna for RF energy harvesting from a dedicated RF-ET to realize the SWIPT operation. However, it is worth nothing that various other techniques utilize different antenna configurations in coordination with signal diversity in frequency, time, and polarization domain to facilitate SWIPT functionality [7].

In modern IoT networks SWIPT technology enables unification of information and power transfer, providing significant improvements in terms of latency, interference management, energy and spectral efficiency [4, 6, 7, 8]. In addition, with the advancement in chip technology the IoT devices have become power efficient, enabling the practical realization of SWIPT technology for powering ultra-low power IoT devices. However, like any wireless system, implementation of SWIPT in IoT network requires quality aware synthesis of antenna systems for each front end network component. This approach is crucial to

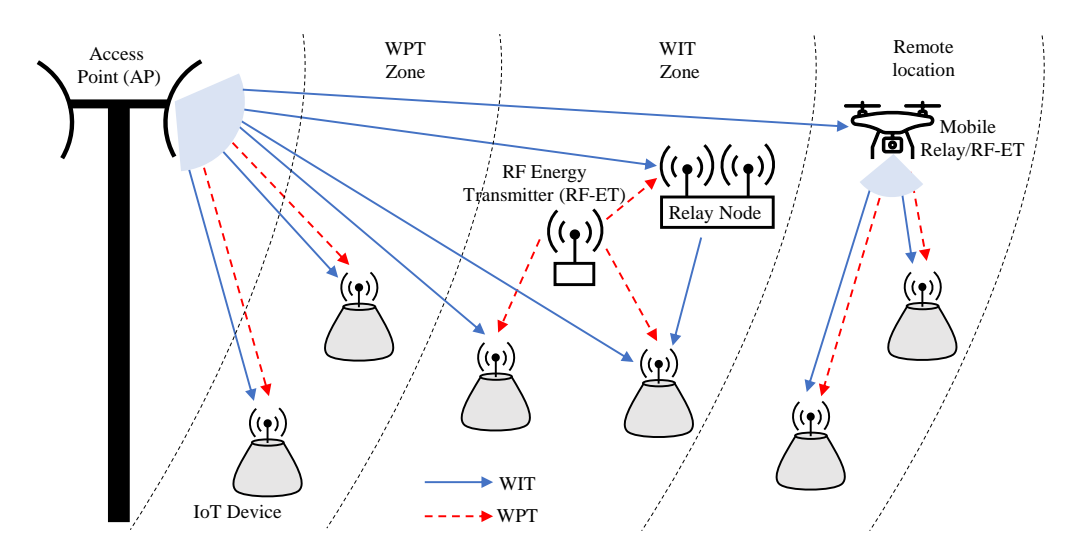


Figure 1.3: A general architecture of SWIPT enabled IoT application scenarios.

optimizing various performance metrics and achieving the maximum enhancement in system performance.

In the subsequent section, a comprehensive description of a general architecture of SWIPT enabled IoT network is presented. This analysis includes a detailed examination of various system components required to concurrently facilitate both WIT and WPT for realizing SWIPT operation in IoT applications.

1.2 System Architecture of SWIPT Enabled IoT Network

A typical architecture of SWIPT enabled IoT network is depicted in Fig. 1.3, indicating four major front end system components [12]:

Access Points are the information gateways, which receive data from the IoT devices and forward it to a remote server or cloud over the internet for further processing. Moreover, they can also act as RF sources for IoT devices in specific application scenarios.

RF Energy Transmitters serve as dedicated RF sources for WPT-enabled IoT devices to ensure their continuous operation.

IoT Devices generally sense the surrounding environment using sensors and after pre-processing the sensor data send it to the access point or relay node for further processing.

Relay Nodes are employed to establish connectivity between the access point and remote IoT devices. In addition they facilitate cooperative relaying, which minimizes the adverse effects of path loss and fading, resulting in enhanced network throughput.

APs and RF-ETs are usually powered by a fixed energy supply but can alternatively operate using ambient energy sources to achieve sustainable operation and reduce dependence on conventional power sources [12]. Conversely, WPT-enabled IoT devices and RNs recharge their batteries through WPT. As depicted in Fig. 1.3, the space surrounding the AP can be divided into WPT zone, WIT zone, and distant remote locations. The performance of WIT is influenced by the signal-to-noise ratio (SNR)

or signal-to-interference-plus-noise ratio (SINR), while WPT efficiency depends on the RF power received at the rectenna aperture. Consequently, the information decoding circuitry has lower signal sensitivity (ranging from $-130\,\mathrm{dBm}$ to $-60\,\mathrm{dBm}$) compared to the rectification circuit (which requires $\geq -30\,\mathrm{dBm}$), resulting in a smaller WPT zone relative to the WIT zone [12] .

The IoT devices can establish an adhoc network with a cluster head device commonly referred to as a wireless sensor network (WSN) to collaboratively perform environment sensing, data processing and communication task. For continued operation IoT devices within the WPT zone can harvest RF energy from the AP, whereas those outside the WPT zone require a separate RF-ET. Additionally, RNs can be deployed in the WIT zone to enhance network coverage and throughput. Moreover, implementation of SWIPT enabled relay nodes can enhance energy efficiency and sustainability of the IoT networks. Furthermore, a UAV equipped with a specialized antenna system can serve the dual functions of an RF-ET and RN, thereby facilitating RF energy and communication links for IoT devices in remote and difficult to reach or challenging environments. The next section discusses IoT applications and challenges associated with their implementation.

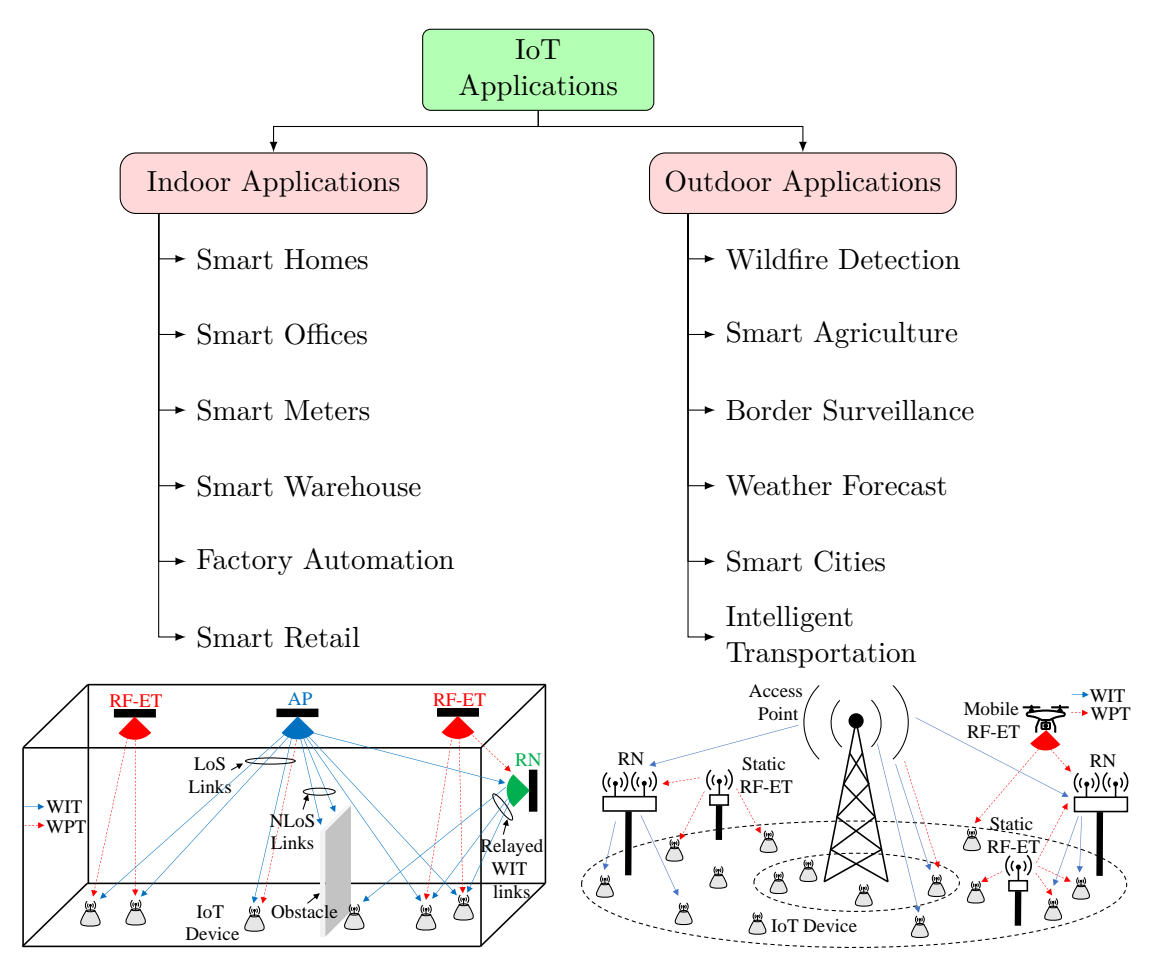


Figure 1.4: IoT application scenarios and respective example use cases.

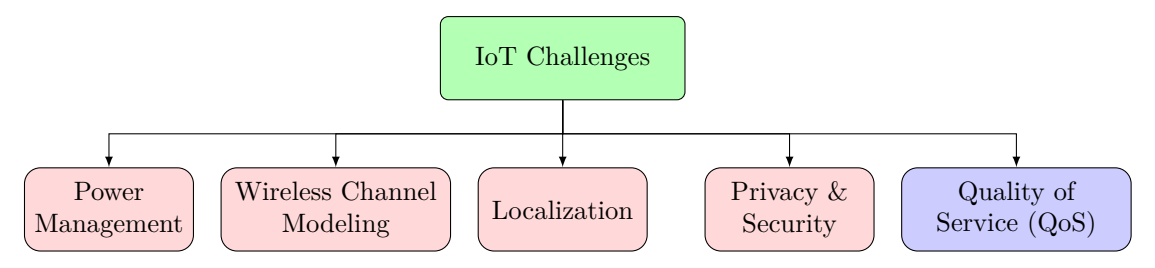


Figure 1.5: Challenges in IoT technology.

1.3 IoT Applications and Challenges

The system architecture outlined provides a broad and idealized overview of the IoT application landscape. The practical use cases can be more precisely categorized into indoor and outdoor applications as demonstrated in Fig. 1.4 with a list of corresponding example use cases. The challenges associated with the implementation of these IoT applications, as depicted in Fig. 1.5, encompass power management, wireless channel modeling, localization of IoT devices, security, and quality of service (QoS) [13].

The primary challenge in IoT technology is maintaining the QoS, a measure of reliable operation of network components. The exponential growth in data traffic, driven by the proliferation of IoT devices, has made it essential to ensure QoS guarantees for end users [14]. In addition, the non-line-of-sight (NLoS) condition arises in both indoor and outdoor environments due to various obstacles, which contribute to multipath fading and signal attenuation. These factors collectively degrade the quality of communication links, impacting overall signal reliability and performance. This degradation necessitates data packet re-transmissions, which in turn increases power consumption and diminishes the energy efficiency of the IoT network.

The QoS metric facilitates efficient WIT throughout the network by managing bandwidth, latency and packet loss. In addition, QoS should also guarantee efficient WPT to IoT devices for sustainable operation. This thesis concentrates on enhancing the QoS of SWIPT-enabled IoT networks by employing a quality-aware approach to synthesize the antenna systems for all the network components. The following section provides an in-depth discussion on QoS metrics, outlining the various factors that impact network services and exploring how optimal antenna design can lead to significant improvements in performance.

1.4 QoS Metrics of SWIPT Enabled IoT Network

The fundamental operations within any IoT network are sensing, data processing, and communication [15], as depicted in Fig. 1.6. Moreover, the integration of WPT is essential for implementing a SWIPT enabled IoT network. The quality of these operations depicted as QoD, QoP, QoWIT, and QoWPT in Fig. 1.7 ultimately determines the QoS of the network. This thesis presents antenna system design for improving the QoWIT and QoWPT and a concise overview of various associated metrics is further discussed below.

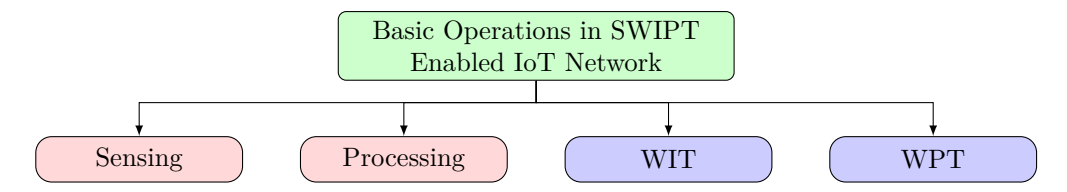


Figure 1.6: Basic operations in SWIPT enabled IoT network.

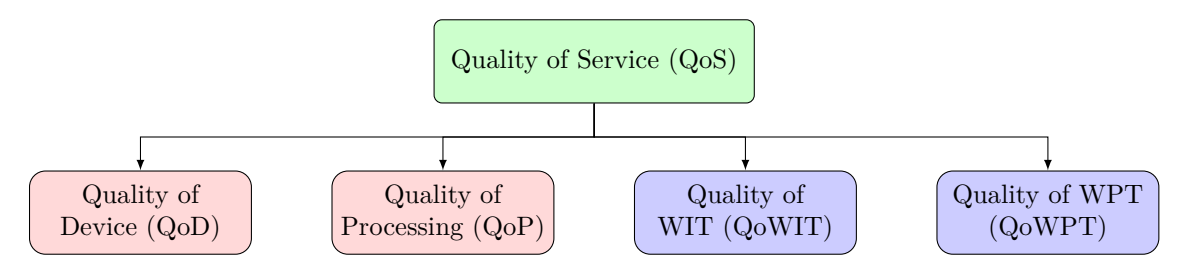


Figure 1.7: QoS metrics of SWIPT enabled IoT network.

Quality of WIT (QoWIT) is a measure of communication link reliability between various network components. A wider bandwidth and lower latency are desirable to minimize jitter and packet retransmissions, thereby enhancing network throughput and overall efficiency. Additionally, a large network coverage is essential to facilitate mobility and ensure reliable communication with a large number of IoT devices, particularly those deployed in rural or sub-urban locations.

Quality of WPT (QoWPT) is determined by the rectenna efficiency and the RF power delivered by RF-ET to IoT device integrated with a rectenna or a SWIPT antenna system. The path loss and multipath effect reduce the RF power delivered by the dedicated RF-Tx to the rectenna integrated with the IoT device. Additionally, the density of IoT devices within the application area impacts the duration and frequency of RF energy delivery.

The major challenge is to find innovative and cost effective solutions to enhance each quality metric and improve the end user experience. The parameters of QoWIT and QoWPT are dependent on the performance of antenna system designed for network components involved in data communication and power transfer, respectively.

This thesis specifically targets the enhancement of QoWIT and QoWPT by employing quality aware synthesis of the antenna systems for each system component within the IoT network. The antenna systems are specifically designed for 5 GHz WiFi band while considering maximum output RF power of 4W except in case of the RF-ET, where high RF power can be transmitted depending upon the application scenario. In addition, the BLE sensor beacon module utilized for experimental demonstration of battery-less operation of IoT sensor nodes operating in 2.45 GHz band. The subsequent sections provide a detailed description of system requirements and challenges, along with a brief review of state-of-the-art antenna design solutions in the literature.

1.5 Antenna System Requirements and Challenges

1.5.1 Quality of Wireless Information Transfer

The QoWIT experienced by end-user nodes in a given area is predominantly governed by the performance of the access points and relay nodes. Consequently, the antenna systems installed at these access points and relay nodes are crucial in determining the overall communication link quality. The design and configuration of these antennas significantly impact the effectiveness of the network in delivering reliable and high QoS to the end users.

1.5.2 Access Point

- The exponential rise in number of IoT devices resulted in significant amount of data traffic, requiring high system capacity and wide bandwidth. The limited availability of the frequency spectrum poses a significant constraint on the bandwidth available for communication systems. Moreover, the IoT devices can be deployed anywhere in the 3-D space of the application region.
- The large number of IoT devices increase interference from neighboring nodes, leading to a degradation in SINR. This reduction in SINR subsequently elevates the bit error rate (BER), causing an increase in packet re-transmissions. Such re-transmissions degrade communication efficiency and result in higher power consumption, which poses a significant challenge for power-constrained IoT devices and affects the QoS in the IoT network.

1.5.3 IoT Devices

- The antenna at IoT devices should exhibit wide beam radiation characteristics to
 effectively receive information signals from the access point or relay node from any
 direction.
- Similar to the relay node, the antenna at the IoT device should also support information transfer within the same frequency band as the access point to ensure compatibility and seamless communication.

1.5.4 Relay Nodes

- The antenna at the relay node must facilitate communication with both the access
 point and IoT devices, necessitating the incorporation of either multibeam or wide
 beam characteristics to ensure optimal connectivity and coverage.
- The antenna at the relay node must support communication within the same frequency band as the access point to ensure seamless connectivity and compatibility within the network.

• The antenna at the relay node should possess the capability to reconfigure its radiation pattern, enabling reliable communication with both the access point and IoT devices, regardless of their relative orientations.

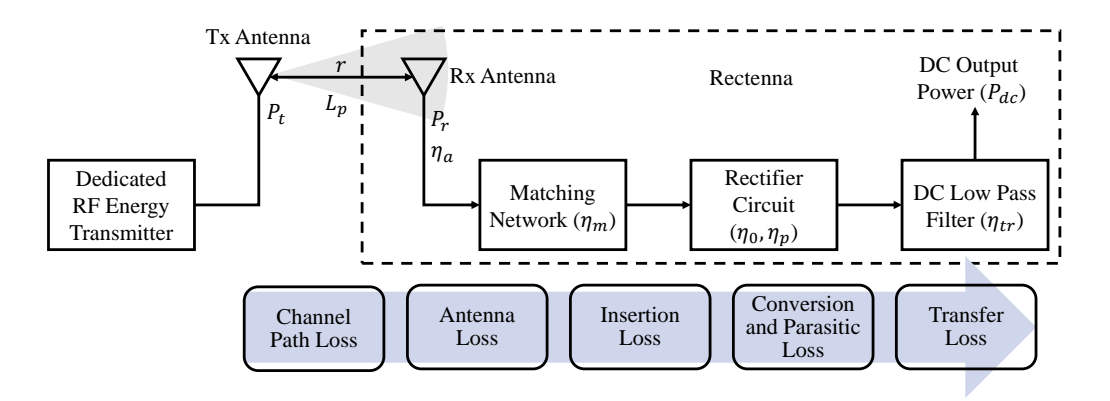


Figure 1.8: Design components and loss parameters of a WPT system.

1.5.5 Quality of Wireless Power Transfer

The RF-ET and the rectenna or SWIPT antenna integrated with the IoT devices and relay nodes collectively determine the QoWPT. Thus, a comprehensive understanding of the dedicated WPT system is essential to understand the system requirements and the implementation challenges. Figure 1.8 provides a detailed depiction of various design components along with their efficiency (η_a , η_m , η_0 , η_p , η_{tr}) and loss parameters within a WPT system. The RF power received (P_r) by the rectenna located at r distance from the RF-ET can be evaluated using Friis equation given in (1.1)

$$P_r = SA_e \cos^2 \phi \tag{1.1}$$

where, $S = P_t G_t / 4\pi r^2$ is the RF power density at Rx antenna, $A_e = \lambda^2 G_r / 4\pi$ is the effective aperture area of Rx antenna and $\cos^2 \phi$ is the polarization loss factor (PLF) which is due to the angular misalignment of ϕ between RF-ET antenna and Rx antenna, resulting in polarization mismatch [4, 8]. The path loss (L_p) is inversely proportional to m^{th} power of the transfer distance (r^m) , where m is generally ≥ 2 and depends upon the channel conditions. Therefore, given that effective isotropic radiated power (EIRP $= P_t G_t$) is constant, which is usually the case, the RF-ET efficiency can be enhanced by employing a high-gain antenna system directing maximum RF energy towards the Rx antenna. Moreover, a high aperture or high gain (G_r) Rx antenna can also be utilized to increase the received input RF power.

The output DC power generated by the rectenna from the input RF power P_r can be evaluated using (1.2) [11]

$$P_{dc} = \eta_a \times \eta_m \times \eta_0 \times \eta_p \times \eta_{tr} \times P_r \tag{1.2a}$$

$$P_{dc} = PCE \times P_r \tag{1.2b}$$

In the context of rectenna systems, the power conversion efficiency (PCE) is defined as the product of several key efficiencies: η_a (antenna efficiency), η_m (matching network efficiency), η_0 (conversion efficiency of the rectifier circuit), η_p (parasitic efficiency of the rectifier circuit), and η_{tr} (transfer efficiency of the DC low pass filter) [11]. To maximize the direct current power output (P_{dc}) , it is crucial to ensure optimal impedance matching between the receiving antenna and the rectifier circuit. It is also worth noting that PCE is directly proportional to P_r , which implies that enhancing η_a will improve η_0 . Thus, a high-efficiency receiving antenna enhances the amount of RF power delivered to the matching circuit, thereby contributing to improved overall system performance. The immediate discussion regarding the WPT system, including the primary design requirements and the associated challenges in improving QoWPT, can be summarized as follows:

1.5.6 Dedicated RF Energy Transmitter

- The dense and random deployment of a large number of IoT devices throughout the 3-D space of the application region significantly impacts the effectiveness of RF power transfer to each device.
- The spatial distribution requires localization of device for delivering high RF energy.
- Ensuring reliable and adequate amount of RF energy to each IoT device distributed in the 3-D space for maintaining the sustainable operation of the IoT network.

1.5.7 IoT Devices

The Rx antenna depicted in Fig. 1.8 can be configured for either simultaneous WPT and WIT or can utilize distinct antennas for each function. Existing literature on rectenna module design has predominantly focused on harnessing the DC power generated via WPT to power EH enabled IoT devices, typically employing separate antennas for the WPT and WIT functions. Conversely, studies related to SWIPT have concentrated on developing integrated antenna systems that facilitate both power and data transmission.

In both scenarios, several key challenges persist regarding the enhancement of QoWPT. These challenges are as follows:

- Angular misalignment between the RF-ET and Rx antenna.
- Reducing circuit losses and enhance power conversion efficiency.
- compact size and small form factor.
- Radiation efficiency of the Rx.
- Enhance isolation between the information and power signals in a compact integrated antenna system.

1.5.8 Relay Nodes

Utilizing a separate antenna system for WPT and WIT in relay nodes can lead to a complex and bulky configuration. Consequently, implementing a single antenna system for concurrent information and power transfer is a more efficient approach, enabling a more compact design. The design challenges associated with enhancing QoWPT in this context mirror those faced by IoT devices, highlighting the need for effective solutions to optimize performance in SWIPT enabled IoT applications.

1.6 Prior Works and Motivation

An exhaustive review of state-of-the-art antenna designs has been carried out, leading to a comprehensive classification of the literature based on network components. This classification encompasses key elements such as Access Points, RF-ET, IoT devices, and Relay Nodes. The analysis highlights how different antenna designs are tailored to meet the specific system requirements and overcome the design challenges presented in the previous section.

1.6.1 Access Point Antenna System

To address the challenges of low Signal-to-Interference Ratio (SIR) and limited capacity, techniques such as frequency reuse [16] and directional antennas [17, 18, 19, 20] are commonly utilized. However, directional antennas provide only limited spatial coverage [21] with high SIR. To improve SIR coverage, multibeam antennas are used at APs to emit multiple high-gain beams, covering a broader angular range and enhancing frequency reuse to boost system capacity [21]. Multibeams are implemented using smart array techniques like adaptive beamforming arrays (ABA) and switched beam arrays (SBA). ABA employs complex beamforming networks to dynamically steer beams by adjusting the phase profiles of antenna elements. In contrast, SBA uses multiple fixed beams that are activated or deactivated with RF switches depending on node locations [21, 22]. Due to its simplicity and cost-effectiveness, SBA is well-suited for deployment in low-power scenarios.

Recent research on SBA antennas reveals two primary types: single-port and multi-port designs. Single-port SBA designs, which use a central radiating element with switchable parasitic elements [23, 24, 25, 26, 27], produce one beam at a time and often include features like frequency reconfigurability [28, 29, 30, 31] and dual polarization [32] to improve performance. However, these designs are constrained by their inability to generate multiple beams simultaneously, limiting their service capacity. In contrast, multi-port SBA designs are developed to support multiple beams [33, 34], offering enhanced 360° azimuthal coverage. These designs include 2-D planar systems for applications such as UAVs and vehicles, and 3-D sectoral arrays used in omnidirectional 5G base stations [35]. Multi-beam SBA designs improve capacity and coverage but face challenges such as interference from neighboring sectors, which affects bit error rate (BER) and coverage reliability. Advanced

multi-sector arrays with dual polarization [36], dual-band [37], and flat-top [38] beam radiation pattern have been proposed to boost system capacity and reduce interference. Despite these advancements, many SBA designs focus primarily either on azimuthal or elevation plane coverage, often neglecting comprehensive 3-D space coverage. Only a few SBA designs have targeted full 3-D coverage, with existing solutions typically using frequency selective surfaces for beam steering [39, 40, 41] and generally supporting single-beam switching. Recent developments, such as shared aperture antennas [42] for wide-angle elevation coverage, address some challenges but are often suited for high-power applications and face issues related to cost and compatibility. Although some studies have evaluated SIR performance [21, 43, 44], many rely on conventional approaches that do not consider interference effects within the antenna synthesis. Furthermore, the benefits of beam tilt in the elevation plane, which could reduce interference and enhance performance, have been investigated in a few sector array antenna studies [45, 30, 27, 46] but for a limited number of sectors and discreet tilt angle values. Overall, achieving effective multibeam coverage in 3-D space remains a significant challenge. Existing designs often fail to integrate comprehensive performance measures, such as SIR, into their synthesis processes, leading to suboptimal coverage and capacity.

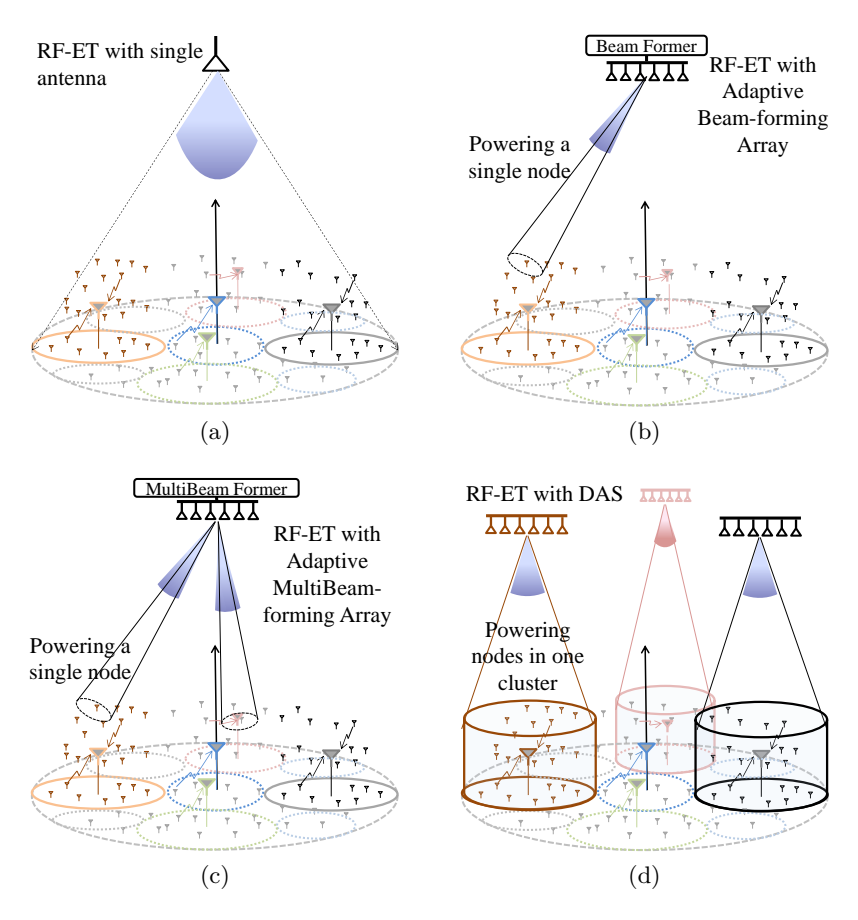


Figure 1.9: Various wireless power transmission schemes for the proposed 3-D clustered wireless sensor network (a) Single antenna, (b) Single beam adaptive array, (b) Multi beam adaptive array, and (c) Distributed antenna system.

1.6.2 Dedicated RF Energy Transmitter

To achieve a power-efficient WSN with high node density, nodes are typically organized into clusters with a cluster head (CH) in each, which communicates with a remote gateway [47]. CHs consume significantly more power than other cluster nodes, requiring higher power supplies. In a 3-D cluster-based WSN using WPT, the RF-ET design must address the varying power needs of the nodes. The RF-ET system should ensure that CHs receive more power while all nodes get sufficient energy by optimizing beam collection efficiency (BCE), which measures the ratio of power received by the rectenna to the total transmitted power [48].

To meet the power needs of high node density WSNs, various RF-ET schemes can be used. A single wide-angle antenna (Fig. 1.9(a)) covers the entire multi-cluster area but provides uneven RF power, requiring large aperture antennas at the Rx [49] that are impractical for miniaturized nodes. Alternatively, an adaptive beamforming antenna array (Fig. 1.9(b)) creates narrow, directional beams [50, 51, 52] that improve BCE but needs accurate channel state information [53] and can be slow to adjust in dynamic environments. The multibeam adaptive beamforming scheme (Fig. 1.9(c)) offers simultaneous beam coverage, reducing adjustment time but increasing complexity and cost. A distributed antenna system (Fig. 1.9(d)) uses multiple antennas [54, 55, 56] to direct RF power to specific clusters but requires precise placement of antennas. All these schemes face challenges in dense 3-D WSN scenarios, highlighting the need for a low-cost, energy-efficient WPT system.

1.6.3 Rectenna Module for IoT Devices

The random deployment of sensor nodes often results in lower RF energy capture and reduced PCE due to varying locations and orientations. To improve this, rectenna systems need to offer isotropic coverage [57], especially for applications like smart homes and smart farming, where multipath RF signals and distributed transmitters are common. Isotropic coverage is challenging to achieve with a single rectenna, so integrated rectenna array systems (ReASs) have been proposed to enhance harvested DC power [58, 59, 60, 61, 62, 63, 64, 65]. Recent designs focus on 3-D spherical coverage [61, 62, 63], such as multisector 3D-ReAS with beamforming networks, but these systems are bulky. To mitigate this problem, a few planar [65] multisector [58, 59, 60] ReASs have been studied in the literature, offering 3-D coverage in the upper hemisphere but suffer from low output DC voltage and incomplete isotropic coverage.

1.6.4 SWIPT Antenna System for IoT Devices

Several EH methods have been explored to enhance the battery longevity of IoT devices. Among these, WPT technique has emerged as a leading solution due to its seamless integration with existing communication circuitry [12]. IoT sensor nodes gather environmental data and transmit it to a remote gateway via an integrated WIT antenna.

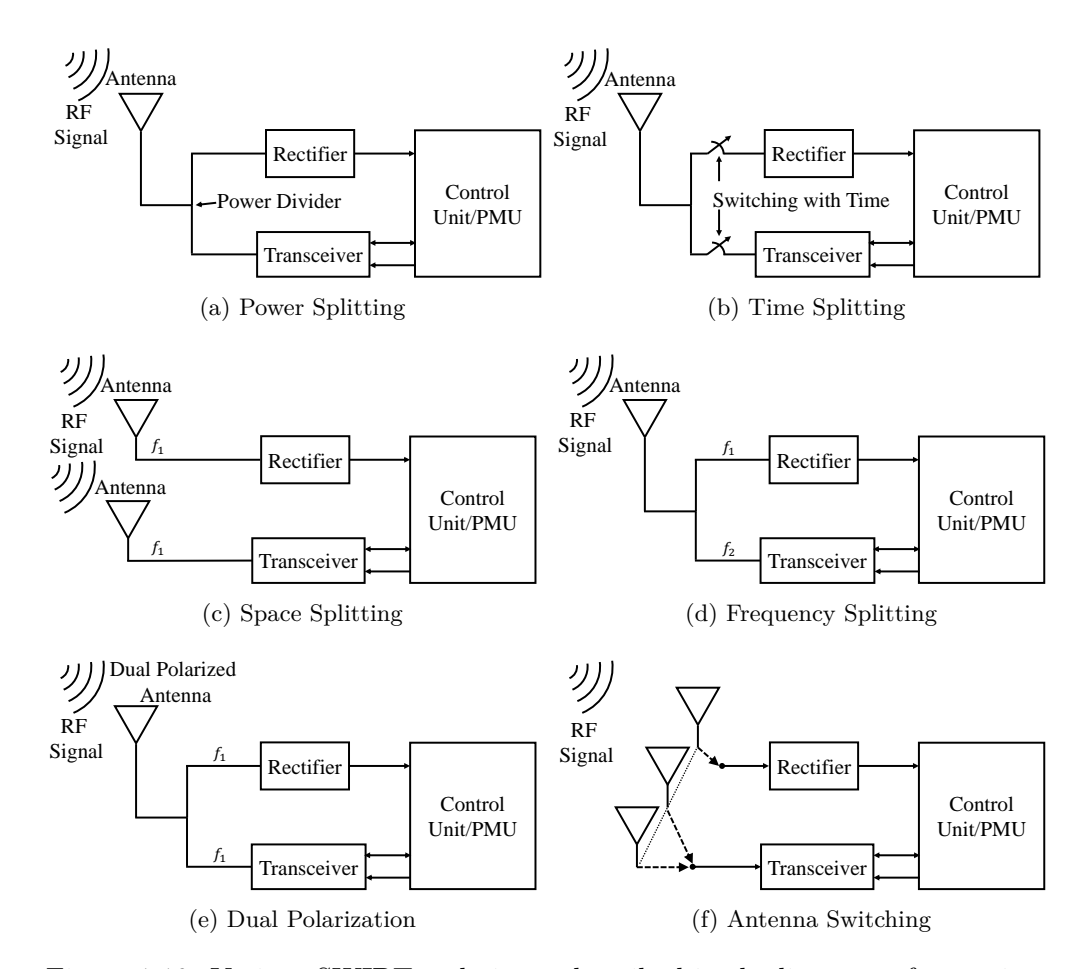


Figure 1.10: Various SWIPT techniques described in the literature for receivers.

The use of separate antennas for WPT and WIT would result in a bulky prototype. Recent research efforts focus on developing a SWIPT antenna system to enable concurrent data and power delivery to remote sensor nodes [4].

Several techniques for implementing SWIPT have been investigated in the literature, including power splitting [66, 67, 68], time splitting [66], dual polarization [69, 70], frequency splitting [71], space splitting [72, 73], and antenna switching [74]. power-splitting method divides the received signal into two parts: one for information decoding and the other for RF power harvesting, as illustrated in Fig. 1.10(a). This approach, however, reduces both the SNR and the PCE of the rectifier circuit. Conversely, the time-splitting technique, shown in Fig. 1.10(b), theoretically provides full RF signal power with improved SNR and PCE by using different time slots for information and power transfer. The primary limitation of this method is the need for precise time synchronization between the transmitter and receiver [75], and varying optimal time divisions for different sensor nodes complicate IoT operations. The space-splitting technique, depicted in Fig. 1.10(c), uses separate antenna elements for WIT and WPT at the same frequency. In contrast, the frequency-splitting technique, as shown in Fig. 1.10(d), allocates different frequency channels for information and power transfer [71, 76, 77]. dual-polarization technique, illustrated in Fig. 1.10(e), employs cross-polarized ports at the same frequency [69, 70, 78]. The antenna switching is quite similar to space splitting technique, with the exception of employing multiple antenna elements for information and power transfer in a complete set of antennas with switching capability [74]. In addition, hybrid SWIPT antenna systems, such as shared aperture antennas [79] with frequency splitting, dual-polarized full-duplex antennas [80, 81], and frequency splitting combined with dual-polarization [76], have also been proposed. However, these designs often involve multiple antenna elements [79, 80, 81] or require rectifier impedance matching networks [76], resulting in larger sensor nodes.

Frequency splitting and dual-polarization techniques are relatively simpler to implement, as they use distinct frequency channels and orthogonal polarization for information and power transfer, respectively. This configuration provides high isolation between WIT and WPT ports, enhancing the SNR and PCE of the SWIPT antenna. In SWIPT systems, antenna and rectifier circuit matching is typically achieved using impedance matching networks [76, 77] or loop-based conjugate matching techniques [69, 71, 78]. The latter method, which requires a partial ground plane, can impact antenna performance, particularly when the IoT sensor node is placed on substrates with varying dielectric properties [82]. Conjugate-matched SWIPT antennas [69, 78] often use a voltage doubler topology for full-wave rectification (FWR), achieving high PCE (70%) at high input RF power ($\geq 500 \,\mu\text{W}$) [83]. However, achieving FWR for ultra-low power ($-10 \, \text{dBm}$) applications with such high PCE remains a significant challenge [71]. Furthermore, ultra-low power RF transmission is preferred in IoT applications to ensure compliance with the specific absorption rate limit of 1.6 W kg⁻¹ for health and safety [50]. Thus, there is a need for compact integrated antennas that provide high WIT efficiency and PCE for ultra-low power WPT in SWIPT applications.

1.6.5 SWIPT Antenna System for Relay Node

To achieve energy-efficient, high data rate, and spectral-efficient communication in 5G and beyond (B5G) networks [6], cooperative relaying (CoR) can enhance transmission range and reliability by mitigating path loss and signal fading [84]. WPT and SWIPT are promising for recharging battery-assisted RNs in IoT applications, fostering sustainable communication [85, 86, 87, 88, 89]. Effective antenna systems for RNs should offer wide beam coverage and employ omnidirectional radiation patterns [90], although multi-antenna systems with beamforming capabilities are preferred to reduce multipath fading and interference and to boost power harvesting [91]. Research on SWIPT-enabled RNs has focused on techniques like time splitting, power splitting, and antenna switching to optimize data rates [92, 93] and power allocation [94, 95]. While theoretical analyses are abundant, practical evaluations of SWIPT systems in terms of SNR, BER, and PCE are limited. This highlights the need for practical studies to assess and enhance the performance of SWIPT antenna systems for RNs in real-world CoR communication scenarios.

1.7 Thesis Objectives

The SWIPT enabled IoT networks involves concurrent transmission of information and power signals. The network components involved can be segregated into: Transmitter, Receiver, and Relay, based on their primary operation which collectively implement SWIPT operation. For instance, access points are primarily used for transmitting communication signals but can also function as RF energy sources for nearby WPT enabled devices. Conversely, dedicated RF energy transmitters form directed beam towards IoT devices and relay nodes integrated with either rectenna modules or SWIPT antenna system. The rectenna modules are placed at the receiver devices for harvesting the incident RF energy to either replenish their battery or directly power the device functions. In contrast, recently SWIPT antenna systems capable of both data and power transfer have been designed to realize IoT devices with small form factor. Additionally, battery-assisted relay nodes integrated with SWIPT antenna system have been introduced to enhance network energy efficiency and throughput by leveraging cooperative relaying Based on the above discussion the antenna systems designed for various components in SWIPT enabled IoT network can be categorized into three types: Transmitter, Receiver, and Relay node antennas, as illustrated in Fig. 1.11. Each category aligns with the primary function of network components within a SWIPT enabled IoT network.

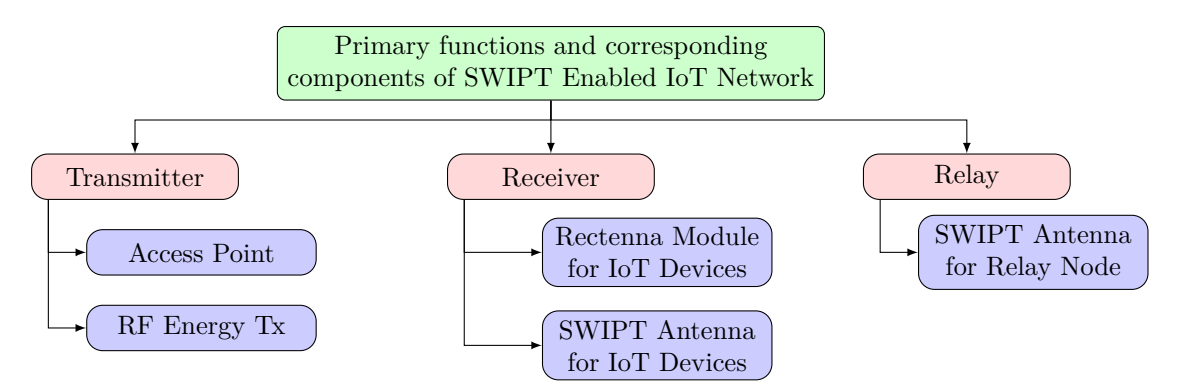


Figure 1.11: Primary functions and corresponding network components of SWIPT enabled IoT network.

The objectives of the thesis are divided based on the above categorization of the antenna systems for SWIPT enabled IoT network.

1.7.1 Transmitter Antenna System

- 1. **O**−1: Quality aware synthesis of multi sector switched multi beam Access Point antenna system.
 - O-1A: Analyze and design multi-sector multi beam SBA to enhance the 2-D coverage region in the azimuth plane.

- O-1B: Analyze and design multi-sector multi beam SBA to enhance the 3-D (azimuth as well as elevation plane) spatial coverage with wide bandwidth.
- 2. **O**-2: Analyze and design a dedicated switched beam RF energy transmitter for wireless powering of 3D distributed clustered ultra-low power IoT devices.

1.7.2 Receiver Antenna System

- O−3: Design angular misalignment tolerant rectenna module for ultra-low-power IoT devices.
 - O-3A: Analyze the angular misalignment problem in rectenna design.
 - O-3B: Design an isotropic coverage rectenna module for realizing misalignment insensitive WPT operation.
- 2. **O**−4: Design a compact SWIPT antenna with wide information bandwidth for ultra-low-power IoT devices.
 - O-4A: Analyze and design a single antenna element utilizing a new SWIPT technique capable of powering a single IoT sensor.
 - O-4B: Design a SWIPT antenna with enhanced performance through evolutionary process capable of battery-less IoT device operation.

1.7.3 Relay Node Antenna System

1. **O**−5: Design a practical SWIPT relay node capable of wideband WIT with an access point and IoT devices, while also supporting WPT to recharge its battery.

1.8 Thesis Outline

- 1. Chapter-1: This chapter presents the system architecture and the key components of a SWIPT-enabled IoT network. It provides an overview of the diverse IoT applications and the challenges associated with them. Additionally, it includes a comprehensive literature survey related to antenna system design for various IoT network components, outlines the objectives of the thesis, and details the structure of the subsequent chapters.
- 2. Chapter-2: This chapter analyzes and designs a multi-sector, multi-switched beam antenna array system for access points. It introduces a novel synthesis procedure that incorporates link quality parameters to maximize coverage. The designs are presented for both 2D and 3D distributed IoT devices. Next, the chapter focuses on a dedicated RF energy transmitter, detailing the minimum input RF power needed to 3D clustered ultra low power IoT devices within a wireless sensor network. The study addresses optimization challenges related to energy transfer, cluster head locations,

and power requirements in a 3D environment. Insights into effective WPT design considerations are provided.

3. Chapter-3: This chapter addresses angular misalignment in WPT by presenting a multi-sector rectenna design to mitigate this issue. A novel rectenna module with nearly isotropic coverage is introduced, ensuring effective operation in 3D space. The integration of this module with an IoT sensor node demonstrates a WPT-enabled sensor system.

Additionally, a compact SWIPT antenna element is designed specifically for ultra-low-power IoT devices using an evolutionary design process. The chapter explains the innovative SWIPT technique and elaborates on the antenna's working principles and operational procedures, showcasing its functionality.

4. Chapter-4: This chapter presents the design of a novel compact SWIPT antenna array system for energy constraint relay nodes. A comprehensive explanation of the new SWIPT technique, which integrates DC combining with a hybrid approach that employs frequency splitting, dual polarization, and antenna switching. The chapter thoroughly discusses the technique and the operational procedures of the antenna design. It highlights the advantages of this integrated antenna solution, including full-wave rectification at ultra-low power levels and wideband WIT operation with high isolation from the power signal.

This chapter presents the design of a novel compact reconfigurable SWIPT antenna array system for energy constraint relay nodes. A comprehensive explanation of the new SWIPT technique, which integrates DC combining with a hybrid approach that employs frequency splitting, dual polarization, and antenna switching. The chapter thoroughly discusses the technique and the operational procedures of the antenna design. It highlights the advantages of this integrated antenna solution, including full-wave rectification at ultra-low power levels and wideband WIT operation with high isolation from the power signal.

5. **Chapter-5:** This chapter gives the overall conclusion of the thesis and the potential future directions in this area of research.

Chapter 2

QoS Aware Transmitter Antenna System

O-1: Quality aware synthesis of multi sector switched multi beam Access Point antenna system.

 $\mathbf{O}-2$: Analyze and design a dedicated switched beam RF energy transmitter for wireless powering of 3D distributed clustered ultra-low power IoT devices.

This chapter presents quality aware synthesis of multi switched beam transmitter antenna systems for WIT and WPT operations in a SWIPT enabled IoT network. First a minimum QoS performance based approach is discussed to synthesize switched beam multi-sector antenna arrays for Access Point, aimed at maximizing WIT coverage in both 2-D and 3-D spaces. Initially, the chapter addresses a BER-conscious synthesis of a switched multi-beam, multi-sector AP antenna system, specifically designed to enhance reliable communication coverage on a 2-D ground plane. The synthesis approach integrates projected received power levels and SIR constraints into the antenna design process, optimizing the effective coverage area while maintaining an acceptable BER. This optimization leads to improved coverage and more reliable communication, which in turn reduces energy consumption at IoT devices. The chapter then details the analytical synthesis of a multi-sector AP antenna based on this coverage optimization process. Additionally, using the same QoS metric, the synthesis of another multi-sector AP antenna featuring a series feed patch antenna array is explored to achieve comprehensive 3-D coverage within the application region. Two Access point antenna system designs depicted as Design-O1A and Design-O1B are discussed, which fulfill the objectives O-1a and O-1b, respectively as described in Section 1.7.1

To achieve the objective of synthesizing an SBA as an RF-ET for powering a 3-D distributed clustered WSN. The 3-D space is divided into nine clusters; each illuminated individually with RF power using a dedicated patch antenna subarray. The subarrays can be switched ON or OFF based on the energy requirement of the WSN cluster nodes resulting in efficient power transmission. Moreover, the low complexity of switched beam design reduces the cost and processing overhead as compared to the exiting adaptive beamforming systems in a dense WSN scenario. The subarray size and excitation coefficients are optimized with a constraint over the harvested dc power to enhance the 3-D coverage. In addition, the optimal location of the cluster head (CH) is evaluated to minimize the average power consumption of WSN cluster.

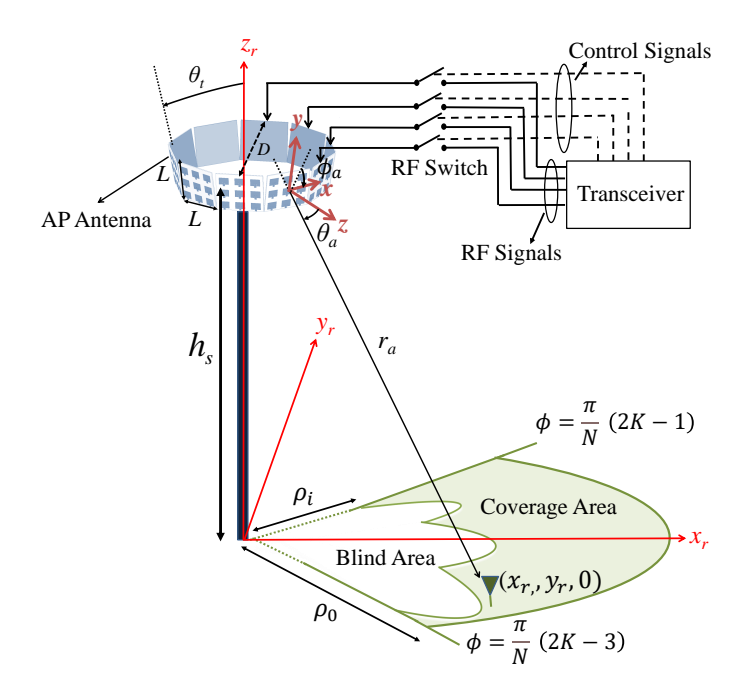


Figure 2.1: Schematic model of the proposed multi-sector SBA antenna as AP and projected communication coverage in one sector.

2.1 System Model of 2-D Coverage Multi-Sector Switched Beam Array Antenna (Design-O1A)

The schematic model of the 2-D coverage multi-sector SBA antenna comprising N sectors is presented in Fig. 2.1 to provide a complete 360° azimuth coverage. The reliable communication coverage area of a sector is highlighted in Fig. 1 and analytically modeled. Each sector of the proposed AP antenna houses a $Q \times R$ patch antenna array (PAA) which has a mechanical down tilt θ_t from the vertical axis. Each PAA forms a focused beam within their respective target sector area of a circular region around the AP antenna having radius ρ_0 and ensures quality links with the randomly deployed sensor nodes. The parameters, N, Q, R, and θ_t , of the PAA, are optimized to maximize the reliable coverage area by constraining the diameter (D) of the antenna. The beams can be switched on based on communication demand from the nodes of corresponding sectors. The switching operation can be realized by using either of a network of RF switches [40] connected to each PAA; a reconfigurable feed network implemented using Pin diodes [41], or one-bit phase shifters [31], which are integrated into and centrally controlled by a transceiver unit as depicted in Fig. 1. In the scenario, the WSN nodes are assumed to be distributed on the ground plane in a communication region of maximum radius $\rho = \rho_0$ and the proposed array antenna as AP is positioned at a height h_s above the ground, as depicted in Fig. 1. The highlighted region is the communication area (CA) of the sector-k bounded by $((2k-3)\pi/N \le \phi \le (2k-1)\pi/N) \cap (\rho_i \le \rho < \rho_0)$, whereas the light region around the SBA antenna bounded by $(0 \le \rho < \rho_i)$ denotes the blind area (BA) where reliable communication is not achieved due to high interference from the neighboring sectors. The analytical model and design optimization of the proposed antenna array are subsequently presented.

2.1.1 Analytical Model for Received Power Projection and SIR

To analyze the received power projection of each PAA in the target region, two coordinate systems are defined. The global coordinates x_r , y_r , z_r (spherical coordinates-r, θ , ϕ) define the sensor node deployment region with its origin coinciding with the center of the total target communication region. Whereas (x, y, z) corresponds to the local coordinate system of the individual PAA whose origin coincides with the PAA center as depicted in Fig. 2.1. ϕ denotes the azimuth angle corresponding to the k^{th} PAA centre and is denoted by $\phi = \frac{2\pi}{N}(k-1)$. The two coordinate systems are interrelated by the following relations

$$x = -x_r \sin \phi + y_r \cos \phi \tag{2.1a}$$

$$y = x_r \sin \theta_t \cos \phi + y_r \sin \theta_t \sin \phi + (z_r - h_s) \cos \theta_t \tag{2.1b}$$

$$z = x_r \cos \theta_t \cos \phi + y_r \cos \theta_t \sin \phi - (z_r - h_s) \sin \theta_t \tag{2.1c}$$

$$x_r = -x\sin\phi + y\sin\theta_t\cos\phi + z\cos\theta_t\cos\phi \tag{2.2a}$$

$$y_r = x\cos\phi + y\sin\theta_t\sin\phi + z\cos\theta_t\sin\phi \qquad (2.2b)$$

$$z_r = h_s + y\cos\theta_t - z\sin\theta_t \tag{2.2c}$$

Denoting (r_a, θ_a, ϕ_a) as the local spherical coordinates of an arbitrary sensor node positioned at (x_r, y_r, z_r) and evaluated with respect to antenna location as

$$r_a(x_r, y_r, z_r) = \sqrt{x_r^2 + y_r^2 + (z_r - h_s)^2}$$
 (2.3a)

$$\theta_a(x_r, y_r, z_r) = \cos^{-1}\left(\frac{z}{r_a}\right) \tag{2.3b}$$

$$\phi_a(x_r, y_r, z_r) = \tan^{-1}\left(\frac{y}{x}\right) \tag{2.3c}$$

The normalized spherical field patterns, E, of a single patch antenna which is constituted as one element of the PAA is given by [96] as

$$E_{\theta_a} = \cos v \, \frac{\sin u}{u} \cos \phi_a \tag{2.4a}$$

$$E_{\phi_a} = \cos v \, \frac{\sin u}{u} \cos \theta_a \sin \phi_a \tag{2.4b}$$

$$v = \frac{kl_p \sin \theta_a \cos \phi_a}{2}, \quad u = \frac{kw_p \sin \theta_a \sin \phi_a}{2}$$
 (2.4c)

where, k is the propagation constant in free space, w_p is width and l_p is length of the

patch. Thus, the total normalized element factor (EF) spherical pattern corresponding to the patch element of the PAA is obtained using

$$EF(\theta_a, \phi_a) = \sqrt{E_{\theta_a}^2 + E_{\phi_a}^2} \tag{2.5}$$

Since the PAA is a $Q \times R$ array of the patch elements contained in a sector, the normalized array factor (AF) of the PAA is given by

$$AF(\theta_a, \phi_a) = \sum_{m=1}^{Q} \sum_{n=1}^{R} w_{m,n} \exp\left[jkx_{m,n}\sin\theta_a\cos\phi_a + jky_{m,n}\sin\theta_a\sin\phi_a\right] \text{ and } [w_{m,n}] = [w_m]^{\top}[w_n] \quad (2.6)$$

where, $x_{m,n}$ and $y_{m,n}$ denote the individual element position in the PAA local coordinate system. The normalized excitation coefficient represented by $w_{m,n} \in [0,1]$ is assigned to antenna element placed at m^{th} and n^{th} location along the vertical and horizontal axis of an array, respectively. To control interference level in the azimuth plane, the PAA is synthesized with Chebyshev distribution to achieve an optimal beamwidth and side-lobe level (SLL_x) . Hence using (2.5) and (2.6), the normalized spherical gain pattern of the PAA is evaluated using

$$G_t(\theta_a, \phi_a) = |AF(\theta_a, \phi_a) \times EF(\theta_a, \phi_a)|^2$$
(2.7)

which represents the conventional radiation pattern in the spherical coordinate system. However, to properly characterize the received power at the WSN node located at (x_r, y_r, z_r) , the projected gain pattern $G_t[\theta_a(x_r, y_r, z_r), \phi_a(x_r, y_r, z_r)]$ of the PAA is utilized. For analysis, a line-of-sight (LOS) channel is assumed between the PAA and the sensor nodes. Therefore, the received power due to any sector-i PAA at the WSN node location (x_r, y_r, z_r) within sector-k is evaluated using the Friis transmission equation as

$$P_r^i(x_r, y_r, z_r) = P_t^i G_{t0} G_t^i [\theta_a^i(x_r, y_r, z_r), \phi_a^i(x_r, y_r, z_r)] \times G_r \left(\frac{\lambda_0}{4\pi r_a^i(x_r, y_r, z_r)}\right)^{\alpha}$$
(2.8)

where, α is the path loss factor (for free-space propagation $\alpha=2$), P_t^i and $G_t^i[\theta_a^i(x_r,y_r,z_r),\phi_a^i(x_r,y_r,z_r)]$ are the transmitted power and projected gain pattern of the sector-i PAA, G_{t0} is the peak gain of the PAA, G_r is the receiver antenna gain at the sensor node assumed as 4 dBi, and λ_0 is the free space wavelength at the operating frequency. The $P_t^iG_{t0}$ in (2.8) represents the EIRP set to a maximum value of 4 W. Since the adjacent sectors cause high co-channel interference at the boundary of their respective communication region, alternate sectors are considered for the frequency re-use and contribute to co-channel interference. Therefore, the SIR γ_k distribution that is

projected on the ground within the sector-k can be formulated as

$$\gamma_k(x_r, y_r, z_r) = \frac{P_r^k(x_r, y_r, z_r)}{\sum_{\substack{i \in N_a \\ i \neq k}} P_r^i(x_r, y_r, z_r)}$$
(2.9)

 $\forall (x_r, y_r, z_r) \in \text{sector-}k$, where N_a is the set of alternate sector PAAs causing interference to the intended signal generated by the PAA of sector-k. Given the γ distribution, the corresponding link-quality in terms of BER at the WSN node location (x_r, y_r, z_r) can be obtained as [97]

$$BER_k(x_r, y_r, z_r) = \mathcal{Q}_M \left[\gamma_k(x_r, y_r, z_r) \right], \qquad (2.10)$$

where $Q_M[\cdot]$ denotes the expression involving Marcum Q-function relating the BER and SIR for an M-array modulation scheme used for communication.

2.1.2 BER-Conscious Array Synthesis Process

Effective Coverage Area as Performance Metric

Conventionally, the coverage area of the AP is defined as the region where the received signal strength P_r evaluated in (2.8) is greater than the IoT device's sensitivity given by a minimum required power threshold (P_{th}) [98]. However, this definition fails to represent the actual coverage performance in the scenario where multiple co-channel beams are radiated. The multi-beams cause interference with the intended signal to degrade the SIR and result in communication outage (blind area) in the region where the BER exceeds the limit, BER_{th} , set for reliable communication. The BER_{th} corresponds to a SIR threshold (γ_{th}) related in (2.10) based on the modulation technique applied for communication. Therefore, the projected SIR distribution of γ in the ground plane as given by (2.9) is another essential parameter along with the P_r to define the coverage based on communication link quality. Therefore, the projected γ along with the projected P_r profile is included in the proposed definition of the effective communication coverage area (ECA), which serves as the optimization metric for the proposed array synthesis process. Besides, the ECA is defined in a manner to incorporate a potential reduction in blind areas. Moreover, since the system capacity of a multi-sector antenna is proportional to the number of sectors N, the ECA also includes the parameter N for maximization. Thus, the ECA definition is proposed in terms of Communication Area, CA, which stands for the area where $(BER \leq BER_{th}) \cap (P_r \geq P_{th})$ satisfies, and Blind Area, BA, denoting the area around the AP antenna satisfying $(BER > BER_{th}) \cup (P_r < P_{th})$ as depicted in Fig. 2.1. Since the BER is one-to-one related with γ from (2.10), the conditions $(BER \leq BER_{th})$ and $(BER > BER_{th})$ can be equivalently replaced with $(\gamma \geq \gamma_{th})$ and $(\gamma < \gamma_{th})$, respectively. Hence, the CA and the BA evaluated for sector-k are defined as

$$CA_k = \operatorname{Area}_k \forall (x_r, y_r, 0) : \{ [\gamma_k(x_r, y_r, 0) \geq \gamma_{th}] \cap [P_r^k(x_r, y_r, 0) \geq P_{th}] \}$$
 (2.11)

$$BA_k = \text{Area}_k \forall (x_r, y_r, 0) : \{ [\gamma_k(x_r, y_r, 0) < \gamma_{th}] \cup [P_r^k(x_r, y_r, 0) < P_{th}] \}$$
 (2.12)

Now, the ECA is defined and evaluated using (2.11) and (2.12) as

$$ECA = N \times \sum_{k=1}^{N} (CA_k - BA_k)$$

$$(2.13)$$

Since the proposed ECA definition involves the CA, the BA, and N in the communication region, the design objective function formulated in terms of ECA can enhance the quality coverage area, reduce the blind area in the immediate surrounding of the AP antenna, and enhance capacity by optimizing N with a maximum size constraint of the antenna.

Optimization Problem formulation for Array Synthesis

The proposed BER-conscious array synthesis process targets maximizing the ECA defined in (2.13). The objective function for the optimized array synthesis with a constraint on the antenna parameters, N, Q, R, θ_t , and maximum size of the SBA antenna is formulated as:

$$\max_{N,Q,R,\theta_t,SLL_x} ECA$$

$$s.t. \ 0 \le \rho \le 15\text{m},$$

$$0^{\circ} \le \theta_t \le 80^{\circ}, \ 4 \le N \le 16, \ 1 \le Q \le 3, \ 2 \le R \le 5$$

$$10\text{dB} \le SLL_x \le 30\text{dB}, \ D \le 0.3 \text{ m}$$
(2.14)

where, $D = L/\tan(\frac{\pi}{N}) + 2L\sin\theta_t$ is the diameter of the proposed AP antenna, which is calculated by considering the dimension (L) of the PAA and depends on the inter-element distance d_h between the patch elements along the horizontal axis in the PAA. The Chebyshev current excitation is applied to the patch antenna elements along the horizontal axis to reduce interference in the azimuth plane, whereas uniform excitation is applied along the vertical axis to maximize the gain. SLL_x denotes the side-lobe level in the $\phi = 0^\circ$ plane for the array with isotropic antenna element, i.e, the side-lobe level of the AF. The objective function is maximized using the parametric sweep of N, Q, R, θ_t , and SLL_x within the constraints given in (2.14) such that the diameter D of the AP antenna remains under 0.3 m. In the analysis, only even N values are considered to maintain the number of interfering PAAs symmetrical on either side of the intended sector. The optimization steps are described as follows:

- 1. Set the design parameters to their minimum value and initialize various other parameters as listed in Table. 2.1.
- 2. For constant θ_t and N, sweep Q within the constraint range to maximize ECA radial coverage length ρ_0 .
- 3. For fixed θ_t , N, and the Q achieved in step-2, now sweep R and SLL_x to maximize ECA for enhanced 360° coverage in azimuth plane on the ground.

Parameters	Notation	Values		
Operating frequency	f_0	$5.8\mathrm{GHz}$		
AP height	h_s	4 m		
EIRP	P_tG_{t0}	4 W		
WSN node antenna gain	G_r	$4\mathrm{dBi}$		
Power Threshold	P_{th}	$-30\mathrm{dBm}$		
BER Threshold	BER_{th}	10^{-5}		
SINR Threshold	γ_{th} (BPSK)	$9.5\mathrm{dB}$		
STIVIT THIESHOID	γ_{th} (64-QAM)	$17\mathrm{dB}$		
Inter-element spacing	d_h	$0.5\lambda_0$		
inter-element spacing	d_v	$0.5\lambda_0$		
Noise Power	N_p	$-70\mathrm{dBm}$		

Table 2.1: Parameters values initialized in the synthesis process.

- 4. Sweep N and θ_t and repeat step-2 and step-3.
- 5. Obtain the optimized N, Q, R, θ_t , and SLL_x which results in a maximum ECA.
- 6. Obtain the $w_{m,n}$ coefficients using the optimal R and SLL_x obtained from the step-5 corresponding to the maximum ECA.

The analytical results obtained after performing the optimization are discussed in the following section.

2.1.3 Analytical Optimization Results and Discussion

Variation of ECA with various parameters

In this section, the parametric study for optimization of ECA versus antenna design parameters is presented. Fig. 2.2 and Fig. 2.3 demonstrate the variation of ECA with

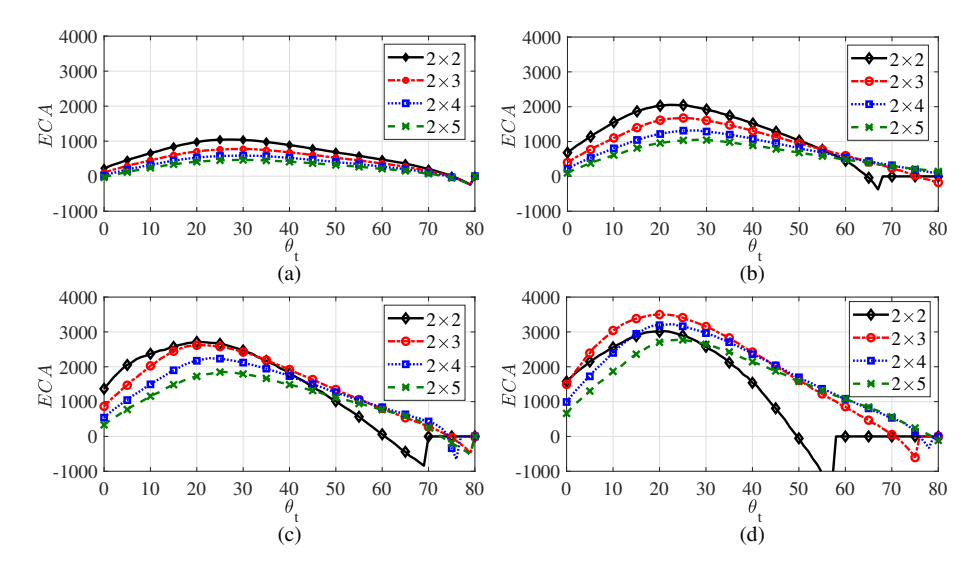


Figure 2.2: ECA versus θ_t plots for (a) N=4 (b) N=6 (c) N=8 (d) N=10 where $SLL_x=15$ dB and $2\times R$ PAA, R=2,3,4, and 5 for BPSK modulation.

respect to θ_t for BPSK and 64-QAM modulation schemes, respectively, and shown for

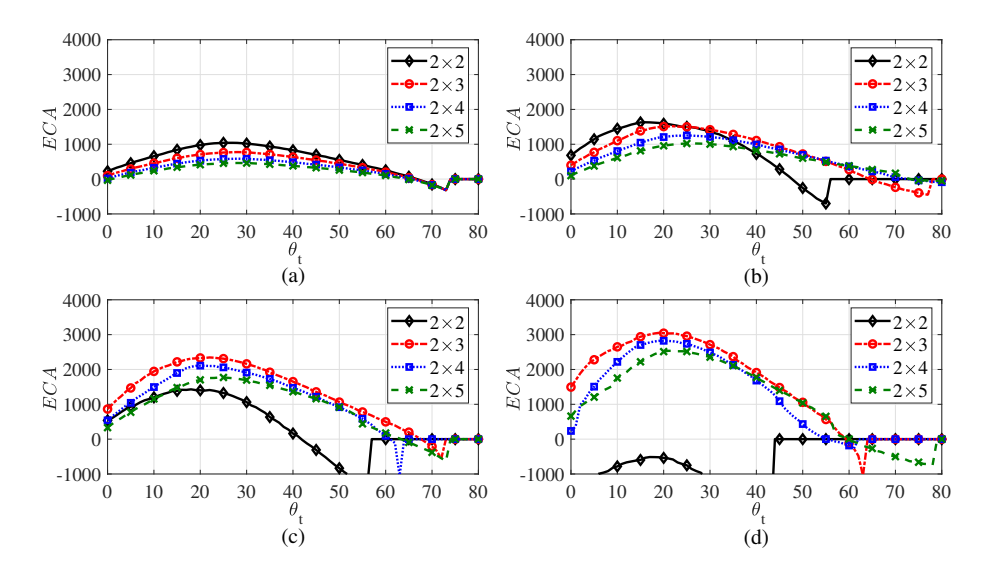


Figure 2.3: ECA versus θ_t plots for (a) N=4 (b) N=6 (c) N=8 (d) N=10 where $SLL_x=15$ dB and $2\times R$ PAA, R=2,3,4, and 5 for 64-QAM modulation.

various N, Q = 2, and $2 \times R$ PAAs. The ECA value is substituted to zero whenever the dimension D of the proposed AP antenna exceeds the maximum value of 0.3 m as per the defined constraint in (2.14). Moreover, D exceeds the limit 0.3 m for N > 10, therefore, $N \le 10$ is taken in the results. The negative values of ECA observed at extreme θ_t values imply domination of the BA over the CA in the ECA defined in (2.13). The plots indicate that the ECA increases with N and attains its maximum value at N = 10, $\theta_t = 20^\circ$, and R = 3 for 2×3 PAA, for both the modulation schemes. Similarly, Fig. 2.4 demonstrate

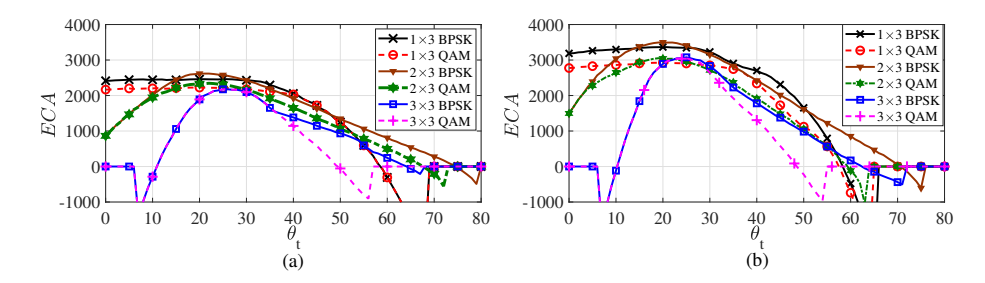


Figure 2.4: ECA versus θ_t for (a) N=8 and (b) N=10 for $Q\times 3$ elements where Q=1,2, and 3.

the ECA variation for various Q and R=3. The plots indicate that for both BPSK and 64-QAM modulation schemes, the maximum ECA is attained for $\theta_t = 20^\circ$, N=10, and Q=2 for 2×3 PAA.

To analyze the effect of non-uniform excitation along the horizontal elements of the PAA, the variation of ECA with respect to SLL_x is plotted in Fig. 2.5 for various R and Q=2. The results show that the maximum ECA is achieved for $SLL_x=15$ dB, N=10 and R=3 for 2×3 PAA when BPSK modulation is employed, whereas, in case of 64-QAM, the maximum ECA is achieved for $SLL_x=11.25$ dB, N=10, and R=3 for 2×3 PAA. However, an abrupt change in performance for 64-QAM at $SLL_x=11.25$ dB is avoided by selecting SLL=15 dB which is also optimized for BPSK modulation. Thus, the

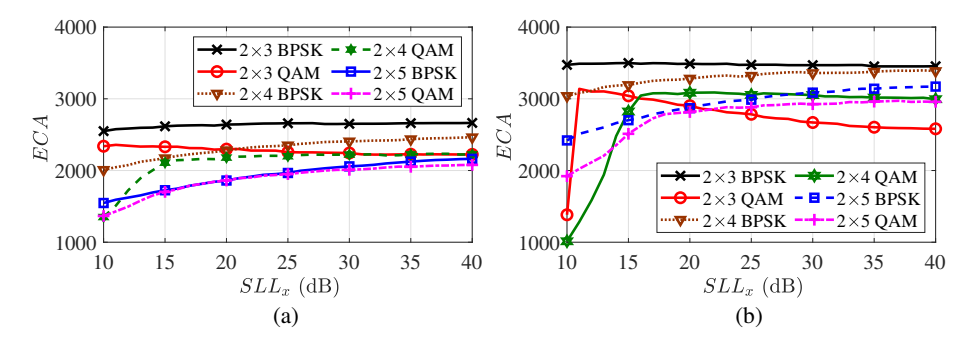


Figure 2.5: ECA versus SLL_x for (a) N=8 and (b) N=10.

parametric optimization results for ECA reveal that $\theta_t = 20^\circ$, $SLL_x = 15$ dB, N = 10, and the PAA of size 2×3 represent the best solution of targeted array synthesis problem formulated in (2.14) to maximize the ECA.

The Achieved ECA with Synthesized CA and BA

To demonstrate the achieved ECA, the synthesized CA and BA variations with various design parameters are investigated and the results in terms of projected γ distributions on the ground plane are shown in Fig. 2.6 and Fig. 2.7. Since, the CA is a function of γ and P_r as defined in (2.11), therefore, $\gamma = \text{NIL}$ is forced in the plots for the region which is out of the coverage area having $P_r < P_{th}$. Also, the region with $\gamma = \text{NIL}$ around the AP antenna near $(x_r = 0, y_r = 0)$ represents the BA in the distribution plots.

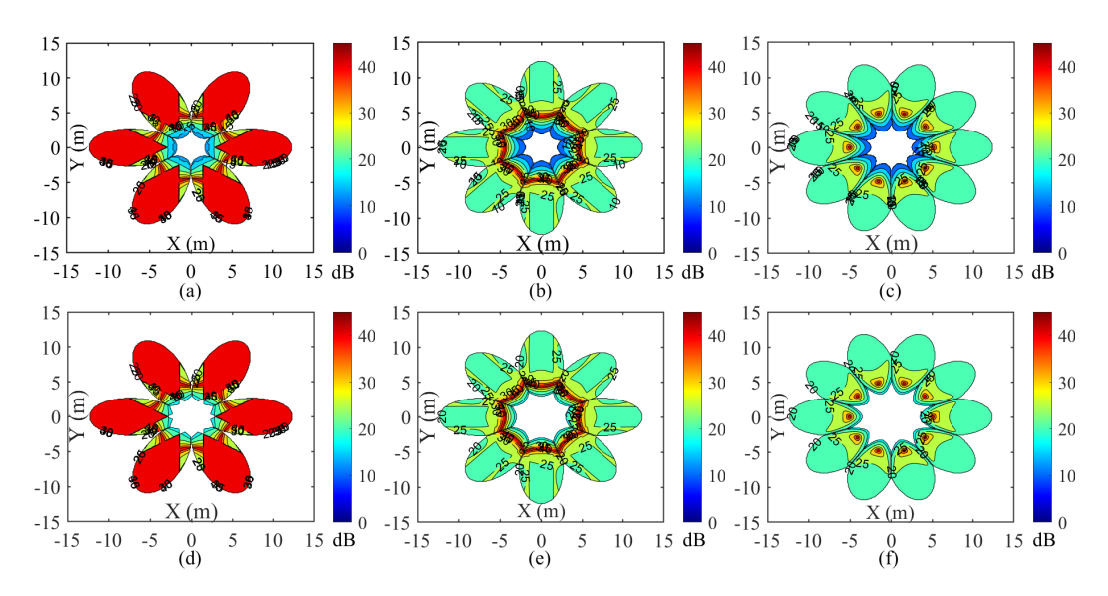


Figure 2.6: γ projection for 2×3 PAA at $\theta_t = 20^\circ$, $SLL_x = 15$ dB with (a) N = 6 (b) N = 8 (c) N = 10 using BPSK modulation and (d) N = 6 (e) N = 8 (f) N = 10 employing 64-QAM .

The projected γ distributions for 2×3 PAA, $\theta_t = 20^\circ$ and $SLL_x = 15$ dB are demonstrated in Fig. 2.6 to study the effect of N (for N = 6, 8, and 10) for both the modulation schemes (BPSK and 64-QAM). The distributions show that the CA region where reliable communication is achieved with $\gamma \geq \gamma_{th}$ increases with higher N for both the modulation

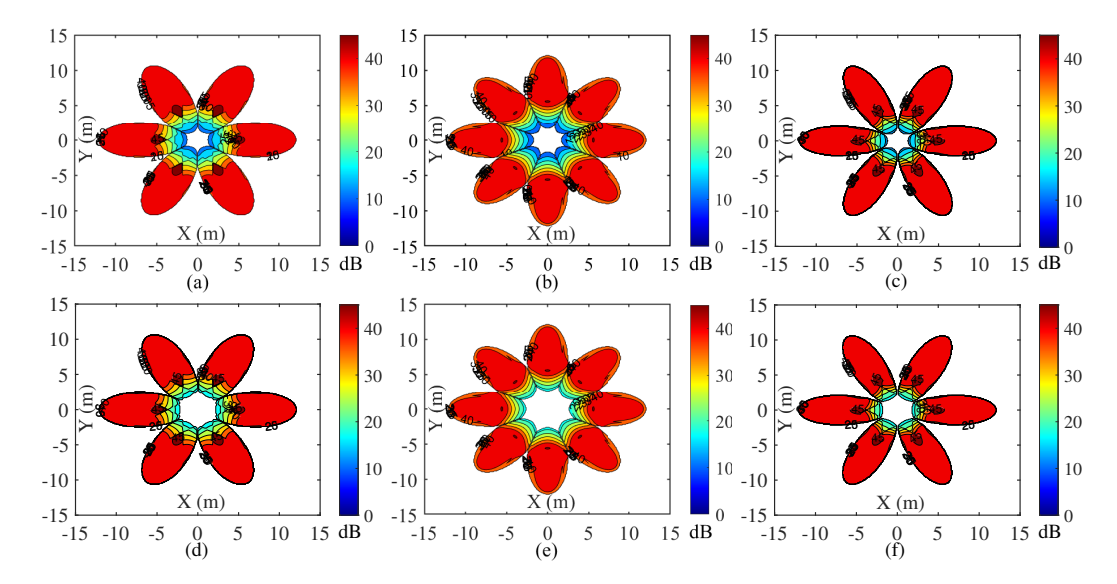


Figure 2.7: γ projection with $\theta_t = 25^\circ$, $SLL_x = 15$ dB for 2×4 PAA: (a) N = 6 (b) N = 8 for BPSK, (d) N = 6 (e) N = 8 for 64-QAM, and for 2×5 : (c) BPSK N = 6 (f) 64-QAM N = 6.

schemes. It is observed that the BA also increases with N due to increased number of interfering sectors N_a (i.e., $N_a = 2$, 3, and 4 for N = 6, 8, and 10, respectively). However, the increase in BA is overcompensated by the enhanced 360° coverage of CA due to reduction in non-coverage area between the adjacent sectors, as a consequence, maximizing the ECA for N = 10.

Similarly, the effect of array size R on the coverage is analyzed by plotting the γ distributions for various $2 \times R$ PAA. In addition to the 2×3 PAA distributions shown in Fig. 2.6, the 2×4 PAA with N=6 and 8, and 2×5 PAA with N=6 are analyzed in Fig. 2.7 for both the modulation schemes. Here, the 2×4 PAA with N=10 and the 2×5 PAA with N=8,10 are not considered because the corresponding AP antennas exceed the size constraint. Since the 2×4 and the 2×5 PAA attain maximum ECA at $\theta_t=25^\circ$, as apparent from Fig. 2.2 and Fig. 2.3, the corresponding distributions are shown for $\theta_t=25^\circ$ and $SLL_x=40$ dB to present a fair comparison. The γ distributions of Fig. 2.6 and Fig. 2.7 together corroborate the optimal choices revealed in Section 2.1.3 as 2×3 PAA and N=10 for the AP antenna to attain the maximum ECA coverage.

To further demonstrate the enhancement in the coverage area achieved by the proposed BER-conscious array synthesis process and the importance of an optimal θ_t selection, a conventional array with uniform current distribution is analyzed for comparison. The γ distributions of the conventional AP array with 2×3 PAA is plotted for $\theta_t = 0^\circ$ with N = 8 and 10 in Fig. 2.8.

As compared to the coverage of the optimized AP in Fig. 2.6 (c, f), the ECA of the conventional array is very low at $\theta_t = 0^{\circ}$ as depicted in Fig. 2.8 (b, d), particularly for 64-QAM, almost no coverage is provided. Therefore, an optimal tilt θ_t is crucial to maximize the projected coverage. Further, the conventional uniform array is also analyzed for $\theta_t = 20^{\circ}$ having 2×3 PAA with N = 10 in Fig. 2.9 (a, b) respectively for BPSK and

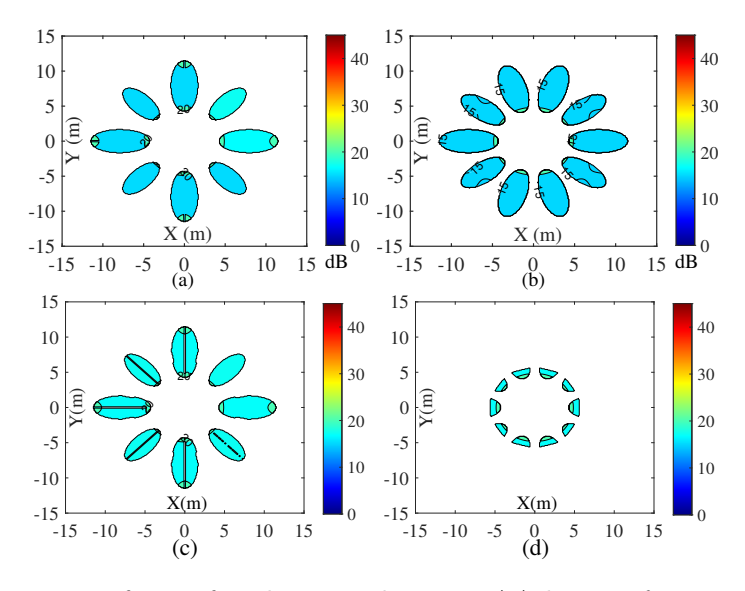


Figure 2.8: γ projection for uniformly excited 2×3 PAA having $\theta_t = 0^{\circ}$ with (a) N = 8, BPSK, (b) N = 10, BPSK, (c) N = 8, 64-QAM and (d) N = 10, 64-QAM.

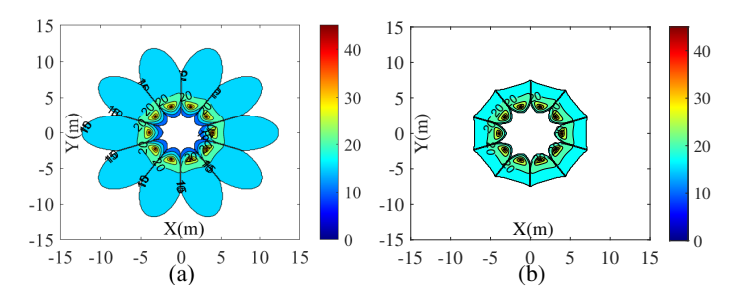


Figure 2.9: γ projection for uniformly excited 2×3 PAA having $\theta_t = 20^\circ$ with (a) N = 10, BPSK, (b) N = 10, 64-QAM.

64-QAM. At $\theta_t = 20^\circ$, the CA is improved for conventional array when BPSK modulation is considered in Fig. 2.9(a), however, for 64-QAM modulation, the coverage in Fig. 2.9(b) is still very low. Furthermore, the average γ in the entire CA for optimally synthesized antenna in Fig. 2.6 (c, f) is higher than that of the uniformly excited antenna Fig. 2.9(a, b) for both the modulation schemes.

Hence, from the overall analysis of all the projected γ distributions, the optimally synthesized AP antenna with $\theta_t = 20^{\circ}$, $SLL_x = 15$ dB, N = 10, and 2×3 PAA has emerged as an optimal solution. Corresponding to the $SLL_x = 15$ dB, the 2×3 PAA has the optimal excitation evaluated as

$$w_{m,n} = \begin{bmatrix} 1 \angle 0^{\circ} & 1.396 \angle 0^{\circ} & 1 \angle 0^{\circ} \\ 1 \angle 0^{\circ} & 1.396 \angle 0^{\circ} & 1 \angle 0^{\circ} \end{bmatrix}$$
 (2.15)

and the corresponding analytically obtained radiation pattern of the PAA is presented later in Section 2.1.4. The analytical beamwidth of the PAA at 5.8 GHz is 35° and 54° in the two orthogonal planes cut at $\phi = 0^{\circ}$ and $\phi = 90^{\circ}$, respectively. Moreover, the analytical side-lobe level (SLL_p) of the total pattern of the PAA is 24.77 dB corresponding to the optimal SLL of the AF pattern obtained as $SLL_x = 15$ dB.

Interference Suppression Techniques

The proposed BER-conscious array design suppresses interference caused by the alternate sectors communicating at the same carrier frequency simultaneously. The other interference suppression methods are based on time sharing of channels, coding scheme like Direct-Sequence Spread Spectrum (DSSS), and frequency hopping techniques like Adaptive Channel Hopping (ACH)/Dynamic Frequency Selection (DFS) [99]. The DSSS along with the features of Transmit power control and Adaptive Data Rate is useful for ultra-low power WSN [100]. The ACH and DFS methods exploit different available channels within the operating band. The immediately mentioned schemes can be employed for communication with sensor nodes placed within the coverage region of the same or neighboring sectors to further improve the reliable communication area. The physical realization of the AP antenna, which is designed using the proposed BER-conscious array synthesis process, is now presented, and analytical results are experimentally verified subsequently.

2.1.4 The Proposed SBA Antenna Design-O1A Realization and Performance Evaluation

The analytically optimized PAA of size 2×3 is designed and simulated using commercial EM software Ansys HFSS. The array feeding network is designed to realize Chebyshev excitation given in (2.15). The antenna is realized on a double-sided FR4 substrate ($\epsilon_r = 4.4$ and $\tan \delta = 0.0025$) having thickness and copper deposition of 1.6 mm and 35 µm, respectively. The inter-element distance between the two adjacent patches along the vertical (d_v) and horizontal (d_h) axis is $0.5\lambda_o$. The proposed SBA antenna as AP with N = 10 and the designed PAA layout are depicted in Fig. 2.10. The optimal chebyshev excitation of (2.15) along horizontal antenna elements of PAA as [1, 1.396, 1] is implemented by optimizing the corporate feed network to achieve the

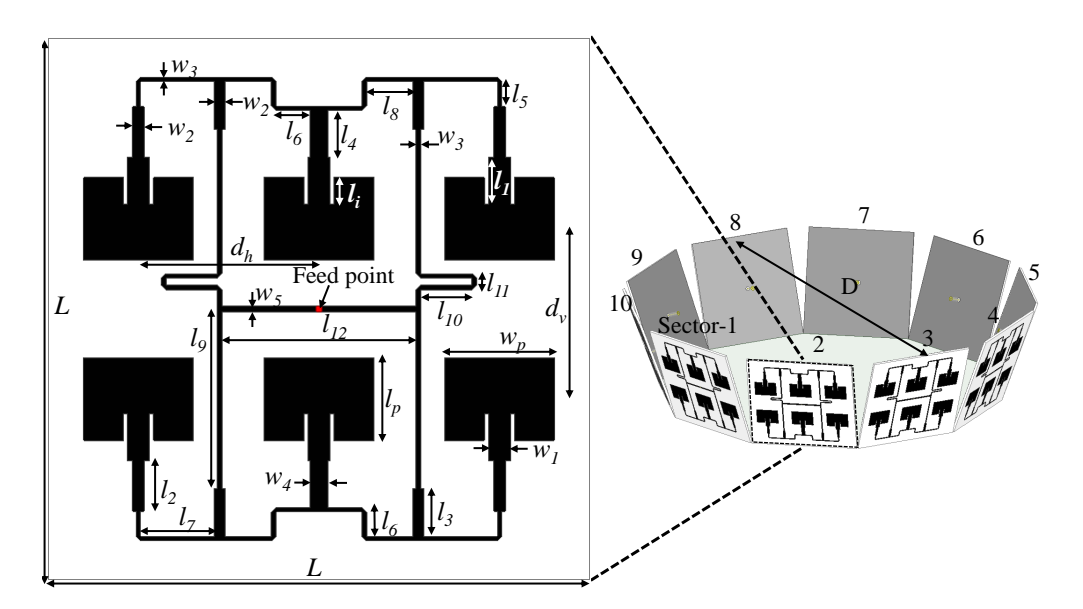


Figure 2.10: Layout of the optimized 2×3 PAA and corresponding AP antenna.

Parameter	Dimension	Parameter	Dimension	Parameter	Dimension	Parameter	Dimension
l_p	15.73	l_i	0.68	l_1	6.77	l_2	7.16
l_3	6.82	l_4	6.59	l_5	3.58	l_6	4.89
l_7	10.49	l_8	6.61	l_9	25.22	l_{10}	7.35
l_{11}	2.36	l_{12}	27.767	w_p	11.74	w_1	3.08
w_2	1.61	w_3	0.68	w_4	2.47	w_5	1
d_v	25.86	d_h	25.86	L	77.58	D	280
	-	-				-	

Table 2.2: The PAA design parameters (dimensions in mm)

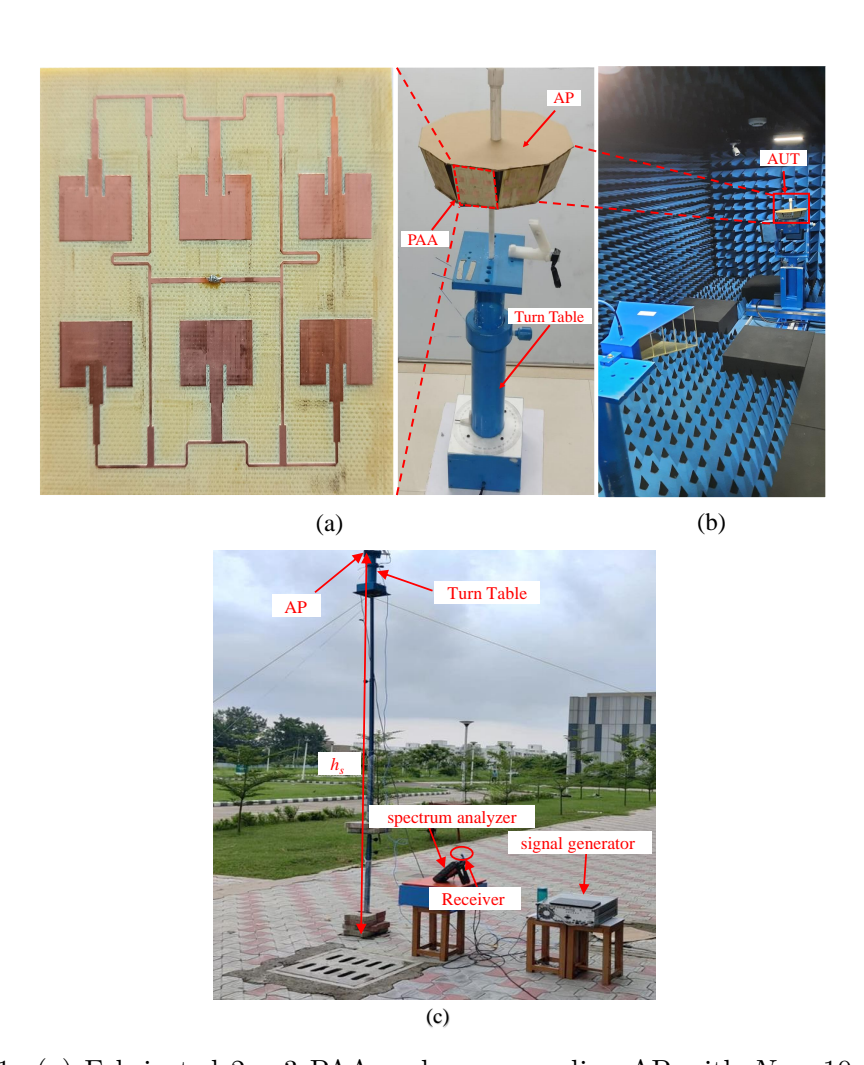


Figure 2.11: (a) Fabricated 2 × 3 PAA and corresponding AP with N=10 sectors (b) Experimental setup inside the anechoic chamber (c) Outdoor experimental setup for γ measurement.

 $SLL_p = 24.77$ dB in azimuth as obtained analytically in Section 2.1.3. The optimized dimensions of the simulated 2×3 PAA as denoted in Fig. 2.10 are listed in Table 2.2. For the experimental study, ten such 2×3 PAA antennas are fabricated using MITS PCB prototyping machine and assembled to the final AP antenna. The fabricated prototype is depicted in Fig. 2.11(a). The radiation pattern and S-parameter of the PAA are evaluated, and the projected γ measurements are conducted for the proposed antenna.

Antenna Measurements and Radiation Pattern Results

The simulated antenna parameters are verified by measuring the fabricated prototype. The S-parameters and radiation patterns are measured using Keysight's PNA-L VNA. The S-parameter responses representing matching (S_{ii}) of port-i and isolation (S_{ij}) between ports -i and -j are shown in Fig. 2.12. The observed impedance bandwidth ($S_{11} \leq -10 \text{ dB}$)

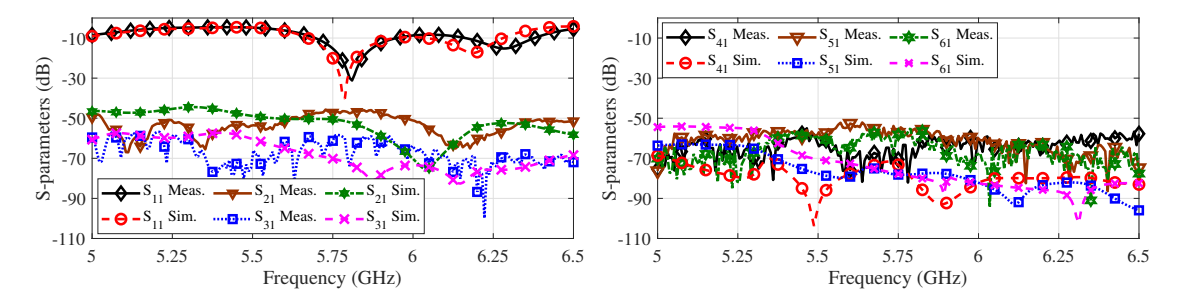


Figure 2.12: S-Parameter results of 2×3 PAA.

for simulated and fabricated 2×3 PAA is 262 MHz (5.690 - 5.952 GHz) and 292 MHz (5.668 - 5.960 GHz), respectively, covering the WLAN band around 5.8 GHz. The adjacent sector shows a low mutual coupling (i.e. S_{21}) less than -45.95 dB, whereas the alternate sector depicts negligible mutual coupling (i.e. S_{31}) less than -58.4 dB. The results show a close agreement between the simulated and measured S-parameters.

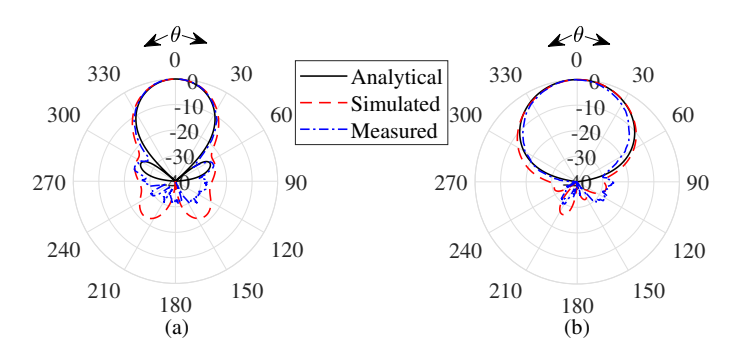


Figure 2.13: Analytical, Simulated and Measured Radiation pattern of 2×3 PAA corresponding to 5.8 GHz for (a) $\phi = 0^{\circ}$ and (b) $\phi = 90^{\circ}$ plane.

The patterns are characterized experimentally inside the Anechoic chamber using the setup shown in Fig. 2.11(b). The normalized radiation pattern of the PAA for both the $\phi = 0^{\circ}$ and $\phi = 90^{\circ}$ planes are depicted in Fig. 2.13. The measured gain of the PAA antenna is $G_{t0} = 10.06$ dBi. The measured beamwidth of the PAA at 5.8 GHz is 36° and 46.8° in planes $\phi = 0^{\circ}$ and $\phi = 90^{\circ}$, respectively. The measured SLL_p is observed as 23.03 dB and found in close agreement with the optimal analytical value 24.77 dB. The simulated and measured radiation patterns are corroborated. The analytically obtained radiation pattern corroborates in the upper hemisphere since the mathematical expression in (2.4a) of the patch antenna pattern predicts the radiation above the infinite ground; however, the realized antenna contains a finite ground. Nevertheless, the measured back radiation is below (by 30 dB) the major lobe, and further, due to the tilt θ_t provided to each PAA, this has negligible contribution in the interference to the other sectors.

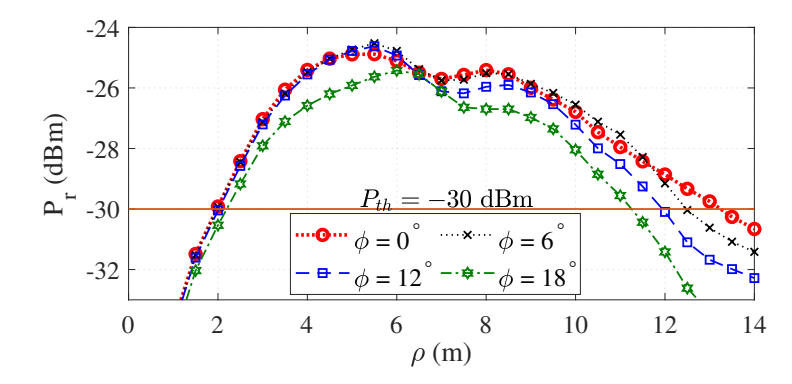


Figure 2.14: Measured P_r from transmitting PAA in sector-1 versus ρ for various ϕ at 5.8 GHz.

Projected P_r and γ Measurement for Coverage Validation

The communication coverage performance of the proposed AP antenna is experimentally verified. The measurement of the projected P_r pattern on the ground is carried out using the experimental setup shown in Fig 2.11(c). The AP antenna as a transmitter is set up on an elevated platform shown in Fig. 2.11(a) and then fixed 4.5 m above the ground on a vertical pole as depicted in Fig. 2.11(b). A receiver antenna depicting a WSN node is set up on a tripod having 0.5 m height from the ground; hence, a relative height of 4 m is maintained between the transmitter and the receiver as used for the analysis. One of the PAA as a transmitter is fed with a sinusoidal signal at 5.8 GHz frequency with strength 25 dBm using an RF signal generator (Agilent Technologies E8257D). The receiver is connected to Kesight's N9915A spectrum analyzer (SA) to measure the received signal strength in dBm units. Both, the transmitter and the receiver, are calibrated to account for the losses in the connecting cables. The receiver is placed within the sector-1 of the AP antenna and moved from $\rho = 0.5$ m to 14 m away with a step size of 0.5 m by repeating measurements for various azimuth angles $\phi = 0^{\circ}, 6^{\circ}, 12^{\circ}$ and 18° . Here, $\phi = 0^{\circ} - 18^{\circ}$ represents the half-sector area of sector-1 from the middle ($\phi = 0$) of the sector which is considered for the measurements. Nevertheless, the other half of the sector area $(-18^{\circ} \leq \phi < 0)$ has symmetrically the same P_r distribution. For signal power measurement, first the sector-1 PAA is fed, whereas, the alternate sectors- (3, 5, 7, and 9) are fed in sequence for interference power measurements. Readings in the SA at the receiver are noted to evaluate the γ by considering the combined interference together. The measured P_r distribution in the sector-1 at various ρ and ϕ are shown in Fig. 2.14. The measurement results indicate that the ρ range satisfying $P_r \geq P_{th}$ are 2 – 13 m, 2-12.5 m, 2-12 m, and 2.2-11.25 m respectively for $\phi = 0^{\circ}, 6^{\circ}, 12^{\circ}, \text{ and } 18^{\circ}.$ Further, the interference signal strengths emanating from sectors- (3, 5, 7, and 9) are measured and contributes to the total interference power (P_I) distribution within the sector-1 region and plotted in Fig. 2.15. The γ distribution is evaluated using the measured P_r and P_I , and the result is shown in Fig. 2.16. The measured γ results verify that the ρ coverage satisfying communication quality condition $(P_r \geq P_{th}) \cap (\gamma \geq \gamma_{th})$ for $\phi = 0^{\circ}$, 6° , 12° , and 18° respectively is 2-13 m, 2-12.5 m, 2-12 m, and 2.2-11.25 m for the BPSK modulation,

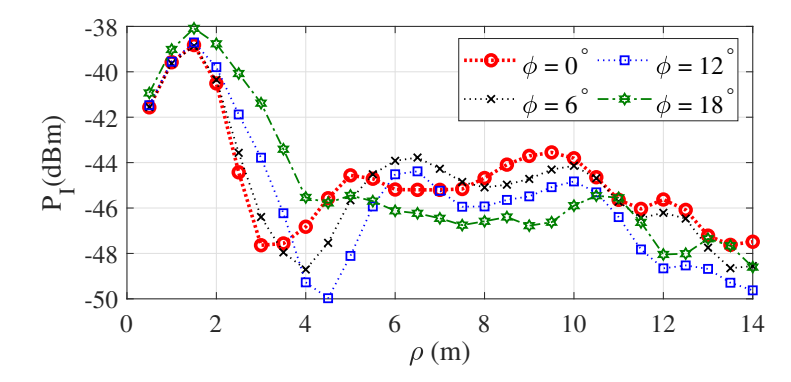


Figure 2.15: Measured P_I from alternate sector PAA versus ρ for various ϕ at 5.8 GHz.

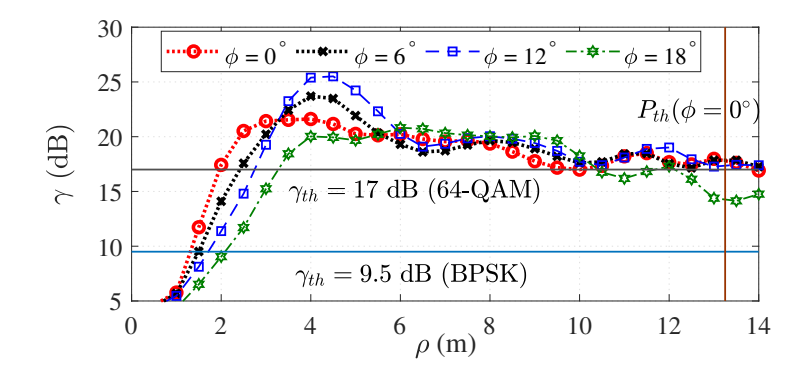


Figure 2.16: γ versus ρ in sector-1 for various ϕ at 5.8 GHz

and 2-13 m, 2.5-12.5 m, 2.75-12 m, and 3.25-10 m for the 64-QAM modulation. The measurement results are in good agreement with the analytically evaluated optimal γ distribution as presented before in Fig. 2.6 (c, f).

The immediately observed measurement results indicate that alternate sectors can operate simultaneously at a common carrier frequency. Moreover, the high port isolation between adjacent sectors enables the operation of adjacent sectors at different carrier frequencies in 5.8 GHz WLAN band. Thus ten simultaneous beams can be operated for enhanced system capacity and communication quality coverage.

Performance Comparison with Prior Pertinent Works and Significance

In this section, the performance of the SBA antenna Design-O1A synthesized using the proposed BER-conscious array synthesis process is compared with the state-of-the-art [36, 43] targeted to enhance the quality communication coverage. The comparison based on various parameters is performed in Table 2.3. For instance, the design in [36] consists of 16 planar Yagi-Uda dipole and that in [43] has 12 dual-band bowtie antennas placed in an orthogonally crossed manner to achieve dual polarization for capacity enhancement. The co-polarized antennas are placed in alternate positions to reduce interference. The maximum interference suppression achieved in the former is 20 dB, whereas this is 35 dB in the latter. However, this does not reflect the actual interference immunity because only a single interfering transmitter is considered at a time for γ evaluation, which does not support the multibeam characteristic. In this case, the actual interference level

Parameters	[36]	[43]	[46]	Design O-1A
Beam scan	2D	2D	2D	2D
Frequency (GHz)	5.5	2.4, 5.5	33	5.8
azimuth coverage	360°	360°	360°	360°
No. of sectors	8	6	12	10
Peak gain (dBi)	6.4	5	9.5 - 10.5	10.06
Peak SIR (dB)	20	35	-	25.51
Peak SLL (dB)	_	12	20	24.77
Isolation (dB)	20	30	45	45.95
Mechanical tilt	_	_	30°	20°

Table 2.3: Performance Comparison with State-of-the-Art

is expected to be much higher for simultaneous multibeam operation. The substrate integrated waveguide (SIW) are aperture horn array is proposed in [46] to achieve 360° azimuth plane coverage using two pairs of non-overlapped 12 simultaneous beams with a high port isolation of 45 dB. A beam tilt of 30° from the vertical axis is obtained by using a metal plate beneath the array structure. The non-overlapped adjacent beams does improve γ performance, however the effect of beam tilt on the communication quality is not analysed. In all the mentioned prior works for comparison, the γ distribution is not considered projected on the plane where device nodes are physically distributed and are only evaluated by conventional radiation pattern sphere with respect to the AP antenna. As an advancement, the proposed AP antenna achieves a peak γ value of 25.51 dB projected on the ground and can emanate 10 simultaneous beams for communication using BPSK and 64-QAM modulation as presented in Section 2.1.4. In addition, the proposed design has a higher peak gain of 10.06 dBi with respect to 6.4 dBi [36] and 5 dBi [43] which enables a longer radial communication coverage range. The proposed analytical framework can be incorporated in the design process of any other antennas or antenna arrays for a high density sensor network application. The designed antenna is the optimal solution for the required BER performance. This reduces the packet re-transmissions resulting in energy efficient communication at the sensor nodes which ultimately enhances the lifetime of the IoT sensor network. The Design-O1A achieves maximum 2-D WIT coverage in the azimuth plane surrounding the access point. However, it is bulky due to its incorporation of mechanical tilt and falls short in providing adequate coverage in the elevation plane, which is critical for application scenarios such as automated warehouses and smart cities. In the next section a novel multi-sector SBA antenna array (Design-O1B) is presented to provide enhanced 3-D spatial coverage around the access point.

2.2 System Model of 3-D Coverage Multi-Sector Switched Beam Array Antenna (Design-O1B)

The limitation of Design-O1A to provide adequate coverage in the elevation plane highlights the need for design enhancements to optimize performance in environments

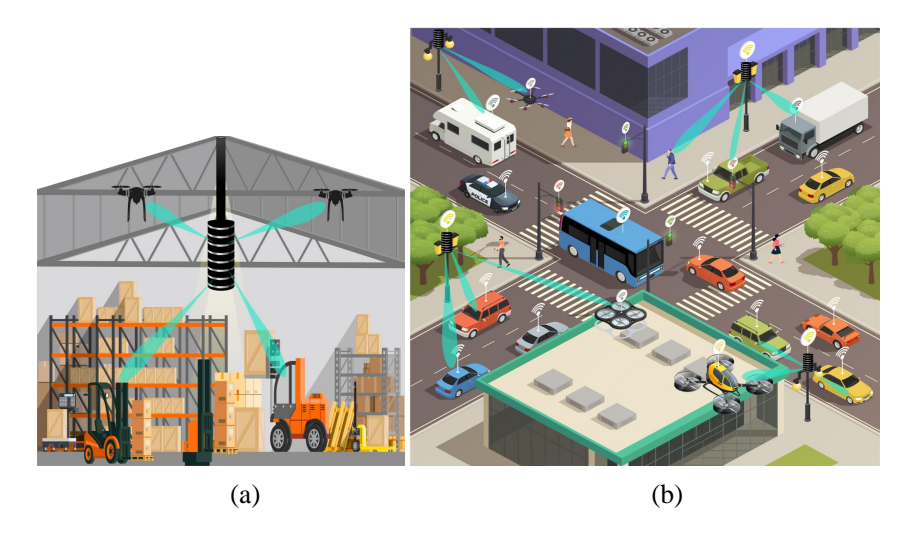


Figure 2.17: An access point antenna providing connectivity to crawlers, ground vehicles, and drone vehicles in 3D coverage scenarios (a) smart warehouse (b) smart city applications.

requiring comprehensive spatial coverage such as automated warehouses, as illustrated in Fig. 2.17(a). The access point is required to control and collect information from the crawler bots and drones. Similarly, in a smart city application, several devices co-exist in the form of vehicles, drones, and pedestals, etc in 3-D space. In this scenario, a distributed network of access points, shown in Fig.2.17(b), is able to provide seamless internet connectivity to all the IoT nodes. Both the applications and other similar ones demand from the access point to provide all-around coverage in azimuth as well as elevation and ability to communicate reliably with multiple user nodes simultaneously. For such scenarios, 3-D coverage with multi-beam switching in azimuth as well as elevation is highly desirable to achieve higher capacity and better SIR coverage. This chapter presents a multi-sector access point array antenna for V2I communication to propagate multiple switched beams in both the azimuth and the elevation directions simultaneously to provide wireless connectivity to multiple vehicular nodes.

2.2.1 The Proposed Multibeam Multi-sector Antenna Design Schematic Model

In this section, a switched-beam octahedral structure array antenna (SBOA) depicted as Design-O1B is proposed which is synthesized using communication quality-conscious approach to provide 3-D coverage, and used as micro base station (access point) in the scenarios exemplified in Fig. 2.17. The schematic model of the proposed array antenna Design-O1B is shown in Fig. 2.18, demonstrating the desired multibeam pattern in 3-D space. The antenna structure consists of N sectors (A to H for optimized N=8), each having two $L \times M$ microstrip array antenna (MAA) (A1, A2....H1, H2), where, L and M are the number of elements along the vertical and the horizontal axis, respectively. The multiple sectors are deployed to provide 360° coverage in the azimuth region. Whereas, to provide vertical (elevation) coverage, two MAAs in the top and the bottom half of each

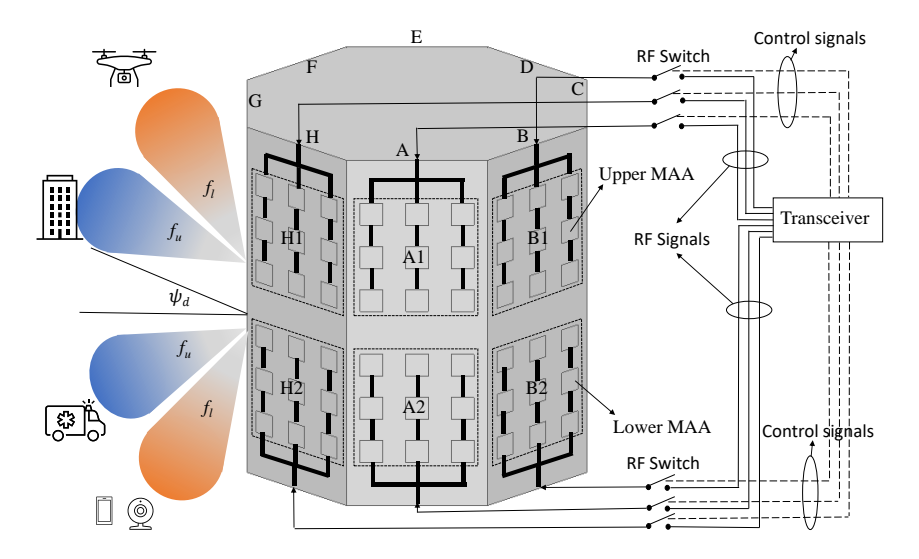


Figure 2.18: The schematic model of the proposed antenna Design-O1B.

sector are designed to direct their beams correspondingly in the upper and the lower halves of the elevation region as depicted in Fig. 2.18. Hence, the total coverage is provided in the 3-D space around the antenna through multiple beams. With switching operation, the MAAs can be individually operated. The switching can be realized by controlling a network of RF switches connected to each port [101], or a re-configurable network of power dividers with Pin diodes [102], implemented in the transceiver depicted in Fig. 2.18. The design optimization of the MAA and array feeding networks is described subsequently to achieve desired radiation patterns for 360° azimuth coverage and beam deflections in the elevation plane.

2.2.2 Analytical Model of SIR and Optimization of 360° Azimuth Coverage

For analysis, a multi-sector antenna having N sectors is assumed elevated at a height h_a from the ground, as depicted in Fig. 2.19. The highlighted area extending from ρ_i to ρ_o represents the desired azimuth coverage area (communication area) projected on the ground for a single sector- r_0 . The received signal power and SIR within this area determine communication quality. Two coordinate systems are used to analyze the coverage. First, the radiation pattern of an MAA in a sector is formulated in spherical coordinate (r, θ, ϕ') system. Second, the locations of the nodes in the communication area is represented in cylindrical coordinate (ρ, ϕ, z) system. The relationship between the two coordinates is given by

$$r = \sqrt{\rho^2 + h_a^2}, \quad \theta = \pi - \arctan(\rho/h_a), \quad \phi' = \phi,$$
 (2.16)

where $-\frac{\pi}{N} \leq \phi \leq \frac{\pi}{N}$ defines boundary of the sector- r_0 coverage. The element field pattern of a single patch element of MAA for the sector shown in Fig. 2.19 is formulated as [103].

$$E_{\phi'} = E_0 \frac{\sin\left(\frac{\pi w \sin\theta \sin\phi'}{\lambda_0}\right)}{\frac{\pi w \sin\theta \sin\phi'}{\lambda_0}} \cos\left(\frac{\pi l \cos\theta}{\lambda_0}\right) \cos\theta \sin\phi'$$
 (2.17)

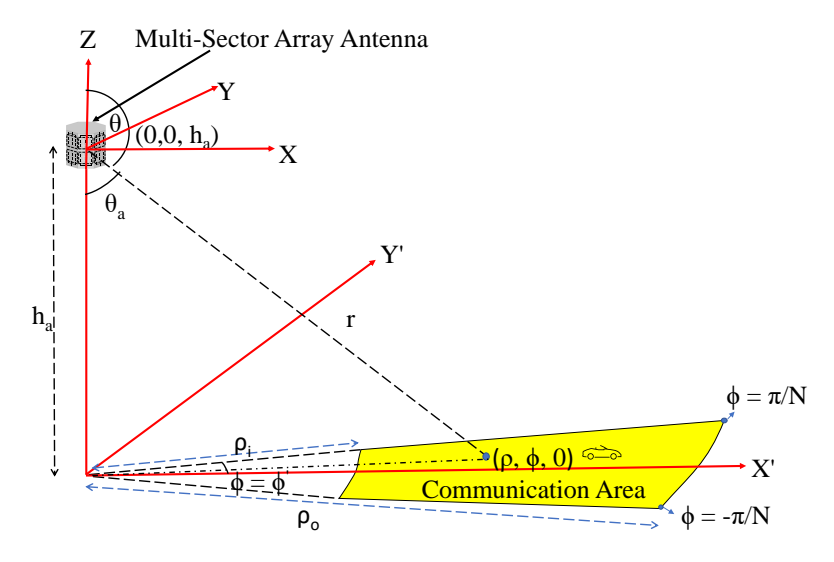


Figure 2.19: Communication coverage in one sector of the multi-sector antenna.

$$E_{\theta} = E_0 \frac{\sin\left(\frac{\pi w \sin\theta \sin\phi'}{\lambda_0}\right)}{\frac{\pi w \sin\theta \sin\phi'}{\lambda_0}} \cos\left(\frac{\pi l \cos\theta}{\lambda_0}\right) \cos\phi'$$
(2.18)

where, λ_0 is the free space wavelength, w is the width and l is the length of the patch. The total normalized element pattern, $f(\theta, \phi')$, is evaluated using (2.17) and (2.18) as

$$f(\theta, \phi') = \sqrt{\left(\frac{E_{\theta}}{E_0}\right)^2 + \left(\frac{E_{\phi'}}{E_0}\right)^2}$$
 (2.19)

Since the elements placed horizontally in MAA are responsible for beam formation in the azimuth plane, a $1 \times M$ linear array is assumed for MAA to analyze the azimuth pattern. The normalized array factor of the $1 \times M$ MAA is given by

$$AF(\theta, \phi') = \sum_{n=1}^{M} w_n \exp\left(jk(n-1)d_h \sin\theta \sin\phi'\right)$$
 (2.20)

where, k is the propagation constant, d_h is the center-to-center inter-element distance along the horizontal axis and $0 \le w_n \le 1$ represents the normalized excitation weight of the n^{th} antenna element. A binomial distribution of excitation is selected to minimize side lobe levels (SLL) for interference reduction and increase beamwidth for a broader signal coverage area; this also reduces N required to provide 360° coverage limiting the maximum antenna size. Using (2.19) and (2.20), the total normalized radiation gain pattern of the MAA is given by

$$G_t(\theta, \phi') = \left| AF(\theta, \phi') \times f(\theta, \phi') \right|^2. \tag{2.21}$$

To analyze the communication quality, the projected power distribution originated from the MAA antenna is evaluated over the communication area in z = 0 (ground) plane. The power, $P_{r_0}^i$, received in sector- r_0 from the transmitting antenna MAA-i at the node

location (ρ_r, ϕ_r, z_r) is evaluated using [104]

$$P_{r_0}^i(\rho_r, \phi_r, z_r) = \alpha^2 10^{\frac{x}{10}} P_t G_0 G_t[\theta(\rho_r, \phi_r, z_r), \phi'(\rho_r, \phi_r, z_r)] \times G_r \left(\frac{\lambda_0}{4\pi r(\rho_r, \phi_r, z_r)}\right)^{\eta}$$
(2.22)

where α^2 and $10^{\frac{x}{10}}$ correspond to shadowing and multipath fading effects, respectively, where x is a zero mean gaussian random variable and α^2 follows Rayleigh distribution with unit mean value, P_t is the transmitted power, G_0 is the peak gain of the transmitting sector array, η is the path loss factor (for free space propagation $\eta = 2$ is chosen) and $G_t[\theta(\rho_r, \phi_r, z_r), \phi'(\rho_r, \phi_r, z_r)]$ is the normalized gain in the direction of the observation point (ρ_r, ϕ_r, z_r) . G_r is the receiver gain and is assumed to be unity. The P_tG_0 in (2.22) represents the EIRP having maximum allowed limit 4 W.

Since the desired signal power is received from the MAA belonging to the same sector- r_0 , the signal power received in the sector- r_0 is $P_{r_0}^{r_0}$ and evaluated using (2.22) for $i=r_0$. Furthermore, the interference power, $P_{r_0}^i$, received in the sector- r_0 from the other sector antennas MAA-i, where $i \neq r_0$, can be evaluated using the same formulation using (2.22) by replacing ϕ' with $\phi' - \frac{2\pi i}{N}$. However, the immediate neighboring MAAs are not preferred to operate simultaneously at a common frequency band, otherwise, a high co-channel interference is caused. Therefore, only the MAAs placed in the alternate sectors are assumed as a source of interference for this model of azimuth coverage. Thus, the average received SIR, γ_{r_0} , at the observation point (ρ_r, ϕ_r, z_r) in sector- r_0 is calculated as

$$\gamma_{r_0}(\rho_r, \phi_r, z_r) = \frac{P_{r_0}^{r_0}(\rho_r, \phi_r, z_r)}{\sum_{i \in N_0, i \neq r_0} P_{r_0}^i(\rho_r, \phi_r, z_r)}$$
(2.23)

where N_a denotes the set of the MAAs of alternate sectors causing the interference in the current sector- r_0 .

Quality-communication Coverage Area Definition

In this work, the coverage area definition is based on received signal power and SIR to meet a defined quality of communication in terms of BER. Whereas in the literature [98], the communication area is evaluated only based on received power sensitivity P_{th} of the node, which does not represent any assurance of reliable communication quality when interference is present. In contrast, the proposed definition of the coverage area denoted as Quality-communication Coverage Area (QCA) takes into account the SIR threshold, γ_{th} , as well as the P_{th} together for a targeted maximum BER performance within the azimuth coverage area. Hence, the QCA is the coverage over which both SIR and received power are greater than their respective thresholds. To note that, the value of γ_{th} can be chosen corresponding to the target BER limit for reliable communication using a specified modulation scheme. Mathematically, the QCA for azimuth coverage is defined as

$$QCA = \text{Area } \forall (\rho_r, \phi_r) : \{ [\gamma(\rho_r, \phi_r, 0) > \gamma_{th}] \cap [P(\rho_r, \phi_r, 0) > P_{th}] \}$$
 (2.24)

where P and γ are the received power and the SIR values over the communication area and determined using (2.22) and (2.23), respectively.

Optimization of N and M using QCA

As apparent from (2.20), (2.22), and (2.23), the QCA value for the multi-sector antenna depends upon the antenna design parameters, N and M. An optimization objective to synthesize a binomial linear antenna array to maximize the QCA is formulated as:

$$\max_{N,M} QCA$$

$$s.t. \ \forall \rho_r \in [\rho_i, \rho_0], \forall \phi_r \in [-\pi/N, \pi/N]$$

$$N \leq 10, \ M \leq 4,$$

$$\rho_i = h_a \times \tan(90^\circ - 0.5\Theta_e), \ \rho_0 = 20\text{m}$$

$$(2.25)$$

where the limits $N \leq 10$ and $M \leq 4$ are applied to restrict the overall dimension of the multi-sector antenna. The desired coverage limits ρ_i and ρ_o are set based on the half power beamwidth (Θ_e) of the MAA in the elevation plane and the required P_{th} value, respectively. To solve the optimization problem (2.25), the MAA gain pattern of (2.21) is synthesized by parametric variation of the design variables N, M using MATLAB, and optimum values are obtained.

Analytical Results for Optimum N and M using QCA Definition

The QCA is evaluated using (2.24) for various N and M for optimization. Since the lowest possible data rate exists at the boundary of the coverage area, the BPSK modulation scheme is chosen to define the threshold for SIR in the analysis. The required γ_{th} limit for the target BER performance of 10^{-5} is theoretically given by $\gamma = 9.5$ dB for BPSK. However, a tolerance of 0.5 dB is considered in the synthesis process and $\gamma_{th} = 10$ dB is assigned. The limit on P_{th} can be as low as -67 dBm in WiFi applications for low data rates; however, $P_{th} = -37$ dBm is considered to support the nodes with higher sensitivity levels and slow mobility. The analytically obtained parametric study results of percentage QCA for various array sizes of 1×2 (M = 2), 1×3 (M = 3), and 1×4 (M = 4) versus N are presented in Fig. 2.20. The other parameter values are set as $l_p = 11.8$ mm, $w_p = 13$ mm, $h_a = 4$ m and $d_h = 0.5\lambda_0$ for the MAA where λ_0 is calculated at 5.8 GHz. Since the $1 \times M$ MAA radiating horizontally has one element in vertical, $\Theta_e \sim 90^{\circ}$ is considered, correspondingly $\rho_i = h_a \times \tan(45^\circ) = 4$ m. The results in Fig. 2.20 indicate that the 1×2 MAA achieves better QCA coverage than 1×3 and 1×4 MAAs. The QCA increases with N, however, the rate of increase is low for higher N. For the 1×2 MAA, the achieved QCAis maximum at N=8. Hence, the optimal N=8 and M=2 are obtained as the solution of optimization problem (2.25). To further gain insight into the obtained QCA and the effect of parameters N and M, the evaluated QCA patterns (SIR distribution coverage in 360° for all the sectors) are depicted in Fig. 2.21. It is apparent from the coverage

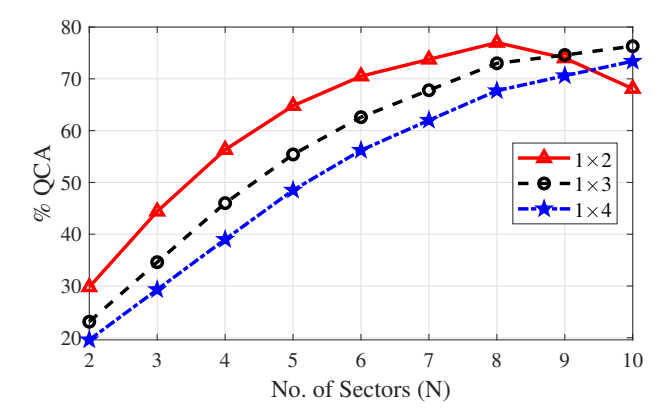


Figure 2.20: The QCA versus number of sectors (N) for various $1 \times M$ MAA.

patterns that the QCA coverage for N=8 sector design with 1×2 MAA is better among other $1\times M$ arrays and also higher compared to the N=6 and N=10 sector designs. This is because, for a fixed M, the lower N does not provide sufficient power coverage in individual sector area to cover 360° ; in contrast, the higher N increases interference from the neighboring sectors causing a reduction in the SIR coverage. Since the lower M implies a wider radiated beam from the sector, this can provide wider power coverage as compared in Fig. 2.21(a, b, c) where 1×2 array has maximum QCA. However, the same lower M can contribute to a higher interference for high N design, causing a reduction in QCA as demonstrated in Fig. 2.21(g, h, i) where coverage is reduced for 1×2 array. Therefore, N=8 sectors with M=2 array is analytically found as the best solution to provide azimuth communication range of $\rho=4\,\mathrm{m}$ to $17.4\,\mathrm{m}$ and achieve 360° azimuth QCA coverage.

The MAA Design Optimization for Elevation Coverage

Once the number of sectors is known, the MAA is designed to optimize the elevation coverage, which is shaped by the vertical elements. L represents the number of vertical elements in the MAA. The patch columns of the proposed MAA are integrated using series feed lines as shown in Fig. 2.22(a); this controls the beam pattern in the elevation. Conventionally, the series feed array antennas are used for only broadside beam coverage [105] while in the proposed design a beam tilt is obtained at the operating frequency by changing feed length. Furthermore, due to frequency dependent beam squint phenomena present inherently in the series feed network, which is otherwise considered as a limitation [106], is exploited well by the proposed design to obtain maximum coverage in the elevation and enhanced SIR.

To synthesize elevation pattern, a higher L value seems a favourable choice to achieve a narrow beam in the elevation to reduce interference. However, this leads to a bulky antenna with a large vertical dimension which is not preferred in the targeted applications. Furthermore, a low L is expected for optimal elevation coverage after observing the recorded result of M=2 in Section 2.2.2. Therefore, although a range of L was considered in the optimization synthesis process, the parametric results of only L=3 MAA are shown

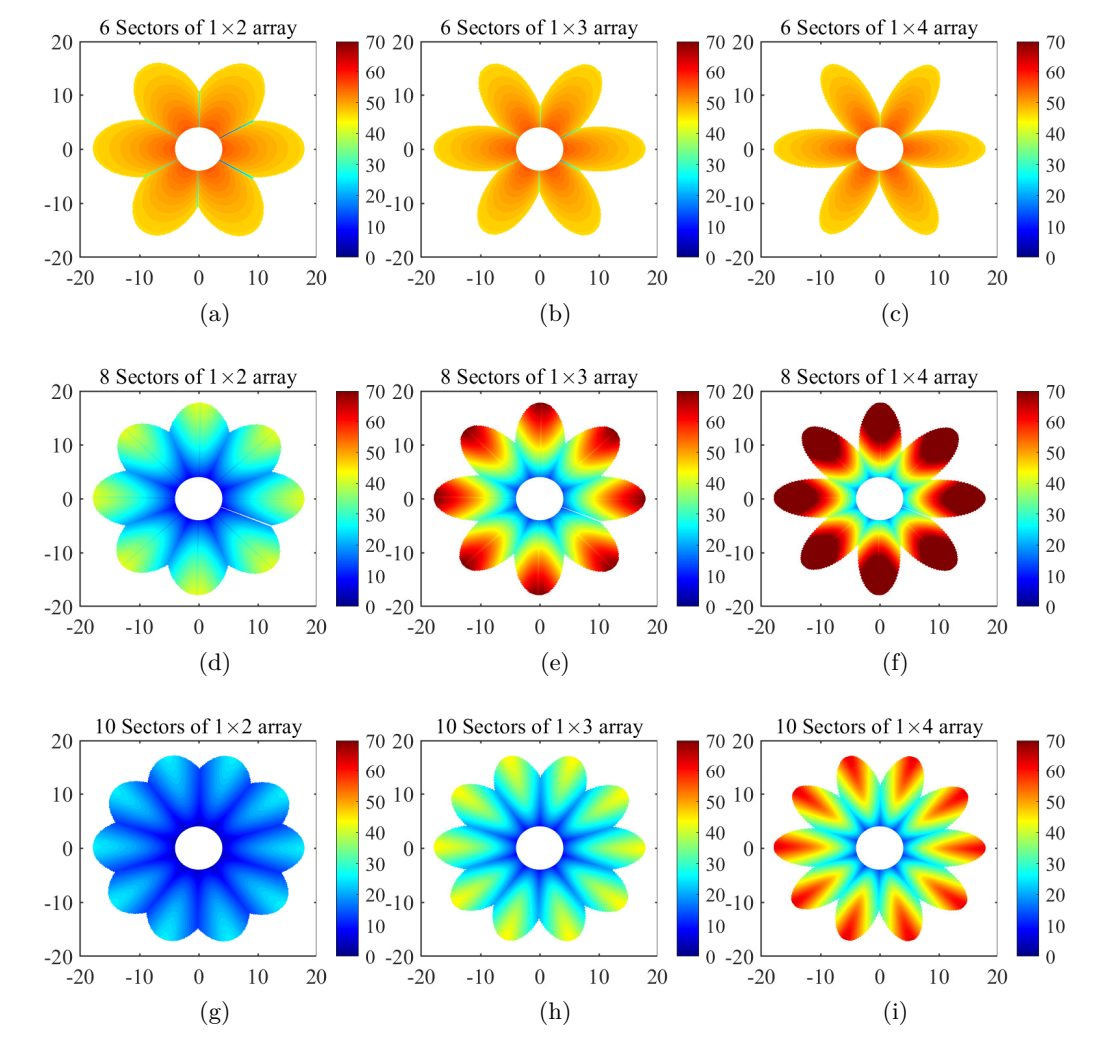


Figure 2.21: The SIR distribution and QCA patterns for $1 \times M$ array and (a, b, c) N = 6 (d, e, f) N = 8 (g, h, i) N = 10.

here for brevity. Since the optimization for the series feed array for elevation coverage is analytically cumbersome, it is performed by simulations by adopting the hybrid approach using HFSS EM software.

To design the array column, the series feed lines are meandered in U shape [107] as shown in Fig. 2.22(a) to reduce the height of the array and the center-to-center inter-element distance (d_v) along the vertical axis. The d_v is kept less than $0.5\lambda_0$ to create a traveling wave like structure, resulting in increased impedance bandwidth [108, 109]. In addition, the U shape feed line length, l_s , is optimized to provide a progressive phase shift, δ , between the array elements vertically so that the beam is formed tilted towards the feed direction (by an angle ψ_d from the horizon as depicted in Fig. 2.18) in the elevation plane. The required δ is evaluated at the operating frequency using $kd_v cos \psi_d + \delta = 0$. The parametric analysis of various series feed parameters are conducted, which are constrained by the relations due to geometry defined in Fig. 2.22(a) as

$$l_s = 2l_{s_1} + l_{s_2} + 2l_{s_3}; d_v = 2l_{s_1} + l_{s_2} + l_p (2.26)$$

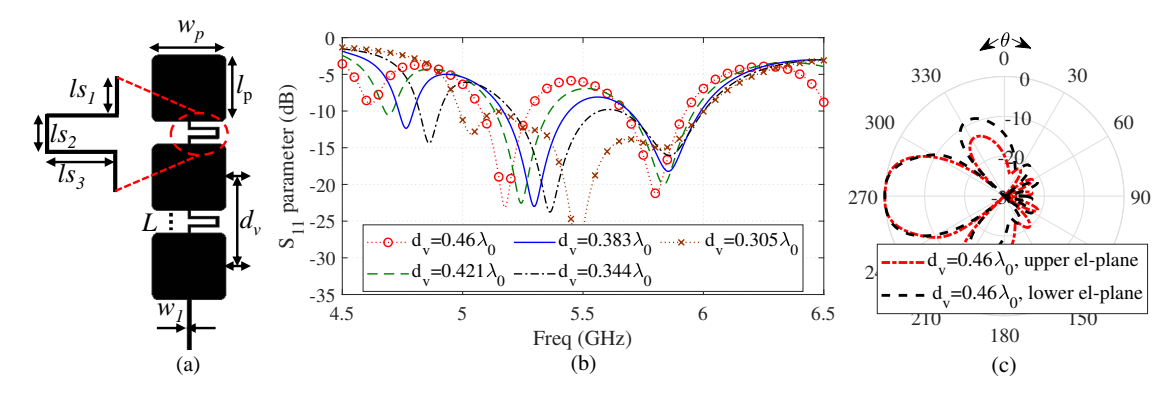


Figure 2.22: For elevation coverage (a) L element patch column (b) matching for various d_v and L=3 (c) upper and lower elevation plane radiation pattern at 5.8 GHz.

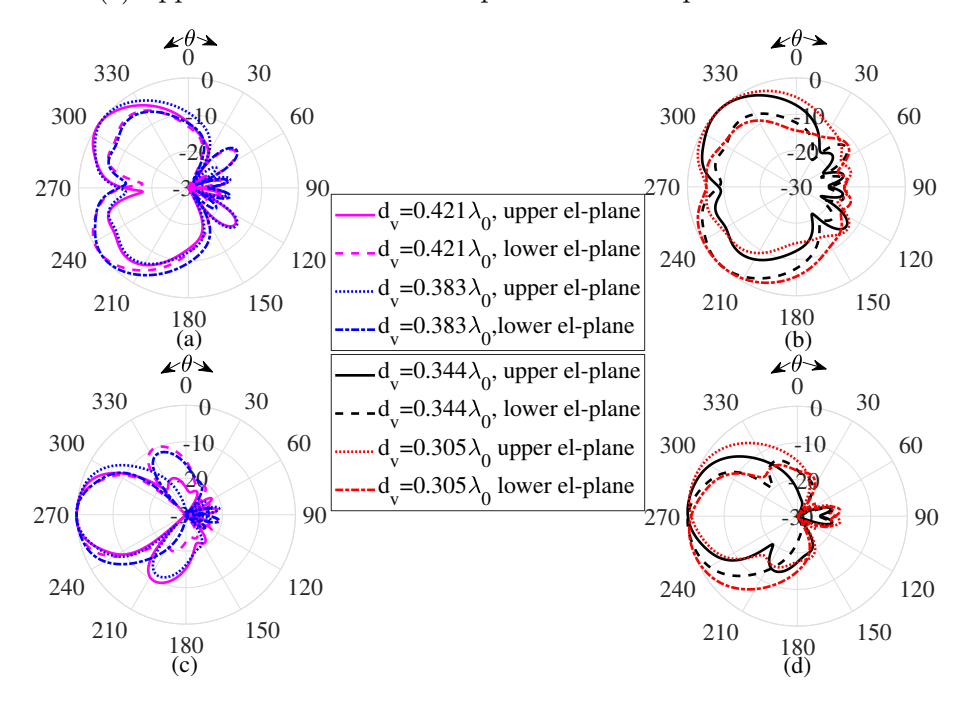


Figure 2.23: Elevation plane radiation pattern of the two MAA of a sector for various d_v (a),(b) 5.15 GHz and (c),(d) 5.8 GHz.

This by substitution results in the design constraint as

$$l_s = d_v - l_p + 2l_{s_3}, (2.27)$$

where, $l_{s_2}=2$ mm is set as minimum value due to fabrication constraint and $l_p=11.8$ mm is the optimized patch length both are fixed. For analysis, $l_{s_3}=1$ mm and $d_v=0.5\lambda_0$ are initialized which gives $l_s=0.5\lambda_0-9.8$ mm and subsequently these parameters are varied for optimization. However, due to design constraint (2.27), a change in d_v corresponds to a defined change in the l_s value when l_{s_3} is fixed. Therefore, d_v remains the only design parameter for optimization. Initially, the d_v is varied for good impedance matching and broadside gain maximization at 5.8 GHz and the best value $d_v=0.46\lambda_0$ and $l_s=14$ mm are obtained in the initial step. For these values, the corresponding S_{11} and radiation pattern results are shown in Fig. 2.22(b) and 2.22(c) for $d_v=0.46\lambda_0$. The radiation patterns are evaluated for the two MAA (upper elevation and lower elevation) consisted in

a sector which are fed from opposite sides as depicted in Fig. 2.18 and the total coverage jointly achieved by the two arrays is observed. In the next step, the $l_s=14$ mm is kept constant and d_v is varied from $0.46\lambda_0$ to $0.305\lambda_0$ which correspondingly vary l_{s3} following (2.27). The value $d_v < 0.305\lambda_0$ is not possible due to fabrication constraints in the laboratory. The parametric variation of S_{11} and radiation pattern of the elevation plane are demonstrated for various d_v in Fig. 2.22(b) and Fig. 2.23, respectively. The plots indicate that a higher impedance bandwidth is achieved for lower d_v value, and the desired bandwidth in frequency range 5-6 GHz is achieved for $d_v=0.305\lambda_0$ and $l_s=14$ mm. Moreover, the upper and the lower beam jointly gives wider elevation coverage at 5.15 GHz and 5.8 GHz as shown in Fig. 2.23. Therefore, the $l_s=14$ mm and $d_v=0.305\lambda_0$ values are selected corresponding to a high impedance bandwidth and enhanced elevation coverage jointly by the two beams of the vertical arrays. This results in the 3-D coverage which can achieve higher beam tilts favorable for the nodes located at extreme altitudes with respect to the access point height.

3-D Coverage with SBOA Antenna

Although the M=2 is analytically obtained in Section 2.2.2 as the optimal choice for azimuth coverage, M=3 is also considered in further investigation using simulation to verify the analytical results. Therefore, the design optimization through simulations and radiation characteristics are investigated for three MAAs having sizes 3×2 , 2×3 , and 3×3 . The corresponding octahedral antenna structures are depicted in Fig. 2.24. The MAAs of the same sector are fed from the top and bottom edges, respectively, and the layout of the proposed feeding networks are shown in the inset of Fig. 2.24 for the three designs. For feeding, the patch columns are integrated horizontally using a T-junction corporate feeding network to implement a binomial distribution of the excitation coefficients horizontally. For the 3×2 MAA shown in Fig. 2.24(a), the two patch columns are fed using one single stage equal power divider to obtain [1:1] excitation. Whereas, for the 2×3 and 3×3 MAAs, the feeding network designs consist of three corporate divider stages to implement [1:2:1] coefficient as illustrated in Fig. 2.24(b) and Fig. 2.24(c). The first and second stages use three equal splitting networks to realize a one-to-four divider with equal output coefficients. In the third stage, the two middle feed lines are combined to double the feeding coefficient of the central patch column to realize the desired binomial excitation [1:2:1]. The design realization of the proposed antenna is presented next.

Design Realization and Simulation Results

The proposed SBOA is designed in commercial CAD software Ansys HFSS. Each sector with two MAAs is realized in PCB technology on a dual-sided FR4 substrate ($\epsilon_r = 4.4$, tan $\delta = 0.02$) having a thickness and copper deposition of 1.524 mm and 35 µm, respectively. The SBOA is designed to achieve specifications discussed in Section 2.2.2. The MAA and its feeding network with parameters defined in Fig. 2.24 are optimized. The obtained design parameter values of the antennas are listed in Table 2.4. The separation between

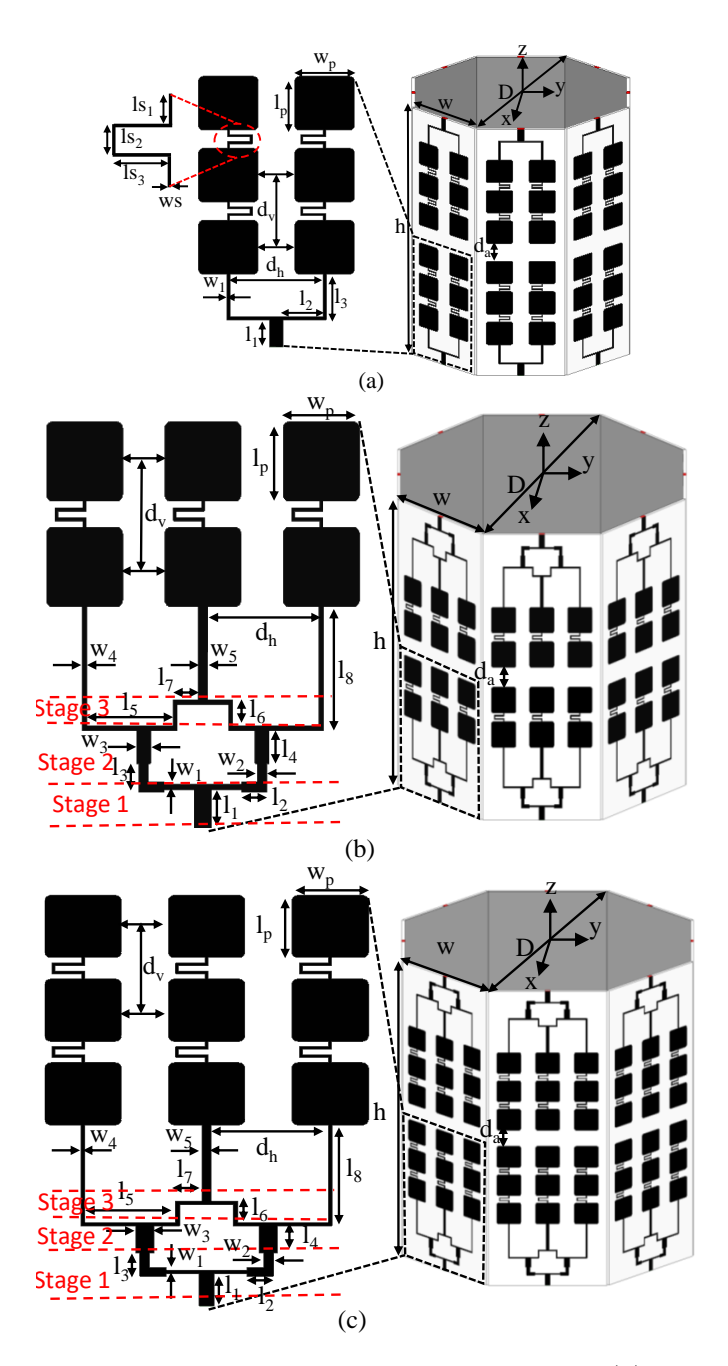


Figure 2.24: The Design-O1B and feed network of the MAA (a) 3×2 MAA (b) 2×3 MAA (c) 3×3 MAA.

the two MAAs of a sector is $d_a = 9.14$ mm evaluated to obtain isolation > 20 dB. The three designs are simulated, and their performances are evaluated. The simulated S-parameter results are shown in Fig. 2.25. The results are presented for the four adjacent MAAs A1, A2, B1, B2 and their corresponding MAAs, as defined in Fig. 2.18, are fed with ports 1, 2, 3, and 4, respectively. The simulated 10 dB bandwidth is 1 GHz (5 GHz to 6 GHz) for all the MAA's. The isolation, $|S_{21}|$, between A1, A2 (the two MAAs belonging to the same sector) is better than 27 dB, 23 dB and 26 dB, respectively for the 3×2 , 2×3 , and 3×3 designs. Moreover, the isolation, $|S_{31}|$ and $|S_{41}|$, between the MAAs of the adjacent sectors is better than 30 dB for the three designs. The simulated gain versus frequency

			Array	y]	ls_1 1	$\mathbf{s_2}$	ls_3	ws	\mathbf{w}_1	\mathbf{w}_2	w ₃	w_4	w_5	l_1	l_2	l_3		
			3×2	0	.75 2	2.5	5	0.5	0.7	-	-	-	-	6	10.06	9.3		
		Ī	2×3	0	.75 2	2.5	5	0.5	0.7	1.6	5 2.5	0.7	1.65	6	4.415	2.815		
			3×3	0	.75 2	2.5	5	0.5	0.7	1.6	5 3.14	0.7	1.65	6	4.44	4.44		
	Array	l_4	l_5	l_6	l_7	1	8	l_p	.	\mathbf{w}_{p}	d_v	$ \mathbf{d}_h $	d_a		w	h	D	
	3×2	-	-	-	-	-	•	11.	.8	13	15.8	21	9.144	43	3.144	127.944	112.71	
	2×3	5	15.4	4	4.45	18.	.93	12	.1	13.5	16.1	21	9.144	64	.644	133.334	167.6	
	3×3	5	15.4	6	4	18.	.93	11.	67	13	15.67	21	9.144	64	1.144	162.94	167.6	
0	000000000000000000000000000000000000000	6						- 0	-000) (1000000)	0	100000	9090000					
-10	_	P	90000 ₀₀	<i>6</i> 90				green and the second		-	-10	-	-96	good G	900000	æ	20000000000000000000000000000000000000	
<u>m</u> -20	_			8		ω	90			_	<u>m</u> -20	-			-96	8		
p) s				1	4						S parameters (dB) -30 -40 -50					\ \ \ \ \ \ \ \ \ \ \ \ \ \ \ \ \ \ \		
leter	and the second		-	ı[`\						nete			- 、		-\L		× .
-40		7	,A	p ^a	BBQ.	1	/	, DE	Q D D	0000	40 aran		Pagagad.	P	`\ -	_ ([- V
S parameters (dB) -30 -40 -50	200		A A	_	N _E	BBB		a ^e	`	` _	od -50	}		4	ø ^{e⊕}	N POOD	88 ₈ _	
-60		_s	Sim.		- S ₂₁ Si	m. –	-	S ₄₁ S	im.		-60					S ₂₁ Sim	S ₄₁ Si	im.
	0	S	22 Sim. •		S ₃₁ Si	m.					70		o S	22 S	m. – –	• S ₃₁ Sim.		
-70 ^L 4.	5	5			5.5			6		6.5	-70 4.	5	:	5		5.5	6	
			Fr		ency (C	Hz)									Frequ	ency (GHz)	
0.5					(a)			,			10 [(b)		
-10		99																
			g00000000	200	e e	0000	ggg		سرر		₹ 7.5				11/			1
⊕ -20				Ì	- P						Ð 5	-	<u></u>	1			1	` `
-30				4		<u> </u>					.ig 2.5		1					1
S parameters (dB) -20 -40 -50 -50		>. /	N / J	26 ₈	1		- ~		. –		Realized Gain (dBi)	,	/ /i					
ned -50	annes	Z			A Page	í	`		-	, L	o o	John St.	/;			3×2 MPA		
-60			Sim.					S ₄₁ Si	m.	X	-2.5	/,	"			2×3 MPA		
	0	S	Sim		S ₃₁ Si	m.				• 1						3×3 MPAA	L	
-70 4.5	5	5			5.5			6		6.5	-5 ¹	5	4	5		5.5	6	
			Fre		ency (G	Hz)									Frequ	ency (GHz)	
					(c)											(d)		

Table 2.4: The SBOA antenna design parameters (dimensions in mm)

Figure 2.25: Simulated S-parameter results between MAAs A1, A2, B1, B2 of the SBOA (a) 3×2 MAA (b) 2×3 MAA and (c) 3×3 MAA (d) Gain vs Frequency plot.

variations are plotted in Fig. 2.25(d). The maximum gain variation shown in the desired frequency range (5.15 – 5.825 GHz) is 3.171 dBi, 1.3 dBi, and 3.173 dBi, respectively for the three designs. Fig. 2.26 shows the normalized radiation patterns of the three designs. The azimuth pattern is shown for the cut of inclination ψ_d containing the direction of maximum radiation. The radiation characteristic parameters are summarized in Table 2.5 for comparison. The minimum azimuth plane beamwidth is 55°, 40°, and 39° for the 3×2 , 2×3 , and 3×3 designs, respectively. Therefore, to achieve 360° azimuth coverage, minimum of eight sectors for 3×2 MAA, and nine sectors for both 2×3 and 3×3 MAA are required. The overall minimum size of the SBOA with 3×2 design is 11.2×12.8 cm². Whereas, if the 2×3 design is employed, the SBOA size becomes 16.7×13.3 cm² and for the 3×3 design it is 16.7×16.3 cm². Therefore, the SBOA antenna design using 3×2 MAA has the smallest size among the three and shows N = 8 which is identical to analytically optimized value. In addition, the 3×2 MAA has lower beam variations in the

 $3 \times 2 \text{ MAA}$ Frequency (GHz) Max Gain Beam tilt BW (Degrees) SLL (dBi) Elevation Azimuth (dB) (ψ_d) 66.81 5.15 5.4 59.24-11.565.35 7.0 44° 54.46 55.46 -12.855.7258.2 24° 51.9358.99 -14.87 $5.82\overline{5}$ 14° 55.8459.48 8.0 -18.11

Table 2.5: Simulated Radiation pattern results of the SBOA antennas

Frequency		$2 \times 3 \text{ MAA}$							
(GHz)	Max Gain	Beam tilt	BW (D	BW (Degrees)					
	(dBi)	(ψ_d)	Elevation	Azimuth	(dB)				
5.15	6.9	48°	57.22	41.12	-12.2				
5.35	8.2	38°	52.71	43.34	-17.57				
5.725	7.5	-12°	90.85	41.84	-14.32				
5.825	7.4	-14°	92.69	40.27	-14.58				

Frequency	$3 \times 3 \text{ MAA}$							
(GHz)	Max Gain	Beam tilt	BW (D	BW (Degrees)				
	(dBi)	(ψ_d)	Elevation	Azimuth	(dB)			
5.15	6.3	42°	61.05	44.02	-13.08			
5.35	8.2	48°	49.40	40.51	-13.38			
5.725	9.1	32°	65.10	39.78	-12.2			
5.825	8.7	28°	72.86	39.62	-17.87			

elevation plane versus frequency and provides broader beam coverage in the azimuth plane compared to the 2×3 and the 3×3 MAA as indicated by the results in Table 2.5 which corroborate the analytically obtained results of Fig. 2.21(d, e, f). Moreover, the change in ψ_d with frequency in the elevation plane for 3×2 MAA is most desirable. Thus, to accomplish the specifications detailed in Section 2.2.2, the SBOA antenna designed using 3×2 MAA is a better choice in terms of smaller size, desired radiation pattern, and beam tilt characteristics compared to the other two MAAs; hence, selected here as the proposed SBOA antenna for further investigation.

2.2.3 Implementation and Radiation Pattern Measurements

The proposed SBOA antenna with 3×2 MAA shown in Fig. 2.24(a) is experimentally verified. Using MITS PCB prototyping machine, eight sectors each with two MAA copies are fabricated and assembled together. The final prototype of the proposed antenna is shown in the inset of Fig. 2.27(a). The antenna is characterized in an anechoic chamber with the measurement setup shown in Fig. 2.27. In the measurements, a linearly polarized horn is used as the reference antenna. The S-parameter and pattern measurements are performed using keysight's PNA-L VNA. The measured 10 dB bandwidth of the proposed SBOA antenna is in the frequency range of 4.94 GHz to 5.94 GHz covering the whole WLAN frequency band, as shown by the measured S-parameter results included in Fig. 2.28. The results indicate that the measured isolation $|S_{21}|$ between A1 and A2 is > 26 dB. Moreover, the measured isolations, $|S_{31}|$ between A1 and B1 is > 29 dB and $|S_{41}|$ between A1 and B2 is > 31 dB. Hence, the measured S-parameter results are in fair agreement with the simulation results. To corroborate the radiation pattern results,

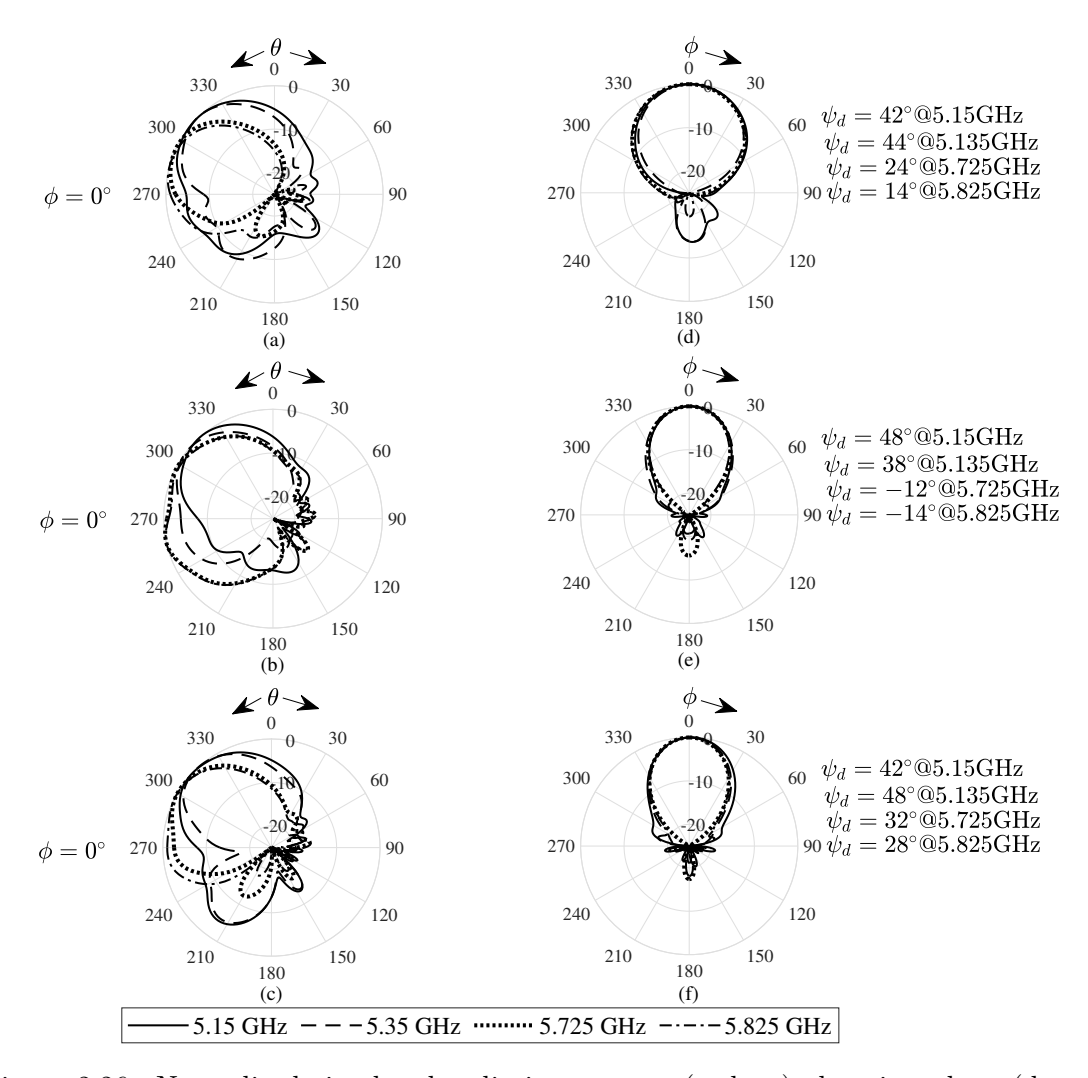


Figure 2.26: Normalized simulated radiation pattern (a, b, c) elevation plane (d, e, f) azimuth plane patterns of 3×2 , 2×3 , and 3×3 MAA respectively.

the measured normalized elevation and azimuth radiation patterns are plotted for various frequencies in Fig. 2.29 and Fig. 2.30, respectively.

A slight deviation between the simulated and the measured results is attributed to the fabrication and measurement tolerances. The measured radiation performance of the proposed SBOA antenna is summarized in Table 2.6. The measured results show an average BW achieved by one MAA in the elevation and azimuth plane is 50° and 54°, respectively. Moreover, the achieved beam deflection in the elevation plane increases from 10.8° to 46.8° when the operating frequency band is lowered from 5.825 GHz to 5.15 GHz. The obtained performance characteristics indicate that the proposed SBOA is a suitable antenna for 3-D coverage access point applications. To evaluate the communication quality, an interference measurement study is conducted, and results are discussed subsequently.

2.2.4 Received RF Power Measurements and SIR Evaluations

The outdoor measurement setup to evaluate the performance of 3-D coverage by the proposed antenna in terms of SIR (γ) is depicted in Fig. 2.27. The SBOA antenna as an

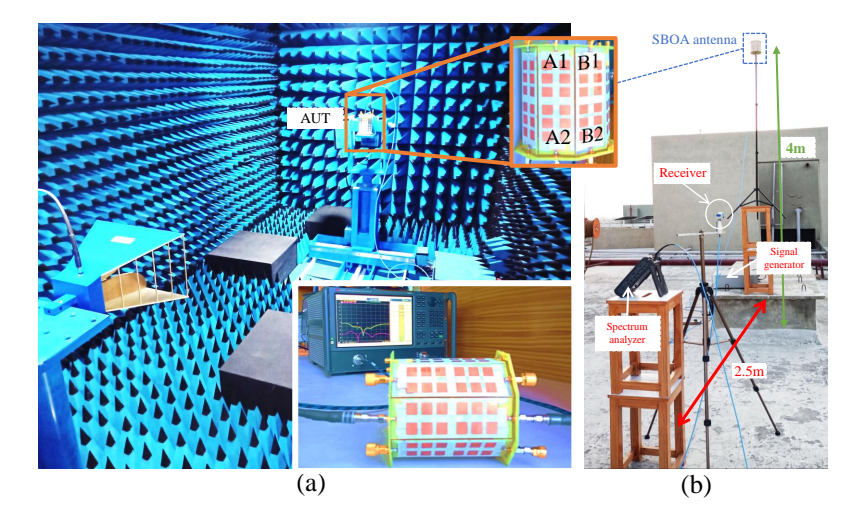


Figure 2.27: Measurement setup of the proposed SBOA antenna (a) Anechoic chamber characterization (b) SIR measurements in open space.

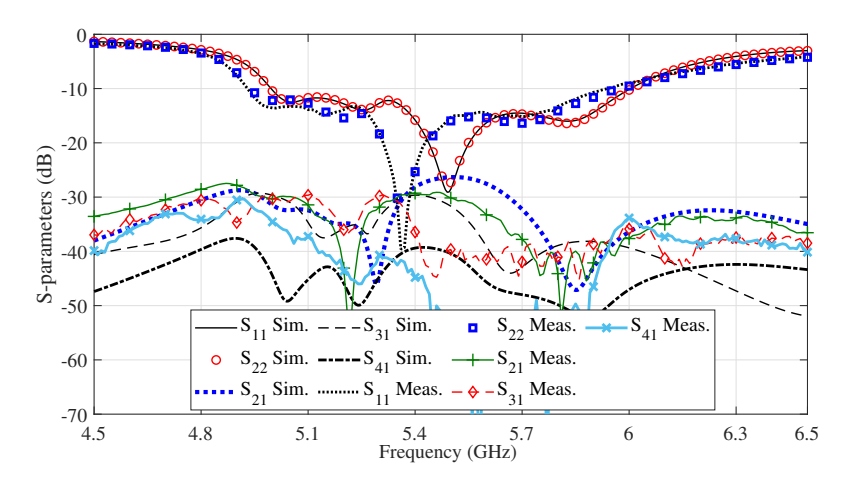


Figure 2.28: Measured and simulated S-parameter results of the the proposed SBOA antenna with 3×2 MAA.

access point transmitter is installed at 4 m height above ground and fed using RF signal generator (Agilent Technologies E8257D). The user node (receiver) antenna is connected to the Keysight's N9915A handheld spectrum analyzer (SA). The transmitting power of the signal generator is set at 25 dBm, and the received signal strength (P_{Rx}) is measured using the SA.

Measurements of γ in Azimuth Plane on the Ground

The user node is placed on the ground within sector-A and moved away from the SBOA antenna for 3 m $\leq \rho \leq$ 20 m range at angles $\phi = 0^{\circ}$, 10° , and 20° , the setup is demonstrated in Fig. 2.27(b). The projected P_{Rx} from the MAA (A2) covering the azimuth plane and the interference power from the MAAs (C2 and G2) of the alternate sectors are measured at 5.8 GHz. The measured signal power and the evaluated γ values are plotted against ρ in Fig. 2.31(a) and Fig. 2.31(b), respectively. The measured transmission range ρ_o satisfying both, $P_{th} = -37$ dBm and $\gamma_{th} = 10$ dB together, is achieved as 16.25 m, 15.5 m, and

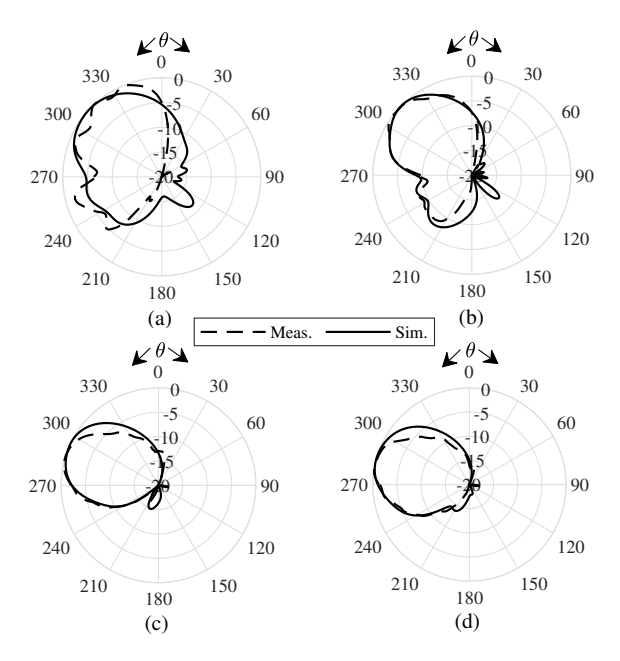


Figure 2.29: Normalized elevation radiation pattern of A1 of the SBOA with 3×2 MAA at (a) 5.15 GHz (b) 5.35 GHz (c) 5.725 GHz (d) 5.825 GHz

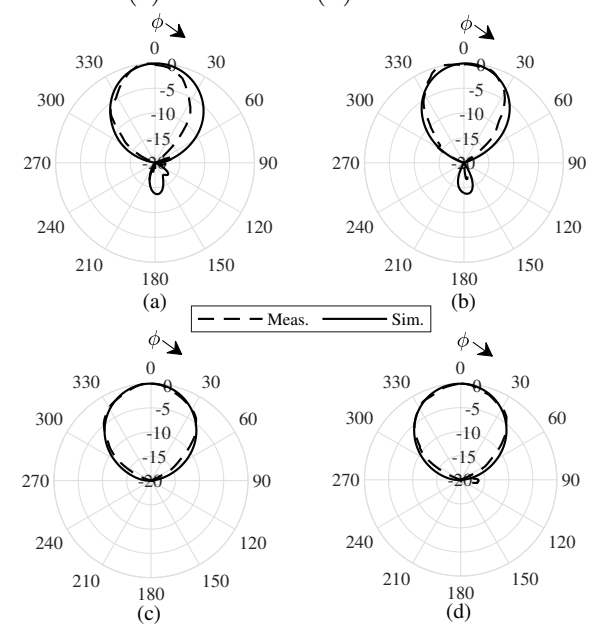


Figure 2.30: Normalized azimuth radiation pattern of A1 of the SBOA with 3×2 MAA at (a) 5.15 GHz (b) 5.35 GHz (c) 5.725 GHz (d) 5.825 GHz

14 m at $\phi = 0^{\circ}$, 10° , and 20° , respectively. The measured results corroborate with the analytically obtained range observed in Fig. 2.21 of Sec-2.2.2.

Measurements of γ in the Vertical Plane

To evaluate the coverage performance for the nodes distributed vertically, the receiver is moved above the ground at a height (h_{Rx}) in a range 0 m $\leq h_{Rx} \leq 25$ m within the sector-A for various distances from the SBOA antenna at $\rho = 4$ m, 10 m, 15 m, and 19 m; the measurement setup is shown Fig. 2.27(c). The measurements are carried out at the

Frequency	$3 \times 2 \text{ MAA}$						
(GHz)	Max Gain	Beam Tilt	Beam	Beamwidth			
	(dBi)	ψ_d	Elevation	Azimuth	(dB)		
5.15	4.8	46.8°	63.2°	43.2°	-15.8		
5.35	7.45	36°	54°	52.2°	-16.57		
5.725	7.85	18°	41.4°	59.4°	-19.37		
5.825	7.4	10.8°	41.4°	61.2°	-16.2		

Table 2.6: Measured radiation performance of the proposed antenna

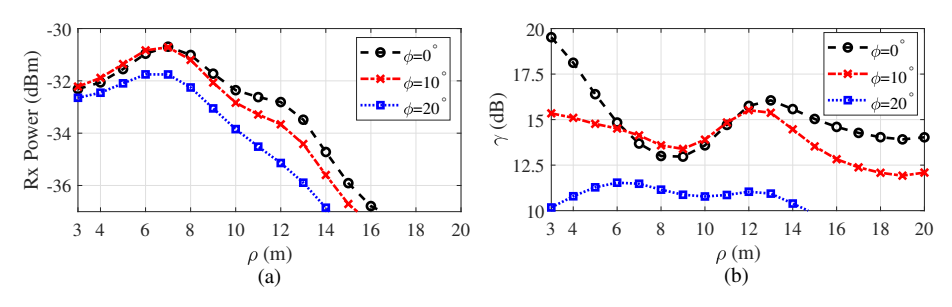


Figure 2.31: Measured results of (a) P_{Rx} from A2 and (b) γ versus ρ in sector-A at 5.8 GHz.

lower 5.25 GHz and the upper 5.8 GHz bands to evaluate the titled beam coverage. The

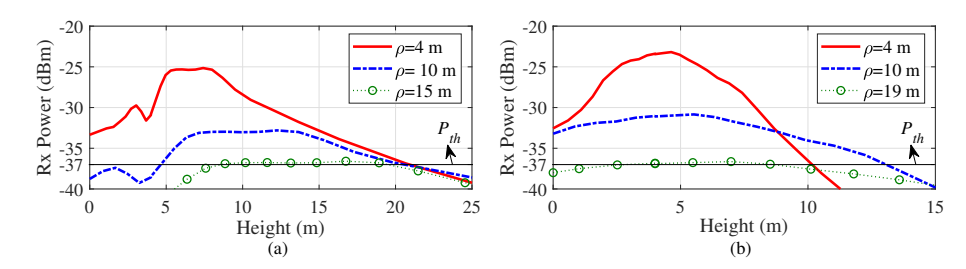


Figure 2.32: P_{Rx} value in sector-A from upper MAA (A1) at (a) 5.25 GHz (b) 5.8 GHz.

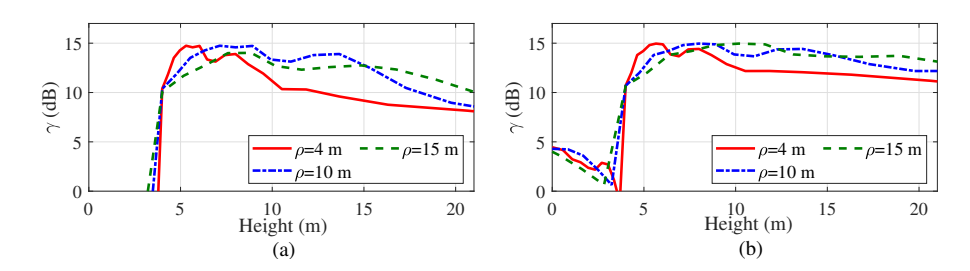


Figure 2.33: γ value in sector-A (signal from A1) with respect to interference from (a) C1 and G1 (b) C2 and G2 at 5.25 GHz.

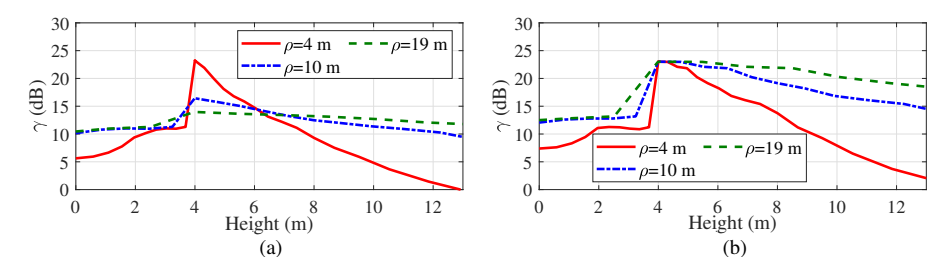


Figure 2.34: γ value in sector-A (signal from A1) with respect to interference from (a) C1 and G1 (b) C2 and G2 at 5.8 GHz.

measured P_{Rx} distribution versus h_{Rx} is shown in Fig. 2.32 for the upper MAA A1 as transmitter at the two frequencies. The measurements indicate that the maximum range of ρ within sector-A where the azimuth coverage satisfies $P_{Rx} \geq P_{th}$ is observed as 15 m and 19 m at 5.25 GHz and 5.8 GHz, respectively, therefore, Fig. 2.32 is plotted considering these upper ρ limits. Fig. 2.32 (a) shows that the elevation range h_{Rx} at 5.25 GHz where $P_{Rx} \ge P_{th}$ is 0-20.6 m, 4.76-20 m and 8.8-20 m at $\rho = 4$ m, 10 m, and 15 m, respectively. Similarly, at 5.8 GHz, the elevation range h_{Rx} noted from Fig. 2.32 (b) is 0-10 m, 0-13 m, 2.5-8.5 m, at $\rho=4$ m, 10 m and 19 m, respectively. The corresponding γ results are plotted in Fig. 2.33 and Fig. 2.34 by measuring the signal emanating from the A1 of the intended sector-A and the interference generated by the MAAs of alternate sectors, upper (C1 and G1) and lower (C2 and G2), employing frequency re-use. The results indicate that a higher elevation coverage range satisfying $(\gamma > \gamma_{th}) \cap (P_{Rx} \geq P_{th})$ is obtained when C2 and G2 are the interfering MAA's instead of C1 and G1. The elevation coverage range, as depicted in Fig. 2.33(b), is 4-20.6 m, 4.76-20 m and 8.8-20 m respectively for $\rho = 4$ m, 10 m, and 15 m at 5.25 GHz due to enhanced beam tilt in the elevation plane. Furthermore, at 5.8 GHz as observed from Fig. 2.34(b), $(\gamma > \gamma_{th}) \cap (P_{Rx} \ge P_{th})$ is achieved in the elevation coverage range 1.7-9 m, 0-13 m, and 2.5-8.5 m at $\rho=4$ m, 10 m, and 19 m, respectively, which indicate low beam tilt towards upper elevation plane. Therefore, the lower frequency carriers around 5.25 GHz are suitable for the nodes positioned at extreme altitudes, while the higher carriers around 5.8 GHz can be utilized for the nodes located at intermediate heights. This corroborates with the measured radiation pattern results of Fig. 13 indicating a higher beam tilt in elevation at lower frequency carriers. The immediately discussed SIR distribution results for A1 as transmitter show that the overall elevation coverage by A1 is easily provided in the range $h_{Rx} > 4$ m, identically, the A2 covers the lower heights in the 3-D space. Moreover, the results suggest that the two groups of MAA's, e.g., A1-C2-E1-G2 and A2-C1-E2-G1, each including four MAAs from alternate sectors and one operating at 5.25 GHz and other at 5.8 GHz, can achieve communication coverage satisfying $(\gamma > \gamma_{th}) \cap (P_{Rx} \geq P_{th})$ within respective alternate sectors with maximum elevation range of $h_{Rx} = 20.6$ m and azimuth range of $\rho = 16.25$ m on the ground. These operating conditions enable the projection of eight simultaneous beams in the 3-D space. Similarly, the other two groups, e.g., B1-D2-F1-H2 and B2-D1-F2-H1, can simultaneously operate over two frequency carriers other than the frequency channels of A1-C2-E1-G2 and A2-C1-E2-G1 within the operating band, thus, enables the operation of sixteen simultaneous beams from sixteen MAAs.

2.2.5 Performance Comparison with prior work

The performance of the proposed Design-O1B with the state-of-the-art antenna designs is compared in Table 2.7 in terms of beamforming technique, 3-dB coverage, gain, SIR, and SLL. The designs proposed in [39, 41, 40] provide 3D beam switching. However, achieve maximum beam coverage of 60° in elevation and 360° in azimuth. The immediately mentioned designs, in general, employ FSS along with several pin diodes for beam

	[39]	[40]	[41]	[110]	[36]	Design-O1B
Beam scan	3D	3D	3D	2D	2D	3D
elevation/	adaptive/	switched	switched/	-	-	switched & beam squint/
mechanism	phase shifter	FSS	FSS			RF switch
azimuth/	switched/	switched/	switched/	switched/	switched/	switched/
mechanism	FSS	FSS	FSS	PIN diode	RF switch	RF switch
azimuth coverage	360°	360°	360°	360°	360°	360°
elevation coverage	31°	60°	50°	-	-	93.6°
sectors	cylindrical structure	6	6	4	8	8
simultaneous beams	1	1	1	-	8	16
Peak gain (dBi)	9.2	8.1	5.2	17.25	6.40	7.85
Peak SIR (dB)	-	-	-	-	20	17
Peak SLL (dB)	-9	-	-	-6	-	-15.8

Table 2.7: comparison with state-of-the-art

switching, which increases the system complexity. The full channel capacity is not utilized in these designs since they generate a single switched beam at a time in 3D space. In contrast, in [36], the antenna can form eight beams simultaneously, however, with a limitation of 2-D beam coverage only. Similarly, in [110] antenna is designed for 2-D coverage. In comparison, the proposed design is able to generate sixteen beams simultaneously, enabling the coverage of 360° in azimuth and enhanced elevation coverage of 93.6°. Moreover, the beam squint phenomena is exploited for this enhancement in elevation coverage and to improve interference performance. The planar PCB design of sectors makes the design simple to implement. Furthermore, peak SIR and SLL for the proposed antenna are also competitive to the state-of-the-art designs. In [36], a higher peak SIR is shown but only for a particular height of the receiver. Moreover, though the peak gain of the proposed antenna is slightly lower than some of the literature designs, it is sufficient for the low power access point application and the maximum achieved SIR value is appreciable for the 3-D coverage antenna which is the real metric for quality assessment. As described in Section 1.2 of Chapter 1, access point can only provide WPT to IoT devices that are in close proximity. Consequently, dedicated RF-ETs are necessary to effectively power IoT devices through WPT within the designated application region. This approach is essential for ensuring reliable energy delivery to support the functionality of nearby IoT devices.

2.3 RF Eenergy Transmitter

A dedicated WPT system consists of RF-ETs also called as RF showers and several sensor nodes integrated with power receivers (Rx). The Rx comprises either a rectenna module or a SWIPT antenna which converts the incident RF waves into usable DC power for powering the sensor node. To realize an efficient WPT system, the deployment strategy of RF-ET depends on the node distribution in a particular application scenario. For instance, in the vertical farming application for smart agriculture, a large number of sensor nodes are deployed in 3-D space, as demonstrated in Fig. 2.35. Similarly, several IoT devices and sensor nodes are distributed in 3-D to realize smart warehouse application. This

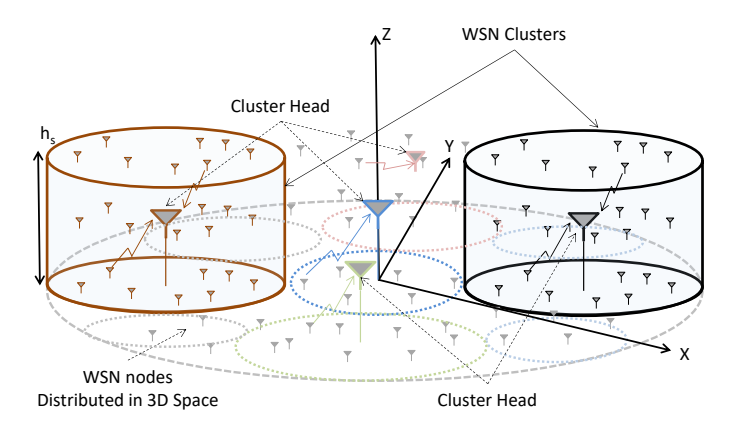


Figure 2.35: Application scenario of the cluster based WSN with 3D distributed sensor nodes.

forms a 3-D distributed WSN where nodes communicate with each other and the gateway device. To realize a power-efficient WSN with high node density, the general approach under communication research includes grouping the nodes into several clusters, each having a cluster head (CH) with which the local neighboring nodes communicate [47], as demonstrated in Fig. 2.35. The CHs further communicate with a remote gateway. Indeed, the power consumption of a CH is several times higher than the rest of the cluster nodes. Therefore, the CHs require higher power supplies to cater to the need. Further, if the WPT technique is employed to supply RF power in a 3-D cluster-based WSN of Fig. 2.35, the RF-ET design should consider the uneven need of the WSN nodes. Hence, the RF-ET system should distribute microwave power in space such that the CHs receive more power than the other nodes, and each node receives power above a certain threshold to fulfill its energy requirement. The latter can be achieved by maximizing the beam collection efficiency (BCE), which is the ratio of the power received by the rectenna to the total transmitted power [48]. This chapter presents a switched beam array RF-ET system to power the proposed 3-D distributed nodes in clustered WSN scenario demonstrated in Fig. 2.35. Instead of BCE or PCE at a single node, maximization of 3-D coverage is taken as the design objective to optimize the subarray elements excitation coefficient. A minimum DC power threshold (P_{th}) constraint is taken in objective function of 3-D coverage maximization to ensure harvested DC power delivery of at least P_{th} level at all the sensor nodes within the cluster region. Moreover, the optimal location of the CH node is analytically derived to minimize the average energy consumption of the sensor nodes within the WSN cluster.

2.3.1 Analytical Model for Projected 3-D Power Pixel

System Architecture

In this section, the analytical model shown in Fig. 2.37 is discussed to analyze the projected power pattern over the Rx plane called as power pixel area (PPA). The distance (h_t) between the Tx and Rx plane is varied to analyze the RF power distribution in 3-D

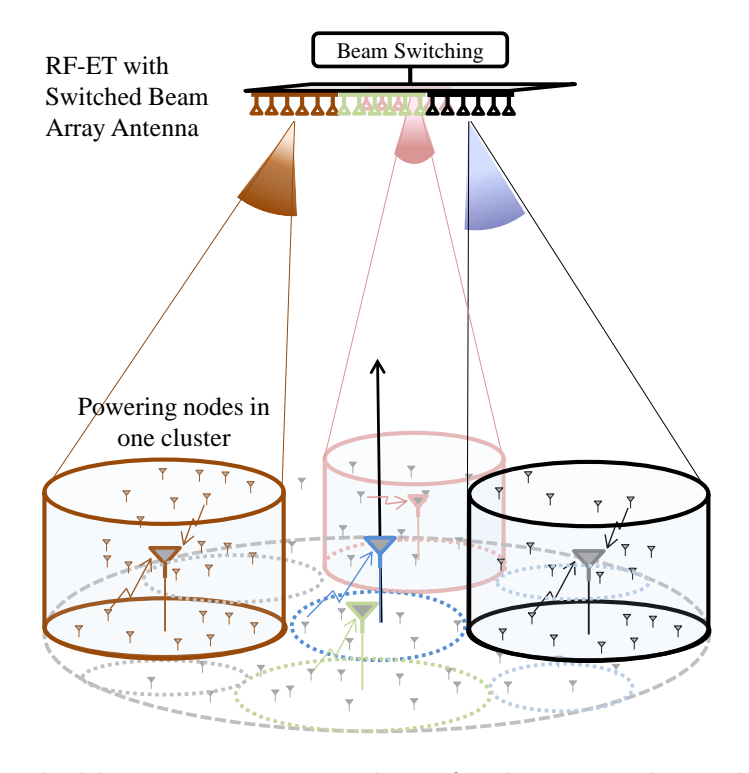


Figure 2.36: Switched beam array RF-ET scheme for the proposed 3-D clustered wireless sensor network

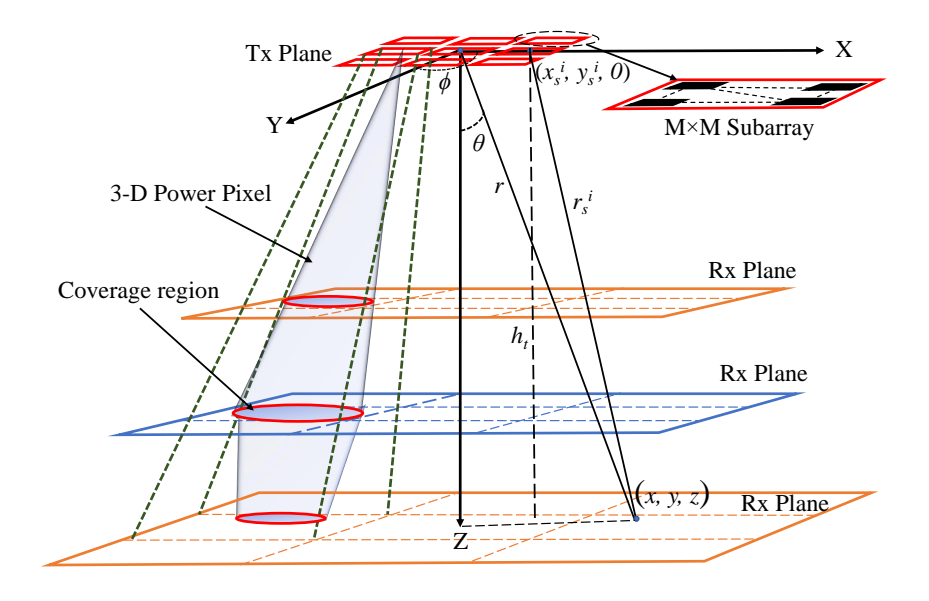


Figure 2.37: Analytical Model for proposed SBA RF-ET system.

space referred to as power pixel volume (PPV). The Rx plane is divided into $N \times N$ rectangular grids. The proposed RF-ET contains $N \times N$ subarrays designed using an $M \times M$ size microstrip patch array (MPA). The subarray-(p,q) directs the RF energy towards their assigned WSN-cluster-(p,q). As shown in Fig. 2.37 two coordinate systems are used to analyze the projected power patterns over the WSN cluster region. The radiation pattern of each subarray is formulated in spherical coordinates (r, θ, ϕ) . The Rx plane and the planar subarray are represented in Cartesian coordinate (x, y, z). The

center of the subarray-i [i = N(p-1) + q] is denoted by $(x_s^i, y_s^i, 0)$, where $z = h_t$. The relation between the two coordinates is given by

$$r = \sqrt{x^2 + y^2 + h_t^2}, \ \phi = \tan^{-1}\left(\frac{y - y_s^i}{x - x_s^i}\right),$$

$$\theta = \cos^{-1}\left(\frac{z}{r_s^i}\right), \ r_s^i = \sqrt{(x - x_s^i)^2 + (y - y_s^i)^2 + h_t^2}$$
(2.28)

where, r and r_s^i are the distance of any point on the Rx plane from the origin and the center of the subarray-i, respectively. The field pattern of single patch antenna in a subarray is formulated as [103]

$$E_{\theta} = -E_0 \cos v \, \frac{\sin u}{u} \sin \phi, \ E_{\phi} = E_0 \cos v \, \frac{\sin u}{u} \cos \theta \cos \phi \tag{2.29a}$$

$$v = \frac{\beta l \sin \theta \sin \phi}{2}, \quad u = \frac{\beta w \sin \theta \cos \phi}{2}$$
 (2.29b)

where, w is the width and l is the length of the patch, and β is the free space propagation constant at 5.8 GHz frequency. In the literature UHF, 2.45 GHz and 5.8 GHz bands are primarily used for wireless power transmission application. The low frequency bands offer high transmission range due to the low free space path loss component. However, the 5.8 GHz is chosen to reduce transmitting antenna aperture area and rectenna size for small sensor nodes with component efficiency close to the lower frequency band [111]. The total normalized element pattern, $f(\theta, \phi)$, is evaluated using (2.29a) as

$$f(\theta,\phi) = \sqrt{\left(\frac{E_{\theta}}{E_{0}}\right)^{2} + \left(\frac{E_{\phi}}{E_{0}}\right)^{2}}$$
 (2.30)

The normalized array factor of subarray-i designed using $M \times M$ MPA such that M is even and antenna elements are symmetrically distributed in four quadrants is evaluated by [112]

$$AF^{i}(\theta,\phi) = 4\sum_{n=1}^{M} w_{n} \cos(\beta u_{i}) \times \cos(\beta v_{i})$$
(2.31a)

$$u_i = (x_n^i - x_s^i)(\sin\theta\cos\phi - \sin\theta_0\cos\phi_0)$$
 (2.31b)

$$v_i = (y_n^i - y_s^i)(\sin\theta\sin\phi - \sin\theta_0\sin\phi_0)$$
 (2.31c)

where, (x_n^i, y_n^i) is the position of element-n in the first quadrant of the subarray-i, (θ_0, ϕ_0) is the beam maxima direction and w_n represents the excitation coefficients. Using (3.4) and (2.31), the total normalized radiation gain pattern of the subarray-i is given by

$$G_t^i(\theta,\phi) = \left| AF^i(\theta,\phi) \times f(\theta,\phi) \right|^2 \tag{2.32}$$

Received RF Power Evaluation

Considering G_{tmax}^i as the maximum gain of subarray-i of size $M \times M$ with $r_s^i(\theta, \phi)$ as the distance of the sensor node from subarray-i center which is located at (θ, ϕ) in a Rx plane at a distance h_t from Tx, the power received by the assigned WSN cluster region is

evaluated as follows [113]

$$P_{rx}^{i} = \alpha^{2} 10^{\frac{\zeta}{10}} P_{t}^{i} G_{tmax}^{i} G_{t}^{i}(\theta, \phi) G_{r}^{i}(\theta, \phi) \left(\frac{\lambda_{0}}{4\pi r_{s}^{i}(\theta, \phi)}\right)^{\gamma}$$

$$(2.33a)$$

$$G_{tmax}^{i} = G_{e} \times G_{AFmax}^{i} \tag{2.33b}$$

$$G_{AFmax}^{i} = 4\pi \frac{|AF^{i}(\theta,\phi)|_{max}^{2}}{\int_{0}^{2\pi} \int_{0}^{\pi} |AF^{i}(\theta,\phi)|^{2} \sin\theta \ d\theta \ d\phi}$$
(2.33c)

where, α^2 and $10^{\frac{\zeta}{10}}$ represent shadowing and multipath fading effects, respectively, where α and ζ are the values of the random variables [50]. The directional patterns of the Tx and Rx antenna makes the line of sight path dominant and hence lowers the scattering losses. Therefore, a strong line of sight signal path is assumed between the Tx and the sensor node location resulting in average received power equal to the general friis equation utilized in [50] for analytical evaluation. P_t^i denotes the power transmitted, G_e is the maximum gain of single patch antenna element, G_{AFmax}^i is the maximum array factor gain, $G_t^i(\theta, \phi)$ is the normalized pattern of array factor with respect to angular distribution (θ, ϕ) , and $G_r^i(\theta, \phi)$ is the receiver antenna gain mounted at the sensor node having a flat top beam pattern with 1 dB beamwidth of 90° [114].

Harvested DC Power Evaluation

The rectenna module at the sensor node converts the received RF power P_{rx}^{i} to dc power P_{dc}^{i} in the 3D coverage region of subarray-i which is evaluated as

$$P_{dr}^{i}(r,\theta,\phi) = \eta(P_{rr}^{i}) \times P_{rr}^{i}(r,\theta,\phi)$$
(2.34)

where, $\eta(P_{rx}^i)$ is the PCE of the rectenna module which is dependent on intensity of RF power impinging on Rx antenna aperture. Since, the received RF power is dependent on sensor node position with respect to the Tx. Therefore, η is also a function of sensor position (r, θ, ϕ) . Moreover, η is also called the power conversion efficiency (PCE) [115] and in many existing works is taken as the design objective to enhance the harvested DC power.

2.3.2 Problem Formulation

In this section, the analytical problem is formulated to maximize the PPV and minimize the average power consumption in the 3-D WSN cluster.

PPA and PPV Definition

In this work, the 2-D and 3-D coverage denoted as PPA and PPV, respectively, are defined based on the DC power harvested at the Rx from the RF power received from the Tx. The parameters are evaluated based on the minimum harvested DC power sensitivity P_{th} to ensure power delivery of at least P_{th} level at the sensor node location. Mathematically, PPA and PPV are defined as

$$PPA = \text{Area } \forall (x, y, h_t) : P_{dc}(r, \theta, \phi) \ge P_{th}$$
 (2.35)

$$PPV = \text{Volume } \forall (x, y, z) : P_{dc}(r, \theta, \phi) \ge P_{th}$$
 (2.36)

where, P_{dc} is the harvested dc power at the sensor node location.

WSN Cluster Volume maximization

The objective here is to maximize the PPV such that there is no space between the cluster regions where $P_{dc} < P_{th}$. For analysis, $P_{dc} = 100 \mu \text{W} \ (-10 \text{ dBm}) \ [116]$ with a channel tolerance of 0.5 dBm is considered at ultra low power sensor nodes which results in $P_{th} = -9.5$ dBm. A rectifier prototype is designed at 5.8 GHz and its η is evaluated from DC voltage measured for -11 dBm to 11 dBm input RF power range at 980Ω output load. For analytical evaluation of PPA and PPV, the measured values are curve fitted as presented in Fig. 2.38. Thus the optimization objective to determine the excitation

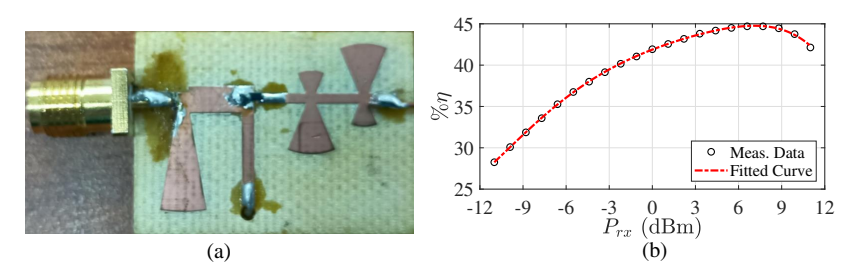


Figure 2.38: (a) Fabricated prototyped of the rectifier circuit (b) Measured and fitted η vs input RF power for rectifier.

amplitude and phase can be formulated as

$$\max_{P_{\Omega \in \Omega_{vi}}} PPV \tag{2.37a}$$

s.t.
$$0 \le w_n \le 1, 0 \le \theta_0 \le 0.5\pi, 0 \le \phi_0 \le 2\pi$$
 (2.37b)

$$2 \le h_t \le 10, P_{\Omega \in \Omega_{vi}} \ge P_{th}, \text{ and } \bigcap_{i=1}^{i=N^2} P_{\Omega \in \Omega_{vi}} \ge P_{th}$$

$$(2.37c)$$

where, Ω_{vi} is the PPV energized by subarray-i. The objective function in (2.37a) is optimized by using the genetic algorithm (GA), which is a population-based meta-heuristic algorithm. The optimization procedure followed to determine the optimal excitation coefficients of the Tx subarray is demonstrated by the flowchart given in Fig. 2.39 and a step-wise description is given below.

- 1. Initialize $2 \le h_t \le 10$, scan parameters $0^{\circ} \le \theta_0 < 90^{\circ}$ and $\phi_0 = 135^{\circ}$, 90° , and 180° for SA1, SA2, and SA4, respectively. $\theta = 0^{\circ}$ and $\phi = 0^{\circ}$ for SA5 since no scanning is required.
- 2. Generate the initial population for SA1, SA2, SA4 and SA5, where genes correspond to the weight (w_n) of the antenna elements such that $0 \le w_n \le 1$.
- 3. Evaluate the PPA for each member of the population
- 4. Generate new population from the current population members using the selection, mutation and elitism process to maximize the PPA.

- 5. If the maximum number of generation limit is not reached repeat the procedure from step-2, else go to the next step
- 6. Check if there is a non-covered region ($P_{dc} < P_{th}$) between the PPA of SA1, SA2, SA4 and SA5. If present, change the value of θ_0 , h_t and repeat the procedure from step-1, else save the excitation coefficient values from the previous step providing maximum PPA.

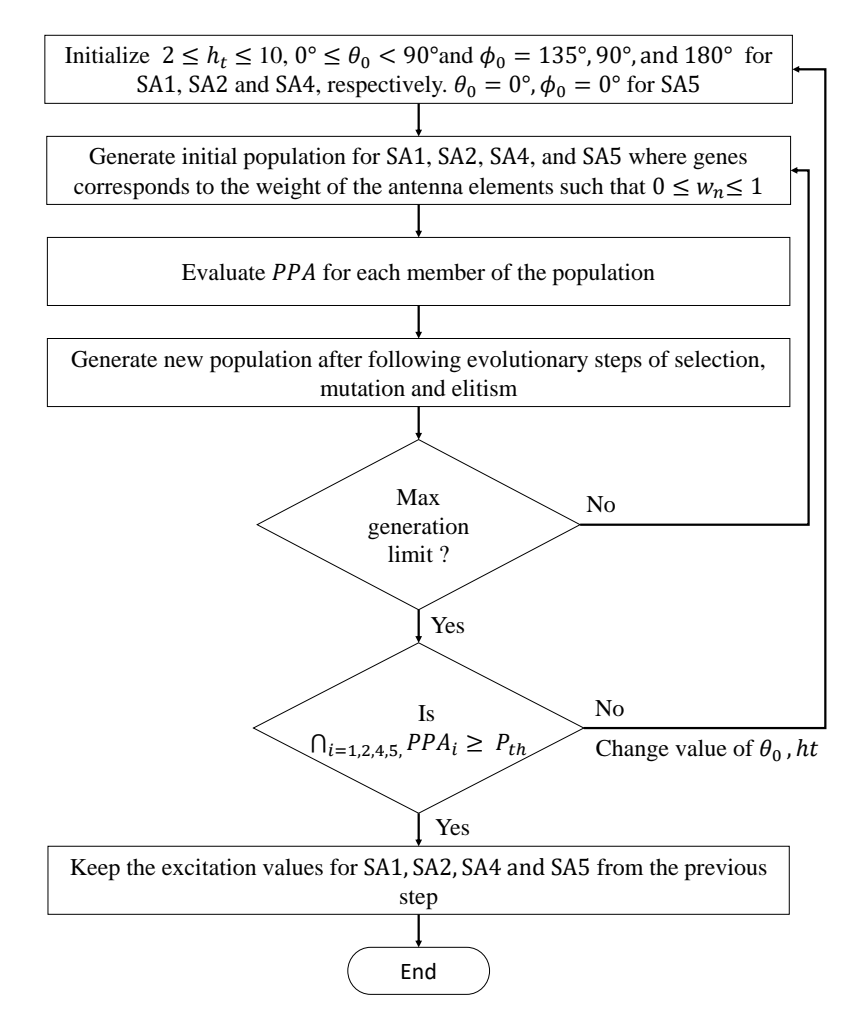


Figure 2.39: Flowchart of the Genetic Algorithm to maximize PPV.

Optimal CH Location

The average power consumption (P_{avg}) at the sensor nodes in a WSN cluster-i depends upon the CH location as the energy consumption increases approximately proportional to the square of the communication link length (d^2) . Moreover, CH requires more P_{dc} at its location to carry out uninterrupted network operations. Therefore, the locus for CH placement should be along the direction of the main lobe of the Tx radiation pattern. The objective function to determine the optimal CH location in cluster-i is defined as

$$\min_{P_{\Omega \in \Omega_{vi}}} P_n^i = \frac{1}{T} \sum_{j=1}^T \frac{d_j^2}{P_{dc}^j}$$
 (2.38a)

s.t.
$$P_{dc}^{j} \ge 10^{-0.95} \ \forall P_{dc}^{j} \in \Omega_{vi}$$
 (2.38b)

where, P_n^i is the normalized power ratio which is directly proportional to P_{avg} , d_j^2 is the communication link length between the CH and sensor node-j, P_{dc}^j is the harvested DC power at sensor node-j and T is the total number of sensor nodes present inside the PPV of WSN cluster-i.

2.3.3 Analytical Results and Discussion

For the analysis of PPV, nine subarrays (SA1 to SA9) of MPA arranged in a 3×3 grid are considered for the RF-ET system because the lower number of subarrays would provide lower coverage area whereas the higher number of subarrays will provide insignificant increase in coverage area due to large scan angles. The Rx plane is also divided into 3×3 grid housing nine WSN cluster regions (PPA1 to PPA9) as illustrated in Fig. 2.40. For

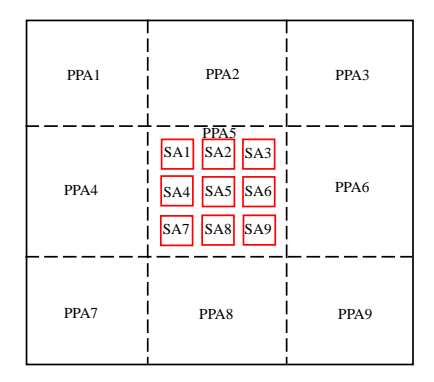


Figure 2.40: Subarray and corresponding PPA distribution for analytical analysis

analysis, $P_t^i = 39$ dBm, $G_r^i = 6$ dBi, and $G_e = 5$ dBi are considered in (2.33a) to evaluate P_{rx}^i . Moreover, to keep the PPA region symmetrical to the coordinate axes, three pairs of subarrays viz. (SA1, SA3, SA7, SA9), (SA2, SA8), and (SA4, SA6) are assigned with mirror excitation considering x and y axis as mirrors.

Evaluation of Optimal Subarray Size

The optimal array size is determined by analysing the PPA for uniformly excited SA5. The size of the MPA in SA5 is varied from 2×2 to 6×6 considering $0.5\lambda_0$ inter-element distance. The variation of %PPA is evaluated for various h_t in 10×10 m² receiver plane area is illustrated in Fig. 2.41. It is observed that PPA increases up to a specific h_t and then decreases. At lower h_t the RF radiation spread is low, resulting in a small PPA. The radiation spread increases with h_t , and the gain of the Tx compensates for the path loss. However, after the maximum PPA is achieved, the path loss starts dominating, resulting in a smaller PPA with further increase in h_t . The analytical results shown in Fig. 2.41 demonstrate that 4×4 MPA is the optimal choice for RF-ET system design for the considered mid transmission range of 2-10 m. The 4×4 MPA is utilized to design all the subarrays (SA1-SA9), and the evaluation of optimal excitation coefficients to maximize the PPV is discussed in the subsequent subsection.

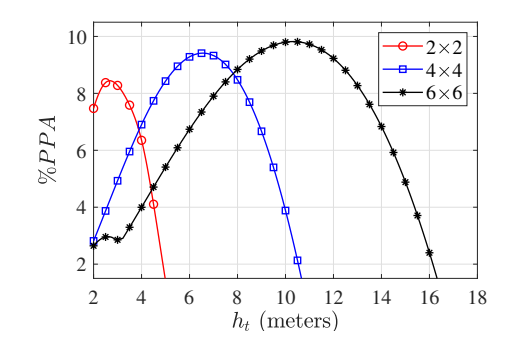


Figure 2.41: %PPA for SA5 at different h_t for 2×2 , 4×4 , and 6×6 MPA.

Table 2.8:	Subarray	antenna	element	excitation	coefficients

S.No.		SA1		SA2		SA4		SA5
	Amp	phase (°)						
1	0.562	-124.71	0.537	-117.56	0.537	-117.56	0.573	0
2	0.775	-83.14	0.708	-58.78	0.757	-117.56	0.702	0
3	0.775	-41.57	0.708	58.78	0.757	-117.56	0.702	0
4	0.562	0	0.537	117.56	0.537	-117.56	0.573	0
5	0.701	-83.14	0.721	-117.56	0.791	-58.78	0.747	0
6	1	-41.57	1	-58.78	1	-58.78	1	0
7	1	0	1	58.78	1	-58.78	1	0
8	0.701	41.57	0.721	117.56	0.791	-58.78	0.747	0
9	0.701	-41.57	0.721	-117.56	0.791	58.78	0.747	0
10	1	0	1	-58.78	1	58.78	1	0
11	1	41.57	1	58.78	1	58.78	1	0
12	0.701	83.14	0.721	117.56	0.791	58.78	0.747	0
13	0.562	0	0.537	-117.56	0.537	117.56	0.573	0
14	0.775	41.57	0.708	-58.78	0.757	117.56	0.702	0
15	0.775	83.14	0.708	58.78	0.757	117.56	0.702	0
16	0.562	124.71	0.537	117.56	0.537	117.56	0.573	0

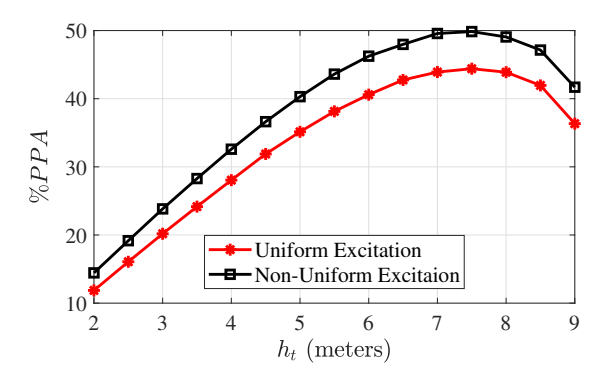


Figure 2.42: %PPA for 4×4 MPA subarray at various h_t for uniform and non-uniform excitation.

PPA and PPV Analysis

The maximum possible PPV is achieved by optimizing the main lobe tilt angle of all the uniformly excited SAs. The maximum $h_t = 8.6$ m is obtained such that there

is no uncovered region ($P_{dc} < P_{th}$) between the neighboring PPAs. This ensures full coverage within the PPV for uniform excitation. Similarly, to further enhance the PPA and maximize the coverage distance to $h_t = 8.7$ m, the excitation of all the SAs are optimized using GA. The corresponding optimal excitation amplitude and phase values of the subarrays are listed in Table 2.8. Moreover, the total enhancement in %PPA by GA optimized excitation over uniform excitation is illustrated in Fig. 2.42. The results indicate that initially, PPA increases with h_t up to a particular range and then decreases, corroborating with the analysis done in Section 2.3.3. Additionally, the RF PPA for the uniformly and non-uniformly excited RF-ET subarrays are demonstrated in Fig. 2.43 and Fig. 2.44 at $h_t = 7$ m which illustrates the enhancement in coverage area using GA optimized excitation coefficients. The harvested DC PPA from $h_t = 2$ m to $h_t = 8.7$ m

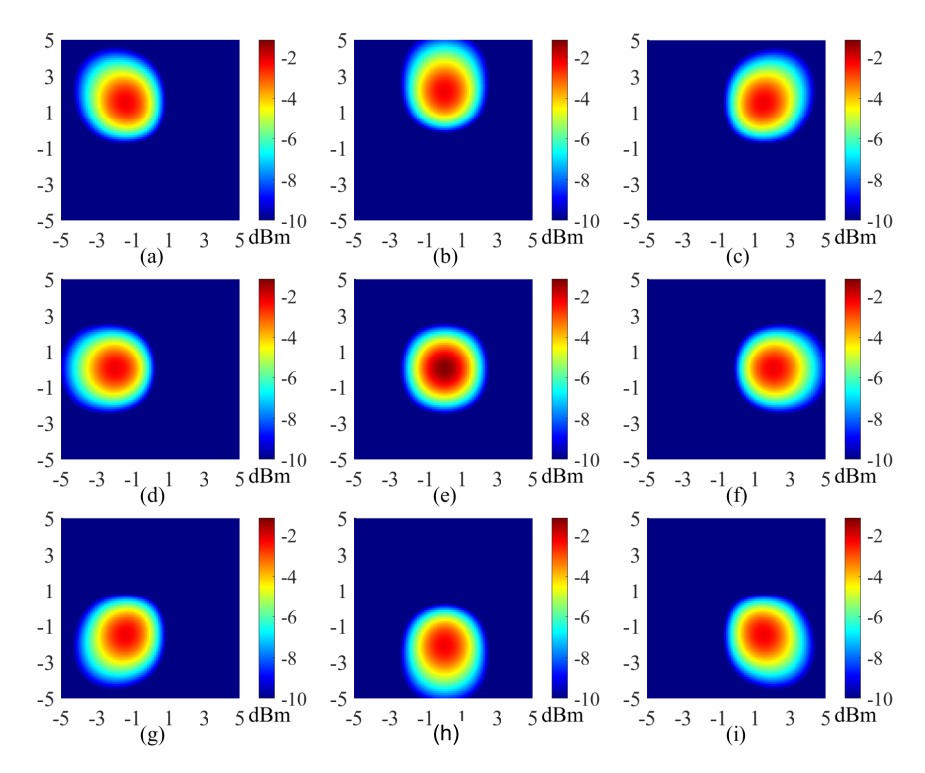


Figure 2.43: RF Power Pixel by 4×4 uniformly excited (a) SA1 (b) SA2 (c) SA3 (d) SA4 (e) SA5 (f) SA6 (g) SA7 (h) SA8, and (i) SA9 at $h_t = 7$ m.

are illustrated in Fig. 2.45 which are in line with %PPA vs h_t result shown in Fig. 2.42. The total PPV for the uniform element excitation is 229.57 m³ and increases to 261.38 m³ for GA optimized excitation achieving an improvement of 13.86%. The next section discusses the evaluation of optimal CH location to lower the energy consumption of sensor nodes in the WSN cluster.

Evaluation of Optimal CH Location

The sensor nodes are assumed to be placed uniformly within the PPV. The optimal location for CH should be along the radiation pattern peak of the subarray as discussed in Section 2.3.2, and is demonstrated in Fig. 2.46 (a). First, h_t is varied and the corresponding point on the locus of radiation peak is determined on each plane. In the next step, the

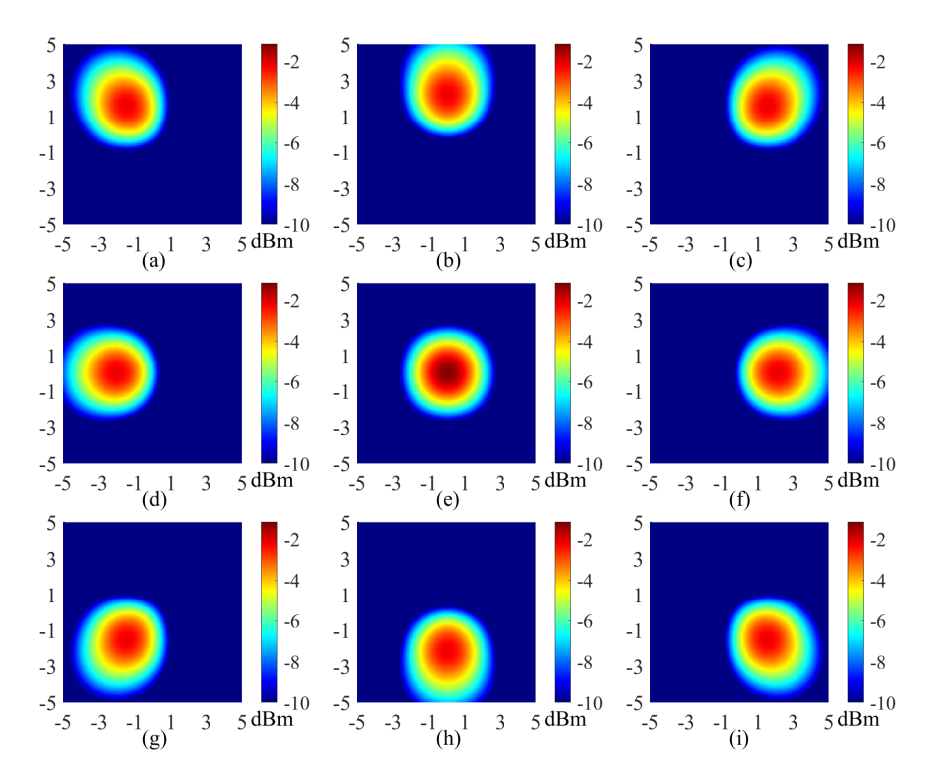


Figure 2.44: RF Power Pixel generated from GA optimized 4×4 non-uniformly excited (a) SA1, (b) SA2, (c) SA3, (d) SA4, (e) SA5, (f) SA6, (g) SA7, (h) SA8, and (i) SA9 at $h_t = 7$ m.

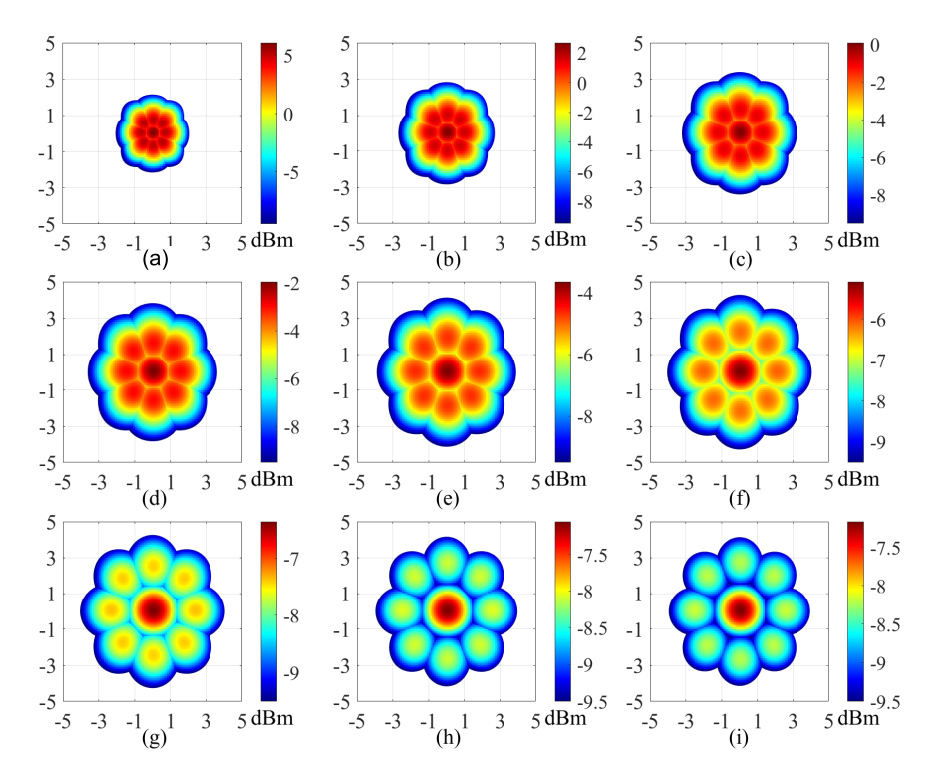


Figure 2.45: Optimal harvested DC Power Pixel for 4×4 non-uniformly excited Tx MPA at (a) $h_t = 2$ m, (b) $h_t = 3$ m, (c) $h_t = 4$ m, (d) $h_t = 5$ m, (e) $h_t = 6$ m, (f) $h_t = 7$ m, (g) $h_t = 8$ m, (h) $h_t = 8.6$ m and (i) $h_t = 8.7$ m with $P_{th} = -9.5$ dBm.

distance of this point is calculated from all the sensor nodes within PPV of the subarray. This process is continued till the maximum limit for h_t is reached. The calculated distances

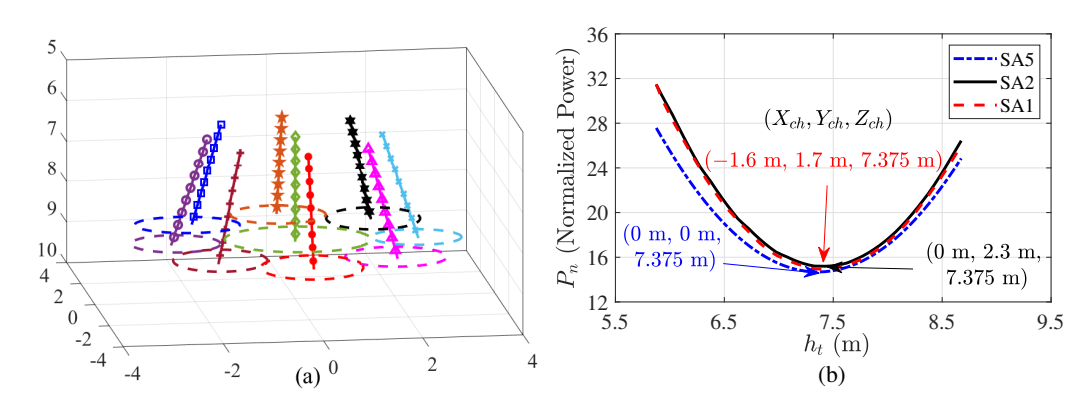


Figure 2.46: (a) Cluster head locus for all the power pixel regions generated by 4×4 MPA subarray (b) P_n at various h_t for SA1, SA2, and SA5.

are utilized to evaluate P_n by using (2.38). The point corresponding to the minimum P_n gives the optimal CH location. The variation of P_n with respect to h_t is plotted in Fig. 2.46(b). The lowest point of the plots indicate the lowest achievable P_n . The optimal location of the CH for SA1 (-1.6, 1.7, 7.375) m, SA2 (0, 2.3, 7.375) m and SA5 (0, 0, 7.375) m are evaluated using h_t and tilt angle of the subarray.

2.3.4 Design Realization and Verification

This section discusses the design and fabrication of subarrays SA1, SA2, SA4, and SA5 of the proposed RF-ET system. The corresponding PPA values are measured to verify the analytically evaluated results. The mentioned subarrays are sufficient for validation due to the symmetrical structure of the proposed RF-ET system as discussed in Section 2.3.3.

Design Process

All the subarrays comprise a 4×4 MPA with the interelement spacing of $0.5\lambda_0$, and are designed to achieve radiation pattern characteristics corresponding to analytically obtained amplitude and phase values listed in Table 2.8. Each subarray is realized on a dual-sided FR4 ($\epsilon_r = 4.4$, $\tan \delta = 0.02$) substrate having 1.6 mm thickness with 35 μ m copper deposit. The designs are optimized at 5.8 GHz using HFSS to achieve the desired radiation pattern with reflection coefficient (S₁₁) ≤ -10 dB. Fig. 2.51 shows the prototype of the subarrays fabricated using the MITS PCB prototyping machine.

Measurement Results and Discussion

The S_{11} and S_{21} parameter of the subarrays are measured using keysight's PNA-L VNA and are demonstrated in Fig. 2.47 and Fig. 2.48, respectively. The results show impedance matching better than -10 dB and mutual coupling lower than -40 dB between all the subarrays at the operating frequency. The radiation pattern and gain of the subarrays are measured in an anechoic chamber. The patterns generated using analytical equations given in Section 2.3.1 are compared with the measured patterns. The elevation and azimuth plane radiation patterns are represented in Fig. 2.49 and Fig. 2.50, respectively. Further,

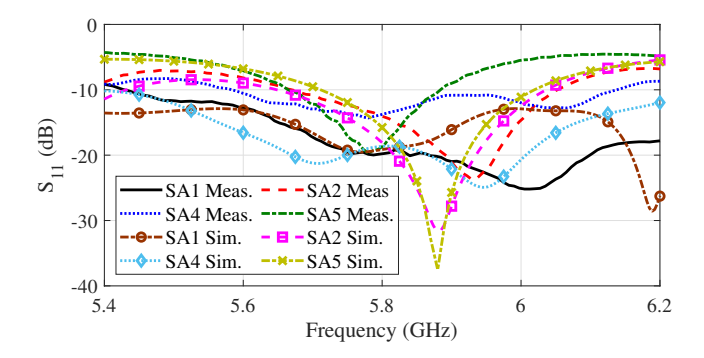


Figure 2.47: Simulated and Measured S₁₁ parameter for SA1, SA2, SA4, and SA5.

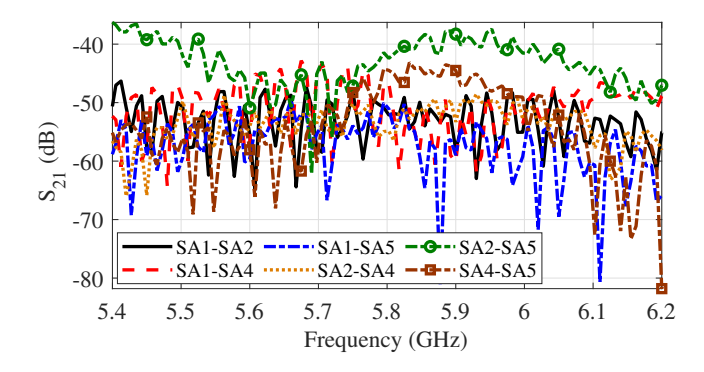


Figure 2.48: Measured S_{21} parameter between SA1, SA2, SA4, and SA5.

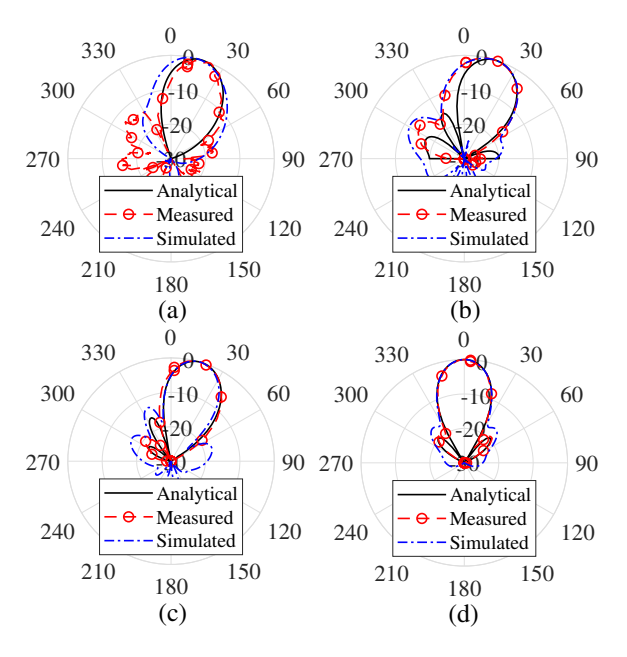


Figure 2.49: Analytical, measured, and simulated elevation plane radiation pattern of (a) SA1, (b) SA2, (c) SA4, and (d) SA5.

the simulated and measured gain of the subarrays are listed in Table 2.9. The measurement

Table 2.9: Simulated and Measured Gain values

Subarray	SA1	SA2	SA4	SA5
Simulated Gain (dBi)	11.5	12.4	13.3	13.6
Measured Gain (dBi)	11.5	12.4	12.8	13.6

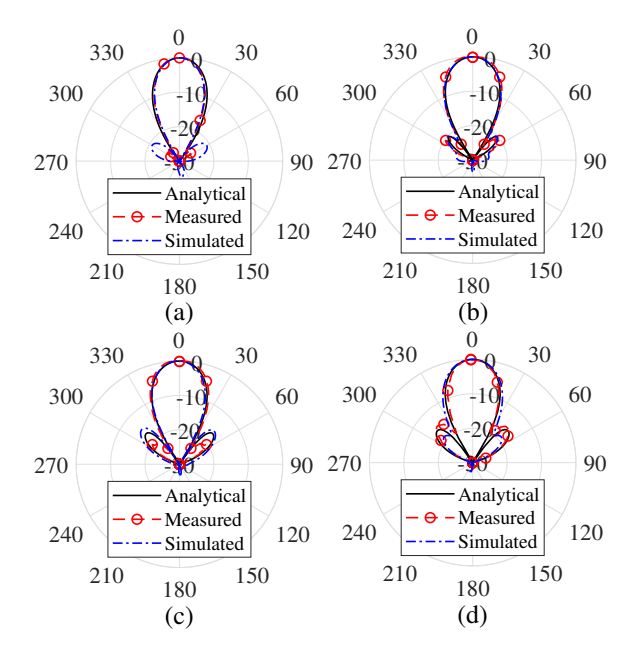


Figure 2.50: Analytical, measured, and simulated azimuth plane radiation pattern of (a) SA1, (b) SA2, (c) SA4, and (d) SA5.

setup to measure the PPA at $h_t = 4$ m and 8 m from the sub-arrays is shown in Fig. 2.51. The subarrays are excited using an RF signal generator capable of generating maximum

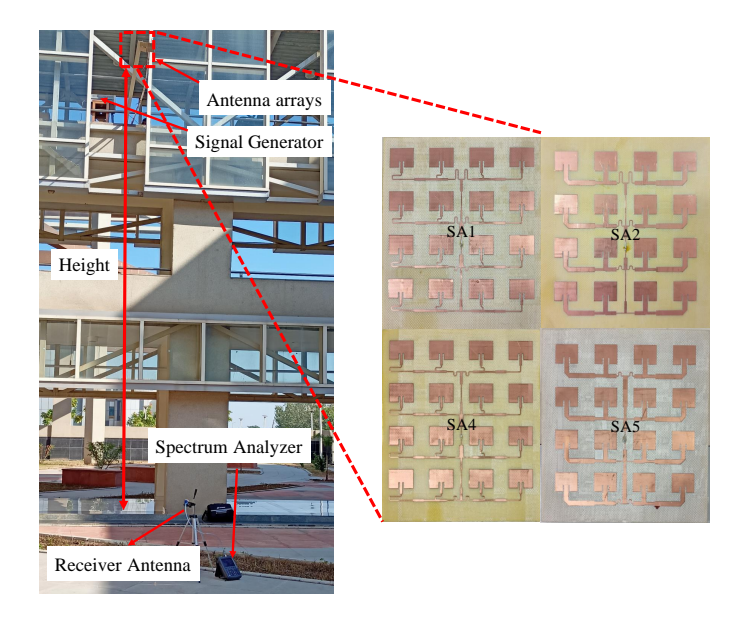


Figure 2.51: Measurement setup and subarray (SA1, SA2, SA4, and SA5) designs.

27 dBm of RF power whereas 39 dBm is the required transmit power, which can be achieved by using a 12 dBm power amplifier. However, due to the unavailability of a power amplifier in the laboratory, the measurement of the harvested DC is carried out in two steps. In the first step, the subarrays are excited using an RF signal generator (27 dBm) and the receiver antenna is connected to a spectrum analyzer (SA) and the received RF power is measured using the SA. In the next step, the measured received RF power is scaled up by 12 dBm and the resultant value is generated using the signal generator

(imitating the operation of the power amplifier) and directly fed to the rectifier circuit to measure the harvested DC power. Fig. 2.52 and Fig. 2.53 demonstrate the measured PPA in the plane placed at a distance of 4 m and 8 m from the transmitter plane, respectively. Moreover, the comparison between the analytical and measured PPA range is given in

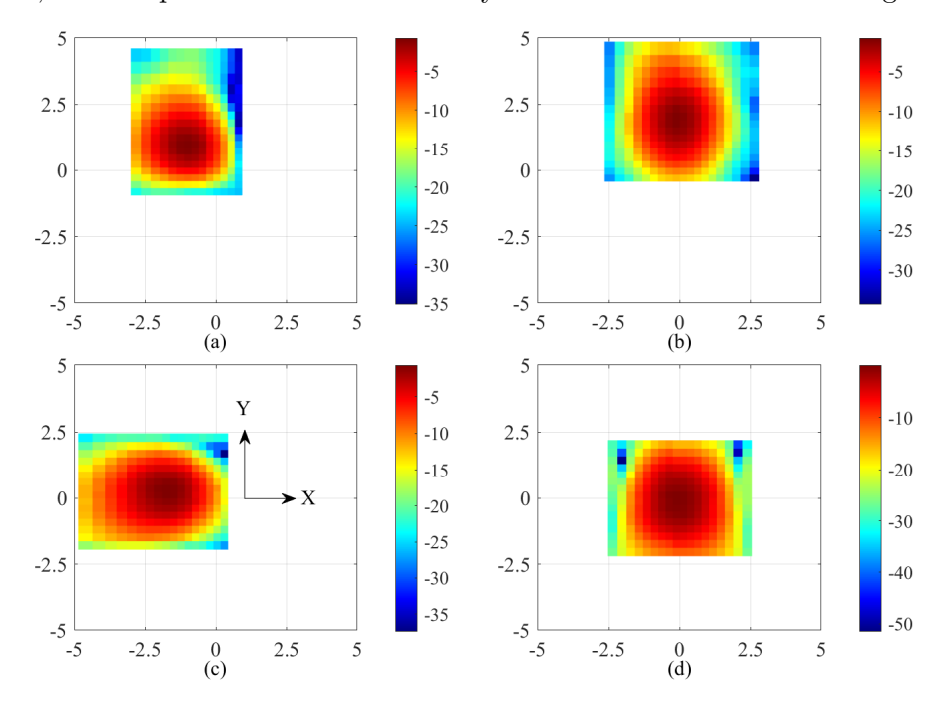


Figure 2.52: Measured harvested DC Power Pixel patterns on Rx plane at $h_t = 4$ m from (a) SA1, (b) SA2, (c) SA4, and (d) SA5.

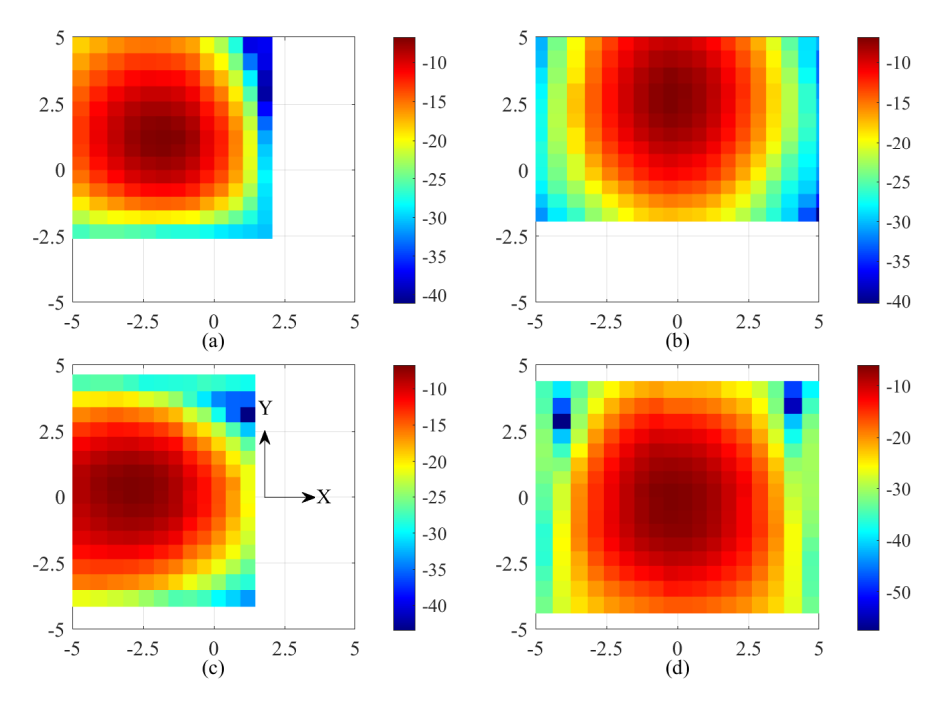


Figure 2.53: Measured harvested DC Power Pixel patterns on Rx plane at $h_t = 8$ m from (a) SA1, (b) SA2, (c) SA4, and (d) SA5.

Table 2.10 and Table 2.11. The x represents the horizontal axis, and y is the vertical axis and corresponds to the coordinate system given in Fig. 2.37. The results obtained are

close to the analytically evaluated PPA values. The deviation in results can be attributed to misalignment and interference from the surroundings.

Table 2.10: PPA range (in m) on a plane at 4 m from Tx

Subarray	Anal	ytical	Measured		
	\mathbf{x}_{min} - \mathbf{x}_{max}	ymin-ymax	\mathbf{x}_{min} - \mathbf{x}_{max}	y_{min} - y_{max}	
SA1	-2.7 to 0.4	-0.5 to 2.8	-2.6 to 0.4	-0.4 to 2.5	
SA2	-1.5 to 1.5	-0.1 to 3.4	-1.5 to 1.5	-0.1 to 4	
SA4	-3.2 to 0	-1.5 to 1.5	-3.7 to -0.1	-1.5 to 1.5	
SA5	-1.5 to 1.5	-1.5 to 1.5	-1.4 to 1.5	-1.5 to 1.5	

Table 2.11: PPA range (in m) on a plane at 8 m from Tx

Subarray	Analy	tical	Measured		
	xmin-xmax	ymin-ymax	xmin-xmax	ymin-ymax	
SA1	-3.3 to -0.3	0.3 to 3.4	-3.2 to -0.4	0.1 to 3	
SA2	-1.5 to 1.5	1 to 4.2	-1.4 to 1.5	0.6 to 4.3	
SA4	-4 to -0.9	-1.5 to 1.5	-4.4 to -1.2	-1.5 to 1.5	
SA5	-1.7 to 1.7	-1.7 to 1.7	-1.7 to 1.7	-1.5 to 1.6	

2.3.5 Comparison with state-of-the-art

The proposed RF-ET antenna design is compared with the state-of-the-art in Table V. The

[117] This Work 51 [53] [55]56 [115]Beam Scan Mechanism Adaptive Adaptive Adaptive Adaptive Adaptive Adaptive Adaptive Switched Design STBF STBF Coverage max max max max Objective STBF PCESTBF BCEProbability PCEPCEPPA, PPVWSN Distribution 2D3D2D2D2D2D3D3D Clustered WSN No No No No No No Yes No Need for complete CSI Yes Yes Yes Yes Yes Yes Yes No 0.920 0.9150.920 Frequency (GHz) 5.75.8 0.920 5.8 5.8

Table 2.12: Comparison with State-of-the-Art

beam scan mechanism, design objective, and sensor node distribution strategy are utilized to do the comparative analysis. In the existing designs [50, 51, 117, 53, 55, 56, 115] adaptive beamforming technique is utilized to either generate a focused beam over each sensor node for enhanced PCE/BCE or improve the coverage probability by optimizing excitation of transmitter array elements by utilizing complete CSI obtained from the receiver. The space time beamforming (STBF) algorithm adopted in [50, 117] optimizes the time interval to charge the sensor node battery. However, there is a possibility that the previous cycle of charging is not enough for sustainable operation. Moreover, 3-D distribution of sensor nodes is not considered for analysis in most of the existing works and if considered [51, 115] the clustering of sensor nodes is not incorporated which limits the enhancement of WSN lifetime. The existing RF-ET systems require complete CSI for node localization which increases system latency in a dense sensor node deployment scenario. In contrast, the proposed work utilizes the switched beamforming technique to power the proposed 3D clustered WSN. Multiple subarrays with optimized excitations are utilized to generate

static beams toward various WSN cluster regions which can be switched on or off based on sensor node energy consumption requirements within a cluster. The proposed method does not require any phase shifter, attenuator and CSI making the system design simple and cost-effective.

2.4 Summary

This chapter introduces the quality aware synthesis of 2-D and 3-D coverage switched mulitbeam (SMB) multi-sector AP antenna systems to enhance the reliable communication coverage for IoT applications. The sector-based design of multi-beam AP antenna is necessary for a densely deployed IoT nodes to achieve high system capacity with 360° azimuth coverage. However, the neighboring sectors cause high co-channel interference resulting in a low signal to interference (SIR) ratio and hence degrades the communication link quality. This leads to frequent packet re-transmissions resulting in increased energy consumption at the power deficient sensor nodes. The QoS aware array synthesis scheme incorporates projected power and SIR limits within the antenna design process to maximize the effective coverage area with acceptable BER for different modulation schemes. The optimized coverage with reliable communication implies energy saving at the sensor nodes. Based on the proposed process of coverage optimization, multi-sector AP antenna are analytically synthesized, and the prototypes are fabricated to validate the results.

The 2-D coverage antenna system designated as Design-O1A is a 10 sector antenna array. Each sector comprises a 2×3 MAA each configured with 20° tilt angle from the vertical axis. The maximum radial range of 2 m-13 m with 360° communication coverage is achieved. Moreover, high port isolation of 45.95 dB between adjacent sectors enables the generation of multiple simultaneous beams in the communication region resulting in high system capacity. The achieved performance indicates that the synthesized Design-O1A using the proposed scheme is a good candidate for AP in IoT applications. In contrast SMB multi-sector array antenna designated as Design-O1B for 3-D coverage houses two MAA to obtain coverage in the upper and lower halves of the elevation region. Moreover, unlike mechanical tilt Design-O1B leverages frequency-dependent beam squint phenomena to achieve multibeam coverage in the elevation region. The results demonstrate that a series fed 3×2 MAA meets the desired radiation characteristics effectively. The antenna system operates within the WLAN band, spanning from 5.15 GHz to 5.825 GHz. It exhibits a maximum realized gain of 7.85 dBi. The beam tilt varies from 10.8° to 46.8° in the elevation plane, corresponding to frequencies of 5.15 GHz and 5.825 GHz, respectively. The coverage obtained is 360° in azimuth and 93.6° in elevation. The high interference suppression between the MAAs of alternate sectors and high port isolation, enabled frequency re-use in the 3-D space around Design-O1B to communicate with multiple sensor nodes in IoT applications.

The access points can only provide WPT to IoT devices that are in close proximity. Consequently, dedicated RF-ET are necessary to effectively power IoT devices through

WPT within the designated application region. In this chapter a switched beam array antenna RF-ET is presented to power the 3-D distributed IoT sensor nodes in clustered WSN scenario. The synthesis of low-cost switched beam antenna array comprising multiple subarrays is proposed to power each WSN cluster individually. An analytical model is presented to evaluate the optimal subarray size for enhanced 3-D coverage. Instead of BCE or PCE at a single node, maximization of 3-D coverage is taken as the design objective to optimize the subarray elements excitation coefficient. A minimum DC power threshold (P_{th}) constraint is taken as objective function of 3D coverage maximization to ensure harvested DC power delivery of at least P_{th} level at all the sensor nodes within the cluster region. The optimal location of the CH node is analytically derived to minimize the average energy consumption of the sensor nodes within the WSN cluster.

In addition to Tx systems, Rx design for IoT devices plays a crucial role in achieving optimal WIT and WPT performance. The following chapter delves into WPT-enabled receiver systems tailored for ultra-low-power IoT devices. These receivers employ either rectenna modules or SWIPT antenna systems to facilitate the powering of IoT functions. Consequently, these designs are essential for realizing a sustainable IoT network.

⁰CHAPTER OUTCOMES:

^{[1].} S. Kumar, S. Jain and A. Sharma, "A BER-Conscious Synthesis of Switched-Beam Antenna to Maximize Reliable Coverage in WSN Applications," in IEEE Sensors Journal, vol. 22, no. 4, pp. 3785-3795, 15 Feb.15, 2022, doi: 10.1109/JSEN.2022.3142137.

^{[2].} **S. Kumar**, A. Sharma, S. Kalra and M. Kumar, "Communication Quality-Conscious Synthesis of 3-D Coverage Using Switched Multibeam Multi-Sector Array Antenna for V2I Application," in IEEE Transactions on Vehicular Technology, vol. 71, no. 2, pp. 1631-1642, Feb. 2022, doi: 10.1109/TVT.2021.3132304.

^{[3].} S. Kumar and A. Sharma, "Switched Beam Array Antenna Optimized for Microwave Powering of 3-D Distributed Nodes in Clustered Wireless Sensor Network," in IEEE Transactions on Antennas and Propagation, vol. 70, no. 12, pp. 11734-11742, Dec. 2022, doi: 10.1109/TAP.2022.3209744.

Chapter 3

Receiver Antenna for Ultra Low Power IoT Devices

O-3: Design angular misalignment tolerant rectenna module for ultra-low-power IoT devices.

O-4: Design a compact SWIPT antenna with wide information bandwidth for ultra-low-power IoT devices.

The receiver systems in IoT devices utilize either rectenna modules or SWIPT antenna systems to enable the wireless powering of various IoT functions. Rectenna modules harvest energy from dedicated RF-ETs positioned within a WPT-enabled smart application environment. Devices that employ rectenna modules typically integrate a separate antenna with their communication circuitry for WIT. In contrast, IoT devices equipped with SWIPT antenna systems do not require a separate antenna for WIT, allowing for a more compact design.

This chapter provides an analysis of an innovative rectenna designs for angular misalignment-tolerant WPT. Additionally, we present a novel SWIPT technique featuring a unique antenna design, aimed at realizing a compact receiver system for IoT devices.

3.1 Angular Misalignment Tolerant Rectenna Module

The major design objective in WPT scheme is to enhance PCE at the Rx. However, to achieve the above mentioned objective is a challenging task since a Rx can be placed in any arbitrary orientation, resulting in polarization mismatch between the Tx and the Rx. In a smart home application, generally the Tx is placed on the ceiling and the Rx is located at various devices which are randomly placed inside the room as illustrated in Fig. 3.1. Consequently, polarization mismatch between the transmitter (Tx) and receiver (Rx) is an inherent challenge. To address this issue, a robust rectenna module that operates with polarization insensitivity is essential for the receiver in such applications. In our prior collaborative studies [60, 118], we established that a multisector rectenna module necessitates eight patch antenna elements to accommodate angular misalignment in the azimuth plane. However, this configuration proves unsuitable for the aforementioned application scenario. Furthermore, these designs employ a cumbersome DC combining strategy, which contributes to an overall bulky system design. In addition, these designs

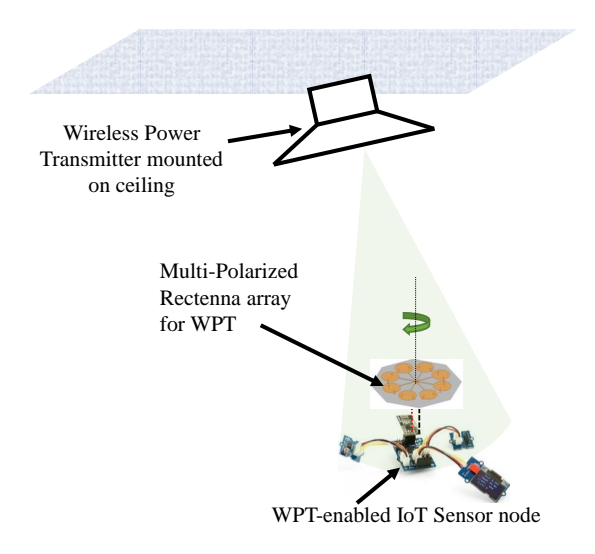


Figure 3.1: Application scenario for the proposed polarization insensitive rectenna system

are only capable of half wave rectification of the incident RF waves. This chapter first inverstigates the validity of the eight patch antenna element requirement and a fully integrated rectenna array utilizing parallel dc combining technique is proposed to achieve miniaturization along with polarization insensitive operation. In addition, a novel compact stacked multi-sector near isotropic coverage rectenna array system (iReAS) is proposed for IoT applications.

3.2 Multi-Polarized Circular Rectenna Array (Design-O3A)

3.2.1 Single Integrated Rectenna Element

In general rectenna components utilize a matching network (MN) [119], and a dc low pass filter (LPF) to achieve impedance matching between the rectifier and 50 Ω antenna port. However, the MN and LPF add insertion losses and also increase the overall size of the rectenna module. Therefore, to achieve miniaturization and reduce the losses the antenna impedance is conjugate matched with the Schottky diode to maximize the harvested DC power. The impedance of the Schottky diode (SMS-7621 – 079LF) is evaluated in ADS using the LSSP technique and is found to be 25-j92 Ω for shunt diode connection at -10 dB input RF power. The antenna simulation is carried out using Ansys HFSS simulation software. The proposed rectenna is designed at 5.8 GHz on a low-cost dual-side FR4 substrate ($\epsilon_r = 4.4$, $\tan \delta = 0.002$) having 1.6 mm thickness with 35 μ m copper deposition. The proposed rectenna module comprises a circular patch antenna, and two Schottky diodes, as illustrated in Fig. 3.2. The two shunt connected schottky diodes are placed on the opposite sides of the circular patch antenna center to realize full wave rectification. Since each diode harvests every alternate cycles. Moreover, the circular patch antenna works as parallel plate capacitor to provide the required LPF operation.

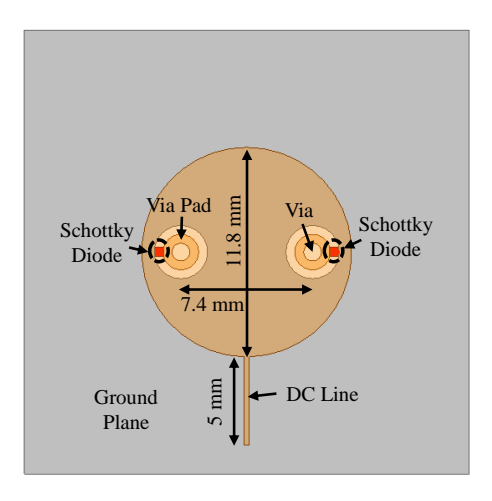


Figure 3.2: Design layout of the proposed single rectenna module.

3.2.2 Circular Integrated Rectenna Array

The proposed multi-polarized rectenna array comprises eight rectenna modules placed at 45° to each other as shown in Fig. 3.3. The dc is picked from the high impedance line (dc

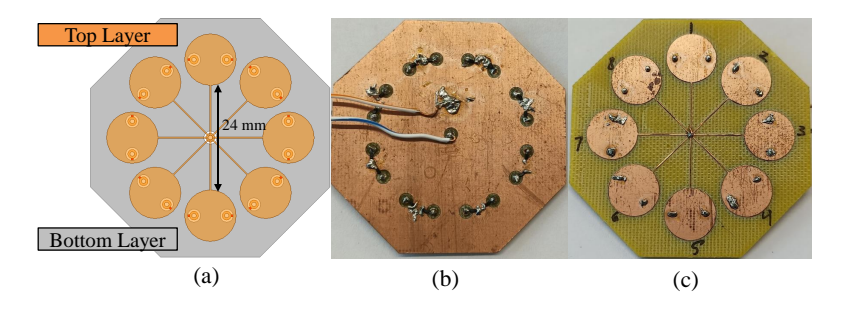


Figure 3.3: (a) Layout of the proposed rectenna array, fabricated prototype (b) Bottom layer, and (c) Top layer.

line) connected in perpendicular to the feed location to achieve high isolation. The dc lines from all the rectenna modules are connected to the via at the center to provide DC output connection between the via and the ground plane. The simulated reflection coefficient of a single rectenna module is evaluated at the port impedance conjugate to the schottky diode impedance and is demonstrated in Fig. 3.4, showing good impedance matching at 5.8 GHz. In addition, the simulated elevation plane pattern of a single rectenna module are also evaluated and are shown in Fig. 3.5, showing a tilt away from the center of the rectenna array. The proposed rectenna achieves the maximum realized gain of 4.2 dBi at 5.8 GHz frequency. Further, the isolation between the rectenna modules is higher than the desirable 20 dB margin with a small footprint of $1.06 \times 1.06 \lambda^2$..

3.2.3 Results and Discussion

The prototype of the proposed circular rectenna array is fabricated and is shown in Fig. 3.3. The performance of the proposed rectenna array is validated by measuring the RF-DC conversion efficiency and the harvested dc power patterns at various orientations. The

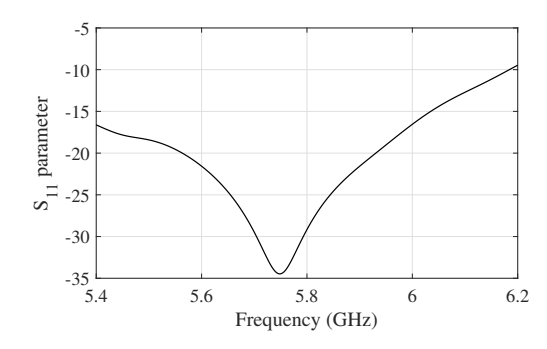


Figure 3.4: Simulated reflection coefficient of the proposed single rectenna module for conjugate impedance matching.

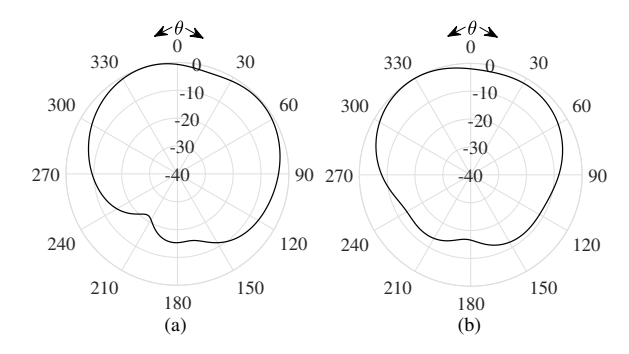


Figure 3.5: Simulated normalized elevation plane RF radiation pattern of the proposed single rectenna module in (a) $\phi = 0^{\circ}$, and (b) $\phi = 90^{\circ}$ elevation plane at 5.8 GHz.

detailed results and their description is discussed in the following subsections.

Measurement Setup

The signal generator transmits RF power of 25 dBm through an 8.6 dBi gain horn antenna (Tx) mounted on an antenna stand. The proposed rectenna array is affixed the turn table at 1 m away from the Tx as shown in Fig. 3.6. The received RF power at rectenna is

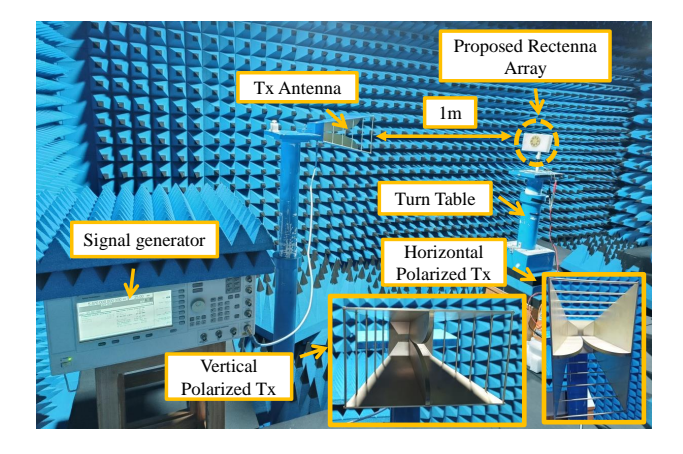


Figure 3.6: Measurement setup for harvested DC power pattern in elevation and azimuth plane.

measured using spectrum analyzer and a multimeter is utilized to measure the harvested DC voltage. The measurement is conducted by placing Tx in both the horizontal and

the vertical polarization to completely analyze the performance of the rectenna array. Although, the measurements can be performed by using a circularly polarized Tx antenna. However, due to resource constraints in the laboratory, the measurement for both the polarization are carried out separately.

Measurement Results

RF-DC efficiency versus load

The harvested DC voltage is measured across the potentiometer to determine the optimal load and the RF-DC conversion efficiency (η). This harvested dc power measurement is conducted for a single rectenna module and the evaluated η plotted against varying load in Fig. 3.7. The results indicate a maximum efficiency of 59.7% is achieved at an optimal load of 650 Ω with 175.8 mV harvested dc voltage.

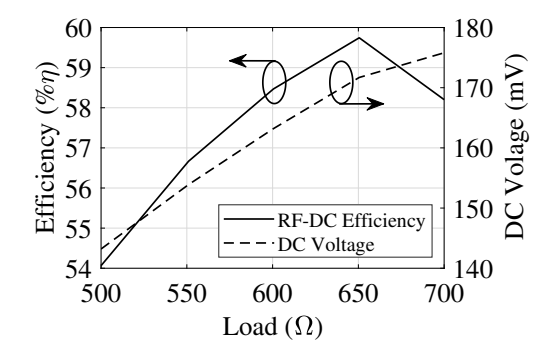


Figure 3.7: Measured RF-DC conversion efficacy (η) versus load for a single proposed rectenna element.

DC Pattern Measurement

The DC power pattern of the rectenna array are evaluated in the elevation as well as azimuth plane to show the performance tolerance against angular misalignment and the polarization mismatch between the Tx and the rectenna array, respectively. The elevation plane DC pattern demonstrated in Fig. 3.8 confirms good tolerance against the angular

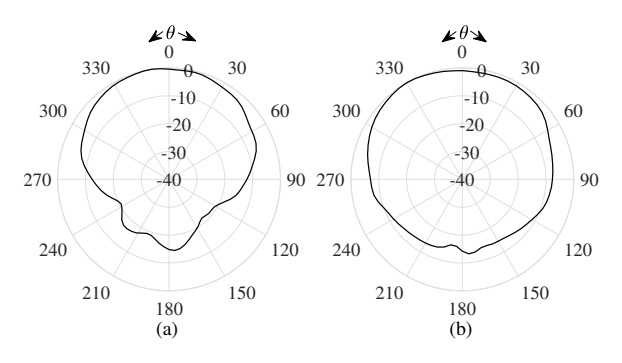


Figure 3.8: Measured normalized DC power pattern of the proposed rectenna array for (a) horizontal, and (b) vertical polarized Tx with Rx rotated in elevation plane

misalignment. Moreover, the harvested dc power variation due to rectenna array rotation

in azimuth plane is shown in Fig. 3.9 for horizontal and vertical polarized Tx. The results

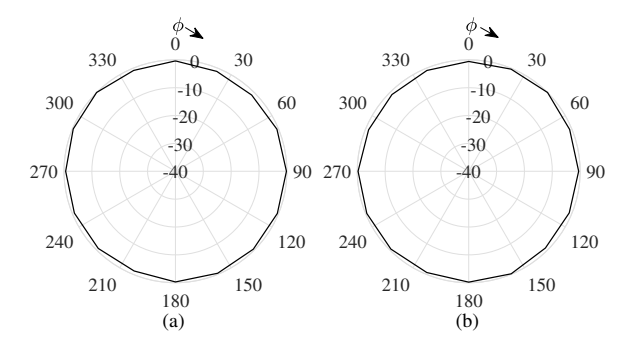


Figure 3.9: Measured normalized DC power pattern of the proposed rectenna array for (a) horizontal, and (b) vertical polarized Tx with Rx rotated in azimuth plane

indicate good tolerance against polarization mismatch and almost uniform harvesting capability in the entire 360° of the azimuth plane. The slight variation in the harvested dc power can be attributed to the fabrication and measurement errors.

The rectenna array discussed herein offers tolerance against angular misalignment in the broadside direction. However, it does not perform effectively in scenarios where the RF energy transmitter is oriented in the plane or end-fire direction. Therefore, to address this issue, the rectenna system should exhibit isotropic coverage [57] with respect to the dedicated RF power transmitter (RF-Tx) for IoT application scenarios like smart homes, smart offices, smart farming, etc. Moreover, the isotropic coverage is suitable for such scenarios due to the presence of multipath RF signals and distributed RF-Txs [120]. In addition, high radiation efficiency [121, 122] with a small footprint is desired to capture the large portion of the RF waves impinging on the rectenna aperture.

3.3 Isotropic Rectenna Array System Design (Design-O3B)

The proposed isotropic coverage ReAS (iReAS) is simulated on a dual-sided 1.56 mm thick FR4 substrate ($\epsilon_r = 4.4$, $\tan \delta = 0.02$) using Ansys HFSS. The detailed description of the proposed iReAS is demonstrated in Fig. 3.10, and the design parameters are listed in Table 3.1. First, a planar ReAS comprising four radially oriented rectenna elements

Table 3.1: Dimensions of the proposed iReAS.

D .	***	***	***	***	***	· r	r	7	· ·	· ·	r	7	_
Parameters	$ W_1 $	$ W_2 $	W_3	$ W_4 $	W_5	L_1	L_2	L_3	L_4	L_5	L_6	L_7	a
Dimension (mm)	3	3	1	0.4	0.8	11.7	3.6	6.8	6	22	7	2.8	8

(ReE) is designed and simulated at 5.9 GHz. A single ReE comprises two radiators, each having a separate reflector ground. The Schottky diode (SMS-7621-079LF) is connected between the RF feed lines which are capacitively coupled with the radiator to obstruct dc backflow into the antenna. Moreover, the feed lines are shorted with their respective grounds through a $\lambda/4$ stub for extracting dc voltage across the Schottky diode to a 10 pF capacitor connected in between the reflector grounds. In addition to providing isolation between the RF signal and the dc output, the $\lambda/4$ short stub suppresses the

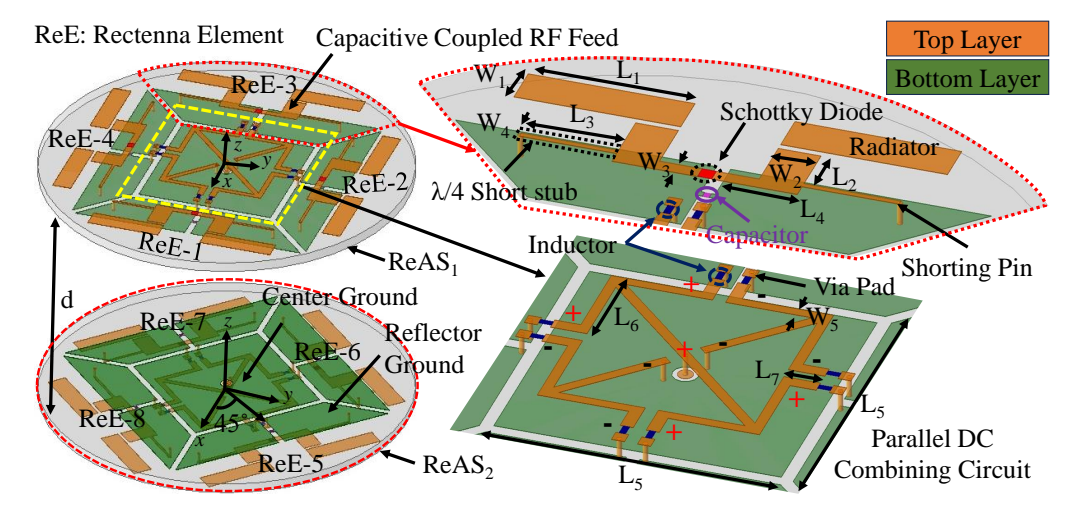


Figure 3.10: Proposed isotropic spherical coverage iReAS.

even harmonic components generated by the Schottky diode. To retrieve the dc voltage across the capacitor for dc combining, reflector grounds are connected to a through-hole via-in-pad on the top layer. Further, 1.5 nH inductors are utilized to connect the via pads with the output dc terminals, isolating the RF signal in the reflector grounds from the dc output. The ReEs in each ReAS are connected in parallel and the total dc output from each ReAS are connected in series to implement the hybrid dc combining topology. The orientation of the Schottky diode terminals in each ReE is reversed (considering circular movement around ReAS) with respect to the adjacent ReE. The proposed scheme enabled simple connection of the positive (+ve) and the negative (-ve) terminals of the adjacent ReEs, resulting in two radially opposite +ve and -ve terminals. A diagonal metal trace (+ve dc trace) integrates the radially opposite +ve terminals. Further, using a shorting via the center point of the +ve dc trace is connected to a dc pad (ReAS +ve terminal) on the bottom layer. On the other hand, the radially opposite -ve terminals are extended beside the +ve dc trace and shorted to the center ground (ReAS -ve terminal) to maintain structural symmetry. Since each ReAS harvest RF power in any random orientation, their dc outputs are connected in series to achieve high dc output voltage.

3.3.1 Simulation Results and Discussion

The Schottky diode impedance $Z_d = R_d + jX_d$ ($R_d = 20\,\Omega$, $X_d = 120\,\Omega$) is evaluated using the LSSP and HB technique in Keysight ADS software for $-10\,\mathrm{dBm}$ input power level at 5.9 GHz. This Schottky diode is selected for its low junction capacitance, high cut-off frequency, and excellent power threshold efficiency within a low-input RF power range. The ReAS design is optimized to conjugate match the input impedance ($Z_{ReAS} = R_{ReAS} + jX_{ReAS}$) of each ReE with $Z_d = R_d + jX_d$, as shown in Fig. 3.11 (a). In addition, the optimal output load is evaluated to $1.5\,\mathrm{k}\Omega$ at $-10\,\mathrm{dBm}$ input power. Moreover, the design parameters of the ReAS are optimized to realize wide beam coverage (1 dB beamwidth of $\sim 90^\circ$) along the elevation planes ($\phi = 0^\circ$, 45°, and 90°), as demonstrated in Fig. 3.12 (a). On the other hand, the RF pattern in the azimuth plane

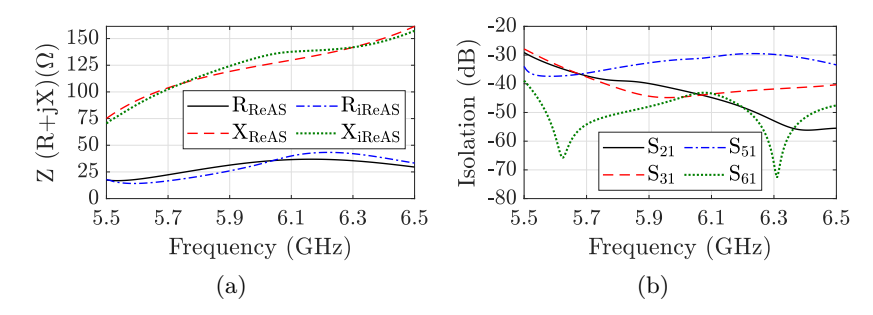


Figure 3.11: (a) Input impedance of a ReE in the proposed ReAS and iReAS, (b) Isolation between adjacent ReE in iReAS.

 $(\theta=90^\circ)$ has a narrow 1 dB beamwidth of $\sim 40^\circ$, as shown in Fig. 3.12(b). Thus the normalized gain value of adjacent rectenna elements at the overlapping angle is less than the required $-0.8\,\mathrm{dB}$ to achieve uniform azimuth coverage [118]. Therefore, as illustrated in Fig. 3.10, a second ReAS (ReAS₂) is placed vertically in mirror position (xoy as reference plane) and at 45° relative angular offset in the azimuth plane with respect to ReAS₁. The distance $d=8\,\mathrm{mm}$ is the minimum space required between the ReAS₁ and ReAS₂ for achieving the enhanced elevation and azimuth plane coverage. Moreover, the space between the two ReASs can be utilized for integrating power management unit (PMU), sensors, data processing and RF communication circuitry to realize a compact wireless sensor node. The 1 dB beamwidth of a ReE in the proposed iReAS is enhanced to about 180° in the elevation plane, as demonstrated in Fig. 3.13. In addition, the azimuth

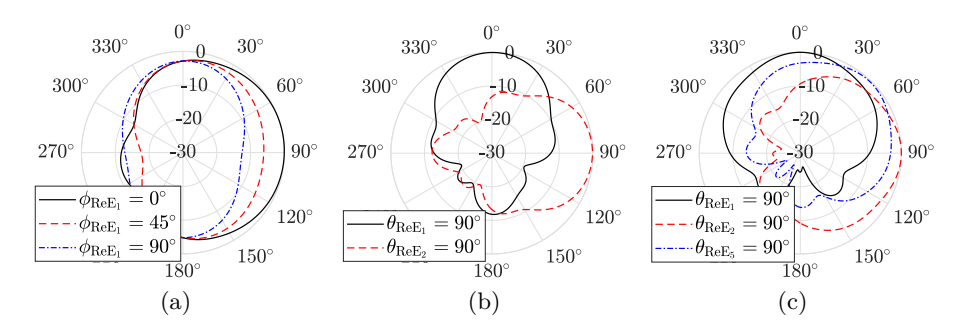


Figure 3.12: (a) Elevation plane ($\phi = 0^{\circ}, 45^{\circ}, 90^{\circ}$) RF patterns of an ReE in ReAS, and Azimuth plane ($\theta = 90^{\circ}$) RF patterns of (b) ReE₁ and ReE₂ of single ReAS, and (c) ReE₁, ReE₂, and ReE₅ in the proposed iReAS.

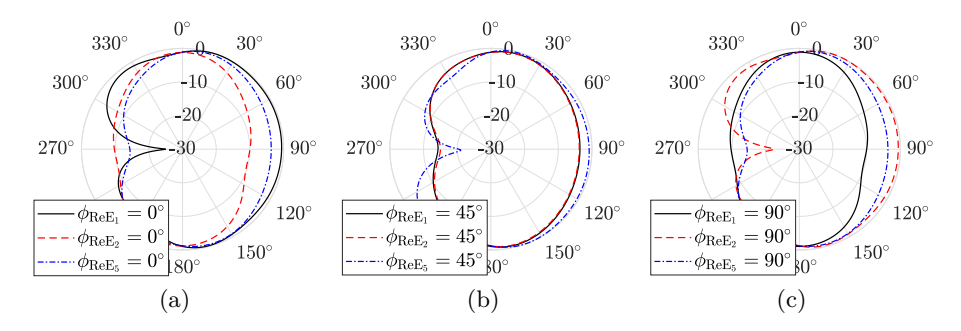


Figure 3.13: (a) $\phi = 0^{\circ}$, (b) $\phi = 45^{\circ}$, and (c) $\phi = 90^{\circ}$ elevation plane RF patterns of rectenna ReE₁, ReE₂ and ReE₅ in the proposed iReAS.

plane radiation patterns of ReE₁, ReE₂, and ReE₅ are demonstrated in Fig. 3.12(c), indicating a normalized gain value of $\sim 1\,\mathrm{dB}$ at the overlapping angle. The results validate the capability of the proposed iReAS to achieve a near-uniform dc power pattern in the azimuth plane. Further, the Z_{iReAS}, as illustrated in Fig. 3.11(a) show a small variation from Z_{ReAS}, indicating low mutual coupling between ReAS₁ and ReAS₂ and is verified by the isolation plots in Fig. 3.11(b). Although, the maximum gain of a single ReE (G_{ReE}) reduces from 5.27 dBi for ReAS to 3.12 dBi in the proposed iReAS. However, the reduction in gain is compensated by the additional dc output of ReAS₂ along with the advantage of achieving the desired isotropic spherical coverage.

3.3.2 Experimental Verification

The performance of the proposed system is measured using the experimental setup, as demonstrated in Fig. 3.14. The iReAS is mounted on a turn table and illuminated with

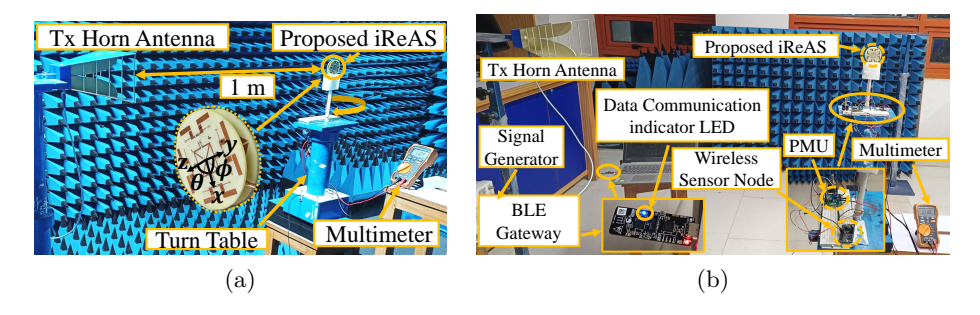


Figure 3.14: (a) Experimental setup to measure performance of iReAS, (b) wireless sensor node operation utilizing power management unit (PMU) with iReAS.

RF waves emanated by a transmitter (Tx) horn antenna positioned at a distance of r=1 m. The RF power ($P_t=25\,\mathrm{dBm}$) is fed into the Tx, having a gain $G_t=11\,\mathrm{dBi}$, using a signal generator through an RF cable with a loss of $L_c=1.8\,\mathrm{dB}$. The dc voltage supplied by iReAS is measured using a digital multimeter and the captured RF received (P_r) at the antenna aperture is evaluated using the Friis transmission equation. Initially, the open-circuit dc voltage (V_{dc}^{oc}) is measured at different orientations in the azimuth and the elevation planes. The measured V_{dc}^{oc} patterns (in dBV) are illustrated in Fig. 3.15.

The results indicate a uniform dc voltage pattern in the $\theta=90^{\circ}$ plane, whereas in the case of elevation plane patterns, the maximum variation in voltage is within 1.5 dBV at certain angles. The measured DC patterns corroborate the RF patterns discussed in Section II, and any slight deviations can be attributed to fabrication and measurement errors, indicating near-isotropic coverage. The output DC voltage (V_{dc}) is measured, and the PCE is evaluated across different load values $(R_L=0.25\,\mathrm{k}\Omega$ to $6\,\mathrm{k}\Omega)$ for both the proposed ReAS and iReAS. The results are presented in Fig. 3.16. The measurements are carried out by placing the Tx in $(\theta=0^{\circ})$, $(\theta=180^{\circ})$, and $(\theta=90^{\circ}, \phi=0^{\circ})$ direction with respect to the proposed iReAS. The $\theta=0^{\circ}$ ($\theta=180^{\circ}$) corresponds to broadside direction in upper hemisphere (lower hemisphere), whereas $\theta=90^{\circ}, \phi=0^{\circ}$ corresponds to endfire direction. The adopted measurement scheme determine the variation of PCE and

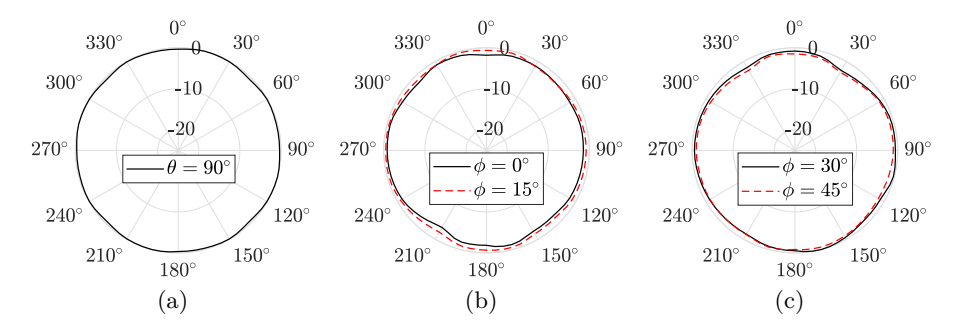


Figure 3.15: Normalized V_{dc}^{oc} (in dBV) (a) $\theta = 90^{\circ}$ azimuth plane pattern, (b) $\phi = 0^{\circ}$, 15° and (c) $\phi = 30^{\circ}$, 45° elevation plane patterns at 5.9 GHz.

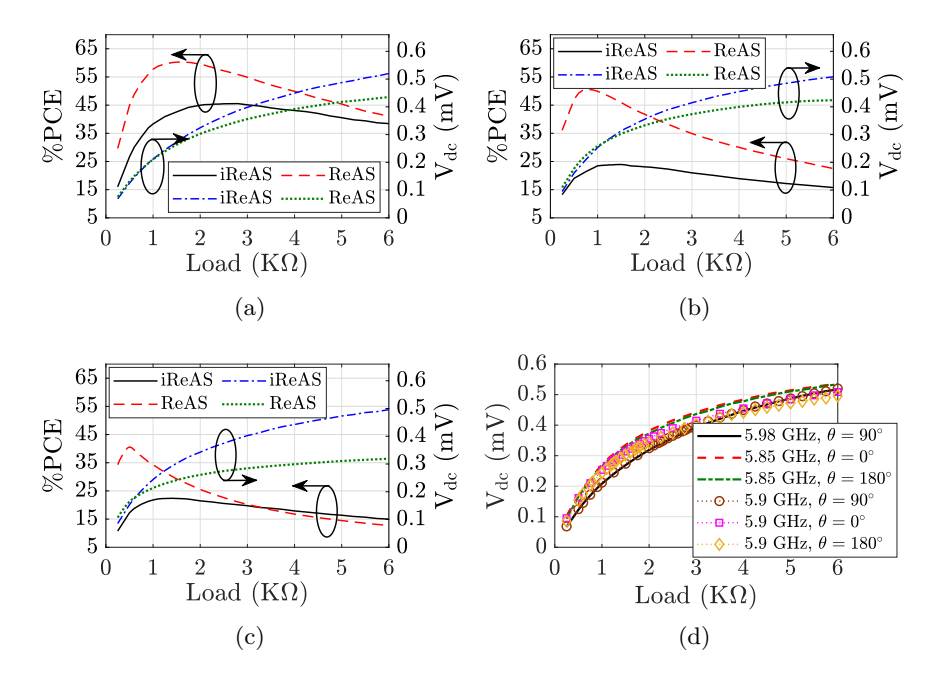


Figure 3.16: Measured PCE and V_{dc} versus Load for proposed iReAS and ReAS with Tx placed along (a) $\theta = 90^{\circ}$, $\phi = 0^{\circ}$ (b) $\theta = 0^{\circ}$, and (c) $\theta = 180^{\circ}$ direction (d) V_{dc} at various frequencies.

dc voltage from broadside to the endfire direction in 3D space.

The results shown in Fig. 3.16(a) specify the maximum PCE of 45.54% (60.3%) at $2.8\,\mathrm{k}\Omega$ (1.6 k Ω) load for iReAS (ReAS) with Tx positioned in the endfire direction. Similarly, in the upper and lower hemisphere broadside direction the maximum PCE is 23.94% (50.6%) at $1.5\,\mathrm{k}\Omega$ (802 Ω) load and 22.37% (40.6%) at optimal load of $1.4\,\mathrm{k}\Omega$ (500 Ω), as demonstrated in Fig. 3.16(b) and Fig. 3.16(c), respectively. Moreover, the variation in harvested dc voltage of iReAS is $\sim 1.56\,\mathrm{dBV}$ and corroborates the near-isotrpic harvested V_{dc}^{oc} results illustrated in Fig. 3.15. Further, the measurement of dc voltage at different frequencies is also carried out and are depicted in Fig. 3.16(d). The results specify higher harvested dc voltage at 5.85 GHz than 5.9 GHz for Tx placed in $\theta = 0^{\circ}$, 180° direction, whereas for $\theta = 90^{\circ}$, $\phi = 0^{\circ}$ the dc voltages are almost identical at 5.9 GHz and 5.98 GHz. The results imply close to uniform harvesting capability in 5.85 GHz to 5.98 GHz frequency

range.

3.3.3 Performance comparison with state-of-the-art

Table 3.2: Performance comparison with state-of-the-art

	Freq	Peak	RF	Combining	V_{dc}^{oc}	optimal	Near	size
	(GHz)	PCE	Input	Topology	(mV)	load	Isotropic	(mm^3)
		(%)	(dBm)			$(k\Omega)$	dc pattern	
[61]	2.42	42*	-11.61*	RF	~ 1400	5.1*	No	130×130
[01]	2.42	42	-11.01	101	1400	0.1	110	$\times 290$
[62]	5.2	49*	-10*	DC	~ 600	1.2*	No	74×74
[02]	0.2	40	10	DC parallel	1 000	1.2	110	$\times 1.56$
[63]	5.8	69.1*	-10*	DC	~ 600	1 28*	No	130×130
[00]	0.0	03.1	-10	DC parallel	" 000	1.28* 0.64**	110	$\times 1.56$
Design-	5.85 -	61.96*	-11.26*	DC	~ 1103	1.6*	Yes	60×60
O3B	5.98	45.54**	-9.31**		1103	2.8**	res	$\times 11.12$

^{*}single rectenna element (ReE); **complete rectenna system (iReAS)

The comparison of the proposed iReAS system (Design-O3B) with the state-of-the-art 3D coverage rectenna system is illustrated in Table 3.2. The proposed iReAS achieves near isotropic coverage with harvesting capability in the frequency range of 5.85 GHz to 5.98 GHz, compared to the single frequency operation of existing designs. In [61], a five-sector rectenna system is proposed to provide 360° azimuth coverage with each sector comprising a vertically orientated linear array of four rectangular patch antennas. Each patch antenna is connected to a four port beamforming network (BFN) for easy implementation of multi beam coverage in the elevation plane, resulting in a bulky 3D system design, which makes it unsuitable for small sensor nodes. To overcome the challenges of a large footprint, parallel dc combining designs [62, 63] have been proposed. The parallel combining does reduce circuit losses, however, it results in low output do voltage and optimal load of the system, rendering it unsuitable for battery-less operation. In contrast, the hybrid dc combining utilized in proposed design enhances the dc voltage and optimal load with a smaller footprint. Moreover, the realized single-element efficiency of 61.96% (P_r = -11.26 dBm) is close to the reported works. Although the optimal load $(1.6 \,\mathrm{k}\Omega)$ is less than that achieved in [61] $(5.1 \,\mathrm{k}\Omega)$. However, for the complete system (iReAS) a maximum PCE of 45.54% is achieved at $2.8 \,\mathrm{k}\Omega$ optimal load, with only $\sim 5\%$ variation in PCE for $1 \text{ k}\Omega$ - $5 \text{ k}\Omega$ load range, as depicted in Fig. 3.16(a).

IoT devices integrated with rectenna modules necessitate a separate antenna for WIT, leading to a complex receiver design that complicates SWIPT operation. To address this challenge, we propose SWIPT antennas for ultra low power IoT devices that are capable of concurrent WIT and WPT operations, thereby enabling a more compact receiver design. In the subsequent sections of this chapter, we present novel SWIPT antenna designs developed through an evolutionary design process, incorporating an innovative SWIPT technique aimed at facilitating battery-less operation of ultra-low-power IoT devices. The primary focus of these designs is not angular misalignment tolerant WPT operation but to create a highly compact system that supports SWIPT using a single antenna element.

Additionally, the designs are engineered to attain a wide WIT bandwidth comparable to that of access point antenna systems.

3.4 SWIPT Antenna For Ultra Low Power IoT Devices

The wireless power transfer (WPT) technique has emerged as the most popular choice [12, 119] as it provides easy integration with the existing communication circuitry. Moreover, sensor nodes collect information related to the surrounding environment and communicate it with a remote gateway through a wireless information transfer (WIT) antenna. However, housing two separate antenna modules for WPT and WIT respectively, would result in a bulky prototype. To smaller their size, several research works have recently been reported towards implementing simultaneous wireless information and power transmission (SWIPT) antenna to achieve concurrent data and power transfer to remote sensor nodes [4]. This chapter proposes and investigates miniaturized integrated SWIPT antenna having high WIT efficiency, wide WIT bandwidth and high PCE at ultra-low input RF power for WPT in SWIPT application scenarios. A novel SWIPT technique demonstrated in Fig. 3.17 is introduced, where a SWIPT single antenna system uses frequency splitting and dual

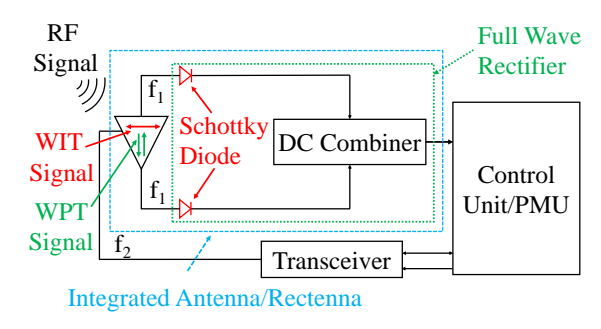


Figure 3.17: The proposed SWIPT technique.

polarization techniques, resulting in an integrated, miniature, dual-purpose circular patch antenna.

3.4.1 System Architecture

A 50 Ω antenna for WIT at 5.8 GHz (5.7 GHz - 6 GHz) [123], with a bore-sight radiation pattern is targeted first. It is followed by a direct conjugate-matched, dc-combined, to fully integrate within the same structure for WPT with optimum PCE at 5.2 GHz, since low frequencies achieve greater transmission distances (Friis equation) [71]. High isolation between the WIT and WPT is important since the information signal can leak power into the rectifier circuit due to mutual coupling; low isolation reduces the information signal strength, resulting in low communication link quality. A typical application scenario for the proposed SWIPT antenna is illustrated in Fig. 3.18, which shows a SWIPT-enabled IoT sensor node informing wirelessly sensed data either directly through a remote gateway or a mobile drone communication relay. These sensor nodes can harvest RF power from a

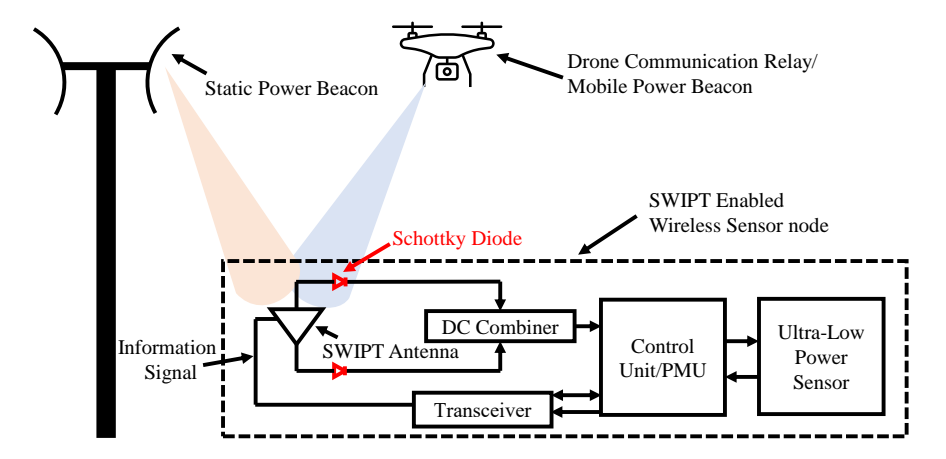


Figure 3.18: Application scenario for the proposed SWIPT antenna.

locally installed static or mobile drone power beacons and be used in vast IoT applications, including smart homes, smart warehouses, smart farming, smart transportation, etc.

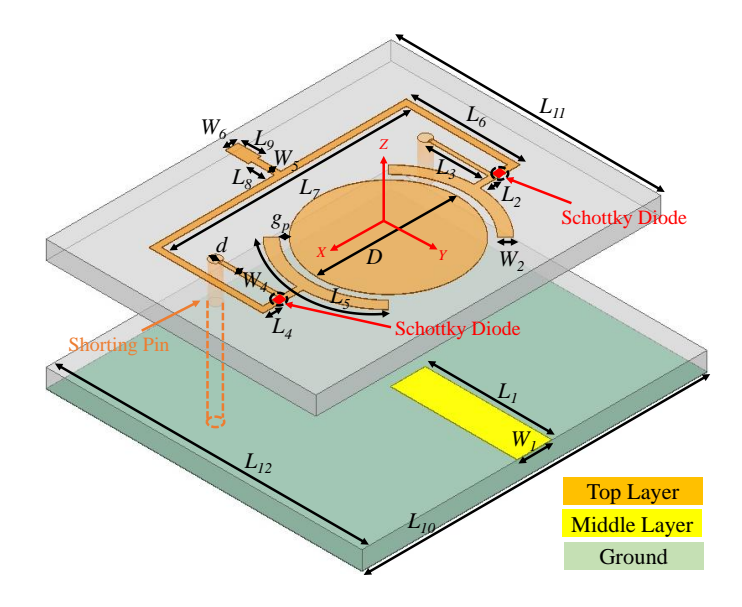


Figure 3.19: Exploded view of the proposed SWIPT antenna.

3.4.2 Description of Proposed SWIPT Antenna (Design-O4A)

The proposed antenna is designed using Ansys HFSS on FR4 substrate ($\epsilon_r = 4.4$, $\tan \delta = 0.02$) having 1.6 mm thickness with 35 μ m copper cladding. The rectifier circuit analysis is carried out in advanced design system (ADS) software. The final design layout is given in Fig. 3.19, indicating various design parameters listed in Table 3.3. The equivalent circuit

Table 3.3: Dimensions of the proposed SWIPT antenna.

Parameters	W_1	W_2	W_3	W_4	W_5	W_6	L_1	L_2	L_3	L_4	L_5	L_6	L_7	L_8	L_9	L_{10}	L_{11}	L_{12}	D	d	g_p
Dimension (mm)	3	1	0.55	0.35	0.55	1.1	11	1.6	5.23	1.37	10.52	9.9	21.25	2	2	30	23.45	27.45	12.2	0.5	0.6

diagram of the proposed SWIPT antenna is shown in Fig. 3.20, detailing its working

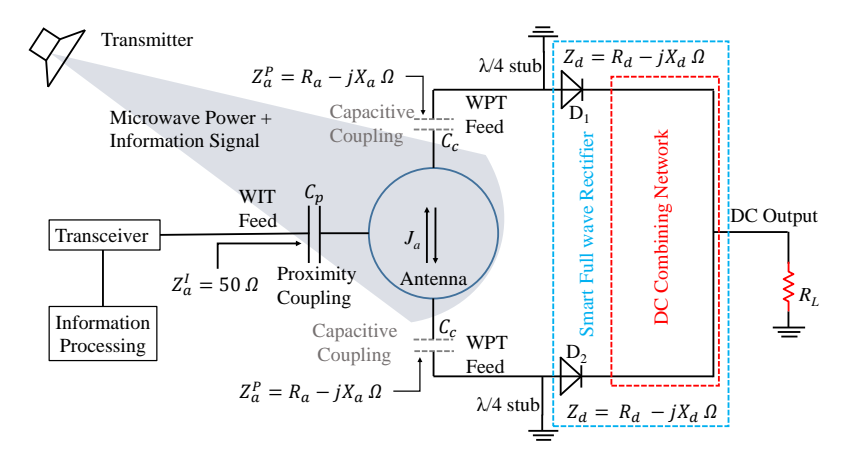


Figure 3.20: Equivalent circuit diagram of the proposed SWIPT antenna.

mechanism. The capacitor C_p represents the proximity coupled WIT feed with $Z_a^I = 50~\Omega$ input port impedance which can be connected to the transceiver for WIT post processing. Two co-polarized fringing field harvesters are capacitively coupled to the patch and represented by capacitors C_c with an input port impedance $(Z_a^p = R_a + jX_a~\Omega)$ that is conjugately matched to the Schottky diode impedance $(Z_d = R_d - jX_d~\Omega)$, which acts as an RF choke by inhibiting DC backflow to the antenna while permitting the integration of the FWR to the circular patch. The WPT feed lines are orthogonal with respect to the WIT feed to achieve high isolation between the WIT and the WPT signals. In Fig. 3.20, from a transmitter RF waves impinging on the SWIPT antenna generate TM₁₁₀ mode current on the circular patch surface. The current direction, denoted by J_a (Fig. 3.20), changes in each subsequent half cycle of the incident RF wave and is noted with two arrows in opposite direction. Therefore, to convert the RF power every half cycle into usable DC energy, the two Schottky diodes are connected in mirror symmetry (diode's anode facing to the circular patch) with respect to the circular patch center.

Fig. 3.21 shows the current distribution in the SWIPT antenna when diodes D_1 and D_2 are

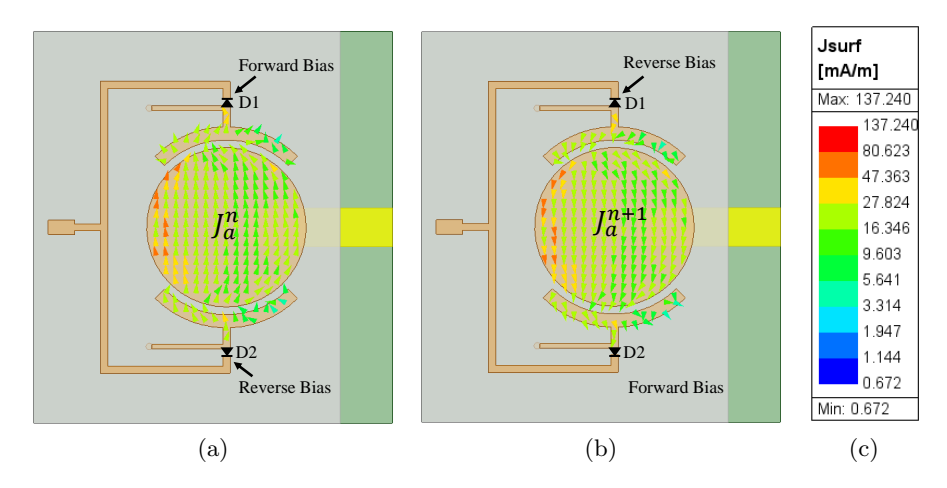


Figure 3.21: Current distribution on the proposed SWIPT antenna for (a) forward bias of D1, (b) forward bias of D2, and (c) range.

in excitation. Fig. 3.22 shows the working principle of the FWR by voltage sources V_{D1-D2}

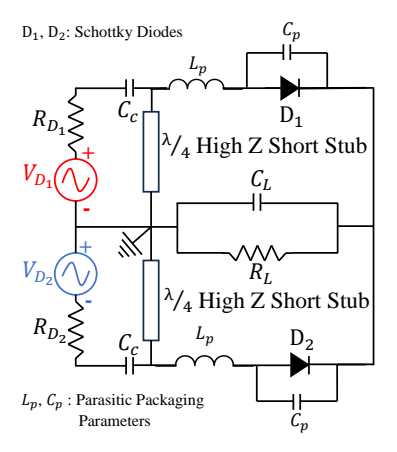


Figure 3.22: Working Principle of the FWR in the proposed SWIPT antenna.

having an internal impedance of R_{D1-D2} . The surface current is excited (J_a^n) in patch antenna during the n^{th} half cycle of incident RF wave forward bias Schottky diode D_1 . In the next $(n+1^{th})$ half cycle, the surface current (J_a^{n+1}) flows in reverse direction to J_a^n , forward biasing Schottky diode D_2 . In reverse bias conditions, the Schottky diode does not contribute to the dc output and acts as an open load, indicating high S_{21} and S_{12} isolation between the ports. Further, the cathode terminals of both diodes are joined together through dc connection lines to combine output dc voltage in subsequent half cycles. This dc terminal grounds through an output load (R_L) using a $\lambda/4$ short stub connected to the anode of each Schottky diodes to provide necessary isolation between the RF signal and dc output as well as suppress even order harmonics that are generated by the Schottky diodes [124]. Unlike other literature, the proposed SWIPT antenna achieves FWR by dc combining a dual half-wave rectification (HWR) out of the two diodes that are integrating two co-polarized ports of a single circular patch antenna. The step-by-step design process with a detailed explanation of the evolution of the proposed SWIPT antenna is discussed in the subsequent subsection.

3.4.3 Circuit Simulation and Design Evolution

The analysis of non-linear rectifier circuit (SMS7621 – 079LF Schottky diode) is conducted using the HB and LSSP technique in the ADS software. These specific techniques facilitate the characterization of the nonlinear current-voltage characteristics of the diode through Fourier series expansion. The SMS7621 – 079LF Schottky diode was employed for the rectifier circuit due to its low junction capacitance, high cutoff frequency, and excellent power threshold sensitivity for low incoming RF signals [125]. The Schottky Diode SPICE parameters from the manufacturer's data sheet [126] allowed us to model it in ADS while iteratively accounting for the parasitic packaging parameters (L_p , C_p) when the input RF power was $-10 \, \mathrm{dBm}$ at $5.2 \, \mathrm{GHz}$ frequency. That set the input impedance ($Z_d = 25 - j75 \, \Omega$) for the design. The 1 k Ω resistance was taken as reference load to conjugate match the antenna's impedance with the Schottky diode impedance [127]. Corresponding to this impedance, the proposed SWIPT antenna was optimized in Ansys HFSS with conjugate

impedance matching with Schottky diode impedance. This approach was selected to reduce insertion losses and the footprint of the overall SWIPT system. The detailed design procedure is elaborated using a flowchart in Fig. 3.23. To start the design process

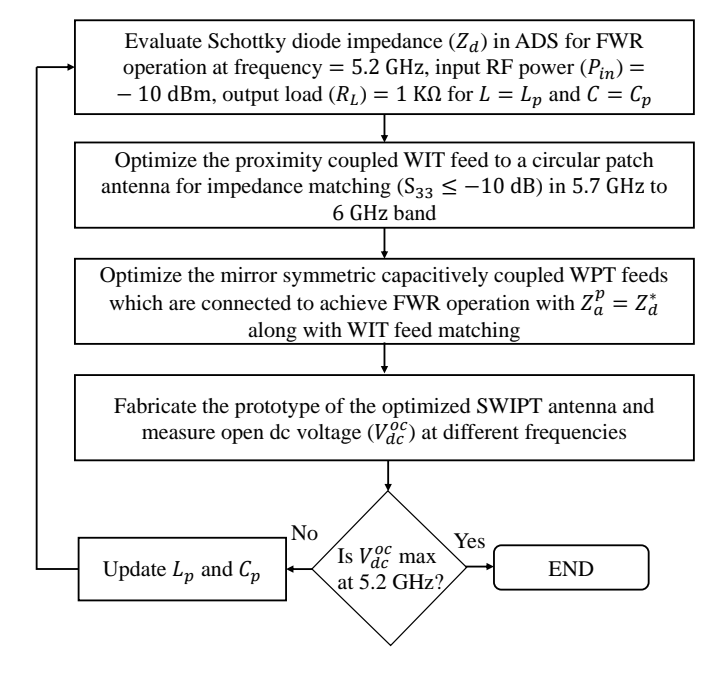


Figure 3.23: Detailed design procedure of the proposed SWIPT antenna.

the initial value of L_p is taken as 3.7 nH which is the addition of packaging inductance of the Schottky diode (0.7 nH) and the series inductance due to the dc combining circuit (~ 3 nH). On the other hand, the initial value of C_p is taken as 0.15 pF. The considered range for L_p and C_p are 3.5 nH to 4 nH and 0.05 pF to 0.15 pF, respectively, resulting in twenty five iterations of the design process to achieve the conjugate impedance matching at 5.2 GHz. The design evolution of the proposed SWIPT antenna is illustrated in Fig. 3.24. The proposed antenna comprises a three-layer structure implemented using two FR4

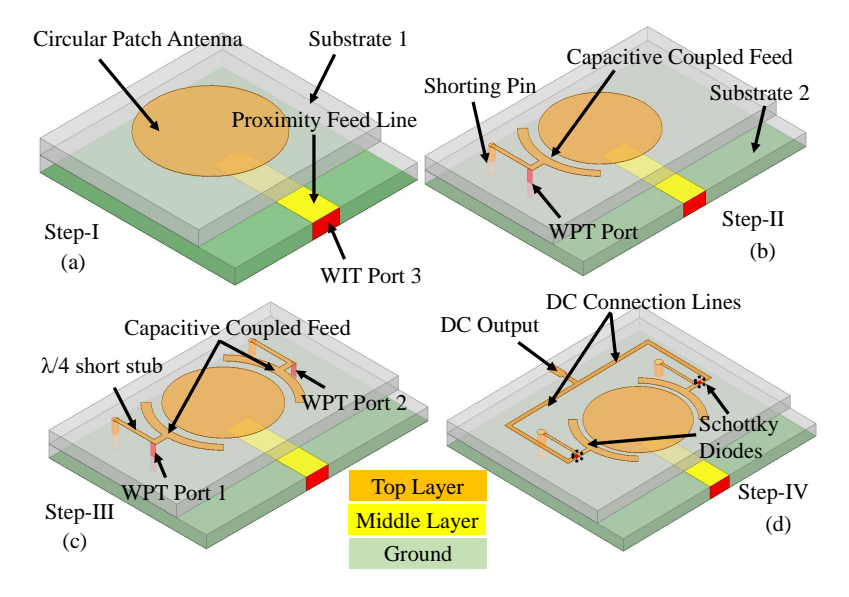


Figure 3.24: Design evolution of the proposed SWIPT antenna.

substrates (substrate 1 and substrate 2) to achieve wider impedance matching for WIT. Moreover, a circular patch geometry was preferred as the main radiator as it possesses the natural ability to reject harmonics $(nf_0, n \in \mathbb{Z})$ generated by diodes, since it resonates at frequencies that are non-integer $(n \notin \mathbb{Z})$ order [128] of the fundamental frequency. Initially (Step-I), the patch was excited with a proximity-coupled microstrip feed line for WIT as illustrated in Fig. 3.24(a). The antenna design parameters were then optimized to achieve the desired impedance (Z_a^I) bandwidth (5.7 GHz-6 GHz) and is demonstrated in Fig. 3.25 (a) for each evolution step. In step-II, a capacitively coupled WPT feed was

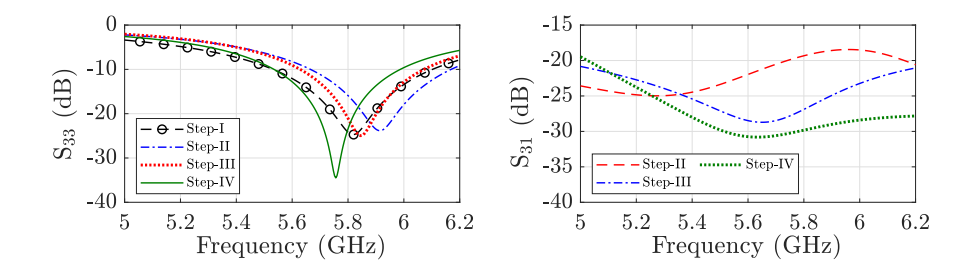


Figure 3.25: (a) Simulated reflection coefficient (S_{33}) of the WIT Port, and (b) Isolation (S_{31}) between the WIT and WPT ports at various design evolution stages of the proposed SWIPT antenna.

cross-polarized with respect to the WIT feed, as shown in Fig. 3.24(c). This arrangement achieved high isolation between information (WIT) and power signals (WPT) greater than 23 dB as confirmed in Fig. 3.25 (b). Moreover, the capacitive coupling technique [129], between the WIT and the WPT, inhibited dc back-flow into the antenna's radiator and enabled good conjugate impedance matching between the antenna's radiator (Z_a^P) and the dc rectifier circuit (Z_d). A $\lambda/4$ high impedance short stub transformer [130] was employed to choke RF signal flowing into the ground while passing dc from the rectifier to the output load (R_L). In step-III, shown in Fig. 3.24 (c), an additional co-polarized

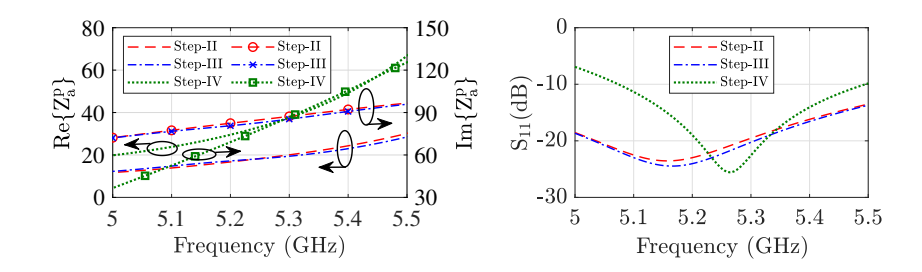


Figure 3.26: (a) Real and Imaginary part of the WPT port input impedance and respective (b) S_{11} at various design evolution stages of the proposed SWIPT antenna.

WPT port 2 was incorporated by connecting a Schottky diode in mirror symmetry to the one connected to WPT port 1. In the final step-IV, the dc outputs from both WPT ports 1 and 2 (Fig. 3.24 (c)) are meticulously brought into a single DC Output terminal using a microstrip line combiner, Fig. 3.24 (d), to achieve a FWR, as described

in earlier section 3.4.2. Fig. 3.26 (a) shows the real and imaginary part of the WPT port input impedance at various design evolution stages of the proposed SWIPT antenna. Fig. 3.26 (b) illustrates the corresponding impedance matching (S_{11}) of the WPT port using (3.1)

$$S_{11} = 20 \log_{10} \left| \frac{Z_a^p - Z_d^*}{Z_a^p + Z_d^*} \right|$$
 (3.1)

for determining the optimal matching of the FWR network. That favored an integrated, miniature, dual-purpose circular patch antenna operating between 5.7 GHz - 6.0 GHz for SWIPT using the proximity coupled feed to the radiative circular patch for WIT. The integrated capacitive coupled feeding network, with FWR, allow to regenerate the opposite fringing fields from the radiating edges of the patch for energizing IoT sensors by means of WPT.

3.4.4 Simulation Results and Discussion

The simulated S_{11} of the circular patch antenna (the WIT) is shown in Fig. 3.25 (a) (Step-IV curve). It shows an impedance bandwidth between 5.53 GHz - 6.0 GHz for WIT. In addition, the tailored SWIPT antenna geometry (Table 3.3) allowed the input impedance of the WPT (29.67+j69.43) Ω to optimally conjugate match the FWR network (25 - j75) Ω covering dual-purpose applications in SWIPT. Furthermore, an isolation (S₂₁) of 24 dB at WPT frequency and \geq 28 dB in the entire WIT band of operation is achieved as illustrated in Fig. 3.25 (b) (Step-IV curve). This helps inhibiting the leakage of information signal from the WIT into the FWR network for improved SNR communications while regenerating the opposite fringing fields from the radiating edges of the patch for energizing IoT sensors. The simulated radiation patterns (normalized)

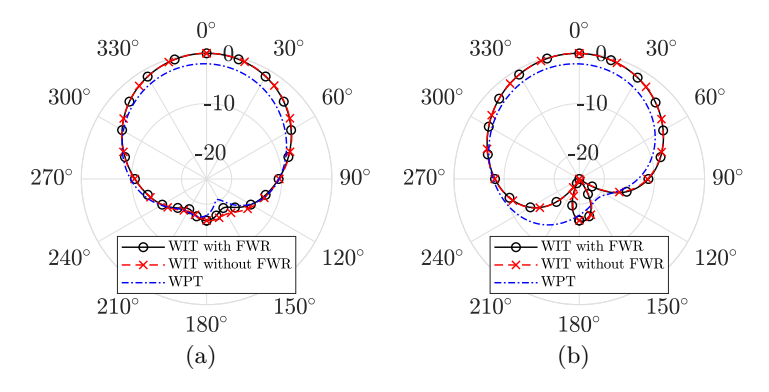


Figure 3.27: Simulated radiation pattern (normalized) of the WIT (with and without FWR) and WPT, for (a) $\phi = 0^{\circ}$, and (b) $\phi = 90^{\circ}$ elevation plane at 5.8 GHz and 5.2 GHz, respectively.

of the SWIPT antenna in the WIT and WPT modes are depicted in Fig. 3.27 (a) and Fig. 3.27 (b), respectively. Results show 5.7 dBi and 3.65 dBi, respectively for the WIT (with and without FWR) and WPT. The $\phi = 0^{\circ}$ and $\phi = 90^{\circ}$ elevation plane patterns for the proposed SWIPT antenna in the WIT mode (WPT mode) have 3 dB beamwidth of 84° and 92° (100° and 108°), respectively. That corresponded to a high radiation efficiency of

80.97% for the WPT operation at $5.2\,\text{GHz}$ and > 78% for the WIT operation (with and without FWR).

3.4.5 Antenna Fabrication and Measurement

Fabrication and Measurement Setup

The proposed SWIPT antenna was fabricated using a MITS PCB prototyping machine. The detailed description of the prototyped antenna is given in Fig. 3.28. The WIT mode

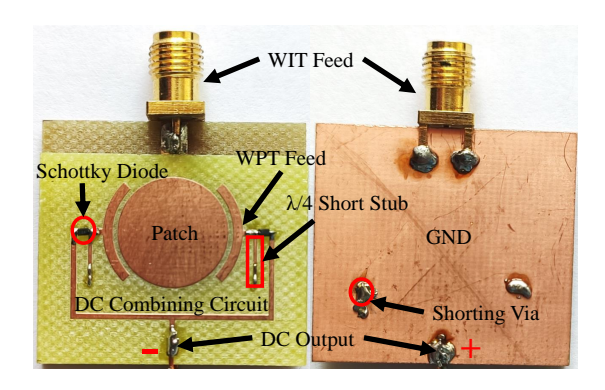


Figure 3.28: Fabricated prototype of the proposed SWIPT antenna.

performance was measured using a Keysight PNA-L (N5234B) VNA. All the measurements were carried out in an anechoic chamber as illustrated in Fig. 3.43(a). To measure the WPT mode performance, a horn antenna was used as a transmitter (Tx) and fed by an RF signal generator. The proposed SWIPT antenna was mounted on the turn table and at d distance from the Tx horn antenna. The received RF power at the antenna aperture was measured using a Keysight spectrum analyzer (N9951A), and the harvested dc voltage measured across the dc output terminals (Fig. 3.28) using a Keysight multimeter (U1232A). The WPT measurements are carried out in an anechoic chamber as shown in Fig. 3.43(b). A detailed description of the WPT link budget used in the measurements is listed in Table 3.4.

Table 3.4: Link Budget parameters

WPT Transmitter and Propagation Parameters										
Frequency (f)	$5.2\mathrm{GHz}$									
RF Signal generator power (P_t)	$25\mathrm{dBm}$									
Measured Cable Loss (L_c)	$2.3\mathrm{dB}$									
Transmitter antenna (horn) gain (G_t)	$10.5\mathrm{dBi}$									
EIRP $(P_t + G_t - L_c)$	$33.2\mathrm{dBm}$									
Distance (d)	1 m									

Measurement Results and Discussion

Impedance matching and Pattern measurements

The reflection coefficient (S_{33}) of the WIT port was measured by using Keysight PNA-L and is shown in Fig. 3.30. The measured S_{33} results reflect good agreement with simulation

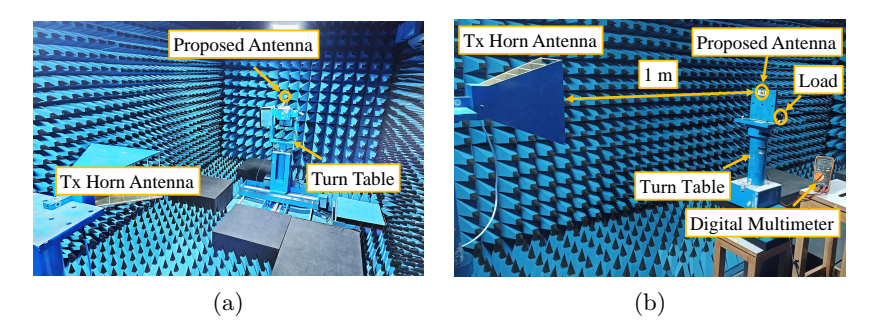


Figure 3.29: Experimental setup in an anechoic chamber for measuring (a) the proposed SWIPT antenna's radiation pattern, and (b) it's DC power pattern and PCE.

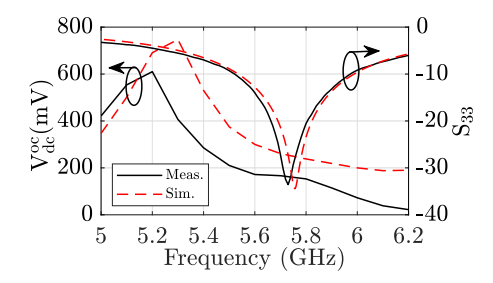


Figure 3.30: Measured reflection coefficient (S_{33}) port and output open dc voltage (V_{dc}^{oc}) of the proposed SWIPT antenna.

results for the proposed SWIPT antenna that achieves an impedance bandwidth of $5.7\,\mathrm{GHz}$ - $6.0\,\mathrm{GHz}$. The conjugate impedance matching poses difficulties in measuring FWR impedance on the Vector Network Analyzer (VNA) in the absence of a balun probe. As an alternative to validate the conjugate impedance matching of the FWR circuit, harvested open dc voltage (V_{dc}^{oc}) is measured for input RF signals ranging from $5\,\mathrm{GHz}$ - $6.2\,\mathrm{GHz}$ using the measurement setup shown in Fig. 3.43. The results shown in Fig. 3.30 illustrate voltage maxima ($610.2\,\mathrm{mV}$) at $5.2\,\mathrm{GHz}$, demonstrating precise impedance matching of the FWR at the desired frequency and in agreement with the simulated WPT port impedance matching (S_{11}) given in Fig. 3.26 (b) (Step-IV curve). The measured radiation patterns of the WIT are depicted in Fig. 3.31, revealing a commendable alignment with the simulation results presented in Fig. 3.27. The results indicate a very insignificant effect of the Schottky

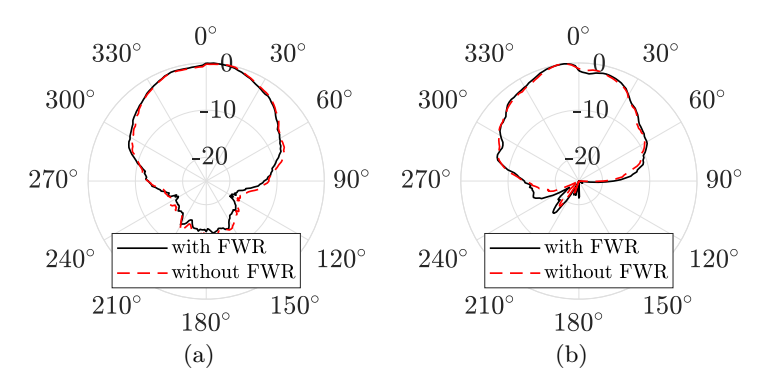


Figure 3.31: Measured radiation patterns (normalized) of the WIT in (a) $\phi = 0^{\circ}$, and (b) $\phi = 90^{\circ}$ elevation plane at 5.8 GHz with and without Schottky diode.

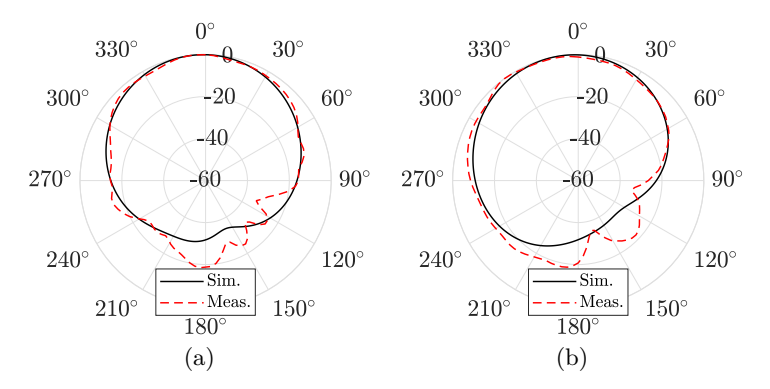


Figure 3.32: Simulated and Measured dc power patterns (normalized) of WPT in (a) $\phi = 0^{\circ}$, and (b) $\phi = 90^{\circ}$ elevation plane at 5.2 GHz.

diode on the radiation patterns, and gains of 5.65 dBi and 5.57 dBi is noted with and without the FWR network. The measured $\phi = 0^{\circ}$ and $\phi = 90^{\circ}$ elevation plane patterns (for the WIT) have 3 dB beamwidths of 66.7° and 75.6°, respectively. The slight deviation between the measured and the simulated results can be attributed to fabrication errors. To verify the simulated radiation patterns, open dc voltage are measured. The output dc power is proportional to input RF power and the rectifier efficiency [60, eq. (3)] which is also a function of the input RF power [60, eq. (4)]. Thus, simulated output dc power is proportional to the square of the input RF power and is equivalent to the square of the radiation pattern gain. In Fig. 3.32 comparison between the measured and simulated dc power patterns are shown, which are in fair agreement.

PCE measurements

The harvested dc voltage and PCE of the SWIPT antenna are measured using the measurement setup shown in Fig. 3.43(b). The received power (P_r) is evaluated using the Friis formula given in (3.2),

$$P_r(dBm) = EIRP(dBm) + G_r(dBi) + 20\log_{10}\left(\frac{\lambda}{4\pi d}\right)$$
 (3.2)

where, G_r is the receiver realized antenna gain, and λ is the transmitting signal wavelength, EIRP is the effective isotropic radiated power and d the distance (Table 3.4). The evaluated P_r is later validated through measurement by the spectrum analyzer for complete characterization of the WPT. Using the setup of Fig. 3.43(b) and the link budget of Table 3.4, the P_r for the proposed SWIPT antenna was $-9.91\,\mathrm{dBm}$. Results with a varied range between $-19\,\mathrm{dBm}$ to $-9\,\mathrm{dBm}$ and varied output load (R_L) of the WPT is plotted in Fig. 3.33(a) which indicates a maximum PCE of 66.52% with 203.5 mV output dc voltage $\left(V_{\mathrm{dc}}^{\mathrm{R_L}}\right)$ at an optimal load of 610 Ω corresponding to measured dc power (P_{dc}) of 67.9 μ W. The P_{dc} can be evaluated from the $V_{dc}^{R_L}$ plots shown in Fig. 3.33 using (3.3) and from

PCE plots in Fig. 3.34 using (3.4).

$$P_{dc}(\mu W) = \frac{\left(V_{dc}^{R_L}\right)^2}{R_L} \tag{3.3}$$

$$P_{dc}(\mu W) = \frac{\% PCE}{100} \times 10^{\left(\frac{P_r(dBm)}{10}\right)} \times 10^3$$
 (3.4)

Moreover, one Schottky diode was removed to compare the PCE response for a HWR vs the FWR of the proposed SWIPT antenna. Since the SWIPT antenna was designed for FWR, the diode removal resulted in a upshifted impedance matching frequency to $5.56\,\mathrm{GHz}$, G_r of $5.44\,\mathrm{dBi}$ and $P_r = -8.7\,\mathrm{dBm}$. A maximum PCE of 41.76% at $552.7\,\Omega$ load in Fig. 3.33 (a) indicates a significant PCE improvement for the FWR configuration.

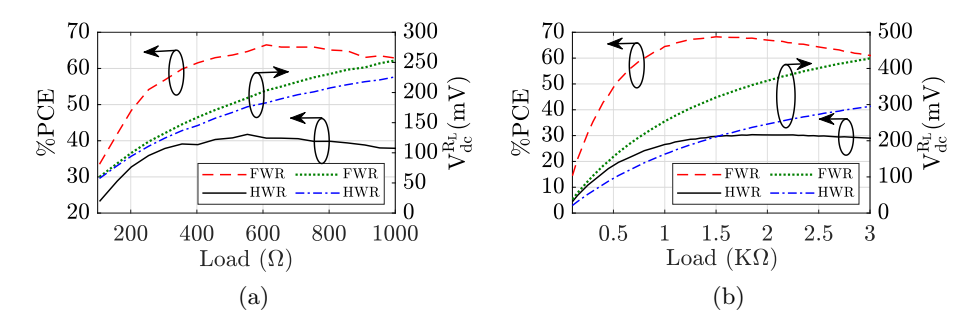


Figure 3.33: (a) Measured and (b) Simulated PCE and harvested DC voltage of the WPT vs the load.

The simulated output dc voltage and PCE for various output load (R_L) are shown in Fig 3.33 (b) respectively, indicating a maximum efficiency of 68.3% (30.2%) for FWR (HWR) at $1.5 \,\mathrm{k}\Omega$ (1.75 k Ω) for an input RF power of $-10 \,\mathrm{dBm}$ at 5.2 GHz. The measured and simulated PCE with varied input RF power is given in Fig. 3.34 (a) and Fig. 3.34 (b), respectively. The results show a non-linear increase in PCE and output dc voltage with

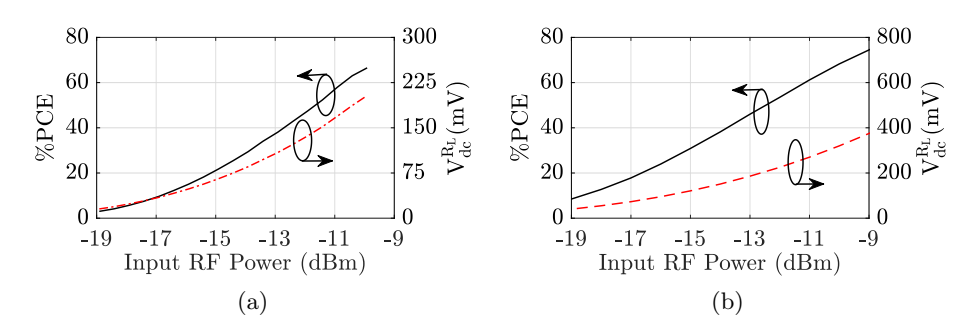


Figure 3.34: (a) Measured and (b) Simulated PCE and harvested DC voltage of the WPT vs input RF power at $5.2\,\mathrm{GHz}$ for $610\,\Omega$ and $1.5\,\mathrm{k}\Omega$, respectively.

respect to the input RF power. This input RF power corresponds to the non-linear I-V characteristics of the Schottky diode. The difference in the measured and simulated results can be attributed to the different input RF power levels and optimal output load R_L .

Isolation measurements

The isolation between the WIT and WPT ports is validated using a two-step measurement process. In the first step, the proposed SWIPT antenna is incident with a 5.7, 5.8, and 5.9 GHz RF signal using the measurement setup illustrated in Fig. 3.43 (b) and the corresponding output open dc voltages ($V_{dc}^{oc} = 166.6, 153$, and $114.6 \,\mathrm{mV}$). That gave a P_r (-8.81, -8.92, and $-9.2 \,\mathrm{dBm}$) at the antenna aperture using (3.2). In the next step, the WIT feed of the proposed SWIPT antenna was directly connected to the signal generator using an RF cable of $L_c = 1.6 \,\mathrm{dB}$ loss as shown in Fig. 3.35 (a). The output V_{dc}^{oc} , generated

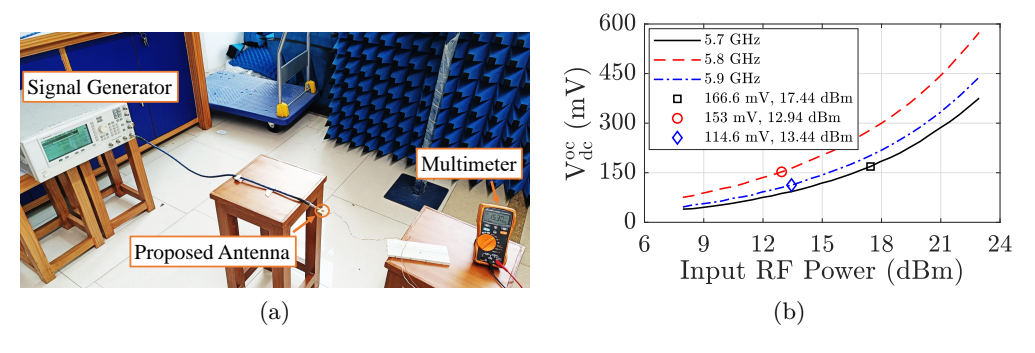


Figure 3.35: (a) Experimental setup to measure isolation between WIT and WPT port of the proposed SWIPT antenna, (b) Measured output open dc voltage vs RF power input to WIT feed.

due to coupling between the WPT and the WIT ports was measured using a multimeter at several frequencies. The results are plotted in Fig. 3.35(b) for effective P_r ranging from 7.94 dB to 22.94 dB. The results indicate 153 mV open dc voltage for 12.94 dBm RF input at 5.8 GHz, suggesting coupling of -8.92 dBm power and 12.94 + 8.92 = 21.86 dB isolation between WIT and WPT ports. Similarly, the isolation at 5.7 GHz and 5.9 GHz were 26.25 dB and 21.64 dB, respectively. The measurement results show a fair agreement with the simulated isolation results illustrated in Fig. 3.25 (b) and the small variations can be attributed to fabrication errors.

3.4.6 Demonstration of Proposed SWIPT Antenna For Energizing IoT Sensors

A digital clock with voltage and current ratings of $1.1\,\mathrm{V}$ and $10\,\mu\mathrm{A}$ was set with the proposed SWIPT antenna for demonstration of energizing IoT sensors, as illustrated in Fig. 3.36. Since the voltage rating was set higher than the open voltage (610.2 mV) of the proposed SWIPT antenna, a power management unit (PMU) was combined with the SWIPT antenna as depicted in Fig. 3.36 (a). The PMU is ADP5090-2-EVALZ from Analog Devices which is a plug and play evaluation board for WPT [131]. The complete diagram is shown in Fig. 3.36 (b) and is an ultra-low power booster regulator incorporated with charge management and maximum power point tracking (MPPT) features to provide efficient conversion of the harvested power from 16 $\mu\mathrm{W}$ to 200 mW range [132]. Preliminary

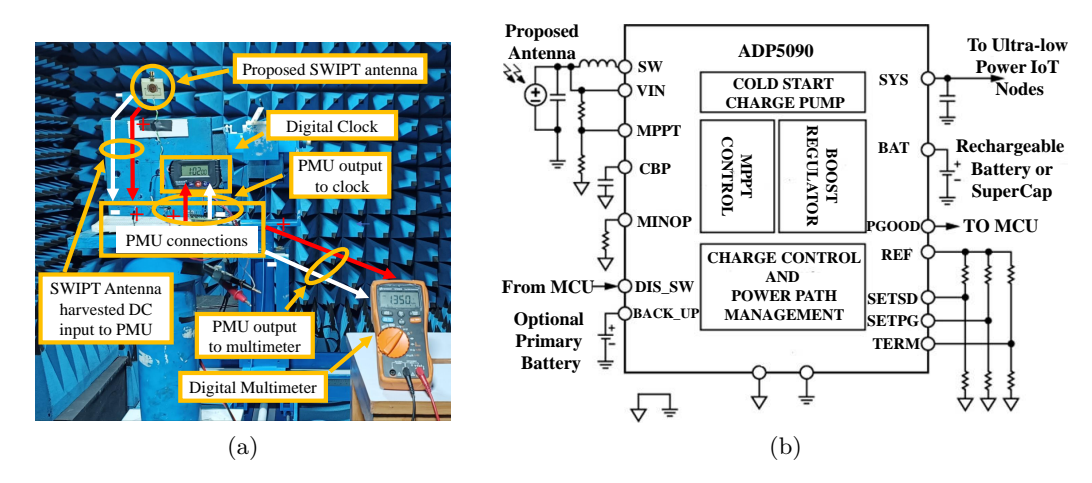


Figure 3.36: (a) Demonstration of the proposed SWIPT antenna for energizing IoT sensors, and (b) Configuration of the ultra low power boost regulator.

measurements corroborated the capability of the proposed SWIPT antenna to operate small IoT sensor nodes if integrated with an ultra-low PMU.

3.4.7 Performance Comparison with state of the art

The performance of the proposed SWIPT antenna is compared in Table 3.5 with other

Parameters	[76]	[71]	[69]	[78]	[68]	[67]	[66]	Design-O4A
Freq (GHz)	5.8 / 6.1	0.868 / 2.4	2.4 / 2.4	2.4 / 2.4	5.8 / 5.8	5.2 & 5.73 /	2.4 / 2.4	5.2 / 5.8
WPT/WIT						5.2 & 5.73		
WIT Gain (dBi)	7	7.2	5	8.4 - 9.6	4.71 - 5.15	4.22 - 5.68	3.64 - 4.10	5.7
WPT Gain (dBi)	7.2	1.7	6.4	2.5 - 4	4.71 - 5.15	4.22 - 5.68	4.10 - 4.57	3.6
Total WIT Efficiency	NG	63%	41%	70% - 88%	NG	NG	90.5%	78% - 80.23%
Min. Port Isolation (dB)	25	30	45	10 – 16	15	15	15	21.64
Input RF Power (dBm)	13.97	-9.5	3	2	0.5	5	6	-9.91
PCE @ -9.91 dBm	NG	60%	44%	55%	33%	≤ 30%	NG	66.52%
DC Combining	No	No	No	No	No	No	No	Yes
Conjugate Matching	No	Yes	Yes	Yes	No	No	No	Yes
SWIPT Technique	hybrid	FS	DP	DP	PS	PS	either PS	FS + DP +
Employed	пуына	rs	Dr	Dr	13	FS	or TS	dc combine
Rectification	half	voltage	voltage	voltage	half	half	half	full
Method	wave	doubler	doubler	doubler	wave	wave	wave	wave
Electrical size	> 0.82	0.74	0.63	0.61	2.5	> 1.57	> 0.984	0.58
$(\lambda_0 @ WIT freq)$	×1	$\times 0.63$	$\times 0.63$	×0.61	×10.6	$> \times 1.05$	$> \times 0.432$	$\times 0.53$

Table 3.5: Performance comparison with state-of-the-art

Abbreviations:- NG: not given; freq: frequency; pol: polarization; PS: power splitting; DP; dual-polarization; TS: time splitting

state-of-the-art. The designs in [76, 71] use frequency splitting for SWIPT operation, that achieves a high port isolation ($\geq 25\,\mathrm{dB}$) utilizing cross-polarization [76] and dual-mode operation [71] for WIT and WPT. However, these prototypes have lower PCE and WIT efficiency than the proposed SWIPT antenna (Table 3.5). Moreover, the matching network in [76] is more bulky than the proposed one. For instance, the proposed SWIPT

antenna is 34%-62.51% smaller than the designs presented in [76, 71], respectively. Other state-of-the-art designs [69, 78, 68, 67, 66] deliver information and power at the same frequency. The linearly polarized design in [69] has cross-polarized WIT and WPT ports with isolation of 45 dB but with compromised WIT efficiency and PCE (Table 3.5). Similarly, in [78], cross-polarized ports are used with dual polarization features. However, the poor co-polarization and cross-polarization isolation (Table 3.5) between WIT and WPT indicate information signal leakage into the rectifier (the voltage doubler). The power split in [68, 67, 66] requires a directional coupler, so that one of the output ports of the branch line coupler is connected to the rectifier with a matching network and a dc low pass filter to achieve the WPT operation. This resulted in a large prototype with lower isolation and PCE compared to the proposed design. Furthermore, the reported state-of-the-art of Table 3.5 have a partial ground planes, thus, resulting in platform dependency since the antenna performance changes with the permittivity materials where it is placed. In summary, driven by the dual polarization [69, 78] and power splitting [68, 67, 66] techniques for an advanced SWIPT operation, a miniature integrated antenna having high WIT efficiency, high port isolation, high PCE (from FWR) for ultra-low power WPT is achieved for SWIPT applications (Table 3.5); making it suitable for integration with ultra-low power sensors.

Design-O4A can effectively operate an ultra-low power IoT sensor when integrated with the PMU. However, the amount of power harvested by the PMU is insufficient to drive the communication circuitry of the sensor node. In addition, the short circuited $\lambda/4$ line utilized for providing RF choke and DC connection to the ground resulted in narrrow band WPT operation. Therefore, further improvement over the Design-O4A are needed to achieve the complete battery-less operation of the IoT sensor nodes.

3.5 SWIPT Antenna for battery-less IoT Node (Design-O4B)

The Design-O4B is evolved from Design-O4A and is simulated in Ansys HFSS, which is subsequently fabricated on FR4 substrate ($\epsilon_r = 4.4$, $\tan \delta = 0.02$) with a thickness of 1.6 mm and 1 oz copper cladding. HB and LSSP simulation in ADS software is used for rectifier circuit analysis. The final PCB design layout is shown in Fig. 3.37, denoting

Table 3.6: Design parameters of the proposed SWIPT module.

Parameters	w_1	w_2	w_3	w_4	w_5	l_1	l_2	l_3	l_4	l_5	l_6	l_7	l_8	d
Dimension (mm)	1	1	0.5	2	3.44	11.04	2.956	2.1	4.982	3	2	2.35	11	12.8

various geometrical parameters and their respective values as listed in Table 3.6. The fabricated prototype of the proposed SWIPT design is depicted in Fig. 3.38 (a), exhibiting various design features and components. The two co-polarized WPT feeds illustrated in Fig. 3.37 extract RF energy from the circular patch through capacitive coupling. The input impedance $(Z_a^{WPT} = R_a + jX_a \Omega)$ of the subsequent WPT ports (depicted as

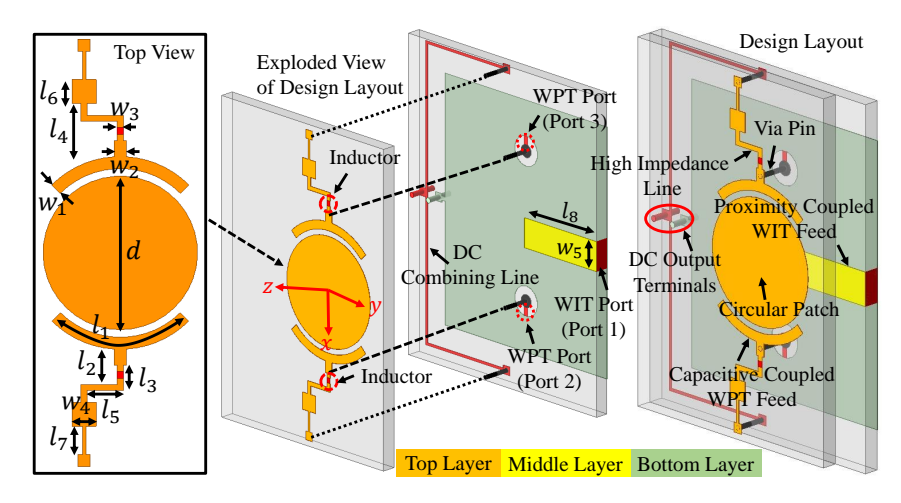


Figure 3.37: Design layout of the proposed SWIPT module.

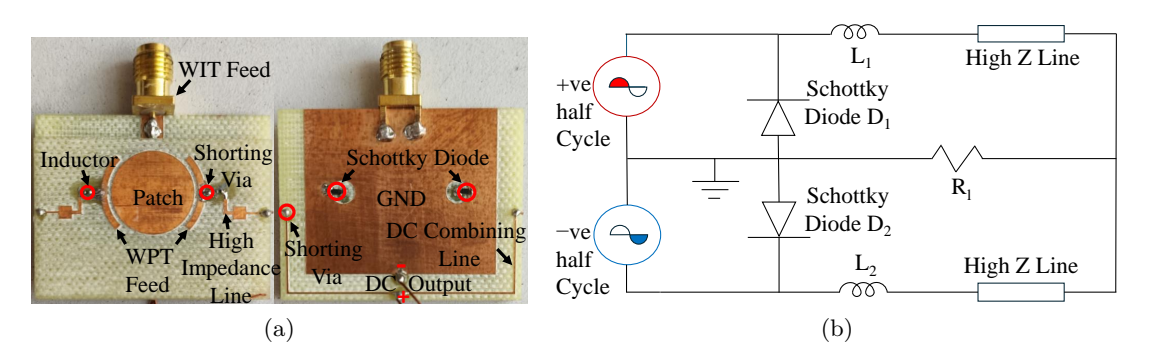


Figure 3.38: (a) Fabricated prototype of the proposed SWIPT module. (b) Equivalent circuit diagram

port2 and port3) are conjugate matched with the shunt SBD (SMS7630-079LF) impedance $(Z_d = R_d - jX_d \Omega, R_d = 65.127, X_d = 94.421)$ to achieve maximum RF power transfer from the circular patch and reduce insertion losses. In addition, the capacitive coupling restricts backward DC flow into the patch, enhancing the PCE of the module. Moreover, an inductor $L_{1-2} = 1.5 \,\mathrm{nH}$ along with a stepped impedance microstrip line acting as low pass filter are utilized as a choke to restrict RF signal flow through DC load. As illustrated in Fig. 3.38 (a), a pair of shunt SBDs are placed symmetrically about the circular patch (anode terminal of diode connected using the defected ground structure and a cathode terminal connected to the patch), which resembles the center-tapped FWR implementation shown in Fig. 3.38 (b). The incident RF waves induce TM₁₁₀ mode current on the aperture of the circular patch, resulting in positive voltage at each diode in the alternate half cycle of the imparted RF waves. For example, as depicted in Fig. 3.38 (b), during the 1^{st} half cycle of the incident RF wave shunt SBD D_1 gets reverse biased whereas in the 2^{nd} half cycle SBD D_2 is reverse biased. Subsequently, parallel connection of DC lines ensures coupling of output DC power generated in each half cycle to realize a fully integrated FWR. For communication, a transceiver module can be connected to the proximity-coupled WIT feed having $Z_a^{WIT} = 50 \Omega$ port impedance (depicted as port1). Further, The cross-polarized arrangement of WIT feed and WPT feed lines ensures high isolation between the information and power signals.

3.5.1 Results and Discussion

Measurement Setup

The WPT and WIT performance of the module is measured in the anechoic chamber. The experimental setup shown in Fig. 3.39(a) is used for measuring the WPT performance

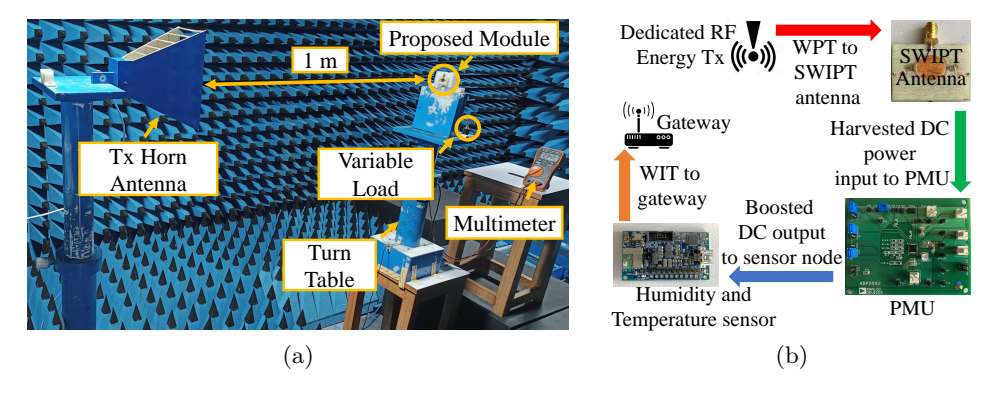


Figure 3.39: (a) Experimental setup, and (b) battery-less operation mechanism of the proposed SWIPT Module.

parameters at 5 GHz frequency. The proposed module is placed on the turn table and exposed to RF waves originated by the transmitter (Tx) horn antenna situated at r = 1m distance. The RF power ($P_t = 25 \,\mathrm{dBm}$) is input to the Tx having gain $G_t = 10 \,\mathrm{dBi}$ from the signal generator via an RF cable having insertion loss of $L_c = 2 \,\mathrm{dB}$, resulting in EIRP ($P_t + G_t - L_c$) of 33 dBm. The path loss calculated from the Friis equation is $-46.92 \,\mathrm{dBm}$, and the overall harvested DC voltage is measured using a digital multimeter. In contrast, the reference transmitter and the proposed antenna are connected to a Keysight PNA-L network analyzer N5234B integrated with the anechoic chamber for measuring RF radiation patterns. The battery-less operation mechanism of the WSN depicted in Fig. 3.39(b) is utilized to validate the performance of the SWIPT module.

WPT Performance Measurement

The simulated reflection coefficient (S₁₁) for port2 and port3 is plotted in Fig. 3.40(a). The results imply conjugate impedance matching between the simulated $Z_a^{WPT} = 46.79 + j115.77 \Omega$ and Z_d at 5 GHz frequency. This is verified by the peak open dc voltage (V_{dc}^{oc}) of 557 mV at 5 GHz in the V_{dc}^{oc} versus frequency measurement result shown in Fig. 3.40(a). Further, the normalized simulated and measured DC power patterns for the WPT port are illustrated in Fig. 3.40 (b) for $\phi = 0^{\circ}$ and Fig. 3.40(c) $\phi = 90^{\circ}$ elevation planes with maximum simulated radiation gain of 4.26 dBi in broadside ($\theta = 0^{\circ}, \phi = 0^{\circ}$) direction. The results suggest a good agreement between the proposed module's simulated and measured WPT radiation characteristics. Further, to determine the WPT capability, the output DC voltage (V_{dc}) is measured using the measurement setup shown in Fig. 3.39

for varying output loads at input RF power $(P_r = \text{EIRP} + G_t + G_r - L_p)$ of $-9.1612 \,\text{dBm}$ and $5 \,\text{GHz}$ frequency. The corresponding PCE is evaluated and the results are plotted in Fig. 3.41 (a), revealing a maximum PCE of 74.5% at an optimal load of $700 \,\Omega$, providing 91.44 µW maximum harvested DC power. Further, V_{dc} for varying P_r is measured and the respective PCE values are calculated. The corresponding results are plotted in Fig. 3.41 (b), suggesting a non-linear increase in PCE and V_{dc} with respect to P_r , which is due to the non-linear characteristics of the SBD.

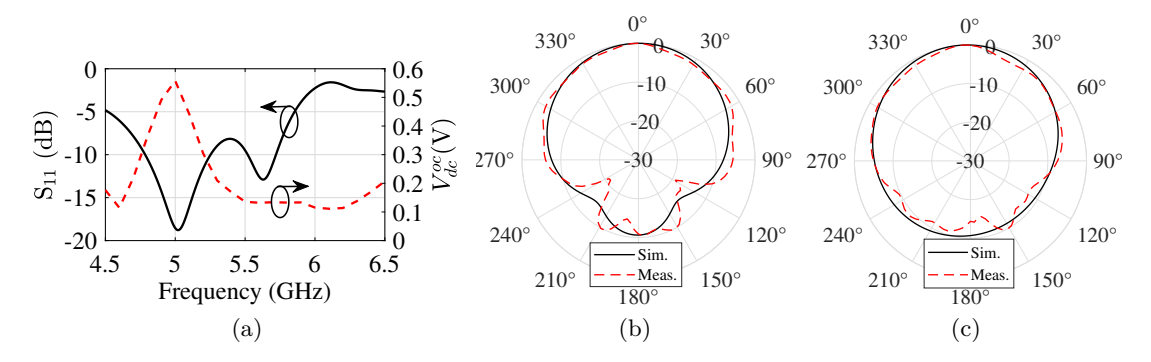


Figure 3.40: (a) S_{11} and V_{dc}^{oc} vs frequency (b) normalized DC power pattern at 5 GHz in $\phi = 0^{\circ}$, $\phi = 90^{\circ}$ elevation plane.

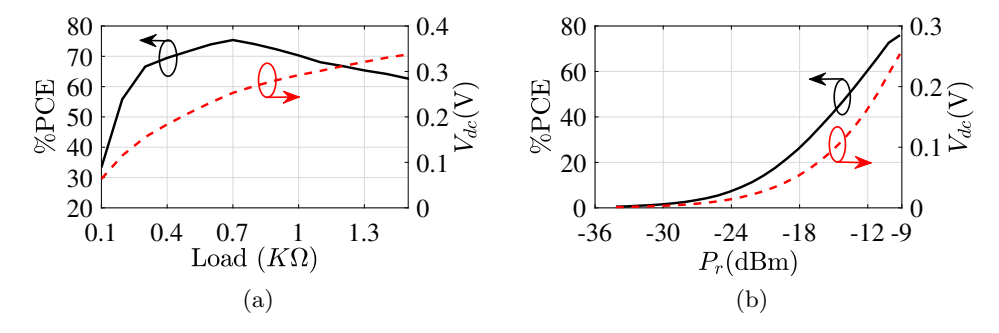


Figure 3.41: (a) PCE and harvested DC voltage variation with load, (b) PCE and V_{dC} variation with input RF power

WIT Performance Measurement

The simulated and measured reflection coefficient (S_{11}) at port1 are illustrated in Fig. 3.42(a). The results specify ($S_{11} < -10 \,\mathrm{dB}$) in 5.15 GHz-5.72 GHz frequency range with simulated $S_{21} \geq 25 \,\mathrm{dB}$ at 5 GHz and $\geq 18 \,\mathrm{dB}$ in the entire 5 GHz WiFi band. The maximum realized gain of $G_r = 5.37 \,\mathrm{dBi}$ is achieved at 5.42 GHz with $\leq 1 \,\mathrm{dBi}$ variation across the WIT operating band with radiation efficiency $\geq 78.5\%$ as depicted in Fig. 3.42(b). The bit error rate (BER) as a function of SNR was measured across different frequency channels for port1 using the USRP B210. The results, as illustrated in Fig. 3.42(c), pertain to BPSK modulation and demonstrate the effective operation of the proposed SWIPT module within the 5 GHz WiFi band. The data indicate that the proposed module performs well in maintaining low BER [133], confirming its suitability

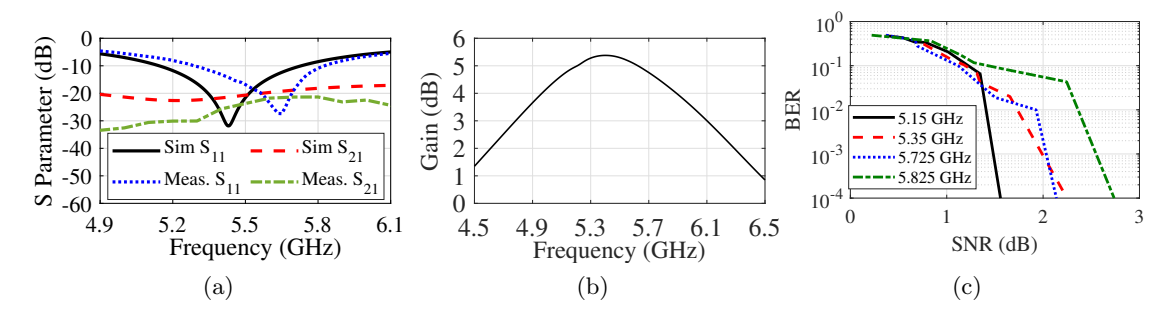


Figure 3.42: (a) S parameters of port 1, (b) gain, radiation efficiency (η_{rad}) vs frequency, and (c) BER vs SNR for WIT.

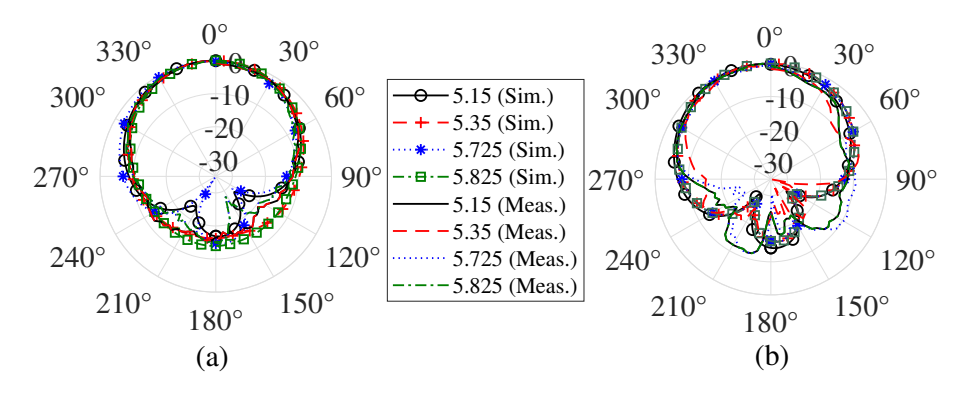


Figure 3.43: WIT radiation pattern at 5 GHz in (a) $\phi = 0^{\circ}$ (b) $\phi = 90^{\circ}$ elevation plane.

for WIT. In addition, the simulated and measured WIT radiation patterns are illustrated in Fig. 3.43. The results indicate 3 dB beamwidth of $\geq 88^{\circ}$ ($\geq 92^{\circ}$) in $\phi = 0^{\circ}$ ($\phi = 90^{\circ}$) plane, with almost similar radiation pattern in the entire WIT band.

Validation of Battery-less WSN Operation

A sensor beacon is integrated with the proposed SWIPT module through a power management unit (PMU, Analog Devices ADP5092-1-EVALZ) [134] having cold start voltage of 380 mV to confirm its capability to provide battery-less autonomous WSN operation. Due to the limited availability of low-power WSN working in 5 GHz WiFi band, a solar-powered IoT device kit (S6SAE101A00SA1002) [135] working at 2.45 GHz is utilized to demonstrate the design's potential for powering low-power 5 GHz Wi-Fi sensor beacons. The kit includes a BLE gateway and a battery-less BLE beacon. The gateway is connected to the PC for logging sensor data received from the sensor beacon, which requires $103\,\mu\text{W}$ - $158\,\mu\text{W}$ power for transmitting sensor data to the gateway in every 6 s time interval. Table 3.7 shows the BLE sensor beacon data log, exhibiting four data frames containing temperature and humidity sensor data being transmitted in every 6 s interval after PMU boosts the input voltage to 3.3 V, which takes approximately 20 s time interval. The BLE beacon again transmits four data frames containing sensor data, and this continues until the proposed module is illuminated with RF radiation at 5 GHz. Moreover, the sensor beacon transmits a single data frame every 35s when the module is illuminated with RF radiation at 4.9 GHz and 5.1 GHz, confirming WPT operation in

Time	Type	Temp	Humidity	Time	Type	Temp	Humidity
15:03:26	BLE Beacon	23.8	52	15:04:59	BLE Beacon	24.5	52
15:03:47	BLE Beacon	23.8	52	15:05:05	BLE Beacon	24.5	52
15:03:53	BLE Beacon	23.8	52	15:05:26	BLE Beacon	24.5	52
15:04:06	BLE Beacon	23.8	52	15:05:32	BLE Beacon	24.5	52
15:04:13	BLE Beacon	23.8	52	15:05:39	BLE Beacon	24.5	52
15:04:33	BLE Beacon	24.5	52	15:05:45	BLE Beacon	24.5	52
15:04:39	BLE Beacon	24.5	52	15:05:52	BLE Beacon	24.5	52
15:04:46	BLE Beacon	24.5	52	15:06:12	BLE Beacon	24.5	52
15:04:52	BLE Beacon	24.5	52	15:06:18	BLE Beacon	24.5	52

Table 3.7: BLE sensor beacon data for WPT at 5 GHz.

4.9 GHz-5.1 GHz band.

3.5.2 Performance Comparison

The battery-less operation of SN has been presented in [136] for structural health monitoring. It is designed for WPT operation at 868/950 MHz and lacks WIT capability. The large footprint makes the design unsuitable for integration with SN. Moreover, it harvests $V_{dc}^{oc} = 431 \,\mathrm{mV}$ for $-10 \,\mathrm{dBm}$ input RF power, which is considerably lower than the proposed work's open-circuit DC voltage of 557 mV. In contrast, port1 of the proposed SWIPT module can also be integrated with a suitable low-power 5 GHz WiFi module in the future for information exchange.

Parameters	[137]	[138]	[78]	Design-O4A	Design-O4B
Freq (GHz)	4.18 - 6.76	5.45 - 6.5	2.4	5.53 - 6.0 /	5.15-5.72/
WIT/WPT	4.18 - 0.70	0.40 - 0.0	2.4	5.2	4.9-5.1
Gain (WIT/WPT)			8.4 - 9.6/	5.7/	5.37/
(dBi)	_	_	2.5 - 4	3.6	4.26
WIT Efficiency	-	-	70% - 88%	78% - 80.23%	78.5%
PCE	53.1%	51.0%	74%	66.52%	74.5%
TCE	$@0\mathrm{dBm}$	@ 0 dBm	@ 2 dBm	$@-9.91\mathrm{dBm}$	$@-9.16\mathrm{dBm}$
Isolation (dB)	< -15	< -15	< -4	< -21	< -21
Conjugate Matching	No	No	Yes	Yes	Yes
Rectification Topology	Half Wave	Half Wave	Full Wave	Full wave	Full wave
SBD Connection	Shunt	Shunt	Voltage doubler	Series	Shunt
Topology	Situit	Siluit	voltage doubler	series	Shunt
Polarization Mode	All Polarization	LP, CP	DLP	LP	LP
SWIPT	HC + PS	PS	DP	FS+DP	FS+DP
m 1 :	110 + 13	1.0	Dr	+DC Combine	+DC Combine
Technique					
Feature size (mm ²)	75×70	90×53	110 × 110	31.64×28.89	37×28.6
	75 × 70	90 × 53	110 × 110		

Table 3.8: Performance comparison with state-of-the-art

Abbreviations-: HC:hybrid coupler; PS:power splitting; DP: dual-polarization; FS: frequency splitting, LP: linear polarization; CP: circular polarization; DLP: dual linear polarization.

The performance parameters and design features of the proposed module have been compared with the present state-of-the-art SWIPT modules [137, 138, 78] and Design-O4A as listed in Table 3.8. Although the use-case scenarios for these comparative works are in the fields of wearable rectennas and other IoT node operations, Table 3 efficiently

provides a concise overview of the advantages of the proposed work. Most of the works except Design-O4A are designed for high-input RF power, which is not applicable to ultra-low-power IoT sensor node applications. The data indicates an improved working frequency range as compared to Design-O4A for both WIT and WPT operations with similar realized gain values. The increased WPT operational bandwidth of 200 MHz (4.9 GHz -5.1 GHz) could be attributed to the elimination of the $\lambda/4$ stub which causes narrow-band operation [140]. A peak power of 91.44 μ W is harvested at optimal load of 700 Ω in comparison to 68 μ W harvested in Design-O4A with nearly the same antenna footprint. Moreover, a substantial improvement of 8% in PCE is achieved, enabling battery-less SN operation.

3.5.3 Relevance to Sustainability

Future 6G communication systems aim at providing energy efficient and sustainable wireless sensor networks (WSN) [141]. Sensor nodes (including IoT) house small batteries limiting the lifespan of WSN and their large scale deployment increases the maintenance costs from vast battery replacements. Therefore, energy harvesting (EH) is envisioned as the indispensable technology component of 6G networks for realizing zero-energy wireless sensor nodes to deploy sustainable IoT applications. Therefore, the proposed SWIPT antenna uses a WPT technology that is perceived as the most suitable choice for EH due to its compact implementation [12] and easy integration with WIT communicating devices; energizing IoT sensors for battery waste/carbon foot print reduction with greener wireless communications.

3.6 Summary

This chapter explores the design of a multi-sector rectenna array system (ReAS) aimed at addressing the angular misalignment challenges encountered in smart home environments. In such applications, the RF energy transmitter is typically mounted on the ceiling, while sensor nodes, each equipped with a rectenna module, are dispersed throughout the 3-D space in various orientations. The investigation focuses on overcoming the alignment issues between the transmitter and the sensor nodes to ensure efficient WPT and reliable operation within the smart home context.

Initially an eight sector ReAS designated as Design-O3A comprising circular patch antenna in each sector is investigated. The antenna elements are sequentially rotated by 45° with each integrated with two shunt Shottky diodes symmetrically about the center point of the patch. The antenna and Schottky diode impedance are conjugate matched to reduce insertion loss. Moreover, the DC outputs form each rectenna element are connected in parallel using a high impedance microstrip line perpendicular to the orientation of the Schottky diode connection to achieve high isolation between the RF signal and DC output. The Design-O3A provides angular misalignment tolerant WPT only against rotation in its own plane. Therefore, an isotropic coverage ReAS (iReAS) is needed to achieve angular

misalignment against rotation in any plane. The Design-O3B which is an eight-sector stacked rectenna array system (ReAS), incorporates incorporates a new Schottky diode connection strategy to simplify the integration of the rectenna elements. The system utilizes a hybrid combining topology and conjugate impedance matching of rectenna elements with Schottky diode impedance. This reduces circuit losses and enhances system power conversion efficiency. Additionally, the hybrid combining scheme improves the output dc voltage and the optimal load. Moreover, after integration with the power management unit Design-O3B provides sustainable battery-less operation of an IoT sensor node.

This chapter also presents two SWIPT antenna designs Design-O4A and Design-O4B. The proposed antennas incorporate a proximity coupled feed to the radiative circular patch for WIT and an integrated capacitive coupled feeding network, with FWR, using regenerative opposite fringing fields from the radiating edges of the patch to energize IoT sensors through WPT. For the realization, two co-polarized fringing field harvesters are capacitively coupled to the radiating edges of the patch to regenerate those opposite fringes whose currents are effectively matched to the FWR using a pair of Schottky diodes for DC energy generation.

The Design-O4A provides WIT operation in 5.7 GHz-6 GHz band and WPT functionality at 5.2 GHz. It can effectively operate an ultra-low power IoT sensor when integrated with the PMU. However, the amount of power harvested by the PMU is insufficient to drive the communication circuitry of the sensor node. The short circuited $\lambda/4$ line utilized for providing RF choke and DC connection to the ground resulted in narrrow band WPT operation. In addition, the high impedance DC combining lines utilized for implementing FWR and providing the necessary conjugate impedance matching affected the radiation pattern of the circular patch. Therefore, another SWIPT antenna Design-O4B is proposed to achieve the complete battery-less operation of the IoT sensor nodes. At first glance, Design-O4A and Design-O4B may appear similar; however, a closer examination reveals several key differences that contribute to the superior performance of Design-O4B in terms of WIT and WPT. These differences, which enhance both WIT and WPT performance, underscore the advantages of Design-O4B over Design-O4A.

The Design-O4B similar to Design-O4A comprises of a circular patch antenna explicitly designed to efficiently operate ultra-low-power sensor nodes. It integrates frequency splitting and dual polarization techniques to achieve high isolation between WIT and WPT signals, resulting in negligible leakage of information signal into the rectification circuit. It features an extended WIT bandwidth of 570 MHz (from 5.15 GHz to 5.72 GHz) and operates WPT across a wide frequency range of 200 MHz (4.9 GHz to 5.1 GHz) with high PCE. In contrast to series Schottky diode connection in Design-O4A, the shunt topology incorporated in Design-O4B provided enhanced PCE at ultra-low input RF power. In addition, an innovative DC-combining technique in coordination with a stepped impedance microstrip line low pass filter further enhances PCE and realizes completely integrated FWR. Moreover, the conjugate impedance matching between the antenna and

the Schottky diode reduces the insertion losses resulting from the matching network. Additionally, the circular patch has the inherent capability of rejecting the harmonics generated by the Schottky diode. The high bandwidth can be attributed to the defected ground structure utilized to integrate the Schottky diode with the antenna. The harvested power successfully energizes a Bluetooth Low Energy module for battery-less operation upon integration with the power management unit. Thus, Design-O4B has the potential to be successfully deployed for autonomous sensing and communication applications in isolated environments, such as cold storage for vaccines and food warehouses.

The QoS aware Tx and Rx antenna systems discussed thus far enable efficient SWIPT operation in IoT networks. However, when IoT sensor nodes are positioned at significant distances from the access point, transmitting information over such long distances can lead to substantial power consumption in power-constrained IoT devices. Additionally, the prevalence of multipath effects in remote locations results in degraded communication link quality.

In these scenarios, relay nodes play a crucial role in facilitating energy-efficient communication with high data rates and improved spectral efficiency. By employing cooperative relaying techniques, relay nodes mitigate the adverse effects of path loss and signal fading while enhancing overall network coverage. The subsequent chapter will discuss a SWIPT antenna system designed for relay nodes, aimed at realizing an energy-efficient and sustainable green IoT network.

⁰CHAPTER OUTCOMES:

^{[1].} **S. Kumar** and A. Sharma, "A Polarization Insensitive Circular Rectenna Array System for Microwave Power Transfer and Energy Harvesting Applications," 2023 17th European Conference on Antennas and Propagation (EuCAP), Florence, Italy, 2023, pp. 1-4, doi: 10.23919/EuCAP57121.2023.10133150.

^{[2].} S. Kumar, M. Kumar and A. Sharma, "A Compact Stacked Multisector Near-Isotropic Coverage Rectenna Array System for IoT Applications," in IEEE Microwave and Wireless Technology Letters, vol. 34, no. 1, pp. 123-126, Jan. 2024, doi: 10.1109/LMWT.2023.3331214.

^{[3].} S. Kumar, M. Kumar, A. Sharma and I. J. Garcia Zuazola, "Energizing an IoT Sensor Using Regenerative Opposite Fringing Fields From an Embedded Communicating Patch Antenna," in IEEE Access, vol. 12, pp. 47951-47960, 2024, doi: 10.1109/ACCESS.2024.3382821.

^{[4].} S. Kumar, V. Sharma, and A. Sharma, "SWIPT Module for Battery Less Ultra Low Power Sensor Nodes," in IEEE Sensors Letters, vol. 8, no. 12, pp. 1-4, Dec. 2024, Art no. 6015404, doi: 10.1109/LSENS.2024.3482409.

Chapter 4

SWIPT Antenna System For Relay Node

O-5: Design a practical SWIPT relay node capable of wideband WIT with an access point and IoT devices, while also supporting WPT to recharge its battery.

The 5G and beyond 5G (B5G) wireless communication networks need to achieve energy-efficient green communication with high data rates and spectral efficiency [6]. Cooperative relaying (CoR) communication can be employed to enhance the range, and reliability of information transmission [84]. CoR reduces the adverse effects of path loss and signal fading, enhancing the coverage area and system capacity. WPT and SWIPT have emerged as promising techniques to recharge battery-assisted relay nodes (RNs) in IoT applications for achieving energy-efficient and sustainable communication [85, 86, 87, 88, 89]. The antenna systems at RNs must provide wider beam coverage to realize wireless information transmission (WIT) with the transmitter (Tx) as well as a receiver (Rx) [90]. Hence omnidirectional radiation pattern appears to be the ideal choice to achieve the desired communication links. However, multi-antenna systems with beamforming capability are highly desirable for RNs to reduce multipath fading and interference to enhance the spectral efficiency [91]. Moreover, multiple antennas enhance the harvested DC power due to an increase in the captured RF power.

4.1 System Architecture

The proposed SWIPT antenna array (SAA) has wide impedance bandwidth, providing WIT operation in both the lower (5.15 GHz - 5.35 GHz), and upper (5.725 GHz - 5.825 GHz) 5 GHz WiFi band. The radiation pattern of the antenna array can be reconfigured in the entire WIT band to achieve the desired wide beam coverage in the application region. In addition, the RF power is harvested by each antenna element at 5 GHz through a directly integrated conjugate-matched FWR circuit. The DC outputs from each antenna element within the array are connected in parallel to enhance the output power with negligible combining losses. In addition, large isolation between the WIT and WPT is highly desirable since the information signal can leak into the rectenna circuit, reducing the strength of the received and transmitted WIT signal. To enhance the desired isolation, frequency splitting technique along with orthogonally polarized feeds

are utilized for WIT and WPT signals. A typical application scenario where the proposed SAA can be deployed is illustrated in Fig 4.1, demonstrating multiple SWIPT-enabled RNs

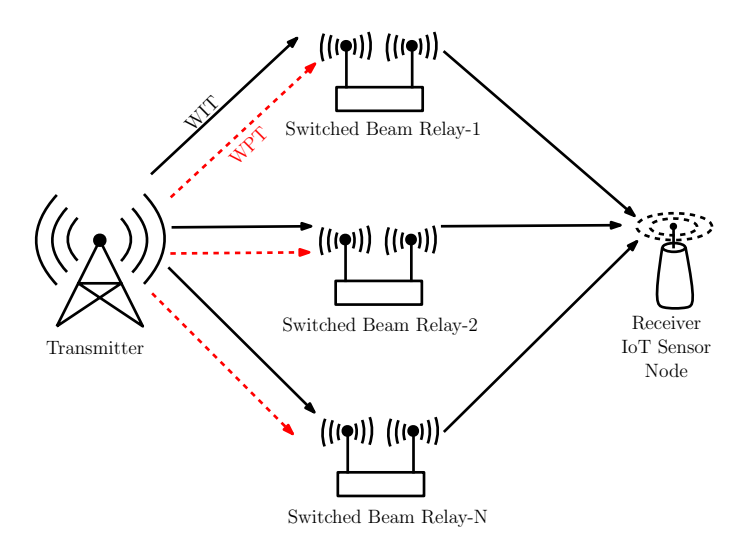


Figure 4.1: Application scenario for the proposed SWIPT antenna array.

equipped with multiple antennas having switched beam patterns to process data received from the Tx and forward it to the Rx or vice-versa. In such a scenario to achieve robust communication link RNs with zero information error should be activated for relaying the information whereas the ones with errors should only be allowed to harvest RF energy to recharge their batteries.

4.2 Proposed Reconfigurable SWIPT Antenna Array

The proposed antenna system is designed in Ansys HFSS on FR4 substrate ($\epsilon_r = 44, \tan \delta = 0.02$) having 1.6 mm thickness and 1 oz copper deposit. The Keysight Advanced Design System (ADS) software is used for the analysis of the rectifier circuit. The design layout of the proposed SAA is illustrated in Fig. 4.2 and the geometrical dimensions are recorded in Table 4.1.

Table 4.1: Dimensions of the proposed SWIPT antenna.

Paramete																		L_9				
Dimension	(mm)	1	1	0.5	2	0.3	1	1.35	0.55	10.9	1.35	2.1	3	2	2.35	1	36.72	27.69	13.1	5.9	6.74	12.6

4.2.1 WIT Design Configuration

The array consists of four SWIPT antenna elements (SAE₁₋₄) excited by a proximity-coupled WIT feed as depicted in Fig. 4.2(a). The SAEs are arranged radially such that each adjacent pair of SAEs has a spatial phase difference (ϕ_{SPD}) of 90°. Moreover, the corresponding WIT feeds are integrated with a reconfigurable feed network (RFN) for switching between various combinations of excited SAEs. The fusion of ϕ_{SPD} with RFN gives rise to fifteen different modes of operation. This enables the realization of

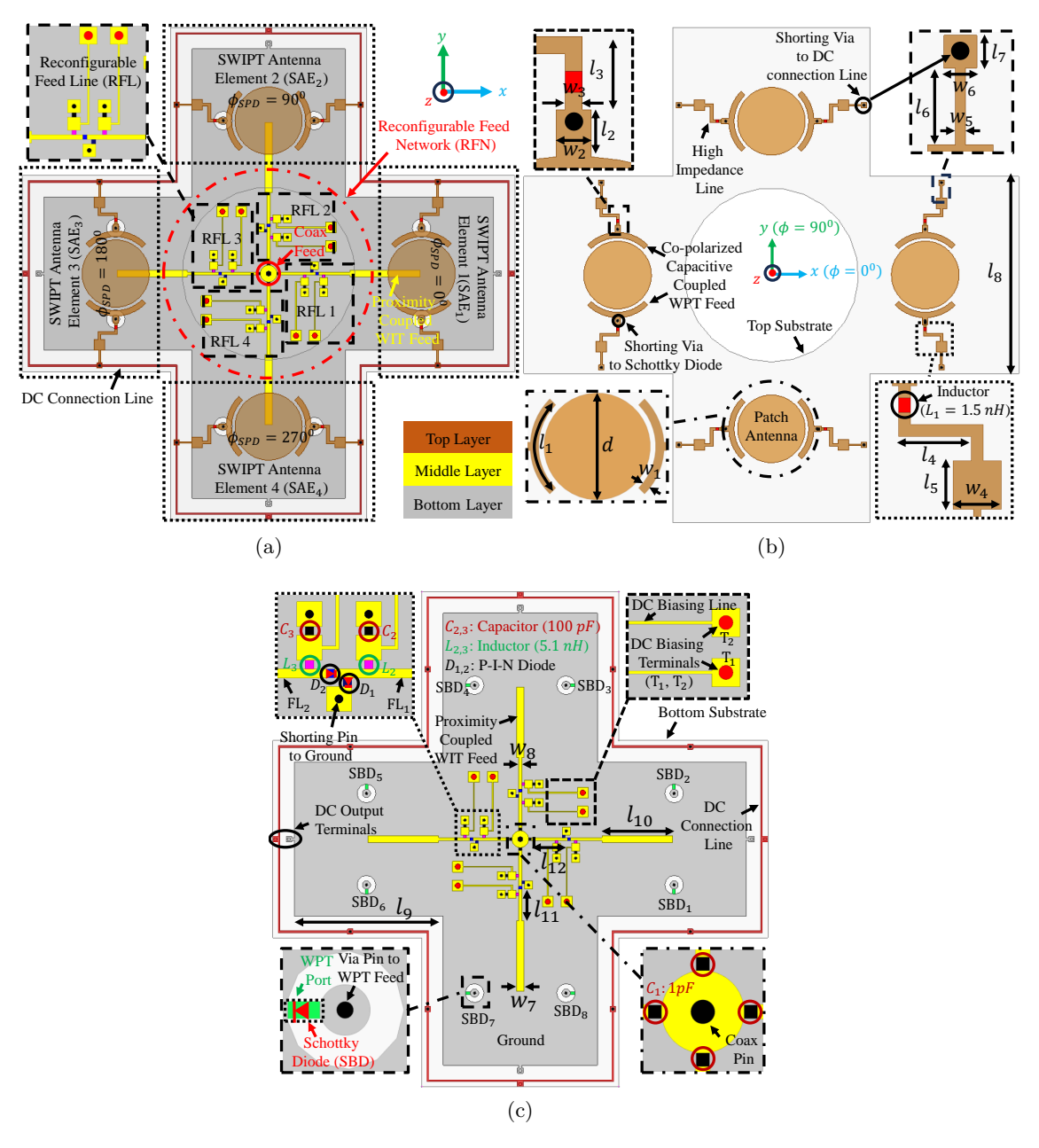


Figure 4.2: (a) Complete design layout, (b) Top layer, (b) Middle layer, and Bottom layer of the proposed SWIPT antenna array.

pattern, polarization, and spatial diversity for WIT, which consequently helps in improving the communication link quality.

The various design features and circuit components utilized in the RFN are outlined in Fig. 4.2(a) and Fig. 4.2(c). The RFN comprises a center coaxial feed that excites four reconfigurable feed lines (RFL₁₋₄), each feeding an SAE. The RFL consists of two P-I-N diodes (SMP1345-079LF) (depicted as $D_{1,2}$) to enable switching between different modes of operation, and two microstrip feed lines (FL₁₋₂) to achieve necessary impedance matching. The P-I-N didoes are biased using a DC biasing circuit consisting of two inductors ($L_{2,3} = 5.1 \,\text{nH}$), two capacitors ($C_{2,3} = 100 \,\text{pF}$), and two DC biasing lines for connecting DC supply through terminals T₁ and T₂. The L and C pairs (L_2, C_2) and

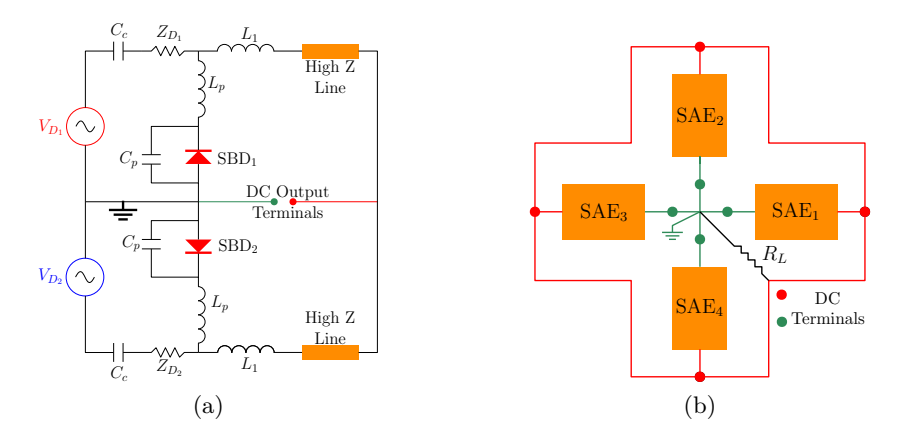


Figure 4.3: (a) Equivalent circuit diagram of an SAE in the proposed SAA for WPT operation, and (b) Paralle DC combining of SAE_{1-4} .

 (L_3, C_3) are connected to DC terminals T_1 and T_2 , respectively to provide necessary low-pass filter operation for isolating RF signal from the biasing circuit. In addition, the coaxial feed is connected to each RFL through a DC blocking capacitor $(C_1 = 1 \,\mathrm{pF})$ to isolate the center feed from the biasing circuit. The RFL is configured to work either in high-impedance or SAE excitation mode by switching the P-I-N diode state. It acts as a high impedance line when D_1 is ON and D_2 is OFF. This is achieved by connecting T_1 to the positive terminal of DC supply and shorting T_2 to ground. It can be switched to SAE excitation mode by swapping T_1 and T_2 terminals, which changes the state of D_1 to OFF and D_2 to ON state. The P-I-N diode is equivalent to a 1.5 Ω during ON state and act as 0.2 pF in the OFF state [67]. Since each RFL has two states, a total of 16 modes are possible, one being an idle mode where no SAE is excited resulting in a total of 15 radiation modes. The detailed description of the reconfigurability achieved by the proposed SAA and the corresponding performance results are discussed in Section 4.3.

4.2.2 WPT Design Configuration

The various WPT design features of the proposed SAA are shown in Fig. 4.2(b) and Fig. 4.2(c). The RF power incident over the circular patch within an SAE is extracted using two co-polarized capacitively coupled WPT feeds. The input impedance $(Z_a^p = R_a + jX_a \Omega)$ at corresponding WPT ports are conjugate matched with the shunt Schottky diode (SMS7630-079LF) impedance $(Z_d = R_d - jX_d \Omega)$ for maximum RF power transfer from the circular patch and reduce insertion losses. Moreover, the harvested DC backflow into the patch is blocked by the capacitive coupling, eventually enhancing the PCE of the WPT operation.

The equivalent circuit diagram of an SAE for the WPT function is exhibited in Fig. 4.3(a). The RF wave incident over the circular patch excites TM_{110} mode current which alters its polarity in every half cycle. The two RF sources V_{D_1} and V_{D_2} represent respective half cycles of the incident RF wave, exciting respective shunt Schottky Diodes SBD₁ and SBD₂, realizing FWR of captured RF energy. The L_p and C_p denote parasitic packaging parameters of the Schottky diode, $Z_{D_{1,2}}$ represents the impedance of the antenna and C_c

depicts the capacitive coupling between the antenna and WPT feed. Moreover, an inductor $L_1=1.5\,\mathrm{nH}$ along with a high impedance line is utilized as a choke to impede RF signal flow through DC load. The DC output terminals from each SAEs are connected in parallel as shown in Fig.4.3(b), enhancing the total harvested output DC power with negligible combining losses. The radially opposite pairs of SAEs (SAE₁, SAE₃) and (SAE₂, SAE₄) are vertically ($\phi=90^\circ$) and horizontally ($\phi=0^\circ$) polarized, respectively. Hence, the proposed SAA has dual-linear polarized WPT capability, providing tolerance for angular and polarization misalignment with the RF-ET within its plane.

4.3 Results and Discussion

4.3.1 Circuit and Design Simulation Setup

The HB and LSSP technique in ADS software is used for the analysis of the non-linear rectifier circuit. The SPICE parameters of the Schottky diode enabled the modeling by accounting for the parasitic packaging parameters $L_p = 0.7 \,\mathrm{nH}$ and $C_p = 0.16 \,\mathrm{pF}$. The analysis is done for an input RF power of $-10 \,\mathrm{dBm}$ at $5 \,\mathrm{GHz}$ frequency and $1 \,\mathrm{k}\Omega$ output load, resulting in Schottky diode impedance of $Z_d = 29.862 - j97.177 \,\Omega$ for a single SAE. The proposed SAA was optimized in Ansys HFSS with WPT port impedance matched to Z_d^* and achieved WIT impedance matching in $5 \,\mathrm{GHz}$ WiFi band.

The proposed SAA layout is initially fabricated using the MITS PCB prototyping machine. Following this, the SMD components are meticulously soldered onto the board to assemble the final prototype. The completed prototype, illustrated in Fig. 4.4, is utilized to validate the performance of the design.

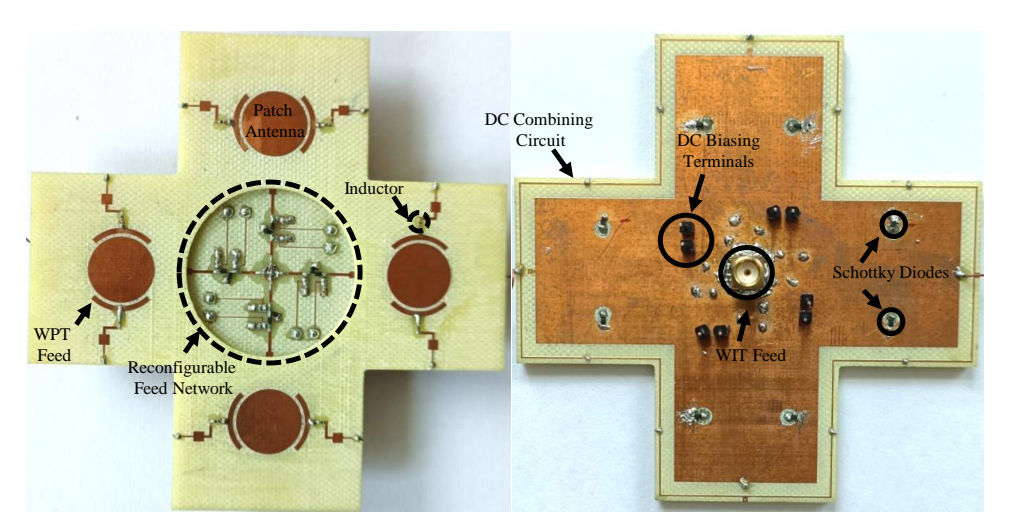


Figure 4.4: Fabricated prototype of the proposed reconfigurable SWIPT antenna array.

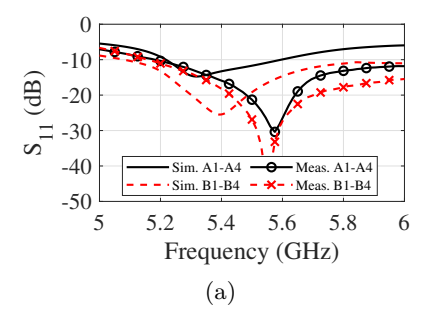
4.3.2 WIT Impedance Matching

The proposed SAA is capable of generating 15 WIT radiation modes depending upon the excitation state of the four RFLs as discussed in Section 4.2.1. The various modes can

be segregated into five groups (A to E) based on the numbers and relative position of excited SAEs. The single SAE excitation is represented by A1-A4, B1-B4 (C1-C2) denote two adjacent (opposite) elements, three-element excitation is indicated by D1-D4 and E1 designates excitation of all four elements. The detailed description of SAEs excited in each mode is presented in Table 4.2, where (\checkmark) and (\times) represent the excited and non-excited

Table 4.2: Excited SAEs in Various WIT Radiation Modes

SAEs	A1	A2	А3	A4	В1	B2	ВЗ	B4	C1	C2	D1	D2	D3	D4	E1
SAE1	✓	×	×	×	✓	×	×	✓	✓	×	√	×	✓	✓	✓
SAE2	X	√	X	X	√	√	X	X	X	√	√	√	×	√	√
SAE3	X	X	√	X	×	✓	√	X	√	×	√	√	√	×	√
SAE4	×	×	×	✓	×	×	✓	✓	×	✓	×	✓	✓	✓	✓



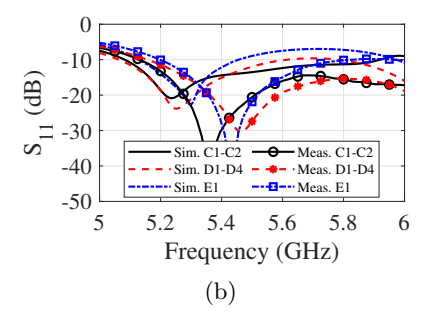


Figure 4.5: Reflection coefficient for various WIT modes of the proposed SAA.

state of the SAE., respectively. The simulated and measured reflection coefficient (S_{11}) results for all the modes are plotted in Fig. 4.5. The results demonstrate impedance matching in the entire 5 GHz WiFi band for all the radiation modes, confirming the wide band WIT capability of the design.

4.3.3 WIT Radiation Characteristics

The simulated WIT 3-D radiation patterns at the edge frequencies of 5 GHz WiFi band (5.15 GHz, 5.35 GHz, 5.725 GHz, and 5.825 GHz) are plotted in Fig. 4.6 for the 1st mode of each radiation group (A – E). In addition, the corresponding max gain, its direction (θ, ϕ) , and HPBW of the 2D pattern comprising the max gain are listed in Table 4.3.

Table 4.3: WIT radiation characteristics of the proposed SAA

		Main Beam												
Me	odes	1	Max Ga	in (dBi)	Dia	rection of M	HPBW						
		5.15	5.35	5.725	5.825	5.15	5.35	5.725	5.825	5.15	5.35	5.725	5.825	
		(GHz)	(GHz)	(GHz)	(GHz)	(GHz)	(GHz)	(GHz) (GHz)		(GHz)	(GHz)	(GHz)	(GHz)	
A	1	4.55	5.4	5.93	4.7	(12°, 134°)	(4°, 128°)	(6°, 188°)	(10°, 238°)	42°	58°	30°	54°	
В	1	5.47	6.37	6.57	5.93	(2°, 240°)	(2°, 228°)	$(2^{\circ}, 206^{\circ})$	(2°, 180°)	36°	38°	42°	52°	
С	1	5	6.54	6.77	6.56	(26°, 202°)	(24°, 168°)	(22°, 186°)	(22°, 198°)	30°	28°	26°	26°	
D	1	5.97	6.33	6.36	6.68	(24°, 14°)	(22°, 358°)	(22°, 158°)	(22°, 160°)	38°	34°	34°	32°	
Е	1	5.39	5.4	5.68	5.89	(32°, 134°)	(32°, 44°)	(30°, 44°)	(30°, 44°)	42°	46°	40°	40°	

The results show maximum gain variation at each frequency (f) across all the modes

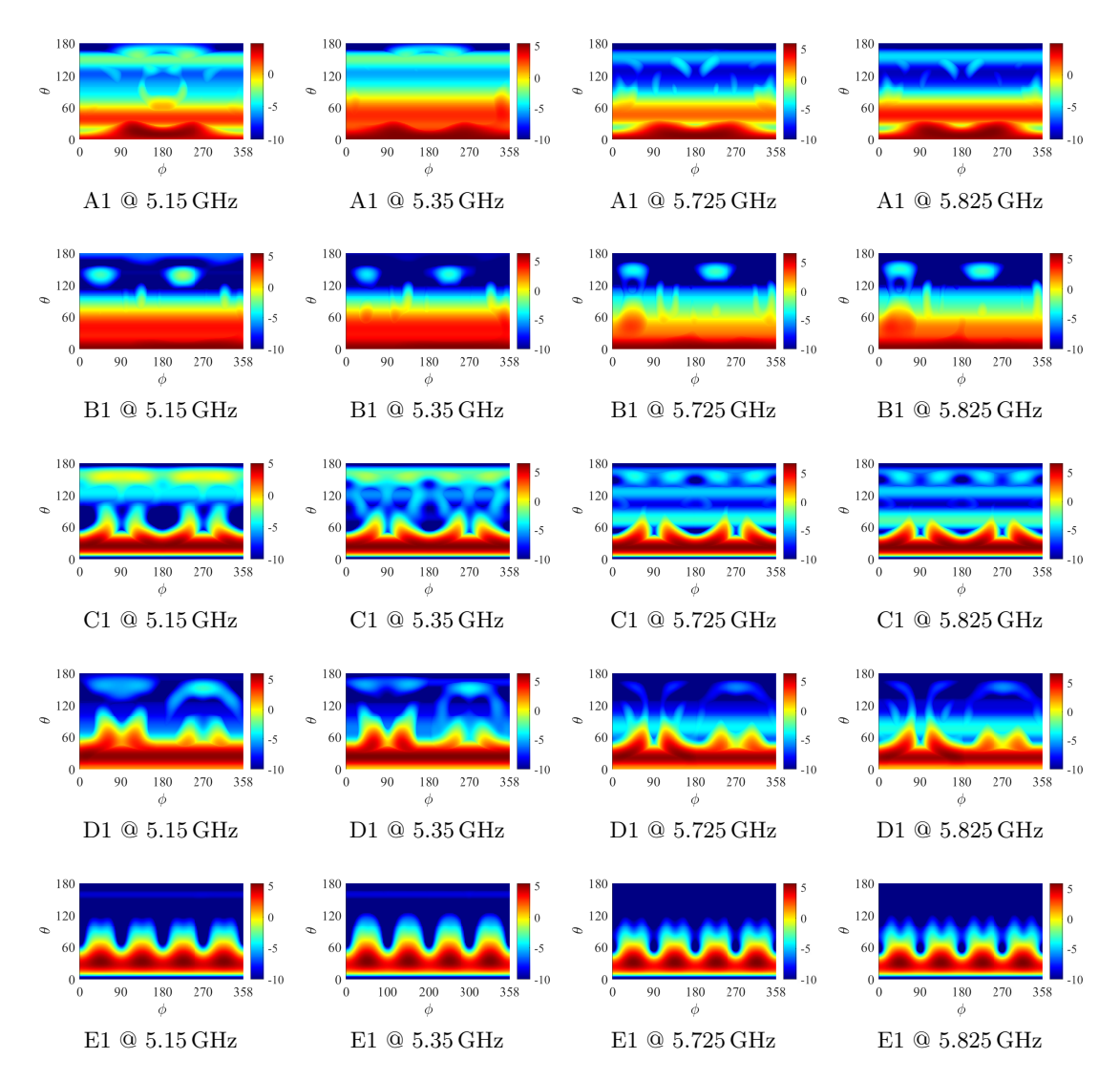


Figure 4.6: 3-D WIT Radiation patterns in A1, B1, C1, D1 and E1 modes at various edge frequencies of 5 GHz WiFi band.

 $\begin{pmatrix} \Delta \\ \forall mode \end{pmatrix} G^{f=f_0}_{max}$ and maximum gain variation for each mode in the entire frequency band $\begin{pmatrix} \Delta G^{mode=M}_{max} \end{pmatrix}$ is < 2 dBi. In A1 and B1 mode SAA radiates in the boresight direction with a small average elevation tilt angle of $\theta=8^\circ$ and 2° , respectively. The θ coverage with ϕ is uniform in case of B1 whereas gaussian pulse type variation in θ is observed for A1 with ϕ . For other remaining modes, SAA radiates its main beam at a larger elevation tilt angle direction with non-uniform θ coverage with ϕ . The C1 mode generates two radiation peaks at an average tilt angle of $\theta=24.5^\circ$ with 31.5° average HPBW with polarization along $\phi=0^\circ$ plane. Similarly, D1 mode emanates radiation at an average elevation tilt angle of 22.25° with 34.25° HPBW in the boresight direction. The E1 enhances the elevation tilt of the radiation pattern to 31° having a null along broadside direction with a wider HPBW of 43.5°. The radiation patterns for other modes in each group are 90° shifted in ϕ from the previous mode due to symmetry in the SAA design along the azimuth plane.

4.3.4 WPT Matching and Coverage Characteristics

The conjugate impedance matching poses difficulties in measuring FWR impedance of a single antenna element on the VNA in the absence of a balun probe. As an alternative to validate the conjugate impedance matching of the FWR circuit, harvested open dc voltage (V_{dc}^{oc}) is measured for input RF signals ranging from 4.5 GHz-5.5 GHz using the measurement setup shown in Fig. 4.7. The results shown in Fig. 4.8(a) illustrate voltage

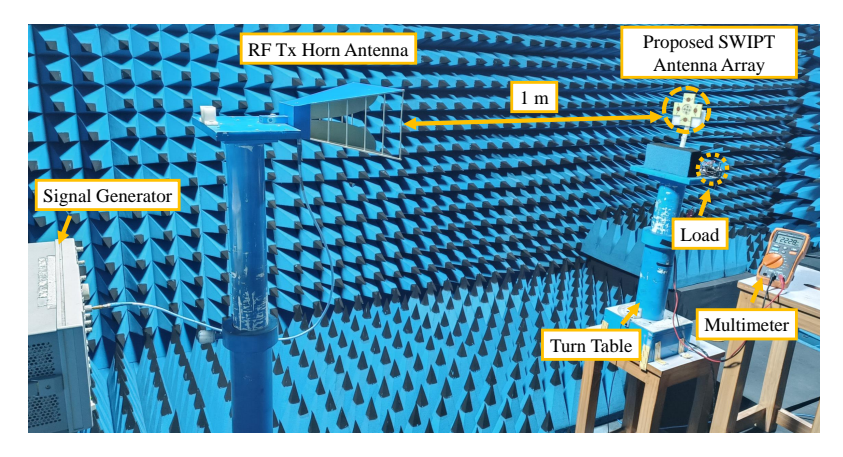


Figure 4.7: Experimental setup to measure WPT performance.

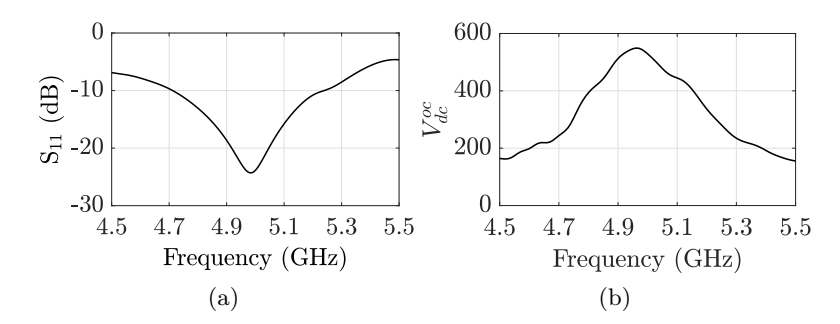


Figure 4.8: (a) Simulated reflection coefficient at WPT port, and (b) Open DC voltage versus frequency of a single antenna element.

maxima (549 mV) at 4.97 GHz, demonstrating precise impedance matching of the FWR near to the desired frequency (5 GHz) and in agreement with the simulated WPT port impedance matching (S₁₁) given in Fig. 4.8(b). The SAA is incident with RF power using a 10 dBi gain horn antenna fed with a 25 dBm input RF power using a signal generator. The output DC voltage across the output load is then measured using a digital multimeter. The measurement results are plotted in Fig. 4.9 for RF-ET polarization is along $\phi = 0^{\circ}$, 90°, and 45° plane. The results indicate that the measured DC pattern is close to the sum of the DC patterns of each element. Moreover, the proposed array has a wide angular coverage in the boresight direction making it usable in a multipath environment.

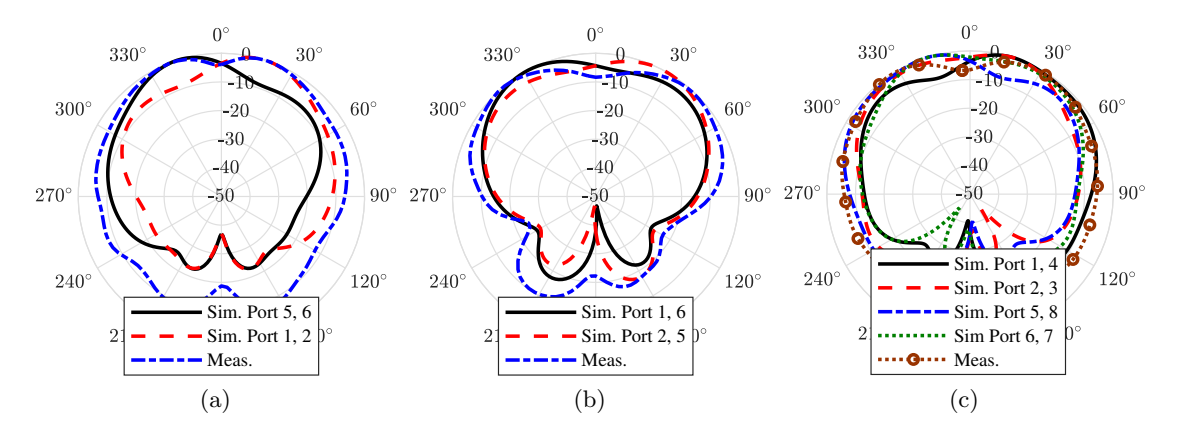


Figure 4.9: Normalized DC patterns of the proposed SAA in (a) $\phi = 0^{\circ}$, (b) $\phi = 90^{\circ}$, and (c) $\phi = 45^{\circ}$ plane.

4.3.5 WPT Power Conversion Efficiency

The harvested dc voltage and PCE of the SWIPT antenna are measured using the measurement setup shown in Fig. 4.7. The received power (P_r) is evaluated using the Friis formula given in (4.1),

$$P_r(dBm) = EIRP(dBm) + G_r(dBi) + 20\log_{10}\left(\frac{\lambda}{4\pi d}\right)$$
(4.1)

where, G_r is the realized antenna gain of the Rx, and λ is the transmitting signal wavelength, EIRP is the effective isotropic radiated power and $d=1\,\mathrm{m}$ is the distance between the Tx and the Rx. The measurements are conducted for Rx planes $\phi=0^\circ$, 90°, and 45° aligned with Tx polarization. This implies that for $\phi=0^\circ$ measurement Tx is placed in horizontal polarization, whereas for $\phi=90^\circ$ it is oriented vertically. However, for $\phi=45^\circ$ the Rx is rotated 45° from the initial orientation to align $\phi=45^\circ$ plane of the Rx with the Tx polarization. The corresponding %PCE and harvested output dc voltage (V_{dc}) are shown versus output load and input RF power (P_r) in Fig. 4.10(a) and Fig. 4.10(b), respectively. The results indicate peak PCE of 58.99%, 35.77%, and 33.26%

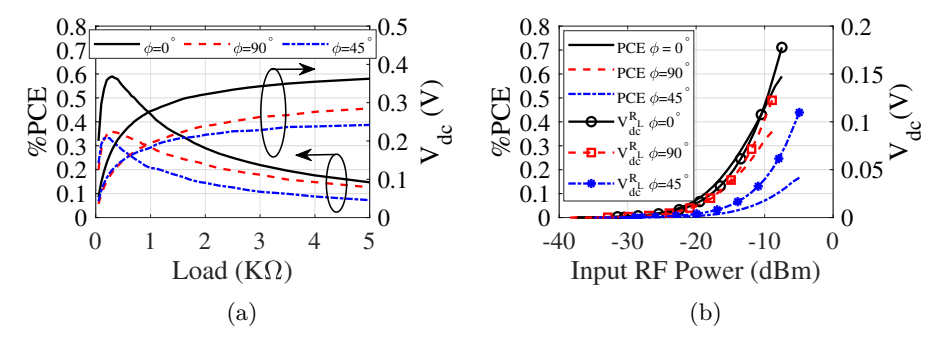


Figure 4.10: %PCE and harvested DC voltage of the SAA versus (a) output load, and (b) input RF power.

for $\phi = 0^{\circ}$, $\phi = 90^{\circ}$, and $\phi = 45^{\circ}$ plane, respectively. The maximum PCE is achieved

at an optimal load of $300\,\Omega$ for $\phi=0^\circ$ and $\phi=90^\circ$ plane and $225\,\Omega$ for $\phi=45^\circ$ plane. The results in Fig. 4.10(b) show a non-linear increase in PCE and output dc voltage with respect to the input RF power. This input RF power corresponds to the non-linear I-V characteristics of the Schottky diode. The difference in the measured and simulated results can be attributed to the different input RF power levels and optimal output load.

4.4 Summary

This chapter introduces a hybrid technique utilizing the integration of antenna switching (AS) with frequency splitting (FS) and dual polarization (DP) to implement a SWIPT antenna system for relay node. The AS helps in achieving pattern and polarization reconfigurable WIT. On the other hand FS and DP techniques make use of separate frequency channels and orthogonal polarization, respectively for WPT and WIT to reduce system complexity. The proposed antenna array design achieves wideband impedance matching (5.15 GHz – 5.825 GHz) for WIT in 5 GHz WiFi band. Moreover, the excitation of different radiation modes allows polarization-insensitive wide beam coverage in both the elevation and azimuth plane. In addition, two Schottky diodes are conjugate impedance matched with each antenna element within the array to achieve FWR of the incident RF waves at 5 GHz. Further, the parallel combining of DC output from each antenna improves the tolerance of WPT for orientation misalignment between the Tx and Rx. The design utilizes proximity and capacitively coupled feed for WIT and WPT signals, respectively to break off the harvested DC flow into the communication circuitry. Moreover, the respective WIT and WPT feeds are oriented orthogonal to each other to enhance isolation between the WIT and WPT signals.

⁰CHAPTER OUTCOMES:

^{[1].} **S. Kumar** and A. Sharma, "TITLE: A system and method for designing an improved SWIPT antenna for a relay node." (*Patent filed with Indian patent office: Application No. 202411086588*).

^{[1].} S. Kumar and A. Sharma, "A Pattern and Polarization Reconfigurable SWIPT Antenna Array for Battery-Assisted Relay Nodes in Cooperative Communication," To be submitted in relevant *IEEE Transactions/Journal*.

Chapter 5

Conclusion and Future Scope

This Thesis presents a quality-aware synthesis approach for antenna systems tailored to various network components in SWIPT enabled IoT networks and applications. Specifically, the synthesis addresses the design requirements for key components including access points, RF energy transmitters, IoT devices, and relay nodes. By optimizing the performance of these antenna systems, this approach aims to enhance the efficiency and reliability of SWIPT-enabled IoT networks. Chapter 2 discusses the synthesis of switched beam multi-sector access point antenna systems, focusing on the integration of BER/SIR and received signal power into the design process. Moreover, a switched beam RF energy transmitter design is also presented for powering WPT-enabled IoT sensor nodes. The Chapter 3 investigates an angular misalignment-tolerant rectenna module designed for WPT-enabled IoT sensor nodes and details the SWIPT antenna design for ultra-low power IoT devices, while Chapter 4 explores the reconfigurable SWIPT antenna array intended for relay node operations.

5.1 Conclusion

5.1.1 QoS Aware Transmitter Antenna System

This chapter introduces QoS aware synthesis of SMB multi-sector access point antennas for enhancing reliable communication coverage. Two antenna array designs Design-1A and Design-1B are synthesized for maximizing the 2-D and 3-D coverage, respectively.

The analytical framework proposed for Design-O1A maximizes the effective communication coverage area (ECA) metric which is defined based on the maximum bit-error-rate and the corresponding signal-to-interference ratio (SIR) limits for the modulation schemes. The required ECA performance is ensured by satisfying power and SIR bounds on their distributions projected on the ground in the desired communication region. As a result, the design parameters such as elevation tilt 20°, number of sectors 10, side-lobe level $SLL_p = 24.77$ dB, and 2×3 size of the patch antenna array (PAA) are analytically optimized. To realize the optimized design parameters, a SBA antenna is fabricated with 2×3 PAA showing maximum gain of 10.06 dBi at 5.8 GHz, $SLL_p = 23.03$ dB, and impedance bandwidth of 292 MHz (5.668 – 5.960 GHz). Moreover, the rigorous measurements revealed that the proposed 10-sector SBA antenna housing 2×3 PAA in each sector could achieve coverage with acceptable quality in the maximum range of 2-13 m with 360° coverage for both BPSK and 64-QAM

modulations. This is achieved even when all the alternate sectors contribute to the co-channel interference. The wide reliable communication coverage, that is achieved by the SBA antenna designed using the proposed BER-conscious approach, implies energy saving by avoiding frequent re-transmissions. In addition, high port isolation $\geq 45.95~\mathrm{dB}$ in the entire band of operation is observed between the PAA of the adjacent sectors permitting their operation at adjacent carrier frequencies. This enables the operation of 10 simultaneous beams implying improved system capacity. The study proved that the proposed BER-conscious array synthesis process and correspondingly designed SBA antenna is a potential candidate for an access point in densely deployed IoT applications.

Similarly, Design-O1B a switched multibeam access point array antenna is proposed to provide 3-D coverage in the IoT applications. The proposed multi-sector antenna is configured with eight sectors which is derived analytically by quality-aware coverage optimization. Each sector having two MAAs to achieve 360° and 93.6° coverage in azimuth and elevation regions, respectively. The beams can be switched among different sectors for azimuth coverage, and the two MAAs incorporated in each sector provide elevation coverage by employing beam switching and beam squint phenomena. The proposed design has a maximum and minimum gain of 7.85 dBi and 4.8 dBi at 5.725 GHz and 5.15 GHz, respectively. Moreover, when the diagonally adjacent MAAs of neighbor sectors are operated at higher (5.725 - 5.825 GHz) and lower (5.15 - 5.35 GHz) WLAN frequency bands, an average interference suppression of 12.65 dB or 11.94 dB, respectively, can be maintained for the drones or crawler bots located at an extreme altitude with respect to the access point height. This enables frequency re-use also in the adjacent sectors and allows the generation of sixteen simultaneous beams in 3-D space resulting in increased system capacity. Furthermore, for the IoT nodes located around the intermediate height range, eight simultaneous beams can be formed covering 360° in azimuth by assigning different frequency bands to any one pair of diagonally adjacent MAAs. In contrast to state-of-the-art designs, the proposed access point eliminates the need for pin diodes or phase shifters for beam switching in the elevation plane. This results in a lower-cost, simpler implementation, making it an excellent candidate for access point antennas in IoT applications that require 3-D quality coverage.

In addition to access points, this chapter introduces a dedicated RF energy transmitter (RF-ET) utilizing the SBA technique, specifically designed to power the proposed 3-D cluster-based WSN. This innovative approach enhances energy efficiency and network performance, facilitating optimal operation in diverse application environments. The proposed RF-ET Tx system comprises nine collocated subarrays, each transmitting RF power to a separate cluster by employing beam switching operation. All the subarrays are designed using an analytically optimized 4×4 microstrip patch array. The excitation coefficients of all the subarrays are optimized using genetic algorithm based on the harvested DC power (P_{dc}) in the 3D coverage region, and an overall improvement of 13.86% in 3-D volume coverage $(P_{dc} \ge -9.5 \text{ dBm})$ is achieved with respect to the uniformly excited subarray. In addition, a coverage range up to 8.7 m is attained such that there

are no blind regions ($P_{dc} < -9.5$ dBm) in between the coverage area of neighboring clusters. Further, The optimal location of the cluster head is determined analytically to reduce the average power consumption of sensor nodes in the WSN cluster. Unlike the state-of-the-art designs, the proposed collocated switched beam array design is compact and easy to deploy. Moreover, the switched beam operation makes the proposed design simple and cheaper than the systems using adaptive beamforming operation in a densely deployed WSN and thus is a good candidate for smart warehouse and smart agriculture applications.

5.1.2 Receiver Antenna for Ultra Low Power IoT Devices

This chapter explores the planar multi-sector ReAS for smart home applications, where RF-ETs are mounted on the ceiling and IoT sensor nodes are deployed in random orientations throughout the home. A multi-polarized circular ReAS (Design-O3A) is proposed for WPT at 5.8 GHz comprising eight circular patch antenna elements. Each ReE is impedance matched with two Shunt Schottky diodes intergrated in mirror symmetry with respect to the patch center for realizing FWR operation. The RF-DC conversion efficiency of 59.7% is achieved at an optimal load of 650 Ω with a small footprint of $1.06 \times 1.06 \lambda^2$. The Design-O3A provides tolerance against polarization mismatch between the RF-ET and rectenna, which enables flexibility in the deployment of sensor nodes at any random orientation within rectenna plane. However, Design-O3A does not provide any tolerance against rotation in any other plane.

To mitigate this problem another compact stacked multi-sector ReAs (Design-O3B) is proposed having nearly isotropic coverage. The Design-O3B utilizes hybrid dc combining of the ReE in eight sectors for WPT at 5.9 GHz, capable of operating in 5.85 GHz-5.98 GHz frequency range. The maximum gain of a single ReE is 3.12 dBi in the proposed system and high isolation ($\geq 30\,\mathrm{dBm}$) with other ReE. The proposed system achieves near isotropic coverage with maximum PCE of 45.54 % at 2.8 k Ω load for $-9.31\,\mathrm{dBm}$ input RF power (Pr) in the endfire direction. Additionally, each ReE within the system is capable of supplying dc power with 61.96 % PCE at 1.6 k Ω for Pr = $-11.26\,\mathrm{dBm}$. Moreover, the system exhibits $\sim 5\%$ variation in PCE over the 1 k Ω to 5 k Ω output load range. The maximum variation in output dc voltage is $\sim 1.56\,\mathrm{dBV}$ at 5.9 GHz with change in orientation for certain output load conditions. The proposed system can easily accommodate a power management unit, sensors, data processing, and RF communication circuitry to realize a compact wireless sensor node for IoT applications.

In order to realize a compact IoT sensor node, this chapter proposes two miniaturized integrated SWIPT antenna designs, Design-O4A and Design-O4B, engineered to provide high WIT efficiency, broad WIT bandwidth, and improved PCE at ultra low input RF power. A novel SWIPT technique that integrates frequency splitting, dual polarization, and DC combining is introduced to achieve high isolation between information and power signal with FWR implementation at ultra low RF power levels, thereby enhancing PCE. Both designs employ a circular patch antenna with a proximity-coupled feed for

information transfer. On the other hand power signal is captured using two co-polarized capacitive coupled feeds orthogonal to the information signal feed. Design-O4A employs conjugate-matched series Schottky diode connections at each capacitive-coupled feed. The DC outputs from each Schottky diode are further combined using a high impedance microstrip line depicted as a DC connection line to achieve FWR operation. The design achieves a PCE of 66.5% at $5.2\,\mathrm{GHz}$ for $-9.91\,\mathrm{dBm}$ input RF power and operates within the WIT band of $5.7\,\mathrm{GHz}$ to $6.0\,\mathrm{GHz}$. It features a radiation efficiency ranging from 78% to 80.23%, all within a footprint of $31.64 \times 28.89\,\mathrm{mm}^2$.

The Design-O4B employs conjugate-matched shunt Schotty diode connections each capacitive-coupled feed. The design integrates an inductor and a stepped impedance low-pass filter to attenuate RF signal transmission through the output load, alongside a modified DC combining network to further improve overall performance over Design-O4A. The design achieves $557\,\mathrm{MHz}$ (5.15 GHz-5.72 GHz) WIT impedance bandwidth (S₁₁ < $-10\,\mathrm{dB}$) with $\geq 78.15\%$ radiation efficiency in the entire 5 GHz WiFi band. Moreover, the WPT operation bandwidth of 4.9 GHz-5.1 GHz with 74.5% peak PCE at 5 GHz is achieved for $-9.16\,\mathrm{dBm}$ input RF power at $700\,\Omega$ optimal load. The harvested DC power enables the operation of the BLE sensor beacon module after integration with PMU, confirming its viability for low-power SWIPT IoT operations at 5 GHz Wi-Fi band. Further, the miniaturized footprint of $37 \times 28.6 \text{ mm}^2$ qualifies the proposed design for battery-less operation of small ultra-lower sensor nodes. This highly optimized design, properly integrated with miniaturized sensor beacon circuitry, facilitates autonomous sensing and communication in isolated environments such as cold storage for vaccines and food warehouses to ensure reliable monitoring and preservation. Advancement in the development of ultra-low power 5 GHz WiFi modules will further allow utilization of the WIT port and allow the proposed work to be utilized to its maximum potential.

5.1.3 SWIPT Antenna Systems for Relay Nodes

This chapter presents a 2×2 SWIPT antenna array for a relay node having reconfigurable radiation characteristic for WIT and angular misalignment tolerant wide beam coverage WPT operation. The antenna elements have an inherent 90° spatial phase difference due to their sequentially rotated placement around the center point. The reconfigurable feed network and the spatial phase difference enabled 15 different radiation modes for WIT function in 5 GHz WiFi frequency band. Moreover, the array has an inherent beam tilt for WPT, providing wide beam coverage. In addition, the sequentially rotated design allows angular misalignment tolerant WPT function. The design achieves maximum WIT coverage of 53° from the broadside direction in the elevation plane. Further, the antenna offers a maximum PCE of 58.99% at an optimal load of $300\,\Omega$ at 5 GHz frequency. The immediately discussed features of the design makes it suitable for battery assisted relay node to realize energy efficient and sustainable cooperative communication relaying in IoT network.

5.1.4 Conclusion on Antenna System Design for IoT Network Components

The proposed designs for IoT applications encompass a range of innovative antenna systems that enhance communication efficiency and energy management. Design-O1A focuses on maximizing the effective communication coverage area by optimizing parameters such as elevation tilt, number of sectors, and side-lobe levels. The resulting patch antenna array achieves impressive metrics, with effective performance under co-channel interference. This approach ensures high port isolation and supports ten simultaneous beams, making it suitable for densely populated IoT environments.

Design-O1B introduces a switched multibeam access point antenna designed for 3-D coverage, featuring eight sectors with each comprising two series fed microstrip antenna arrays placed in mirror symmetry to each other along the elevation plane. This design allows for efficient azimuth and elevation coverage while facilitating frequency reuse, thereby enabling the generation of sixteen simultaneous beams and enhancing overall system capacity. Notably, it eliminates the need for complex components like pin diodes, reducing costs and simplifying deployment.

Additionally, a dedicated RF energy transmitter (RF-ET) is proposed, leveraging the SBA technique for wireless powering of 3-D distributed clustered WSN. This transmitter utilizes nine subarrays, optimized for improved DC power harvesting and coverage without blind spots, making it a viable solution for applications like smart agriculture.

Furthermore, two rectenna arrays systems (Design-O3A and Design-O3B) are introduced to achieve the angular misalignment WPT. Moreover, two miniaturized integrated SWIPT antennas (Design-O4A and Design-O4B) are introduced, combining advanced techniques for high efficiency and broad bandwidth. These antennas demonstrate impressive power conversion efficiencies, suitable for ultra-low power applications, including vaccine storage monitoring.

Overall, these designs highlight significant advancements in antenna technology, addressing the growing demands for efficient and reliable communication in IoT ecosystems, and paving the way for future developments in smart, energy-efficient sensor networks.

5.2 Future Scope

The present work offers significant opportunities for further advancement in the design of antenna systems for IoT network components. The following points provide a detailed discussion on the areas where improvements can be made in each network component antenna system to enhance performance and efficiency.

5.2.1 Access Point

• The current analysis is limited to single-band and linearly polarized antenna designs. Consequently, future investigations should explore the incorporation of multiband capabilities and various polarization schemes, such as dual-linear and circular polarization, into the antenna synthesis process.

- Additional research focused on integrating the propagation channel into the antenna design process may help alleviate the detrimental effects of multipath fading on communication link quality.
- The analysis and optimization of switching circuits to minimize the power consumption.

5.2.2 RF Energy Transmitter

- Further research could be conducted related to the lifespan enhancement of the 3-D clustered WPT enabled WSN.
- Future work could focus on developing localization algorithms to optimize the time intervals of WPT to individual IoT sensor nodes in the application region for the proposed switched beam RF-ET.
- The parametric analysis of WPT systems to maximize the rectification efficiency and minimize the losses.

5.2.3 Rectenna Module

- To reduce the overall footprint of IoT devices, the rectenna module should be designed to be as small as possible. Continued research is needed to further miniaturize the rectenna while preserving the required power conversion efficiency (PCE) and robustness against angular misalignment.
- The proposed iReAS exhibits sensitivity to angular misalignment when the RF
 energy transmitter is vertically polarized, owing to the use of linearly polarized
 end-fire elements. This limitation underscores the need for an innovative rectenna
 module with isotropic polarization coverage to facilitate the seamless deployment of
 IoT devices.
- In the proposed iReAS, only half-wave operation is achievable within a single rectenna element. To enhance power conversion efficiency, future innovations could explore designs that enable full-wave rectification.

5.2.4 SWIPT Antenna Design

- The SWIPT antenna work presented in this thesis can be further advanced to achieve orientation-insensitive isotropic coverage for WPT operations.
- Future research could focus on developing miniaturized SWIPT antenna designs that are fully integrated with the PMU and transceiver modules. This integration

would minimize the overall footprint of the sensor node, potentially enabling novel applications such as endoscopy capsules.

The research presented in this thesis primarily serves as a demonstration, providing a foundation for further detailed analysis and optimization in future works.

References

- [1] L. Chettri and R. Bera, "A Comprehensive Survey on Internet of Things (IoT) Toward 5G Wireless Systems," *IEEE Internet of Things Journal*, vol. 7, no. 1, pp. 16–32, 2020.
- [2] K. Shafique, B. A. Khawaja, F. Sabir, S. Qazi, and M. Mustaqim, "Internet of Things (IoT) for Next-Generation Smart Systems: A Review of Current Challenges, Future Trends and Prospects for Emerging 5G-IoT Scenarios," *IEEE Access*, vol. 8, pp. 23022–23040, 2020.
- [3] S. N. Swamy and S. R. Kota, "An Empirical Study on System Level Aspects of Internet of Things (IoT)," *IEEE Access*, vol. 8, pp. 188 082–188 134, 2020.
- [4] T. D. Ponnimbaduge Perera, D. N. K. Jayakody, S. K. Sharma, S. Chatzinotas, and J. Li, "Simultaneous Wireless Information and Power Transfer (SWIPT): Recent Advances and Future Challenges," *IEEE Communications Surveys & Tutorials*, vol. 20, no. 1, pp. 264–302, 2018.
- [5] M. Agiwal, A. Roy, and N. Saxena, "Next Generation 5G Wireless Networks: A Comprehensive Survey," *IEEE Communications Surveys & Tutorials*, vol. 18, no. 3, pp. 1617–1655, 2016.
- [6] N. Ashraf, S. A. Sheikh, S. A. Khan, I. Shayea, and M. Jalal, "Simultaneous Wireless Information and Power Transfer With Cooperative Relaying for Next-Generation Wireless Networks: A Review," *IEEE Access*, vol. 9, pp. 71 482–71 504, 2021.
- [7] Z. Ding, C. Zhong, D. Wing Kwan Ng, M. Peng, H. A. Suraweera, R. Schober, and H. V. Poor, "Application of smart antenna technologies in simultaneous wireless information and power transfer," *IEEE Communications Magazine*, vol. 53, no. 4, pp. 86–93, 2015.
- [8] I. Krikidis, S. Timotheou, S. Nikolaou, G. Zheng, D. W. K. Ng, and R. Schober, "Simultaneous wireless information and power transfer in modern communication systems," *IEEE Communications Magazine*, vol. 52, no. 11, pp. 104–110, 2014.
- [9] X. Zhu, K. Jin, Q. Hui, W. Gong, and D. Mao, "Long-Range Wireless Microwave Power Transmission: A Review of Recent Progress," *IEEE Journal of Emerging and Selected Topics in Power Electronics*, vol. 9, no. 4, pp. 4932–4946, 2021.
- [10] D. Surender, T. Khan, F. A. Talukdar, and Y. M. Antar, "Rectenna Design and Development Strategies for Wireless Applications: A review," *IEEE Antennas and Propagation Magazine*, vol. 64, no. 5, pp. 16–29, 2022.

[11] X. Gu, S. Hemour, and K. Wu, "Far-Field Wireless Power Harvesting: Nonlinear Modeling, Rectenna Design, and Emerging Applications," *Proceedings of the IEEE*, vol. 110, no. 1, pp. 56–73, 2022.

- [12] O. L. A. López, H. Alves, R. D. Souza, S. Montejo-Sánchez, E. M. G. Fernández, and M. Latva-Aho, "Massive Wireless Energy Transfer: Enabling Sustainable IoT Toward 6G Era," *IEEE Internet of Things Journal*, vol. 8, no. 11, pp. 8816–8835, 2021.
- [13] H. A. H. Alobaidy, M. Jit Singh, M. Behjati, R. Nordin, and N. F. Abdullah, "Wireless Transmissions, Propagation and Channel Modelling for IoT Technologies: Applications and Challenges," *IEEE Access*, vol. 10, pp. 24095–24131, 2022.
- [14] K. Fizza, A. Banerjee, P. P. Jayaraman, N. Auluck, R. Ranjan, K. Mitra, and D. Georgakopoulos, "A Survey on Evaluating the Quality of Autonomic Internet of Things Applications," *IEEE Communications Surveys & Tutorials*, vol. 25, no. 1, pp. 567–590, 2023.
- [15] M. Singh and G. Baranwal, "Quality of service (qos) in internet of things," in 2018 3rd International Conference On Internet of Things: Smart Innovation and Usages (IoT-SIU), 2018, pp. 1–6.
- [16] P. Cardieri and T. Rappaport, "Application of narrow-beam antennas and fractional loading factor in cellular communication systems," *IEEE Transactions on Vehicular Technology*, vol. 50, no. 2, pp. 430–440, 2001.
- [17] T. N. Le, A. Pegatoquet, T. Le Huy, L. Lizzi, and F. Ferrero, "Improving energy efficiency of mobile wsn using reconfigurable directional antennas," *IEEE Communications Letters*, vol. 20, no. 6, pp. 1243–1246, 2016.
- [18] K. S. Hwang, J. Ahn, K.-J. Kim, H. K. Yoon, and Y. J. Yoon, "Pattern reconfigurable antenna for a wireless sensor network sink node," in 2010 Asia-Pacific Microwave Conference, 2010, pp. 2021–2024.
- [19] L. H. Trinh, T. N. Le, R. Staraj, F. Ferrero, and L. Lizzi, "A pattern-reconfigurable slot antenna for iot network concentrators," *Electronics*, vol. 6, no. 4, 2017.
- [20] L. Santamaria, F. Ferrero, R. Staraj, and L. Lizzi, "Slot-based pattern reconfigurable espar antenna for iot applications," *IEEE Transactions on Antennas and Propagation*, vol. 69, no. 7, pp. 3635–3644, 2021.
- [21] W. Hong, Z. H. Jiang, C. Yu, J. Zhou, P. Chen, Z. Yu, H. Zhang, B. Yang, X. Pang, M. Jiang, Y. Cheng, M. K. T. Al-Nuaimi, Y. Zhang, J. Chen, and S. He, "Multibeam antenna technologies for 5g wireless communications," *IEEE Transactions on Antennas and Propagation*, vol. 65, no. 12, pp. 6231–6249, 2017.

[22] Z. Zhang, M. Iskander, Z. Yun, and A. Host-Madsen, "Hybrid smart antenna system using directional elements - performance analysis in flat rayleigh fading," *IEEE Transactions on Antennas and Propagation*, vol. 51, no. 10, pp. 2926–2935, 2003.

- [23] Y. Yang and X. Zhu, "A wideband reconfigurable antenna with 360° beam steering for 802.11ac wlan applications," *IEEE Transactions on Antennas and Propagation*, vol. 66, no. 2, pp. 600–608, 2018.
- [24] M. Burtowy, M. Rzymowski, and L. Kulas, "Low-profile espar antenna for rss-based doa estimation in iot applications," *IEEE Access*, vol. 7, pp. 17403–17411, 2019.
- [25] L. Xing, J. Zhu, Q. Xu, D. Yan, and Y. Zhao, "A circular beam-steering antenna with parasitic water reflectors," *IEEE Antennas and Wireless Propagation Letters*, vol. 18, no. 10, pp. 2140–2144, 2019.
- [26] M. S. Alam and A. M. Abbosh, "Beam-steerable planar antenna using circular disc and four pin-controlled tapered stubs for wimax and wlan applications," *IEEE Antennas and Wireless Propagation Letters*, vol. 15, pp. 980–983, 2016.
- [27] M. S. Alam and A. Abbosh, "Planar pattern reconfigurable antenna with eight switchable beams for wimax and wlan applications," *IET Microwaves, Antennas & Propagation*, vol. 10, no. 10, pp. 1030–1035, 2016.
- [28] —, "A compact reconfigurable antenna with wide tunable frequency and 360° beam scanning," *IEEE Antennas and Wireless Propagation Letters*, vol. 18, no. 1, pp. 4–8, 2019.
- [29] T. Guo, W. Leng, A. Wang, J. Li, and Q. Zhang, "A novel planar parasitic array antenna with frequency- and pattern-reconfigurable characteristics," *IEEE Antennas* and Wireless Propagation Letters, vol. 13, pp. 1569–1572, 2014.
- [30] M. S. Alam, Y. Wang, N. Nguyen-Trong, and A. Abbosh, "Compact circular reconfigurable antenna for high directivity and 360° beam scanning," *IEEE Antennas and Wireless Propagation Letters*, vol. 17, no. 8, pp. 1492–1496, 2018.
- [31] M.-C. Tang, Y. Duan, Z. Wu, X. Chen, M. Li, and R. W. Ziolkowski, "Pattern reconfigurable, vertically polarized, low-profile, compact, near-field resonant parasitic antenna," *IEEE Transactions on Antennas and Propagation*, vol. 67, no. 3, pp. 1467–1475, 2019.
- [32] H. Boutayeb, P. R. Watson, W. Lu, and T. Wu, "Beam switching dual polarized antenna array with reconfigurable radial waveguide power dividers," *IEEE Transactions on Antennas and Propagation*, vol. 65, no. 4, pp. 1807–1814, 2017.
- [33] A. Pal, A. Mehta, D. Mirshekar-Syahkal, and H. Nakano, "A twelve-beam steering low-profile patch antenna with shorting vias for vehicular applications," *IEEE Transactions on Antennas and Propagation*, vol. 65, no. 8, pp. 3905–3912, 2017.

[34] W. Zhang, A. Pal, A. Mehta, D. Mirshekar-Syahkal, and H. Nakano, "Low profile pattern-switchable multibeam antenna consisting of four l-shaped microstrip lines," *IET Microwaves, Antennas & Propagation*, vol. 12, no. 11, pp. 1846–1851, 2018.

- [35] Q. Jia, H. Xu, M. F. Xiong, B. Zhang, and J. Duan, "Omnidirectional solid angle beam-switching flexible array antenna in millimeter wave for 5g micro base station applications," *IEEE Access*, vol. 7, pp. 157027–157036, 2019.
- [36] K.-S. Kim, J.-S. Yoo, J.-W. Kim, S. Kim, J.-W. Yu, and H. L. Lee, "All-around beam switched antenna with dual polarization for drone communications," *IEEE Transactions on Antennas and Propagation*, vol. 68, no. 6, pp. 4930–4934, 2020.
- [37] Y. Gan, P. Yang, and F. Yang, "Dual-band and dual-polarized reconfigurable beam-steering array for wlan applications," in 2019 IEEE International Symposium on Antennas and Propagation and USNC-URSI Radio Science Meeting, 2019, pp. 2059–2060.
- [38] H. Wang, Z. Zhang, Y. Li, and M. F. Iskander, "A switched beam antenna with shaped radiation pattern and interleaving array architecture," *IEEE Transactions on Antennas and Propagation*, vol. 63, no. 7, pp. 2914–2921, 2015.
- [39] C. Gu, S. Gao, B. Sanz-Izquierdo, E. A. Parker, F. Qin, H. Xu, J. C. Batchelor, X. Yang, and Z. Cheng, "3-d coverage beam-scanning antenna using feed array and active frequency-selective surface," *IEEE Transactions on Antennas and Propagation*, vol. 65, no. 11, pp. 5862–5870, 2017.
- [40] A. Kesavan, M. Mantash, J. Zaid, and T. A. Denidni, "A dual-plane beam-sweeping millimeter-wave antenna using reconfigurable frequency selective surfaces," *IEEE Antennas and Wireless Propagation Letters*, vol. 17, no. 10, pp. 1832–1836, 2018.
- [41] M. A. Erni, G. G. Mendoza, and S. M. Cheng, "Design and implementation of a 3d beam steering antenna for cellular frequencies," in 2019 IEEE Asia-Pacific Microwave Conference (APMC), 2019, pp. 1524–1526.
- [42] G.-W. Yang and S. Zhang, "A dual-band shared-aperture antenna with wide-angle scanning capability for mobile system applications," *IEEE Transactions on Vehicular Technology*, vol. 70, no. 5, pp. 4088–4097, 2021.
- [43] W. C. Zheng, L. Zhang, Q. X. Li, and Y. Leng, "Dual-band dual-polarized compact bowtie antenna array for anti-interference mimo wlan," *IEEE Transactions on Antennas and Propagation*, vol. 62, no. 1, pp. 237–246, 2014.
- [44] P. Ngamjanyaporn, C. Phongcharoenpanich, P. Akkaraekthalin, and M. Krairiksh, "Signal-to-interference ratio improvement by using a phased array antenna of switched-beam elements," *IEEE Transactions on Antennas and Propagation*, vol. 53, no. 5, pp. 1819–1828, 2005.

[45] R. Yamaguchi, Y. Ohta, H. Omote, Y. Sugita, and T. Fujii, "Throughput improvement by combined tilting of base station antenna," in 2013 7th European Conference on Antennas and Propagation (EuCAP), 2013, pp. 871–873.

- [46] L. Wang and Q. Liao, "Wideband multibeam siw horn array with high beam isolation and full azimuth coverage," *IEEE Transactions on Antennas and Propagation*, vol. 69, no. 9, pp. 6070–6075, 2021.
- [47] Z. Zhou, S. Zhou, S. Cui, and J.-H. Cui, "Energy-efficient cooperative communication in a clustered wireless sensor network," *IEEE Transactions on Vehicular Technology*, vol. 57, no. 6, pp. 3618–3628, 2008.
- [48] G. Oliveri, L. Poli, and A. Massa, "Maximum efficiency beam synthesis of radiating planar arrays for wireless power transmission," *IEEE Transactions on Antennas and Propagation*, vol. 61, no. 5, pp. 2490–2499, 2013.
- [49] Y. Yao, L. W. Song, and Y. L. Liu, "Subarray partition design of receiving antenna for microwave power transmission," in 2019 International Conference on Microwave and Millimeter Wave Technology (ICMMT), 2019, pp. 1–3.
- [50] G. Pabbisetty, K. Murata, K. Taniguchi, T. Mitomo, and H. Mori, "Evaluation of space time beamforming algorithm to realize maintenance-free iot sensors with wireless power transfer system in 5.7-ghz band," *IEEE Transactions on Microwave Theory and Techniques*, vol. 67, no. 12, pp. 5228–5234, 2019.
- [51] A. A. Aziz, L. Ginting, D. Setiawan, J. H. Park, N. M. Tran, G. Y. Yeon, D. I. Kim, and K. W. Choi, "Battery-less location tracking for internet of things: Simultaneous wireless power transfer and positioning," *IEEE Internet of Things Journal*, vol. 6, no. 5, pp. 9147–9164, 2019.
- [52] N. Shinohara, "History and innovation of wireless power transfer via microwaves," *IEEE Journal of Microwaves*, vol. 1, no. 1, pp. 218–228, 2021.
- [53] Q. Hui, K. Jin, and X. Zhu, "Directional radiation technique for maximum receiving power in microwave power transmission system," *IEEE Transactions on Industrial Electronics*, vol. 67, no. 8, pp. 6376–6386, 2020.
- [54] Y. Tanaka, K. Kanai, R. Hasaba, H. Sato, Y. Koyanagi, T. Ikeda, H. Tani, S. Kajiwara, and N. Shinohara, "A study of received power in distributed wireless power transfer system," in 2020 IEEE International Symposium on Antennas and Propagation and North American Radio Science Meeting, 2020, pp. 1355–1356.
- [55] K. W. Choi, A. A. Aziz, D. Setiawan, N. M. Tran, L. Ginting, and D. I. Kim, "Distributed wireless power transfer system for internet of things devices," *IEEE Internet of Things Journal*, vol. 5, no. 4, pp. 2657–2671, 2018.

[56] Y. Tanaka, H. Hamase, K. Kanai, R. Hasaba, H. Sato, Y. Koyanagi, T. Ikeda, H. Tani, M. Gokan, S. Kajiwara, and N. Shinohara, "Simulation and implementation of distributed microwave wireless power transfer system," *IEEE Transactions on Microwave Theory and Techniques*, vol. 71, no. 1, pp. 102–111, 2023.

- [57] C. M. A. Niamien, "Optimum antenna characteristics for maximally harvesting ambient rf energy," *IEEE Open Journal of Antennas and Propagation*, vol. 3, pp. 1364–1381, 2022.
- [58] W. Deng, S. Wang, B. Yang, and S. Zheng, "A multibeam ambient electromagnetic energy harvester with full azimuthal coverage," *IEEE Internet of Things Journal*, vol. 9, no. 11, pp. 8925–8934, 2022.
- [59] C. Song, P. Lu, and S. Shen, "Highly efficient omnidirectional integrated multiband wireless energy harvesters for compact sensor nodes of internet-of-things," *IEEE Transactions on Industrial Electronics*, vol. 68, no. 9, pp. 8128–8140, 2021.
- [60] M. Kumar, S. Kumar, and A. Sharma, "An analytical framework of multisector rectenna array design for angular misalignment tolerant rf power transfer systems," *IEEE Transactions on Microwave Theory and Techniques*, vol. 71, no. 4, pp. 1835–1847, 2023.
- [61] E. Vandelle, D. H. N. Bui, T.-P. Vuong, G. Ardila, K. Wu, and S. Hemour, "Harvesting ambient rf energy efficiently with optimal angular coverage," *IEEE Transactions on Antennas and Propagation*, vol. 67, no. 3, pp. 1862–1873, 2019.
- [62] M. Kumar, S. Kumar, and A. Sharma, "A planar orbicular rectenna array system with 3-d uniform coverage for wireless powering of iot nodes," *IEEE Transactions* on Microwave Theory and Techniques, vol. 71, no. 3, pp. 1366–1373, 2023.
- [63] M. Kumar, S. Kumar, A. S. Bhadauria, and A. Sharma, "A planar integrated rectenna array with 3-d-spherical dc coverage for orientation-tolerant wireless-power-transfer-enabled iot sensor nodes," *IEEE Transactions on Antennas and Propagation*, vol. 71, no. 2, pp. 1285–1294, 2023.
- [64] S. Roy, J. J. Tiang, M. B. Roslee, M. T. Ahmed, A. Z. Kouzani, and M. A. P. Mahmud, "Quad-band rectenna for ambient radio frequency (rf) energy harvesting," Sensors, vol. 21, no. 23, 2021.
- [65] Y.-Y. Hu, S. Sun, H. Xu, and H. Sun, "Grid-array rectenna with wide angle coverage for effectively harvesting rf energy of low power density," *IEEE Transactions on Microwave Theory and Techniques*, vol. 67, no. 1, pp. 402–413, 2019.
- [66] P. Lu, K. Huang, C. Song, Y. Ding, and G. Goussetis, "Optimal power splitting of wireless information and power transmission using a novel dual-channel rectenna," *IEEE Transactions on Antennas and Propagation*, vol. 70, no. 3, pp. 1846–1856, 2022.

[67] P. Lu, X.-S. Yang, and B.-Z. Wang, "A two-channel frequency reconfigurable rectenna for microwave power transmission and data communication," *IEEE Transactions on Antennas and Propagation*, vol. 65, no. 12, pp. 6976–6985, 2017.

- [68] P. Lu, C. Song, and K. M. Huang, "A two-port multipolarization rectenna with orthogonal hybrid coupler for simultaneous wireless information and power transfer (swipt)," *IEEE Transactions on Antennas and Propagation*, vol. 68, no. 10, pp. 6893–6905, 2020.
- [69] M. Wagih, G. S. Hilton, A. S. Weddell, and S. Beeby, "2.4 ghz wearable textile antenna/rectenna for simultaneous information and power transfer," in 2021 15th European Conference on Antennas and Propagation (EuCAP), 2021, pp. 1–5.
- [70] L. Liao, Z. Li, Y. Tang, and X. Chen, "Dual-polarized dipole antenna for wireless data and microwave power transfer," *Electronics*, vol. 11, no. 5, 2022.
- [71] M. Wagih, G. S. Hilton, A. S. Weddell, and S. Beeby, "Dual-band dual-mode textile antenna/rectenna for simultaneous wireless information and power transfer (swipt)," *IEEE Transactions on Antennas and Propagation*, vol. 69, no. 10, pp. 6322–6332, 2021.
- [72] H. K. Sahu and P. R. Sahu, "Ssk-based swipt with af relay," *IEEE Communications Letters*, vol. 23, no. 4, pp. 756–759, 2019.
- [73] S. Claessens, N. Pan, D. Schreurs, and S. Pollin, "Multitone fsk modulation for swipt," *IEEE Transactions on Microwave Theory and Techniques*, vol. 67, no. 5, pp. 1665–1674, 2019.
- [74] I. Krikidis, S. Sasaki, S. Timotheou, and Z. Ding, "A low complexity antenna switching for joint wireless information and energy transfer in mimo relay channels," *IEEE Transactions on Communications*, vol. 62, no. 5, pp. 1577–1587, 2014.
- [75] D. Kumar, O. L. Alcaraz López, S. K. Joshi, and A. Tölli, "Latency-aware multi-antenna swipt system with battery-constrained receivers," *IEEE Transactions* on Wireless Communications, vol. 22, no. 5, pp. 3022–3037, 2023.
- [76] X.-X. Yang, C. Jiang, A. Z. Elsherbeni, F. Yang, and Y.-Q. Wang, "A novel compact printed rectenna for data communication systems," *IEEE Transactions on Antennas and Propagation*, vol. 61, no. 5, pp. 2532–2539, 2013.
- [77] M. Ali, G. Yang, and R. Dougal, "A new circularly polarized rectenna for wireless power transmission and data communication," *IEEE Antennas and Wireless Propagation Letters*, vol. 4, pp. 205–208, 2005.
- [78] M. Wagih, G. S. Hilton, A. S. Weddell, and S. Beeby, "Dual-polarized wearable antenna/rectenna for full-duplex and mimo simultaneous wireless information and

power transfer (swipt)," *IEEE Open Journal of Antennas and Propagation*, vol. 2, pp. 844–857, 2021.

- [79] J.-H. Ou, B. Xu, S. F. Bo, Y. Dong, S.-W. Dong, J. Tang, and X. Y. Zhang, "Highly-isolated rf power and information receiving system based on dual-band dual-circular-polarized shared-aperture antenna," *IEEE Transactions on Circuits* and Systems I: Regular Papers, vol. 69, no. 8, pp. 3093–3101, 2022.
- [80] G.-L. Zhu, J.-X. Du, X.-X. Yang, Y.-G. Zhou, and S. Gao, "Dual-polarized communication rectenna array for simultaneous wireless information and power transmission," *IEEE Access*, vol. 7, pp. 141 978–141 986, 2019.
- [81] Y.-M. Zhang and J.-L. Li, "A dual-polarized antenna array with enhanced interport isolation for far-field wireless data and power transfer," *IEEE Transactions on Vehicular Technology*, vol. 67, no. 11, pp. 10258–10267, 2018.
- [82] H.-M. Lee, "Effect of partial ground plane removal on the front-to-back ratio of a microstrip antenna," in 2013 7th European Conference on Antennas and Propagation (EuCAP), 2013, pp. 1204–1208.
- [83] B. Clerckx, R. Zhang, R. Schober, D. W. K. Ng, D. I. Kim, and H. V. Poor, "Fundamentals of wireless information and power transfer: From rf energy harvester models to signal and system designs," *IEEE Journal on Selected Areas in Communications*, vol. 37, no. 1, pp. 4–33, 2019.
- [84] I. Krikidis, "Simultaneous information and energy transfer in large-scale networks with/without relaying," *IEEE Transactions on Communications*, vol. 62, no. 3, pp. 900–912, 2014.
- [85] K. Agrawal, S. Prakriya, and M. F. Flanagan, "Optimization of swipt with battery-assisted energy harvesting full-duplex relays," *IEEE Transactions on Green Communications and Networking*, vol. 5, no. 1, pp. 243–260, 2021.
- [86] K. Agrawal, A. Jee, and S. Prakriya, "Performance of a multiuser cooperative iot noma network with battery-assisted energy harvesting," *IEEE Transactions on Industrial Informatics*, vol. 20, no. 2, pp. 2307–2319, 2024.
- [87] K. Agrawal, S. Prakriya, and M. F. Flanagan, "Ts-based swipt in full-duplex relayed noma with intelligent relay battery management," *IEEE Transactions on Communications*, vol. 71, no. 9, pp. 5137–5151, 2023.
- [88] K. Agrawal, A. Jee, and S. Prakriya, "Performance of swipt in cooperative networks with direct link and nonlinear energy harvesting at the battery-assisted relay," *IEEE Transactions on Green Communications and Networking*, vol. 6, no. 2, pp. 1198–1215, 2022.

[89] Y. Zheng, J. Hu, and K. Yang, "Swipt aided cooperative communications with energy harvesting-based selective-decode-and-forward protocol: Benefiting from channel aging effect," *IEEE Transactions on Green Communications and Networking*, vol. 7, no. 3, pp. 1192–1204, 2023.

- [90] A. Raza, R. Keshavarz, and N. Shariati, "Precision agriculture: Ultra-compact sensor and reconfigurable antenna for joint sensing and communication," *IEEE Transactions on Instrumentation and Measurement*, vol. 73, pp. 1–13, 2024.
- [91] M. Oshaghi and M. J. Emadi, "Throughput maximization of a hybrid eh-swipt relay system under temperature constraints," *IEEE Transactions on Vehicular Technology*, vol. 69, no. 2, pp. 1792–1801, 2020.
- [92] M. Amjad, A. Ahmed, M. Naeem, M. Awais, W. Ejaz, and A. Anpalagan, "Resource management in energy harvesting cooperative iot network under qos constraints," Sensors, vol. 18, no. 10, 2018.
- [93] W. Lu, G. Liu, P. Si, G. Zhang, B. Li, and H. Peng, "Joint resource optimization in simultaneous wireless information and power transfer (swipt) enabled multi-relay internet of things (iot) system," *Sensors*, vol. 19, no. 11, 2019.
- [94] H. Kawabata, K. Ishibashi, S. Vuppala, and G. T. F. de Abreu, "Robust relay selection for large-scale energy-harvesting iot networks," *IEEE Internet of Things Journal*, vol. 4, no. 2, pp. 384–392, 2017.
- [95] Y. Zou, J. Zhu, and X. Jiang, "Joint power splitting and relay selection in energy-harvesting communications for iot networks," *IEEE Internet of Things Journal*, vol. 7, no. 1, pp. 584–597, 2020.
- [96] C. A. Balanis, Antenna theory: analysis and design. John wiley & sons, 2015.
- [97] F. J. Lopez-Martinez and J. M. Romero-Jerez, "Asymptotically exact approximations for the symmetric difference of generalized marcum q-functions," *IEEE Transactions on Vehicular Technology*, vol. 64, no. 5, pp. 2154–2159, 2015.
- [98] D. Inserra, W. Hu, and G. Wen, "Antenna array synthesis for rfid-based electronic toll collection," *IEEE Transactions on Antennas and Propagation*, vol. 66, no. 9, pp. 4596–4605, 2018.
- [99] N. Azmi, L. M. Kamarudin, M. Mahmuddin, A. Zakaria, A. Y. M. Shakaff, S. Khatun, K. Kamarudin, and M. N. Morshed, "Interference issues and mitigation method in wsn 2.4ghz ism band: A survey," in 2014 2nd International Conference on Electronic Design (ICED), 2014, pp. 403–408.
- [100] C.-W. Hung, W.-T. Hsu, and K.-H. Hsia, "Using adaptive data rate with dsss optimization and transmission power control for ultra-low power wsn," in 2019 12th

- International Conference on Developments in eSystems Engineering (DeSE), 2019, pp. 611–614.
- [101] H. Fan, X. Liang, J. Geng, R. Jin, and X. Zhou, "Switched multibeam circular array with a reconfigurable network," *IEEE Transactions on Antennas and Propagation*, vol. 64, no. 7, pp. 3228–3233, 2016.
- [102] M. Kahar and M. K. Mandal, "A wideband tightly coupled slot antenna for 360° full azimuthal beam steering applications," *IEEE Transactions on Antennas and Propagation*, vol. 69, no. 6, pp. 3538–3542, 2021.
- [103] C. A. Balanis, Antenna Theory: Analysis and Design. USA: Wiley-Interscience, 2005.
- [104] M. Schwartz, "Characteristics of the mobile radio environment-propagation phenomena," in *Mobile Wireless Communications*. Cambridge University Press, 2004.
- [105] R. Chopra and G. Kumar, "Series-Fed Binomial Microstrip Arrays for Extremely Low Sidelobe Level," *IEEE Transactions on Antennas and Propagation*, vol. 67, no. 6, pp. 4275–4279, 2019.
- [106] H. Mirzaei and G. V. Eleftheriades, "Arbitrary-Angle Squint-Free Beamforming in Series-Fed Antenna Arrays Using Non-Foster Elements Synthesized by Negative-Group-Delay Networks," *IEEE Transactions on Antennas and Propagation*, vol. 63, no. 5, pp. 1997–2010, 2015.
- [107] R. Chopra and G. Kumar, "Series- and Corner-Fed Planar Microstrip Antenna Arrays," *IEEE Transactions on Antennas and Propagation*, vol. 67, no. 9, pp. 5982–5990, 2019.
- [108] C. A. Balanis, Antenna theory: analysis and design. John wiley & sons, 2015.
- [109] D. Pozar and D. Schaubert, "Comparison of three series fed microstrip array geometries," in *Proceedings of IEEE Antennas and Propagation Society International Symposium*, 1993, pp. 728–731 vol.2.
- [110] M. C. Tan, M. Li, Q. H. Abbasi, and M. A. Imran, "A Wideband Beamforming Antenna Array for 802.11ac and 4.9 GHz in Modern Transportation Market," *IEEE Transactions on Vehicular Technology*, vol. 69, no. 3, pp. 2659–2670, 2020.
- [111] J. McSpadden, L. Fan, and K. Chang, "Design and experiments of a high-conversion-efficiency 5.8-GHz rectenna," *IEEE Trans. Microw. Theory Techn.*, vol. 46, no. 12, pp. 2053–2060, 1998.
- [112] X. Li, B. Duan, J. Zhou, L. Song, and Y. Zhang, "Planar Array Synthesis for Optimal Microwave Power Transmission With Multiple Constraints," *IEEE Antennas Wireless Propag. Lett.*, vol. 16, pp. 70–73, 2017.

[113] M. Schwartz, "Characteristics of the mobile radio environment–propagation phenomena," in *Mobile Wireless Communications*. Cambridge Univ. Press, 2004.

- [114] X. Cai, W. Geyi, and Y. Guo, "A compact rectenna with flat-top angular coverage for rf energy harvesting," *IEEE Antennas Wireless Propag. Lett.*, vol. 20, no. 7, pp. 1307–1311, 2021.
- [115] D. Belo, D. C. Ribeiro, P. Pinho, and N. Borges Carvalho, "A Selective, Tracking, and Power Adaptive Far-Field Wireless Power Transfer System," *IEEE Trans. Microw. Theory Techn.*, vol. 67, no. 9, pp. 3856–3866, 2019.
- [116] V. Kuhn, C. Lahuec, F. Seguin, and C. Person, "A Multi-Band Stacked RF Energy Harvester With RF-to-DC Efficiency Up to 84%," *IEEE Trans. Microw. Theory Techn.*, vol. 63, no. 5, pp. 1768–1778, 2015.
- [117] K. Murata, T. Mitomo, M. Higaki, and K. Onizuka, "A 5.8-GHz 64-Channel Phased Array Microwave Power Transmission System Based on Space-Time Beamforming Algorithm for Multiple IoT Sensors," in 2018 48th European Microwave Conference (EuMC), 2018, pp. 170–173.
- [118] M. Kumar, S. Kumar, and A. Sharma, "A compact 3-d multisector orientation insensitive wireless power transfer system," *IEEE Microwave and Wireless Technology Letters*, vol. 33, no. 3, pp. 363–366, 2023.
- [119] —, "Dual-purpose planar radial-array of rectenna sensors for orientation estimation and rf-energy harvesting at iot nodes," *IEEE Microwave and Wireless Components Letters*, vol. 32, no. 3, pp. 245–248, 2022.
- [120] S. Shen, J. Kim, C. Song, and B. Clerckx, "Wireless power transfer with distributed antennas: System design, prototype, and experiments," *IEEE Transactions on Industrial Electronics*, vol. 68, no. 11, pp. 10868–10878, 2021.
- [121] N. Ghassemi and K. Wu, "High-efficient patch antenna array for e-band gigabyte point-to-point wireless services," *IEEE Antennas and Wireless Propagation Letters*, vol. 11, pp. 1261–1264, 2012.
- [122] N. Ghassemi, K. Wu, S. Claude, X. Zhang, and J. Bornemann, "Low-cost and high-efficient w-band substrate integrated waveguide antenna array made of printed circuit board process," *IEEE Transactions on Antennas and Propagation*, vol. 60, no. 3, pp. 1648–1653, 2012.
- [123] Y.-X. Sun, K. W. Leung, and K. Lu, "Compact Dual Microwave/Millimeter-Wave Planar Shared-Aperture Antenna for Vehicle-to-Vehicle/5G Communications," *IEEE Trans. Veh. Technol.*, vol. 70, no. 5, pp. 5071–5076, 2021.
- [124] T. Matsunaga, E. Nishiyama, and I. Toyoda, "5.8-GHz Stacked Differential Rectenna Suitable for Large-Scale Rectenna Arrays With DC Connection," *IEEE Transactions* on Antennas and Propagation, vol. 63, no. 12, pp. 5944–5949, 2015.

[125] R. Trevisoli, H. P. d. Paz, V. S. d. Silva, R. T. Doria, I. R. S. Casella, and C. E. Capovilla, "Modeling Schottky Diode Rectifiers Considering the Reverse Conduction for RF Wireless Power Transfer," *IEEE Trans. Circuits Syst. II, Exp. Briefs*, vol. 69, no. 3, pp. 1732–1736, 2022.

- [126] Skyworks Solutions, "Surface-Mount Mixer and Detector Schottky Diodes," SMS7621-079LF datasheet.
- [127] F. Erkmen, T. S. Almoneef, and O. M. Ramahi, "Electromagnetic Energy Harvesting Using Full-Wave Rectification," *IEEE Transactions on Microwave Theory and Techniques*, vol. 65, no. 5, pp. 1843–1851, 2017.
- [128] J. McSpadden and K. Chang, "A dual polarized circular patch rectifying antenna at 2.45 GHz for microwave power conversion and detection," in 1994 IEEE MTT-S International Microwave Symposium Digest (Cat. No.94CH3389-4), 1994, pp. 1749–1752 vol.3.
- [129] P. Lu, C. Song, and K. M. Huang, "A Compact Rectenna Design With Wide Input Power Range for Wireless Power Transfer," *IEEE Trans. Power Electron.*, vol. 35, no. 7, pp. 6705–6710, 2020.
- [130] M. Kumar, S. Kumar, S. Jain, and A. Sharma, "A plug-in type integrated rectenna cell for scalable rf battery using wireless energy harvesting system," *IEEE Microwave and Wireless Components Letters*, pp. 1–4, 2022.
- [131] Analog Devices, "Ultralow Power Boost Regulator with MPPT and Charge Management," https://www.analog.com/media/en/technical-documentation/data-sheets/ADP5090.pdf, Accessed [online]: Dec. 2023.
- [132] —, "ADP5090-2-EVALZ User Guide," https://www.analog.com/media/en/technical-documentation/user-guides/adp5090-2-evalz_ug-782.pdf, Accessed [online]: Dec. 2023.
- [133] R. P. Sirigina, A. S. Madhukumar, and M. Bowyer, "BER Analysis of Interference-Limited Synchronous Wireless Networks With Line-of-Sight Links," *IEEE Communications Letters*, vol. 23, no. 3, pp. 542–545, 2019.
- [134] Analog Devices, "Ultralow Power Energy Harvester PMUs with MPPT and Charge Management," https://www.mouser.in/datasheet/2/609/ADP5091_5092-1503530. pdf, Accessed [online]: May. 2024.
- [135] Infineon Technologies, "Solar-Powered Internet of Things (IoT) Device Kit User Guide," https://www.infineon.com/dgdl/Infineon-S6SAE101A00SA1002_User_ Guide-UserManual-v01_00-EN.pdf?fileId=8ac78c8c7d0d8da4017d0efa925a107a& utm_source=cypress&utm_medium=referral&utm_campaign=202110_globe_en_all_integration-files&redirId=File_1_8_133, Accessed [online]: May. 2024.

[136] G. Loubet, A. Takacs, and D. Dragomirescu, "Implementation of a Battery-Free Wireless Sensor for Cyber-Physical Systems Dedicated to Structural Health Monitoring Applications," *IEEE Access*, vol. 7, pp. 24679–24690, 2019.

- [137] C. Cao, X. Zhang, C. Song, A. Georgiadis, and G. Goussetis, "A Highly Integrated Multipolarization Wideband Rectenna for Simultaneous Wireless Information and Power Transfer (SWIPT)," *IEEE Transactions on Antennas and Propagation*, vol. 71, no. 10, pp. 7980–7991, 2023.
- [138] X. Zhang, C. Cao, and C. Song, "A Compact Dual-band, Dual-CP Polarization Wideband Rectenna Using Reverse Wilkinson Power Divider for Wireless Information and Power Transfer," *IEEE Antennas and Wireless Propagation Letters*, pp. 1–5, 2024.
- [139] S. Kumar, M. Kumar, A. Sharma, and I. J. Garcia Zuazola, "Energizing an IoT Sensor Using Regenerative Opposite Fringing Fields From an Embedded Communicating Patch Antenna," *IEEE Access*, vol. 12, pp. 47951–47960, 2024.
- [140] P. A. Pichet Moeikham, Chatree Mahatthanajatuphat, "A Compact UWB Antenna with a Quarter-Wavelength Strip in a Rectangular Slot for 5.5 GHz Band Notch," International Journal of Antennas and Propagation, 2013.
- [141] A. A. Benbuk, N. Kouzayha, J. Costantine, and Z. Dawy, "Charging and Wake-Up of IoT Devices using Harvested RF Energy with Near-Zero Power Consumption," *IEEE Internet of Things Magazine*, vol. 6, no. 1, pp. 162–167, 2023.